



SAPIENZA
UNIVERSITÀ DI ROMA

Thesis submitted in partial fulfilment of the requirements for the degree of Doctor of Philosophy in Energy and Environment (Science and Technology for the Industrial Innovation) at the Faculty of Engineering, Sapienza University of Rome, Italy

SOME ANALYSIS ON THE ANOMALIES OCCURRING DURING ENTRY IN MARTIAN ATMOSPHERE

Supervisors

Prof. PAOLO TEOFILATTO

Prof. ANTONELLA INGENITO

Candidate Name

JEANAUSTIN SOLOMON

Matricola: 1889683

XXXV cycle

Department of Astronautics Electrical and Energy Engineering (DIAEE)

Sapienza University of Rome, Italy

2019-2022

CONTENTS

ACKNOWLEDGEMENT.....	vii
NOMENCLATURE.....	viii
LIST OF FIGURES.....	xii
LIST OF TABLES.....	xx
ABSTRACT.....	xxi
CHAPTER 1 INTRODUCTION.....	1
1.1 Description of the Schiaparelli Mission.....	1
1.1.1Module.....	3
1.2 Description of the nominal Schiaparelli re-entry trajectory.....	6
1.2.1 Entry Interface Point (EIP).....	6
1.2.2 Entry.....	9
1.2.3 Parachute Deployment Phase.....	11
1.3 Description of the failure.....	17
CHAPTER 2 HYPOTHESIS OF THE FAILURE.....	29
2.1 Different hypothesis according to the ESA Report.....	29
2.1.1 IMU Malfunctioning.....	30
2.1.2 High Dynamic Oscillatory Motion.....	31
2.1.3 Links between unexpected spin rate and transverse angular rate.....	32
2.1.4 Riser Angle.....	33
2.1.5 Inadequate persistent time of IMU Saturation flag by GNC.....	34
2.2 The failure due to aerial oscillations.....	36
CHAPTER 3 MARS ENVIRONMENT.....	42
3.1 Mars Gravity Field.....	42
3.1.1 Mars orbital Missions.....	43
3.1.2 Data of NASA-DSN with solution of gravity.....	44
3.2 Mars Atmosphere.....	45
3.3 Statistical models of the Mars atmosphere.....	48
3.3.1 Variation in Density along with altitude.....	49
3.3.2 Variation in Temperature along with altitude.....	51
3.3.3 Latitudinal and Longitudinal Variations.....	52
CHAPTER 4 ANALYSIS OF TRAJECTORY.....	56
4.1 The flow around capsules during re-entry phase.....	56
4.2 Reconstruction of the real altitude motion.....	67
CHAPTER 5 NUMERICAL SETUP FOR RE-ENTRY SIMULATION.....	76
5.1 The flow capsules during the re-entry phase.....	77
5.1.1 Governing Equations.....	77
5.1.2 Finite Volume Method.....	80
5.1.3 Turbulence modelling.....	81
5.1.4 Chemical Kinetic model.....	85
5.2 Validation of the numerical algorithm by literature results.....	86
5.2.1 Aerodynamic Analysis for manned space vehicles for mission to mars.....	87
5.2.1.1 Design and meshing of the MSV capsule.....	87

5.2.1.2 Boundary conditions.....	88
5.2.1.3 Validation of Results.....	90
5.2.2 Aerothermodynamic Analysis of Ducted re-entry vehicles.....	100
5.2.2.1 Design and meshing.....	100
5.2.2.2 Method of simulation.....	101
5.2.2.3 Validation of Results.....	101
5.2.3 MSV capsule at M=1.94 and 10.....	104
5.2.3.1 Designing and Meshing of MSV capsule at $\alpha=2^\circ$	104
5.2.3.2 Method of Simulation.....	107
5.2.3.3 Validation of Results.....	107
CHAPTER 6 THE WAKE OF THE PARACHUTE DYNAMICS.....	127
6.1 The flow around the Schiaparelli Capsule and Parachute.....	127
6.1.1 Schiaparelli Capsule.....	127
6.1.1.1 Design and Meshing.....	127
6.1.1.2 Boundary conditions.....	128
6.1.1.3 Validation of Results.....	129
6.1.2 Parachute of Schiapparelli.....	137
6.1.2.1 Design and meshing.....	137
6.1.2.2 Validation of Results.....	138
6.2 Effect of chemical decomposition.....	145
6.2.1 CO ₂ mass fraction.....	148
6.2.2 N ₂ mass fraction.....	151
6.2.3 Ar mass fraction.....	154
6.2.4 CO mass fraction.....	157
6.2.5 O ₂ mass fraction.....	160
6.3 The flow at the different regimes during re-entry.....	163
6.3.1 Subsonic Regime.....	166
6.3.2 Low Supersonic Regime.....	167
6.3.3 High Supersonic Regime.....	168
6.4 The possible oscillation regime occurring during Schiaparelli mission.....	169
CHAPTER 7 SIMULATION OF THE SCHIAPARELLI FINAL ALTITUDE AND TRAJECTORY.....	171
7.1 Simulation of the Schiaparelli Trajectory and altitude in the hypothesis failure due to aerial oscillations.....	171
7.1.1 Design of Schiaparelli Trajectory anomaly with various angle of attacks.....	171
7.1.2 Meshing and Grid Independence Test.....	172
7.1.3 Boundary Conditions.....	173
7.1.4 Validation of Results for final Trajectory.....	174
7.1.4.1 Simulation of parachute using SST k- ω at $\alpha=0^\circ$, M=2.04814.....	177
7.1.4.2 Simulation of parachute using LES at M=1.75, P=538Pa.....	191
7.1.4.3 Simulation of parachute using SST k- ω at $\alpha=20^\circ$, M=2.04814.....	204
CHAPTER 8 FINAL REMARKS.....	216
REFERENCES.....	218

ACKNOWLEDGEMENT

I would like to thank God for blessing me with an opportunity to pursue graduate studies and giving me strength, wisdom, and health to overcome all the difficulties encountered throughout the period.

I acknowledge my sincere indebtedness and gratitude to my parents for their love, and sacrifice they've given throughout their lives. I cannot find the appropriate words to properly describe my appreciation for their devotion, support, and faith in my abilities to attain my goals.

I would like to express my sincere gratitude to my supervisors Professor Dr.Paolo Teofilatto, Full Professor and Professor Dr.Antonella Ingenito,Assistant Professor, School of Aerospace Engineering, for their critical suggestions, constructive criticism, motivation, and guidance for carrying out related research and for preparing the associated reports and presentations. Their encouragement and support towards the current topic helped me a lot in this research and thesis.

I wish to convey my sincere gratitude to Professor Dr.Gianfranco Caruso, Ph.D Coordinator,Dipartimento di Ingegneria Astronautica,Elettrica ed Energetica(DIAEE) ,Dr.Stefano Carletta, Researcher, School of Aerospace Engineering, Professor Dr.Mauro pontani, Assosiate professor, Dipartimento di Ingegneria Astronautica, Elettrica ed Energetica(DIAEE), Professor Dr.Giovanni Battista Palmerini ,Dean, School of School of Aerospace Engineering for permitting me to successfully complete this Research and thesis in the university.

I would also like to thank former Master's degree candidates Relangi Naresh, Laxmi Narayana Phaneendra Peri, Navaid Ali and other Students from School of Aerospace Engineering for their support and constant help in designing, analysing the results from the simulations and also for the preparation of the thesis report.

I would like My Cousin Dr. Deepak Arun Annamalai, Associate Professor, Saveetha School of Engineering, Chennai, Tamilnadu for their guidance and support to complete the Research and thesis.

NOMENCLATURE

ACRONYM	Definition
TGO	Trace Gas Orbiter
EDM	Entry, Descent and landing Demonstration Module
EDL	Entry, Descent and Landing
TPS	Thermal Protection System
BS	Back Sheild
BSR	Back Sheild Release
FS	Front Shield
FSR	Front Shield Release
TPS	Thermal Protection System
GNC	Guidance Navigation Control
DECA	Descent Camera
CTPU	Computer Terminal Power Unit
SDS	Sun Detection Sensor
IMU	Inertial Measurement unit
RDA	Radar Doppler Unit
ESA	European Space Agency
EDDS	ESA EGOs Data Dissemination System
PSA	Planetary Science Archive
MER	Mars Exploration Rover
UHF	Ultra-High Frequency
DGB	Disk Gap Band
EIP	Entry Interface Point
AT	Along Track
FPA	Flight Path Angle
CT	Cross Track
HDG	Heading
DSM	Deep Space Manoeuvre
DMS	Deimos Space
TCM	Trim Correction Manoeuvre
MSA	Main Separation Assembly
AoA	Angle of Attack
AoS	Angle of Sideslip
AGL	Altitude at Ground Level
SEP	Separation
ECP	Entry Control Point
ATDB	Aero Thermodynamic DataBase

AEDB	Aerodynamic Data Base
PDD	Parachute Deployment Device firing
GAT	G-Activated Timer
MOLA	Mars Orbiter Laser Altimeter
JPL	Jet Propulsion Laboratory
OBT	On-Board Telemetry
COG	Centre of Gravity
CFD	Computational Fluid Dynamics
DOF	Degree Of Freedom
MCD	Mars Climate Database
MC	Monte Carlo
EMCD	European Mars Climate Database
RFD	Radio frequency Devotions
RFW	Radio Frequency waiver
NCR	Non-Conformance Re-Entry
SIB	Schiaparelli Inquiry Board
MSL	Mars Science Laboratory
MGS	Mars Global Surveyor
MRO	Mars Reconnaissance orbiter
LST	Local Solar Time
OBSW	On-Board Software
E2E	Entry-2-Entry
GNC-SW	GNC Software
RRC	Retro-Rockets Cut-off
RRI	Retro-Rockets Ignition
MCI	Mass, CoG and Inertia
ESOC	European Space Operations Centre
MMED	Mars Mean Equator of Date
RANS	Reynolds-averaged Navier-Stokes
MSV	Manned Space Vehicle
CEV	Crew Exploration Vehicle
SST	Shear Stress Transport
RCS	Reaction Control System
LES	Large Eddy Simulation
TAS-I	Thales Alenia Space Italia
COMARS+	Combined Aerothermal and Radiometer Sensors Instrument Package
SPICAM	Spectroscopy for the Investigation of the Characteristics of the Atmosphere of Mars
DREAMS	Dust Characterization, Risk assessment and Environmental Analyser on the Martian surface
BS1	Bow Shock at region 1 (Capsule)
BS2	Bow Shock at region 2 (Canopy)

TW1	Turbulent wake at region 1 (Capsule)
TW2	Turbulent Wake at region 2 (Canopy)
RS1	Recompression Shocks at region 1(Capsule)
RS2	Recompression Shocks at region 2 (Canopy)

Greek letters	Description
α	Angle of attack
σ	Stephen Boltzmann constant
k	Turbulent kinetic energy
ω	Specific dissipation rate
ρ	Density
ε	Dissipation per unit time
γ	Gas constant
μ	Dynamic Pressure
λ	Thermal conductivity
τ	Friction factor
$\dot{\omega}$	Angular Acceleration

Roman letters	Description
I_y	Transverse inertia moment
$\Delta\Omega_y$	Yaw angular rate
ΔT	Time interval
DT/DX	Temperature distribution
Dv _x /Dx	Velocity Distribution at X-direction
$\Delta\Omega_z$	Roll angular rate
$\Delta\Omega_x$	Pitch angular rate
M	Mach number
M_{kick}	Torque of the system in Yaw Component
M_{aero}	Aerodynamic Torque
q	Dynamic Pressure
P	Static Pressure
T	Static Temperature
S	Parachute reference surface
L_{tot}	Distance between parachute curve pressure and centre of Mass
M_x	Momentum in x-direction
M_y	Momentum in y-direction
M_z	Momentum in z-direction
I	Gas Index
A_0	Constant related to turbulent model
f	Total external force
u	Flow velocity vector

D	Diffusion coefficient
T_d, T_v	Control Temperatures
$\nabla\phi$	Fluid characteristic,
S_ϕ	Source or sink of ϕ
H_{den}	Scalar factor of altitude
H	Altitude

LIST OF FIGURES

Fig 1. 2D Geometry of the Schiaparelli EDM.....	4
Fig 2. 2D Geometry of the Schiaparelli EDM Parachute.....	4
Fig 3. E4 MC, Position Dispersion at EIP for Nominal.....	8
Fig 4. E4 MC, Attitude at EIP	8
Fig 5. E4 MC, MC statistics for total heat load at stagnation point (Sutton-Graves)....	9
Fig 6. E4 MC, MC statistics for heat flux at stagnation point (Sutton-Graves)	9
Fig 7. E4 MC, MC statistics for maximum sizing heat flux (Steep correlation)	10
Fig 8. E4 MC, MC statistics for load factor during entry.....	10
Fig 9. Conditions at parachute deployment ad inflation.....	12
Fig 10. Bridle angle convention on ExoMars.....	13
Fig 11. MC, MC statistics for altitude at drogue deployment.....	14
Fig 12. E4 MC, MC statistics for Mach at drogue deployment.....	14
Fig 13. E4 MC, Drogue deployment condition in terms of Mach and dynamic pressure.....	13
Fig 14. E4 MC, Drogue deployment condition in terms of flight path angle and altitude.....	13
Fig 15. E4 MC, MC statistics for inflation force at fully drogue deployment.....	16
Fig 16. E4 MC, MC statistics for dynamic pressure at drogue deployment.....	16
Fig 17. E4 MC, MC statistics for flight path angle at drogue deployment.....	16
Fig 18. Impact point (dark spot) localization on the low-resolution MRO image of Meridian Planum.....	17
Fig 19. DM, parachute, and front shield impact points localization on the high-resolution MRO image of Meridian Planum.....	17
Fig 20. Comparison of Maximum Parachute Load with respect to inflation time.....	19
Fig 21. GNC and IMU reference systems definition with respect to EDM global system.....	22
Fig 22. EDM body-axes moments reconstruction (left) and angular rates (right) before blackout.....	23
Fig 23. Attitude angles (with respect to local vertical) during entry, OBT vs most likely profiles.....	24
Fig 24. AoA-AoS trim point used for EDM CoG reconstruction.....	25
Fig 25. EDM body-axes moments reconstruction (left) and angular rates (right) after blackout.....	26
Fig 26. Yaw and pitch moments: comparison between most likely (blue) and reconstructed(red).....	27
Fig 27. Yaw and pitch moments: reconstructed (red, left) and MER (blue, right)	27
Fig 28. Description about Hypothesis of an EDM failure in Factor tree diagram.....	30

Fig 29. Pre-flight (grey, 5000 shots) and post-flight (blue, 3000 shots) dispersions at EIP Credit: DEIMOS Space.....	34
Fig 30. Body axes non-gravitational accelerations: key descent phase events. Credit: DEIMOS Space.....	35
Fig 31. IMU navigation: angular rates and saturation. Credit: DEIMOS Space.....	35
Fig 32. Inertial Euler's angles (red: OBT, green: reconstructed by DEIMOS, blue: most likely trajectory). Credit: DEIMOS Space.....	36
Fig 33. Images of the supersonic instability known as "area oscillations" (from left to right) at Mach 2.0, 2.2, and 2.5 for a 0.8-m DGB parachute.....	37
Fig 34. The angular rates Ω_y , Ω_z during the parachute inflation and stabilization....	38
Fig 35. The lateral aerodynamic coefficient of the parachute.....	40
Fig 36. The symmetry of the pressure on the canopy produces no lateral force.....	41
Fig 37. Map of the global topography of Mars. The projection is Mollweide centered at 0° longitude.....	43
Fig 38. Atmospheric Composition of Mars and Earth.....	47
Fig 39 The spatial and seasonal distribution of the 616 SPICAM solar occultation....	48
Fig 40. Examples of (top) three typical SPICAM CO ₂ density profiles and (bottom)the corresponding derived temperature profiles.....	50
Fig 41. Temperature retrieved between 50°S and 50°N plotted as a function of season (Ls) and interpolated at four pressure levels.....	52
Fig 42. Latitudinal temperature variations in early southern winter (Ls = 90°– 120°) interpolated at four pressure levels. Note the 30 K polar warming above the 0.01 Pa (90 km) level.....	54
Fig 43. E2E Real Re-entry trajectory, ground track (from separation to touchdown)	62
Fig 44. E2E Real Re-entry trajectory, ground track (from separation to touchdown)	63
Fig 45. Most Real Re-entry trajectory, total Load factor as function of time (from EIP to touchdown)	63
Fig 46. Real Re-entry trajectory, total Heat flux at stagnation as function of time (from EIP to touchdown)	64
Fig 47. Real Re-entry trajectory, total Heat load as function of time (from EIP to touchdown)	65
Fig 48. Real Re-entry trajectory, dynamic pressure as function of time (from EIP to touchdown).....	65
Fig 49. Real Re-entry trajectory, altitude above ground as function of co-rotating velocity (from EIP to touchdown).....	66
Fig 50. Real Re-entry trajectory, co-rotating flight path angle as function of time (from EIP to touchdown).....	66
Fig 51. Real re-entry trajectory, EDM mass as function of time (from EIP to touchdown)	67
Fig 52. Real re-entry trajectory, identification of the most likely touchdown position.....	67

Fig 53. Post-SEP attitude reconstruction, reconstructed Poinsot motion vs measured attitude rates.....	69
Fig 54. Post-SEP attitude reconstruction, reconstructed vs measured attitude rates profiles.....	72
Fig 55. Post-SEP attitude reconstruction, reconstructed vs measured attitude angles profiles.....	73
Fig 56. Real Altitude rate comparision (dots: OBT,lines:simulation).....	75
Fig 57. MSV Capsule.....	87
Fig 58. Meshing of MSV Capsule.....	88
Fig 59. Static pressure contour for MSV capsule at $\alpha=10^\circ$ and M=10 (a).[24], (b). Current work.....	91
Fig 60. Static pressure contour for MSV capsule at $\alpha =20^\circ$ and M=20 (a).[24], (b). Current work.....	92
Fig 61. Velocity-Mach number contour for MSV at $\alpha = 10^\circ$ and M= 10 (a).[24], (b). Current work.....	94
Fig 62. Velocity - Mach number contour for MSV at M = 20, and $\alpha = 20^\circ$ a).[24], (b). Current work.....	95
Fig 63. Static temperature contour for MSV at M = 20 and $\alpha = 20^\circ$ (a).[25], (b). Current work.....	97
Fig 64. CO ₂ Mass fraction contour for MSV at M = 20 and $\alpha = 20^\circ$ (a)[24], (b). Current work.....	98
Fig 65. Design of Orion capsule.....	100
Fig 66. Mesh of numerical domain for the Orion CEV Re-entry Vehicle.....	101
Fig 67. Comparison of the baseline re-entry vehicle Pressure at M = 2, (a).[33], (b). Current work.....	102
Fig 68. Comparison of the baseline re-entry vehicle Pressure at M = 5, (a).[33], (b). current work.....	103
Fig 69. Design of MSV capsule at $\alpha = 2^\circ$	104
Fig 70. Domain length of 100m.....	105
Fig 71. Mesh image of Re-entry capsule.....	105
Fig 72. Mesh of computational domain with 100m length.....	106
Fig 73. Static pressure contour for MSV capsule at $\alpha=2^\circ$ and M=1.94.....	109
Fig 74. Static pressure along the domain axial distance at $\alpha=2^\circ$, M=1.94 for domain length 100m.....	109
Fig 75. Static pressure contour for MSV capsule at $\alpha=2^\circ$ and M=10.....	110
Fig 76. Static pressure along the domain axial distance at $\alpha=2^\circ$, M=10 for domain length=100.....	110
Fig 77. Density contour for MSV capsule at $\alpha=2^\circ$ and M=1.94.....	112
Fig 78. Density along the domain axial distance at $\alpha=2^\circ$, M=1.94 for domain length =100m.....	113
Fig 79. Density contour for MSV capsule at $\alpha=2^\circ$ and M=10.....	113
Fig 80. Density along the domain axial distance at $\alpha=2^\circ$, M=10 for domain length =100m.....	114

Fig 81. Static temperature contour for MSV capsule at $\alpha=2^\circ$, M=1.94.....	115
Fig 82. Static temperature along the domain axial distance at $\alpha=2^\circ$, M=1.94 for domain length=100m.....	115
Fig 83. Static temperature contour for MSV capsule at $\alpha=2^\circ$, M=10.....	116
Fig 84. Static temperature along the domain axial distance at $\alpha=2^\circ$, M = 10 for domain length=100m.....	117
Fig 85. DT/Dx contour for MSV capsule at $\alpha=2^\circ$, M=1.94.....	118
Fig 86. DT/Dx along the domain axial distance at $\alpha=2^\circ$, M = 1.94 for domain length = 100m.....	119
Fig 87. DT/Dx contour for MSV capsule at $\alpha=2^\circ$, M=10.....	119
Fig 88. DT/Dx along the domain axial distance at $\alpha=2^\circ$, M=10 for domain length =100m.....	120
Fig 89. Dx _v /DX Contour for MSV Capsule at $\alpha=2^\circ$, M=1.94.....	121
Fig 90. Dx _v /Dx along the domain axial distance at $\alpha=2^\circ$, M= 1.94 for domain length=100m.....	122
Fig 91. Dx _v /Dx contour for MSV capsule at $\alpha=2^\circ$, M=10.....	122
Fig 92. Dx _v /Dx along the domain axial distance at $\alpha=2^\circ$, M = 10 for domain length = 100m.....	123
Fig 93. Velocity-Mach number contour for MSV capsule at $\alpha=2^\circ$ and M=1.94.....	124
Fig 94. Velocity-Mach number along the domain axial distance at $\alpha=2^\circ$, M = 1.94 for domain length = 100m.....	125
Fig 95. Velocity-Mach number contour for MSV capsule at $\alpha=2^\circ$ and M=10.....	125
Fig 96. Velocity-Mach number along the domain axial distance at $\alpha=2^\circ$, M = 10 for domain length = 100m.....	126
Fig 97. Design of a Schiaparelli EDM.....	127
Fig 98. 3D Design of Schiaparelli anomaly with enclosure booleaned.....	128
Fig 99. Mesh of the Schiaparelli EDM.....	128
Fig 100. Static pressure contour of Schiaparelli EDM at H = 10km (from Table 24) above mars at $\alpha=0^\circ$	130
Fig 101. Static pressure along the domain axial distance at H= 10km above mars, $\alpha = 0^\circ$ for domain length=100m.....	131
Fig 102. Density contour of Schiaparelli EDM at H = 10km (from Table 24) above mars at $\alpha=0^\circ$	
Fig 103. Density along the domain axial distance at H= 10km above mars, $\alpha = 0^\circ$ for domain length=100m.....	133
Fig 104. Velocity-Mach number contour of Schiaparelli EDM at H = 10km (from Table 6.3) above mars and $\alpha=0^\circ$	134
Fig 105. Velocity -Mach number along the domain axial distance at H= 10km above mars, $\alpha=0^\circ$ for domain length=100m.....	135
Fig 106. Static temperature contour of Schiaparelli EDM at H=10km (from Table 23) above mars and $\alpha=0^\circ$	136
Fig 107. Static temperature along the domain axial distance at H= 10km above mars, $\alpha=0^\circ$ for domain length=100m.....	137

Fig 108. Design of the parachute.....	137
Fig 109. Mesh of the parachute.....	138
Fig 110. Static pressure contours of the parachute at $\alpha=0^\circ$, H=10 km above mars....	139
Fig 111. Static pressure along the domain axial distance at H=10km, $\alpha=0^\circ$ for domain length=100m.....	140
Fig 112. Density contours of the parachute at $\alpha=0^\circ$, H=10km above mars.....	141
Fig 113. Density along the domain axial distance for at H=10km, $\alpha=0^\circ$ for domain length=100m.....	141
Fig 114. Velocity-Mach number contours of the parachute at $\alpha=0^\circ$ and H = 10km above mars.....	142
Fig 115. Velocity pathlines of parachute Taken from Reference [35]	143
Fig 116. Mach number along the domain axial distance for at H= 10km, $\alpha=0^\circ$ for domain length=100m.....	144
Fig 117. Static temperature contours of the Parachute at $\alpha=0^\circ$ and H=10km.....	144
Fig 118. Static temperature along the domain axial distance at H= 10km, $\alpha=0^\circ$ for domain length =100m.....	145
Fig 119. CO ₂ mass fraction contour of Schiaparelli EDM at H=20km above mars and $\alpha=0^\circ$	148
Fig 120. CO ₂ mass fraction along the domain axial distance for H=20km above mars at $\alpha=0^\circ$ and domain length=100m.....	149
Fig 121. CO ₂ mass fraction contour of Schiaparelli EDM at H=50km above mars and $\alpha=0^\circ$	150
Fig 122. CO ₂ mass fraction along the domain axial distance at H= 50km above mars, $\alpha=0^\circ$ for domain length=100m.....	150
Fig 123. N ₂ Mass fraction contour of Schiaparelli EDM at H=20km above mars and $\alpha=0^\circ$	151
Fig 124. N ₂ mass fraction along the domain axial distance at H= 20km above mars, $\alpha=0^\circ$ for domain length=100m.....	152
Fig 125. N ₂ mass fraction contour of Schiaparelli EDM at H=50km above mars and $\alpha=0^\circ$	153
Fig 126. N ₂ mass fraction along the domain axial distance at H= 50km above mars, $\alpha=0^\circ$ for domain length=100m.....	153
Fig 127. Ar mass fraction contour of Schiaparelli EDM at H=20km above mars and $\alpha=0^\circ$	154
Fig 128. Ar mass fraction along the domain axial distance at H= 20km above mars, $\alpha=0^\circ$ for domain length100m.....	155
Fig 129. Ar mass fraction contour of Schiaparelli EDM at H=50km above mars and $\alpha=0^\circ$	155
Fig 130. Ar Mass fraction along the domain axial distance at H= 50km above mars at $\alpha=0^\circ$ for domain length 100m.....	156
Fig 131. CO Mass fraction contour of Schiaparelli EDM at H=20km above mars and $\alpha=0^\circ$	157

Fig 132. CO Mass fraction along the domain axial distance at H= 20km above mars, $\alpha=0^\circ$ for domain length=100m.....	158
Fig 133. CO Mass fraction contour of Schiaparelli EDM at H= 50 km above mars and $\alpha=0^\circ$	158
Fig 134. CO Mass fraction along the domain axial distance at H= 50km above mars, $\alpha=0^\circ$ for domain length=100m.....	159
Fig 135. O ₂ Mass fraction contour of Schiaparelli EDM at H=20km at $\alpha=0^\circ$	160
Fig 136. O ₂ Mass fraction along the domain axial distance at H= 20km above mars, $\alpha=0^\circ$ for domain length=100m.....	160
Fig 137. O ₂ Mass fraction contour of Schiaparelli EDM at H= 50km at $\alpha=0^\circ$	161
Fig 138. O ₂ Mass fraction along the domain axial distance at H= 50km above mars, $\alpha=0^\circ$ for domain length=100m.....	162
Fig 139. Pressure coefficient C _p vs Axial distance (x/L) plotted along the sectional surface of baseline re-entry vehicle in subsonic regime.....	164
Fig 140. Ballistic Factor Vs Altitude(H) of Re-entry capsule and its canopy.....	165
Fig 141. Drag coefficient (C _D) Vs Altitude(H) of Re-entry capsule and canopy.....	165
Fig 142. Lift coefficient (L _D) Vs Altitude(H) of Re-entry capsule and canopy.....	166
Fig 143. Sub sonic regime of (a) Re-entry capsule and (b) Canopy.....	167
Fig 144. Low-supersonic regime of (a) Re-entry capsule and (b) Canopy.....	167
Fig 145. High supersonic regime of (a) Re-entry capsule and (b) Canopy.....	168
Fig 146. X-yaw and Y-pitch angular rate reconstructed after gyro saturation, interpolated using a cubic function and resampled at 100 Hz.....	170
Fig 147. Design of a re-entry capsule with parachute at $\alpha=0^\circ$	171
Fig 148. Design of a re-entry capsule with parachute at $\alpha=20^\circ$	172
Fig 149. Mesh of the computational domain.....	172
Fig 150. General flow features around the interacting surfaces. Iso-contours indicate streamwise velocity and isolines indicate pressure one instant.....	176
Fig 151. Static pressure contour for Re-entry parachute at $\alpha=0^\circ$, H=10km and M=2.04814.....	177
Fig 152. Static pressure along the domain axial distance at $\alpha =0^\circ$, H=10km, M=2.04814 and domain length 120m.....	178
Fig 153. Static pressure vector for Re-entry parachute at $\alpha=0^\circ$, H=10km and M=2.04814	179
Fig 154. Density contour for Re-entry parachute at $\alpha=0^\circ$, H=10km and M=2.04814.	179
Fig 155. Density along the domain axial distance $\alpha=0^\circ$, H=10km, M=2.04814 and domain length=120m.....	180
Fig 156. Velocity-Mach number contours for Re-entry parachute at $\alpha=0^\circ$, H=10km and M=2.04814.....	181
Fig 157. Velocity-Mach number along the domain axial distance at $\alpha=0^\circ$, H=10km, M=2.04814 and domain length 120m.....	182
Fig 158. Static temperature Contours for Re-entry parachute at $\alpha=0^\circ$, H=10km and M=2.04814	183

Fig 159. Static temperature along the domain axial distance at $\alpha=0^\circ$, H=10km, M=2.04814 and domain length=120m.....	184
Fig 160. CO ₂ Mass Fraction Contours for Re-entry parachute at $\alpha=0^\circ$, H=10km and M=2.04814.....	185
Fig 161. CO ₂ Mass Fraction along the domain axial distance at $\alpha=0^\circ$, H=10km, M=2.04814 and domain length 120m.....	186
Fig 162. N ₂ Mass Fraction Contours for Re-entry parachute for H=10km above mars at $\alpha =0^\circ$ and M=2.04814.....	187
Fig 163. N ₂ Mass fraction along the domain axial distance $\alpha=0^\circ$, H=10km, M=2.04814 and domain length=120m.....	188
Fig 164. Ar Mass fraction contours for Re-entry parachute at $\alpha=0^\circ$, M=2.04814....	189
Fig 165. Ar Mass fraction along the domain axial distance $\alpha=0^\circ$, M=2.04814 and domain length = 120m.....	190
Fig 166. Static pressure contour for Re-entry parachute at $\alpha=0^\circ$, M=1.75.....	191
Fig 167. Static pressure along the domain axial distance at M=1.75, $\alpha =0^\circ$ and domain length = 120m.....	192
Fig 168. Density contour for Re-entry parachute at $\alpha =0^\circ$ and M=1.75.....	193
Fig 169. Density along the domain axial distance at M=1.75, $\alpha=0^\circ$ and domain length = 120m.....	193
Fig 170. Velocity-Mach number Contour for Re-entry parachute at $\alpha=0^\circ$, M=1.75....	194
Fig 171. Velocity-Mach Number along the domain axial distance at M=1.75, $\alpha =0^\circ$ and domain length = 120m.....	195
Fig 172. Static temperature contour for Re-entry parachute at M=1.75 and $\alpha=0^\circ$	196
Fig 173. Static Temperature along the domain axial distance at M=1.75, $\alpha=0^\circ$ and domain length=120m.....	197
Fig 174. CO ₂ Mass Fraction Contour for Re-entry parachute at $\alpha=0^\circ$, H=10km and M=1.75.....	198
Fig 175. CO ₂ Mass fraction along the domain axial distance at M=1.75, $\alpha =0^\circ$ and domain length 120m.....	199
Fig 176. Ar mass fraction contour for Re-entry parachute at $\alpha =0^\circ$, M=1.75.....	200
Fig 177. Ar mass fraction along the domain axial distance at M=1.75, $\alpha=0^\circ$ and domain length 120m.....	201
Fig 178. N ₂ mass fraction contour for Re-entry parachute at $\alpha=0^\circ$, M=1.75.....	202
Fig 179. N ₂ mass fraction along the domain axial distance at M=1.75, $\alpha =0^\circ$ and domain length 120m.....	203
Fig 180. Static pressure contour for Re-entry parachute at $\alpha=20^\circ$, H=10km and M=2.04814.....	204
Fig 181. Static pressure along the domain axial distance at H=10km, M=2.04814, $\alpha = 20^\circ$ and domain length 120m.....	205
Fig 182. Density Contour for Re-entry parachute at $\alpha=20^\circ$, H=10km and M=2.04814....	206
Fig 183. Density along the domain axial distance at $\alpha=20^\circ$, H=10km, M=2.04814 and domain length =120m.....	207

Fig 184. Velocity-Mach number contour for Re-entry parachute at $\alpha=20^\circ$, H=10km and M=2.04814.....	208
Fig 185. Velocity-Mach Number along the domain axial distance at $\alpha=20^\circ$, H=10km, M=2.04814 and domain length 120m.....	209
Fig 186. Static Temperature Contour for Re-entry parachute at $\alpha=20^\circ$, H=10km and M=2.04814.....	210
Fig 187. Static temperature along the domain axial distance at $\alpha=20^\circ$, H=10km, M=2.04814 and domain length 120m.....	211
Fig 188. CO ₂ Mass fraction contour for Re-entry parachute at $\alpha=20^\circ$, H=10km and M=2.04814.....	212
Fig 189. N ₂ Mass fraction contour for Re-entry parachute at $\alpha=20^\circ$, H=10km and M=2.04814	212
Fig 190. CO ₂ Mass fraction along the domain axial distance at $\alpha=20^\circ$, H=10km, M=2.04814 and domain length 120m.....	213
Fig 191. N ₂ Mass fraction along the domain axial distance at $\alpha=20^\circ$, H=10km, M=2.04814 and domain length 120m.....	213
Fig 192. Ar Mass fraction contour for Re-entry parachute at $\alpha=20^\circ$, H=10km and M=2.04814.....	214
Fig 193. Ar Mass fraction along the domain axial distance at $\alpha=20^\circ$, H=10km, M=2.04814 and domain length 120m.....	215

LIST OF TABLES

Table 1.DGB Parachute Geometric Properties.....	5
Table 2. Mass Properties of the Capsule and Parachute.....	5
Table 3. Timeline details for Schiaparelli Related to Altitude, Angular rates, and angles for Nominal and Real Trajectory.....	20
Table 4. Timeline details for Schiaparelli Related to centre of Gravity State variables for Nominal and Real Trajectory.....	28
Table 5. Planetary Parameters for Each Planet including Mars.....	45
Table 6. Table of standard Mars atmospheric density with respect to Altitude.....	55
Table 7. Telemetry events by OBSW.....	57
Table 8. Mission Timelines comparison: OBT, post-SEP TAS-I prediction and E4-0 DEIMOS prediction.....	59
Table 9. Reconstructed descent phase timeline for occurrence of Nominal Flight....	60
Table 10. Mission Timelines Comparison: OBT vs post-SEP DEIMOS prediction vs DEIMOS most Likely.....	61
Table 11. Mission timeline of EDL for Real re-entry trajectory compared to nominal post SEP-Prediction.....	61
Table 12. Re-constructed EDM inertia.....	70
Table 13. MSA performance: reconstructed Real EDM attitude rate in at post-SEP...	70
Table 14. MSA performance: reconstructed EDM delta V at post-SEP.....	71
Table 15. TGO pointing performance: reconstructed EDM attitude at post-SEP.....	71
Table 16. State Vector ay EDM pre-Separation.....	74
Table 17. Reaction's mechanism and rate parameters [24].....	85
Table 18. Free stream conditions [24].....	88
Table 19. Boundary conditions for Simulation of MSV Capsule in Fluent.....	89
Table 20. Boundary conditions for Ducted Re-entry vehicles [32]	101
Table 21. Details of mesh definition.....	106
Table 22. Boundary conditions for Simulation of MSV Capsule.....	107
Table 23. Boundary conditions for Schiaparelli EDM.....	129
Table 24. Implementation of various altitudes above Mars.....	163
Table 25. Mesh details.....	173
Table 26. Boundary Conditions for Areal oscillation of a Schiaparelli Parachute....	174

ABSTRACT

Schiaparelli was a re-entry capsule used in the framework of the ESA ExoMars mission and had a serious anomaly during the descending phase and was destroyed at the impact on the Martian Surface. The failure was generated by unexpected oscillations of the parachute occurring during the parachute deployment (a phenomenon called areal oscillations): these fast oscillations saturated the gyro-sensors so that attitude of the capsule was wrongly determined, and the on-board computer gave wrong recovery commands. The thesis is to perform an analysis of the Schiaparelli mission, reproducing the different re-entry phases to eventually understand the reasons of the mission failure by using CFD analysis of the capsule and parachute during the entry phase into the Mars atmosphere. A preliminary step was the validation of the numerical codes by comparison with existing examples taken from the scientific literature. After this step, the Schiaparelli environment conditions are simulated considering the composition of the Mars atmosphere and the nominal entry conditions of the capsule with chemical reactions. The wake after the capsule is computed and this represents the flow encountered by the parachute during its deploying phase. This phase is analysed considering approximated analytical modes as well as by numerical investigation with ideal gas and perfect gas. The numerical investigation of the aerial oscillations and final trajectory of the Schiaparelli Parachute deployment with various angles of attack using chemical components in Martian atmosphere has been performed in the last part of this thesis.

Keywords: Computational Fluid Dynamics, Mars atmosphere, Areal oscillations, Chemical, Trajectory, Angle of attack.

CHAPTER 1

INTRODUCTION

This thesis is dedicated to the dynamics of entry capsules in the Martian atmosphere with particular reference to the Schiaparelli mission. This mission had a failure during the last phase of re-entry soon after the parachute deployment. Probably the reason of the failure was due to unexpected saturation of the gyros, so the attitude of the capsule was incorrectly determined by the on-board computer and a series of wrong recovery command were executed, causing the crash of the capsule on the Martian ground.

The saturation level of the angular velocity measured by the gyros was compatible with the extensive Monte-Carlo analysis that was performed in the mission design phase. However, a still not understood phenomenon in the parachute deployment, referred as areal oscillations, was not taken into account in the dynamical models simulating the capsule attitude motion.

In this thesis some steps are taken to understand the area oscillations and the effect on the Schiaparelli mission.

1.1 Description of the Schiaparelli Mission

The EXOMARS Program consists of two missions. The first Trace gas orbiter (TGO) with the Schiaparelli Entry Demonstrator Module (EDM) is the First Mission that was launched in March 2016 and the Secondary mission featuring a landing Platform and a rover (which is planned for Launching in 2022 but it was suspended after Russia's invasion on Ukraine). On 16th October 2016, after six months of interplanetary cruise, the TGO delivered Schiaparelli in a ballistic flight path towards Mars. After its

successful entry sustaining the most critical phases of a entry trajectory (the peak of temperature and peak of load), Schiaparelli failed the terminal part of descent and crashed on the Martian Surface.

The capsule was designed as an Entry Descent and Land (EDL) demonstrator. The on-board sensors were selected for the purpose of characterizing the performance of module during EDL and enabling scientific activities. The on-board sensor was located on the front-Shield (FS), ten thermal plugs were embedded on the Thermal protection System (TPS) of both the Black Shell (BS) and the FS. Calorimeter and radiometer sensors were part of the COMARS+ Experiments. The module was also equipped with a down looking Descent Camera (DECA) to take images of the landing site. The camera has configured for acquiring a burst of fifteen low resolution frames starting from the release of FS. Finally, the module has been provided with a sensor suite to characterize the atmospheric condition at the surface called DREAMS (Dust Characterization, Risk assessment and Environmental Analyser on the Martian surface). The Suite comprised sensors are used for measurement of atmospheric temperature, pressure and humidity, windspeed and its direction, illumination conditions and to provide the first measurements of electric fields at the Martian's surface.

Schiaparelli Guidance Navigation and control (GNC) subsystem included the main Computer (CTPU), a Sun Detection sensor (SDS) located in the lander BS, one miniaturized Inertial Measurement Unit (IMU), and a Radar Doppler Altimeter (RDA). The GNC Subsystem was responsible for guiding the module through the atmosphere of Mars and trigger all the EDL key events such as the detection of the interface point with the atmosphere, the opening of the parachute, the release of FS and BS and the activation of the thrusters and their cut-off during the final point of the descent and touchdown. Schiaparelli was designed to collect the data from the sensors which is above mentioned, store them on board and to transmit the data to the availability relay orbiters only after the touchdown. Moreover, during all the EDL

phases, the module also sent a small subset of the collected parameters in real time using UHF antennas (namely the antenna on the BS until separation, afterwards the antenna will be on the surface platform). The UHF carrier recorded by the ground stations an Earth and the real-time TGO and Mars-Express orbiters; this data set is very limited but contains the information's which are needed to reconstruct the chain of events occurred during EDL. The scientific experiment was called AMELIA: the flight data have been used by AMELIA team for reconstruction of Schiaparelli Trajectory to derive the profiles of atmospheric density, pressure and temperature. Flight data was retrieved by AMELIA team from ESA EGOs data dissemination system (EDDS) and all the data were publicly available through ESA Planetary Science Archive (PSA)[4].

1.1.1 Module

The Mass of the Vehicle is weighted as 577kg after separation and 280kg at landing [1]. The geometry has the aero shape inherited from the NASA Mars, 70° sphere cone front shield and 47° conical back shield diameter is 2.4m and its height is 1.32m. The total length of capsule is 1.27 m. It has the blunt end at the front with radius of 0.6m as shown in Fig 1[2]. For thermal shield, the norcoat-liege ablative material is used for both front and back shield of the capsule. The aluminium sandwich with carbon filter reinforced polymer skins with crushable structure to absorb landing loads. The design of the capsule has non-failure tolerant avionics with non-rechargeable batteries and UHF Communication system [1]. The design of the Parachute is shown Fig 2. It has the Disk-Gap-Band (DGB) which is woven with nylon fibre materials [4]. The length and dimensions of the parachute are displayed in Table 1 and Fig 2 [4]. The details of the mass properties of the capsule and parachute are reported in Table 2.

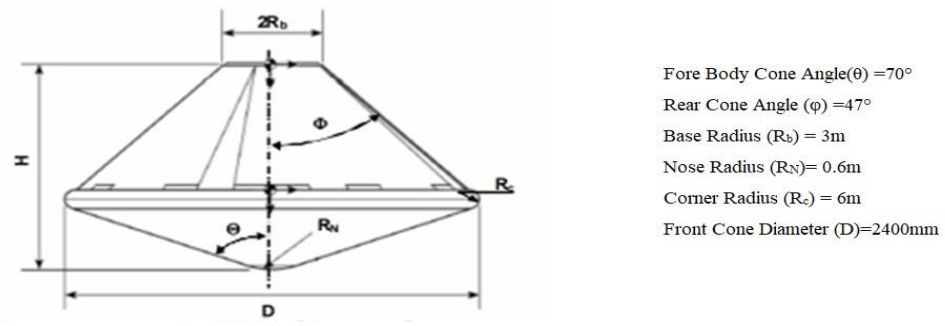


Fig 1. 2D Geometry of the Schiaparelli EDM [2]

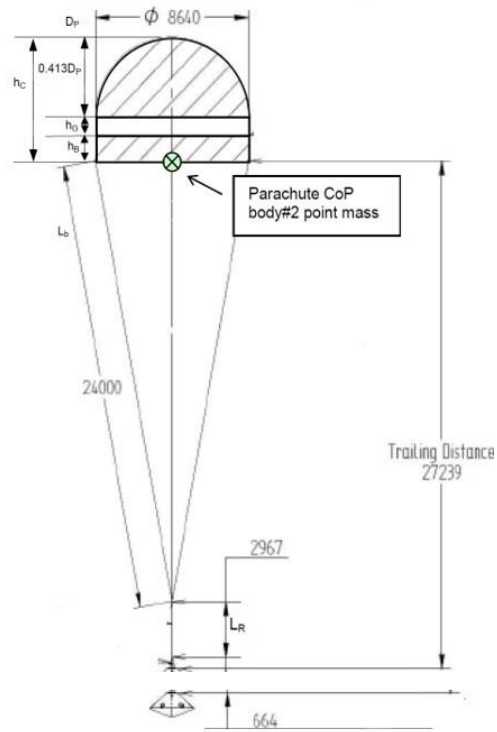


Fig 2. 2D Geometry of the Schiaparelli EDM Parachute [3]

Table 1: DGB Parachute Geometric Properties [3]

Parameter	Symbol	Value
Nominal Diameter	D_0	12.000m
Nominal Area	S_0	113.097m ²
Projected Diameter	D_P	8.640m
Disk Diameter	D_D	8.223m
Gap Height	h_G	0.957m
Band Height	h_B	1.357m
Vent Diameter	D_v	0.848m
Line Length	L_s	24.0m
Riser Length	L_R	2.967m
Bridle Length	L_b	0.688m
Bridle height	h_b	0.664m
Bridle Attachment PCD	b	0.356m
Distance between parachute and capsule	L	27.631m

Table 2: Mass Properties of the Capsule and Parachute [5]

Stages	Nominal
EIP (RADIUS 120+3396km)	576 kg
Parachute Deployment (Mortar Firing)	563 kg
Front Shield Jettision (after)	460 kg
Back shell Release(after)	300 kg
Fuel mass for Power Landing start	3.4 kg
Retro rockets cut-off	297 kg
Touchdown	297 kg

1.2 Description of the nominal Schiaparelli re-entry trajectory

1.2.1 Entry Interface Point (EIP)

EIP (Entry Interface point) is identified as the reference entry point at altitude of 120 km above a reference Mars radius of 3396 km, corresponding to the reference radius of the MOLA database. The GNC-detected EIP (GNC-EIP) is the event representing the transition to inertial navigation for translation in GNC algorithms, and is directly detected on the basis of accelerometric measurements. The threshold occurs at different altitudes / radial distances depending on atmospheric density. The accuracy of position and velocity at the EIP is critical in determining whether the arrival is compatible with the entry corridor limits, specifically the range between the steepest and shallowest entry flight path angles [5].

To be compatible with the entry corridor, the accuracy is determined by Along-Track (AT) position error and flight path angle (FPA) angle dispersion, and Cross-Track (CT) and heading (HDG) errors to determine lateral deviation from the target landing point [6].

The insertion to entry point and the achievement of the landing site are crucial aspects of an entry mission; the source of errors are the following:

- The interplanetary navigation and correction manoeuvres implementation, with Deep Space Manoeuvre (DSM) performed in two parts and Trim Correction Manoeuvres (TCM's) performed as TCMs to correct DSM errors, TCM3 performed 30 days before ECP for B-plane fine targeting of the entry point, TCM4 performed five days before ECP as the final correction and fine targeting of the entry point, TCM5 performed five days before ECP as the final correction and the Main Separation Assembly (MSA) caused axial and lateral velocity errors, with the latter being more important in changing the eccentricity of the incoming hyperbola and thus affecting AT and FPA errors.

- The TGO attitude control, which determines the accuracy of the separation direction pointing to the desired FPA at ECP.
- The atmospheric dispersion during the EDL phase, which reduces landing accuracy.
- The implementation of interplanetary navigation and manoeuvres accounts for 85% of the ECP/EIP errors, with the remaining 15% related to MSA performance.
- The EDL phase accounts for 60% of total landing accuracy, with the EIP/ECP errors outlined above accounting for 40%. Because the EDL analyses are performed with extreme variability in the atmospheric conditions (optical depth ranging from 0.2 to >5), this result is considered extremely conservative [6].

The position accuracy at the entry interface point is shown in Fig 3. The targeting of the EIP location is very good because of both the reduced covariance and the reduced dispersions in the assumed SEP event; the predicted ellipsoid is well within the so called E2 Loop 3 accuracy. The AoA and AoS at EIP are depicted in Fig 4. Because of the knowledge of the reconstructed attitude at separation, the dispersed cloud is very small in comparison to the E2 results. Furthermore, the good performance of the TGO pointing kept the total angle of attack below 1.8 degrees [6]. The post processed data show the excellent quality of the mission operations up to the SEP event.

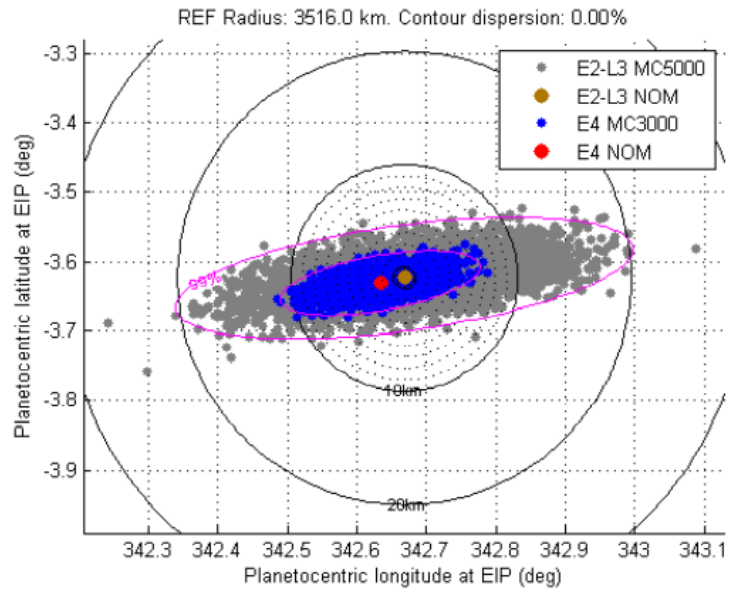


Fig 3. E4 MC, Position Dispersion at EIP for Nominal [5]

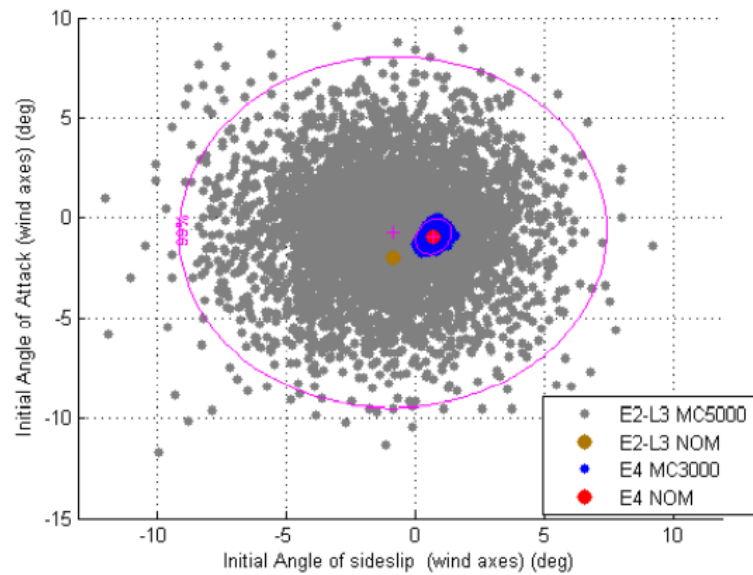


Fig 4. E4 MC, Attitude at EIP [5]

1.2.2 Entry

The flight prediction performed during Entry phase E2 resulted in the prediction of the EDL trajectory that the Schiaparelli module would have flown in nominal conditions. The statistics of the main ATDB parameters during entry are shown in Fig 5 - Fig 8. The obtained dispersions are within the E2 range, and all margins increase when compared to the E2 results. Because of the higher-than-expected delta V at Separation, which caused a steeper than expected entry, the dispersed cloud moved toward the higher side in terms of heat flux, load factor, and total heat load [5].

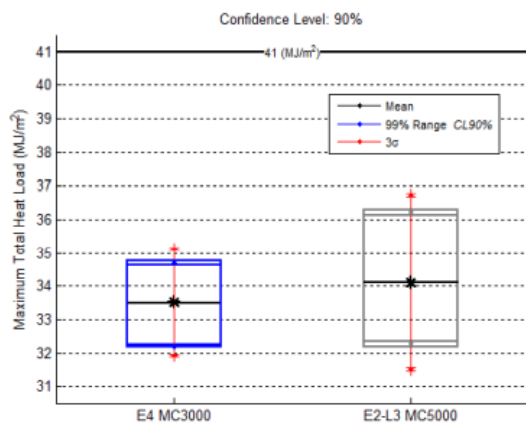


Fig 5. E4 MC, MC statistics for total heat load at stagnation point (Sutton-Graves) [5]

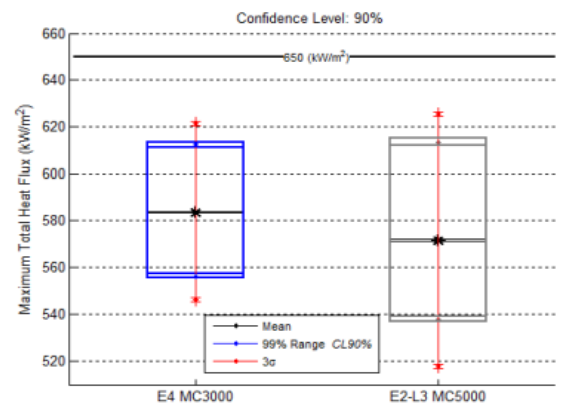


Fig 6. E4 MC, MC statistics for heat flux at stagnation point (Sutton-Graves) [5]

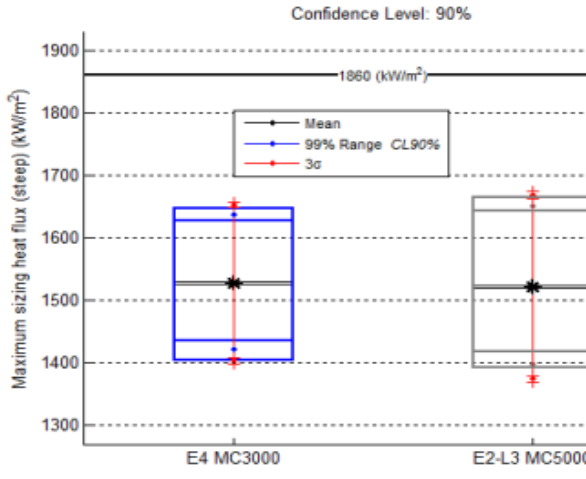


Fig 7. E4 MC, MC statistics for maximum sizing heat flux (Steep correlation) [5]

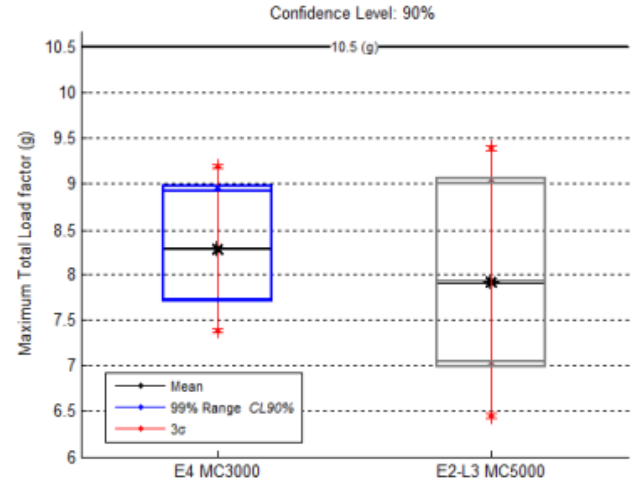


Fig 8. E4 MC, MC statistics for load factor during entry [5]

The entry was within the design range, but slightly steeper than nominal: the most likely entry FPA is around -12.48 degrees (vs -12.4 degrees target) due to the higher axial Delta-V at SEP. Table 3 compares the updated margins budget to the ph. E2 Loop 3 flight prediction. The actual flight adheres to the margins, validating the performance predicted for the nominal and real re-entry trajectory. The actual atmosphere encountered by the EDM during its flight (entry phase) is most likely a combination of different MCD scenarios at various altitudes, with a clearer atmosphere overall than the nominal condition C_{lim} ($\tau = 1$), varying between Cold 112 ($\tau = 0.2$) and Dust 101 ($\tau = 0.5$) [5].

Differences in the co-rotating variables are observed between the reconstructed and most likely simulated trajectories because of the sensors and integration errors injected in the navigation chain, as well as the initial conditions injected post-hibernation (understood to be based on Keplerian propagation of nominal post-Sep conditions estimated before separation) [6].

The IMU's on-board roll rate profile differs significantly from what was considered during the design phase. Under largely off nominal and variable AEDB uncertainties,

a similar trend can be simulated. The true causes of this behaviour could be a lack of fully representative aerodynamic modelling, which missed some contributions, or events that occurred during the entry and caused off-nominal aerodynamic performance of the aero shape (e.g., asymmetry due to non-perfect) [6].

A more detailed analysis involving the team of aerodynamic experts is required to fully understand the cause of such a non-nominal roll rate evolution during entry, as well as to further elaborate on the possible aero shape asymmetry [6].

The reconstructed natural pulsations of the Short Period and Dutch Roll modes validate the prediction made by DEIMOS Space prior to flight using the Flying Qualities Analyses Tool [5].

The estimated range flown during entry was 689 km. The range flown is directly proportional to the drag profile: in the case of a ballistic capsule entry, it is equivalent to the axial load factor. The range flown from EIP to back shell release for a nominal PDD opening at Mach 1.95 [5].

1.2.3 Parachute Deployment Phase

The dynamic pressure condition during parachute deployment and inflation is depicted in Fig 9. The implemented GAT triggering fully meets the PDD limits identified in requirement DM-SYS-3280 (Mach 1.8 to 2.1) [6].

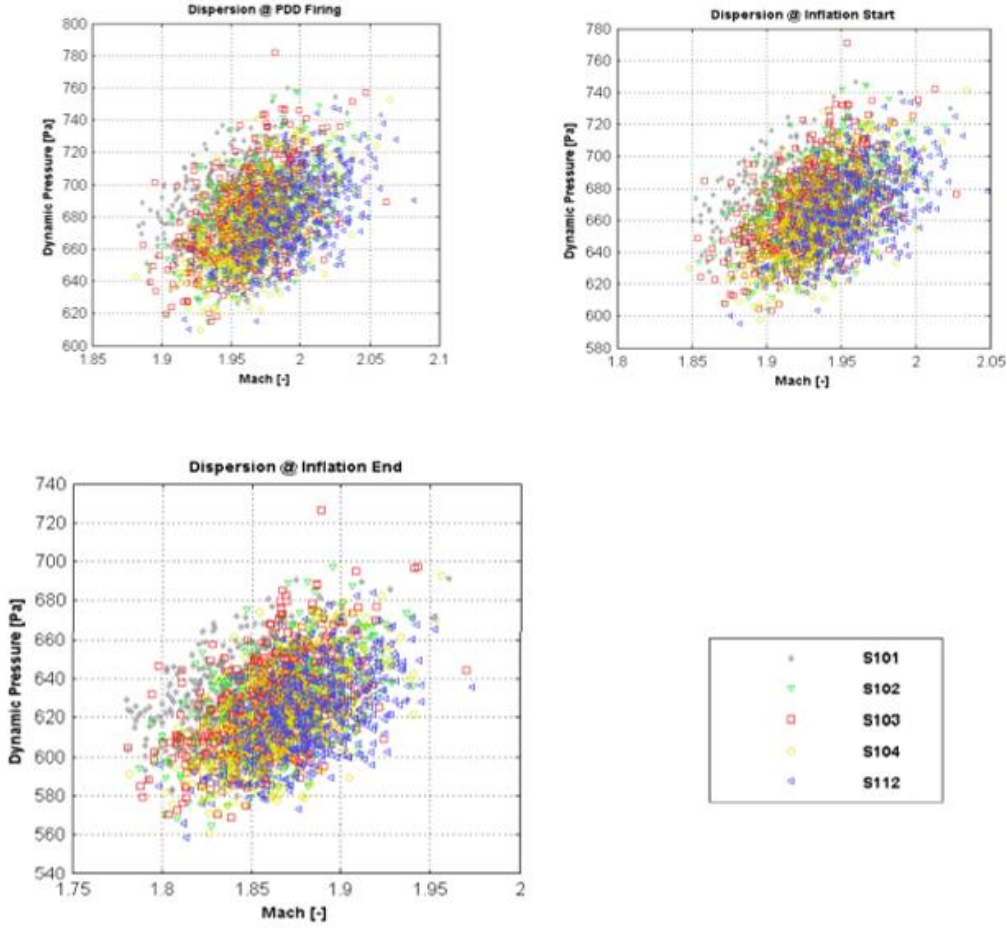


Fig 9. Conditions at parachute deployment ad inflation (FE2E_06 577 kg entry mass) [6]

At PDD firing, the Mach number ranges (at 3-) from 1.89 to 2.04, with a median of 1.96, as required. The range at the GAT event is unavoidably higher, 1.94 to 2.10, and the chosen parameters for g-threshold and lag time demonstrate that the algorithm works well and is resistant to environmental variations. The statistical worst case for dynamic pressure is 745 Pa (99.73%), and the absolute worst case observed is just slightly higher - 760 Pa at GAT, PDD, and inflation-end, all for the dusty environmental scenario. The range is reduced in the case of a 600 kg entry mass (815 Pa). A large margin is thus achieved in comparison to DM-SYS-3280 (980Pa), though it should be noted that the dynamic pressure at PDD is not an active constraint but a figure of merit: the relevant constraint is related to the inflation force estimate [6].

The PDD is fired at an altitude of 8.28 to 11.14 km above MOLA, with a flight path angle relative to the co-rotating velocity of -21.98° to -21.59° . The corresponding range

in altitude above ground level is 9.75 km out of 12.55 km. The parachute is fully inflated at the absolute worst-case scenario of 8.01 km. The dusty environment also represents the worst case in terms of altitude for deployment MOLA values for the 600 kg entry case were lower, as expected (6.62 and 10.39 km range) [6].

The DM-EDS-1790 requirement specifies the boundary conditions for PDD firing with a 15° angle of attack and lateral angular rate limits of 30 deg/s. The angle of attack is 11.69° at the 3-probability level for the reference scenario S102 (=1), with a worst case of 13.49° on the warm scenario and all 2500 simulated cases. The effect of the parachute inflation force on capsule stabilization depends on with the reduction of AoA ranges, however a rapid increase in angular rates was observed, probably due to bridle stiffness, collapse or not considered unstabilities arising in parachute deployment [6].

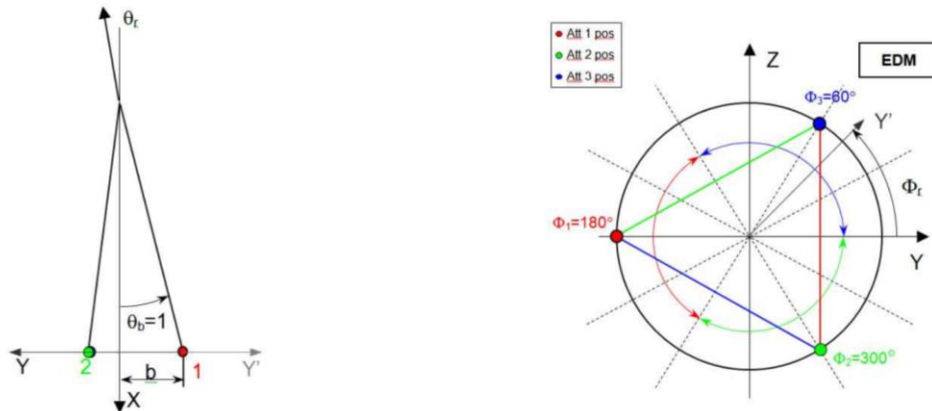


Fig 10. Bridle angle convention on ExoMars [6]

The maximum inflation loads occur for the atmospheric conditions of scenario S103 (warm atmosphere). Peak force is estimated to be 56.36 kN (99.73%), implying a 17% margin over the DMSYS-3280 requirement of 67.9 kN (Limit load) [5].

Fig 11– Fig 17 depicts the drogue deployment condition distribution in terms of altitude, flight path angle, Mach, dynamic pressure, and inflation force at 90% level of confidence. This failure also occurs due to wrong command caused the parachute cut to occur 1.5km to 4.5km higher than the normal altitude as shown in Fig 17. The

Margins increase with respect to E2 results due to the moment of dispersed contour towards the higher side in terms of heat flux load factor and lower sides in terms of total heat load due to unexpected effects. The obtained distributions are like or slightly lower in dispersion than the phase E2 results [5].

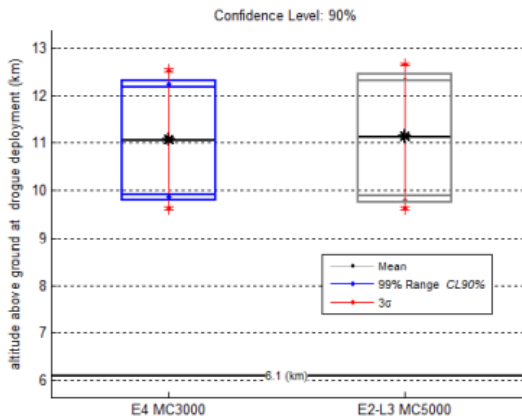


Fig 11. MC, MC statistics for altitude at drogue deployment [5]

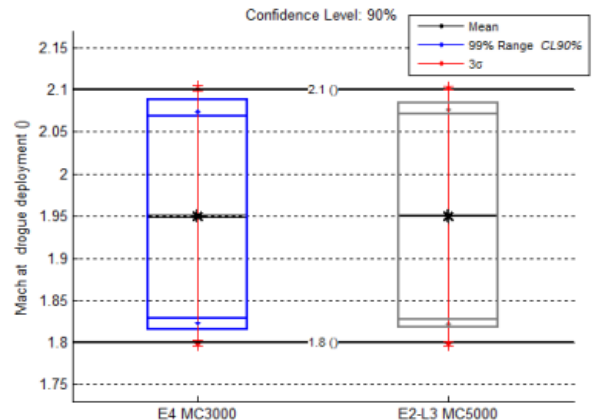


Fig 12. E4 MC, MC statistics for Mach at drogue deployment [5]

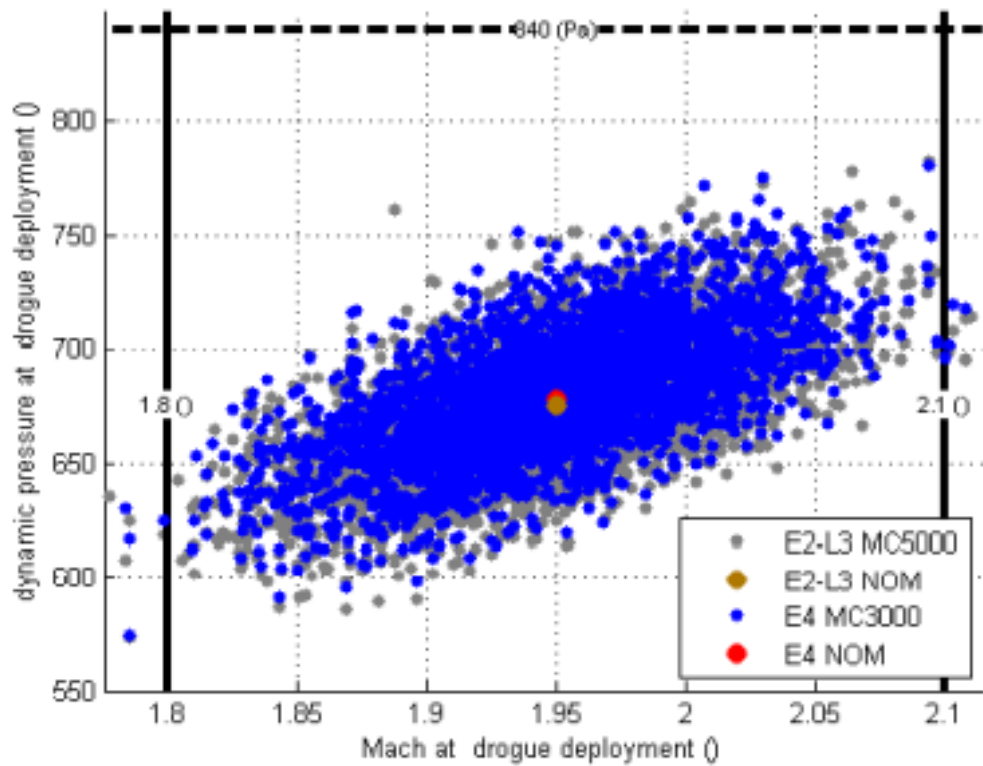


Fig 13. E4 MC, Drogue deployment condition in terms of Mach and dynamic pressure [5]

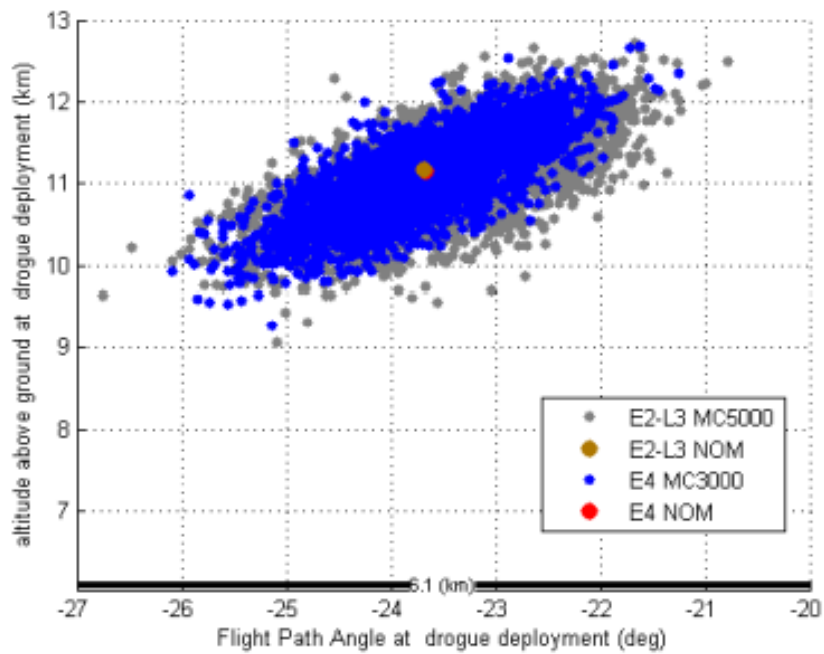


Fig 14. E4 MC, Drogue deployment condition in terms of flight path angle and altitude [5]

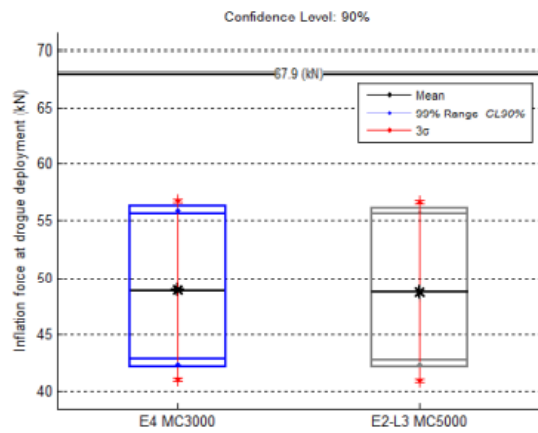


Fig 15. E4 MC, MC statistics for inflation force at fully drogue deployment [5]

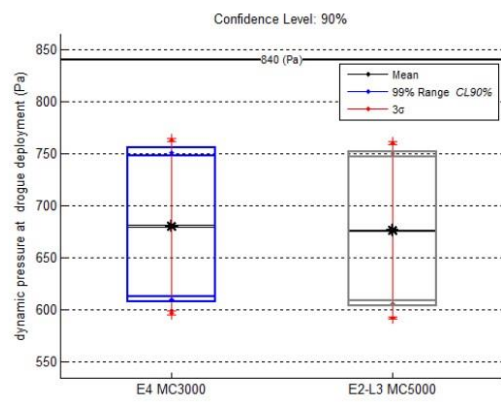


Fig 16. E4 MC, MC statistics for dynamic pressure at drogue deployment [5]

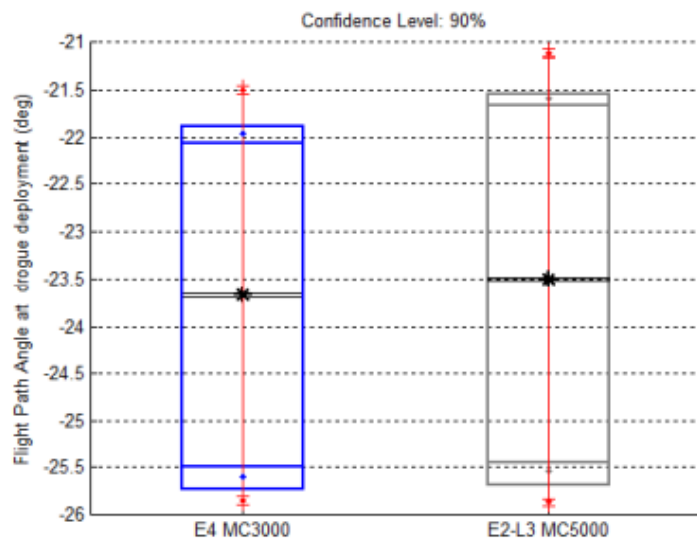


Fig 17. E4 MC, MC statistics for flight path angle at drogue deployment [5]

1.3 Description of the failure

In the impact point, there is a dark patch about 1km North (Fig 18) from there is estimated at 353.79° in longitude and -20.07° latitude at Meridian Planum as shown in Fig 19. The front shield of EDM fell in Mars at 125km distance from ExoMars lander as shown in Fig 18. The parachute and back shield fell at 0.9km from Exo-Mars lander (shown in Fig 18) whereas Fig 18 shows and initial Estimation of dark spots localizes above the mars initially before landing which is the main cause of failure [5].

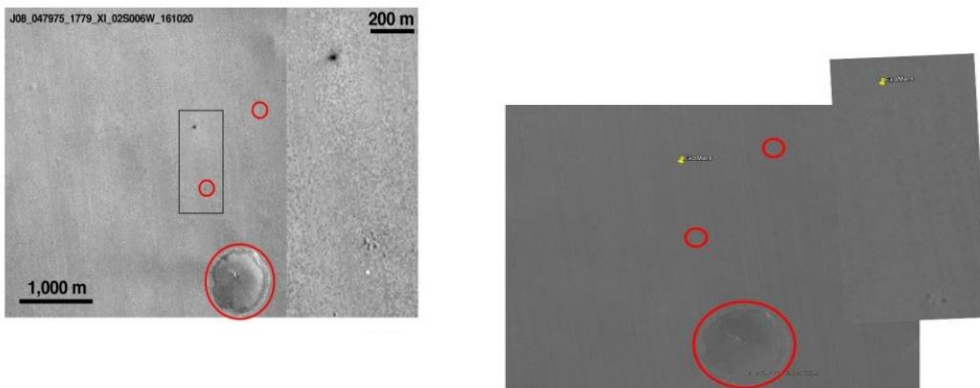


Fig 18. Impact point (dark spot) localization on the low-resolution MRO image of Meridian Planum [5]



Fig 19. DM, parachute and front shield impact points localization on the high-resolution MRO image of Meridian Planum [5]

Table 3 shows the details of timeline for Schiaparelli EDM Related to altitude, angular rates, angles and some of their thermal properties whereas Table 4 shows the timeline details with Centre of Gravity state Variables. The following table shows the centre of mass state variables of Schiaparelli EDM along the nominal trajectory (third column of the table). In the last column the data related to the real trajectory performed by the capsule are reported. Note that up to the parachute deployment phase the nominal and real data are rather close. The anomaly occurred after the parachute deployment [5].

Maximum Inflation force is the peak level of force given during the parachute deployment and its re-inflation. The Maximum inflation force (F_p) which depends on the factor like canopy design, inflation duration, and deployment dynamic pressure. Using a quick method for estimating a conservative value of the peak parachute opening load using the “W/(C_{DA})_p method”. The peak parachute opening force can be estimated as:

$$F_p = (C_{DA})_p q C_x x_i \quad (1)$$

where $(C_{DA})_p$ is the drag area of the full open parachute, q is the dynamic pressure at line stretch, C_x is the canopy opening force coefficient (Maximum Inflation Load factor) at infinite mass, and X_i is a force reduction factor [7].

The force reduction factor is a function of canopy loading and varies between near zero for a finite mass inflation (where there is significant deceleration during inflation) and 1.0 for an “infinite mass” inflation (occurs so rapidly that there is no time for deceleration during inflation) [7]. The Maximum inflation in Parachute deployment stage of Schiaparelli in nominal stage is 48.83811kN whereas in real stage it has obtained as 64.8764kN as shown in Table 3. Inflation loads maximum occurs for the atmospheric conditions of scenario S103 (warm atmosphere). Peak force is estimated in 56.36 kN (99.73%), meaning that a 17% margin exists with respect to DM-SYS-3280 requirement of 67.9 kN (limit load) is shown in Fig 20 [6].

The maximum inflation load factor is derived from (1) as follows [7],

$$C_x = \frac{F_p}{C_D A q x_i} \quad (2)$$

It is defined as the ratio between Maximum inflation force (Peak inflation Force) and drag area, dynamic pressure along with force reduction factor [7].

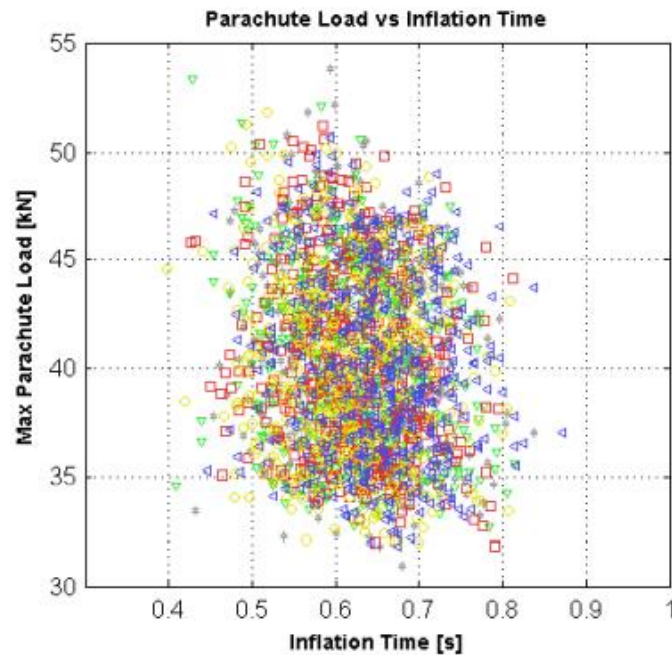


Fig 20. Comparison of Maximum Parachute Load with respect to inflation time [6]

The following Table 3 shows some attitude data along the nominal and real trajectories.

Table 3: Timeline details for Schiaparelli Related to Altitude, Angular rates, and angles for Nominal and Real Trajectory [5]

Event	Parameter	Nominal	Real
EIP (RADIUS 120+3396km)	Time for Pre separation (SEP)-h	72.00201	72.000189
	Co-rotating Velocity(m/s)	5786.31402	5786.34698
	Flight Path Angle (deg)	-12.43220	-12.48352
	Mach	32.32163	0
	Angle of attack-Wind Axes (deg)	-0.97521	-0.67391
	Angle of Side Slip-Wind Axes(deg)	0.69752	0.86582
	Total Angle of Attack(deg)	0.96470	1.10626
	Total Angle of Attack -aerodynamic Velocity (deg)	1.19897	1.09716
Entry	Maximum Total Load factor (entry) (g)	8.00194	8.19996
	Maximum Total Heat Flux (kW/m^2)	572.03233	588.06357
	Maximum Total Heat Load (MJ/m^2)	33.89467	34.56981
	Maximum Dynamic pressure (Pa)	5891.78069	6827.80916
	Maximum Total AoA - aerodynamic velocity (deg)	8.61828	14.33442
	Total AoA at peak of heat flux (deg)	3.09944	2.05853
	Total AoA wind at peak of heat flux (deg)	3.15277	2.05227
	Total AoA wind at peak of heat flux (1% thrust) (deg)	3.89653	4.32227
Parachute Deployment PDD (MOTOR FIRING)	Time for EIP(s)	199.64457	237.66374
	Mach	1.95	2.08500
	Dynamic pressure (Pa)	677.74842	33.65739
	Altitude above ground (EMCD 43) (km)	11.14628	11.17193
	Flight Path Angle (deg)	-23.67633	-22.13461
	Maximum Inflation Load factor (g)	9.73531	12.59752
	Maximum Inflation force (kN)	48.83811	64.8764
	Total angle of attack (deg)	2.66480	0.68764
	Total angle of attack - aerodynamic velocity (deg)	2.66480	0.91448

Event	Parameter	Nominal	Real
Front Shield Jettison	Time from EIP (s)	240.64457	237.66374
	Mach	0.36895	0.36698
	Dynamic pressure (Pa)	33.49136	33.65739
	Altitude above ground (EMCD 43) (km)	7.34145	7.50391
	Flight Path Angle (deg)	-69.67539	-70.89931
	Total angle of attack (deg)	3.49072	1.34879
	Total angle of attack - aerodynamic velocity (deg)	1.04648	4.96017
Back shell Release	Time from EIP (s)	285.64457	282.66374
	Mach	0	0
	Dynamic pressure (Pa)	0	0
	Altitude above ground (EMCD 43) (km)	3.943	4.14487
	Co-rotating velocity(m/s)	0	70.73425
	Vertical Velocity (m/s)	0	-70.62458
	Flight Path Angle (deg)	-89.50098	-86.82209
	Total angle of attack (deg)	5.44660	5.24326
	Total angle of attack - aerodynamic velocity (deg)	1.52364	7.09776
Powered Landing Start	Time from EIP (s)	288.44457	283.46374
	Altitude above ground (EMCD 43) (km)	3.88515	4.08730
	Co-rotating velocity (m/s)	73.64579	73.39175
	Vertical velocity (m/s)	-73.64300	-73.28680
	Flight Path Angle (deg)	-89.50098	-86.93549
Retro-Rockets Cut-off	Time from EIP (s)	289.54457	286.56374
	Altitude above ground (EMCD 43) (m)	3680.45776	3883.18506
	Co-rotating velocity (m/s)	62.52316	62.55738
	Vertical velocity (m/s)	-62.51845	-62.50265
	Flight Path Angle (deg)	-89.29640	-87.60318
Touch Down	Time from EIP (s)	322.73243	321.11878
	Altitude above areoid (km)	-1.44575	-1.44536
	Co-rotating velocity (m/s)	149.30940	151.34470
	Vertical velocity (m/s)	-149.29193s	-151.30377

The difference in reconstructed CoG between the two cases is small, ~ 2 mm in X and ~ 1 mm in Y. Further verification of the CoG reconstruction is recommended, if possible, cross checking the above CoG results with TPS consumption models based on the heat flux information recorded during the flight [6].

The directions of the GNC and IMU reference systems axes, with respect the EDM global system axes is indicated in Fig 21. The EDM global system reference frame definition is as follows:

- The origin is located in the DM back cone vertex ($X_{nose} - 1.585$ m)
- The X-Y-Z axes are defined as follows:
 - EDM_X axis is the revolution axis pointing forward towards the nose of the vehicle.
 - EDM_Z axis perpendicular to XB in the vertical symmetry plane and pointing towards the bottom of the module.
 - EDM_Y axis completes the right-handed system [5].

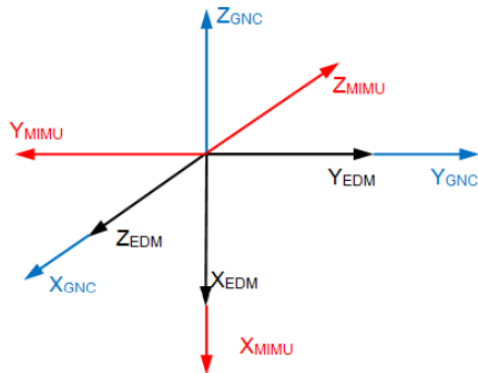


Fig 21. GNC and IMU reference systems definition with respect to EDM global system [5]

The Reconstruction of x, y and z axes using the angular rates and the inertia moments available from most trajectory an estimation of the moments experienced by the EDM has been derived. The aerodynamic moments of the capsules based on Euler's equation for the rigid dynamics are the following:

$$M_x = I_{xx}\dot{\omega}_x - I_{xy}(\dot{\omega}_y - \omega_x\omega_z) - I_{xz}(\dot{\omega}_z + \omega_x\omega_y) + (I_{zz} - I_{yy})\omega_y\omega_z - I_{yz}(\omega_y^2 - \omega_z^2) \quad (3)$$

$$M_y = I_{yy}\dot{\omega}_y - I_{yz}(\dot{\omega}_z - \omega_y\omega_x) - I_{xy}(\dot{\omega}_x + \omega_y\omega_z) + (I_{xx} - I_{zz})\omega_z\omega_x - I_{xz}(\omega_z^2 - \omega_x^2) \quad (4)$$

$$M_z = I_{zz}\dot{\omega}_z - I_{xz}(\dot{\omega}_x - \omega_z\omega_y) - I_{yz}(\dot{\omega}_y + \omega_z\omega_y) + (I_{yy} - I_{xx})\omega_x\omega_y - I_{xy}(\omega_x^2 - \omega_y^2) \quad (5)$$

Angular accelerations ($\ddot{\omega}$) were derived from numerical differentiation of angular rates. Fig 22 shows moments are reconstructed before the blackout which is possible to notice the aerodynamic moments start to rise around 35s after EIP, When capsule around 80km above the aeroid where the dynamic pressure start to rise as a result of density increases. At the point time, some fast variations and yaw pitch rates are observed from OBT, starting from the point of telemetry, an increase in roll rate is observed. The blackout effects enter approximately at 50s after EIP and angular rates are numerically constant for a few second before the end of signal received, so longer evolutions moment cannot be reconstructed [5].

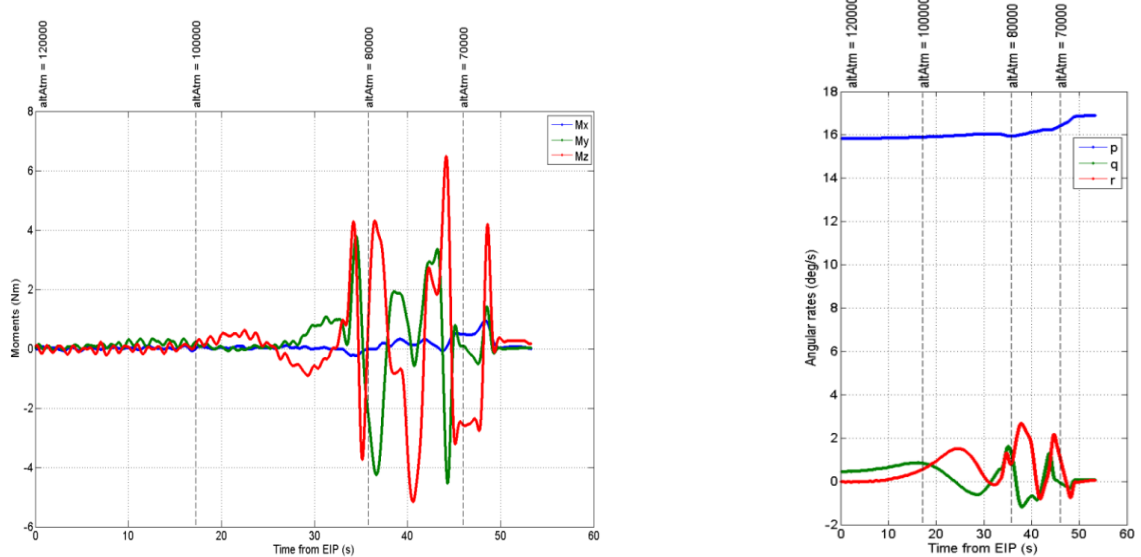


Fig 22. EDM body-axes moments reconstruction (left) and angular rates (right) before blackout [5]

If the estimated position and velocity from OBT are used, the derived angle-of-attack and sideslip are really different from the ones of the most likely trajectory, as presented in Fig 23, even in presence of a good resemblance in terms of roll, pitch, and

yaw angles (the profiles are not phased due to the slower roll rate, but there is a good approximation of oscillations amplitude, see Fig 23) [5].

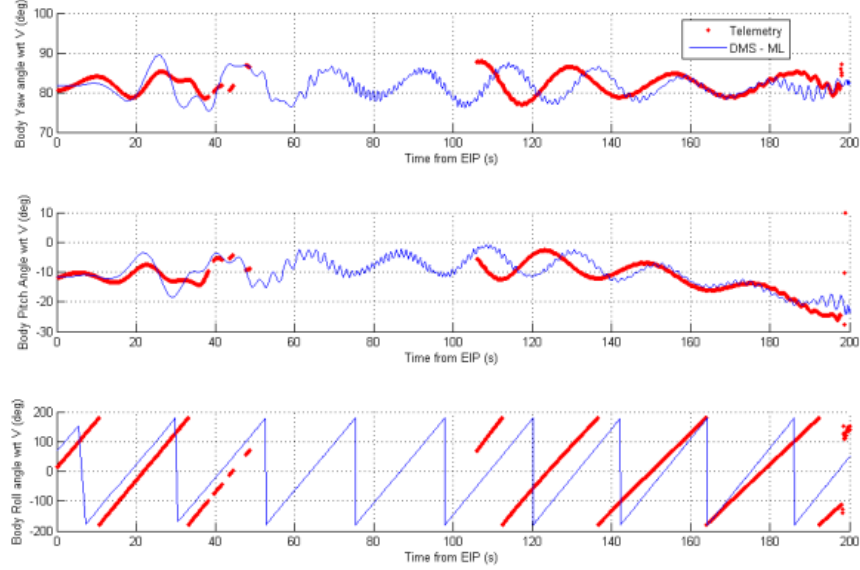


Fig 23. Attitude angles (with respect to local vertical) during entry, OBT vs most likely profiles [5]

Moreover, the high AoA and AoS oscillations observed were not expected, and the only explication found, building on the results presented from the moment reconstruction and MER experience would be a large non-axial symmetric behaviour of the capsule. However, the real effect seen here is probably the OBT integration errors reflected in the derived FPA and Heading. From this, possible EDM CoG is identified [5].

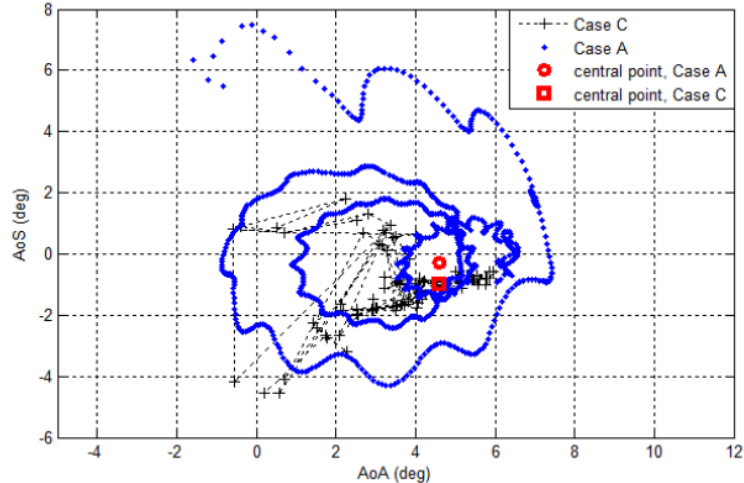


Fig 24. AoA-AoS trim point used for EDM CoG reconstruction [5]

From this reconstruction, a precession is observed around 130 s from the EIP (Mach \sim 7) with a central point around AoA \sim 4.6° and AoS \sim -0.3°, see Fig 24 [5]. The alternative aerodynamic angles reconstruction approach provides a different time evolution of the AoA and AoS: a slightly different EDM CoG can be reconstructed from this profiles: using a central point around AoA \sim 4.6° and AoS \sim -1°, the EDM CoG matching with this static trim, in nominal conditions at Mach = 7 is (Flight Mechanics axes):

- X = -0.607 [mm]
- Y = -1.6 [mm]
- Z = 7.2 [mm]

The moments reconstructed after blackout is shown in Fig 25 .The Roll moment is presently affecting the capsule when the reconstructed moments are analysed compared to the most likely trajectory in Fig 26 [5].

- The roll moment is oscillating far from 0, with peaks beyond -1Nm.
- The yaw and pitch moments present smaller variability than the most likely trajectory.
- The yaw and pitch moments present a non-elliptical shape [5].

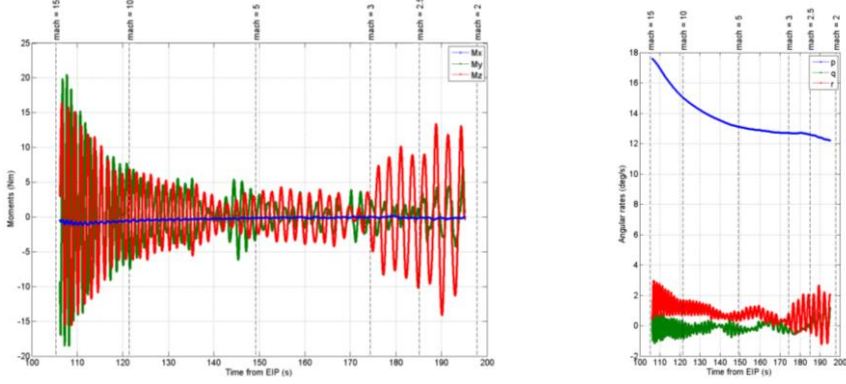


Fig 25. EDM body-axes moments reconstruction (left) and angular rates (right) after blackout [5]

The asymmetric were identified by analysing the moments in the axes perpendicular to the capsule revolution axis. For a perfectly symmetric body at small angle of attack, the unexpected behaviour is an elliptical shape and concave points perturbing torque due to capsule asymmetries as shown in Fig 26. Remnants of the thermal blanket have been identified as the source of this asymmetry in for both Mars Exploration Rover (MER) missions. A comparison between the reconstructed moments between Schiaparelli and MER (Opportunity)is shown in Fig 27, covering a few seconds of flight (122-128 s in Schiaparelli, 130-140 s in MER) [6].

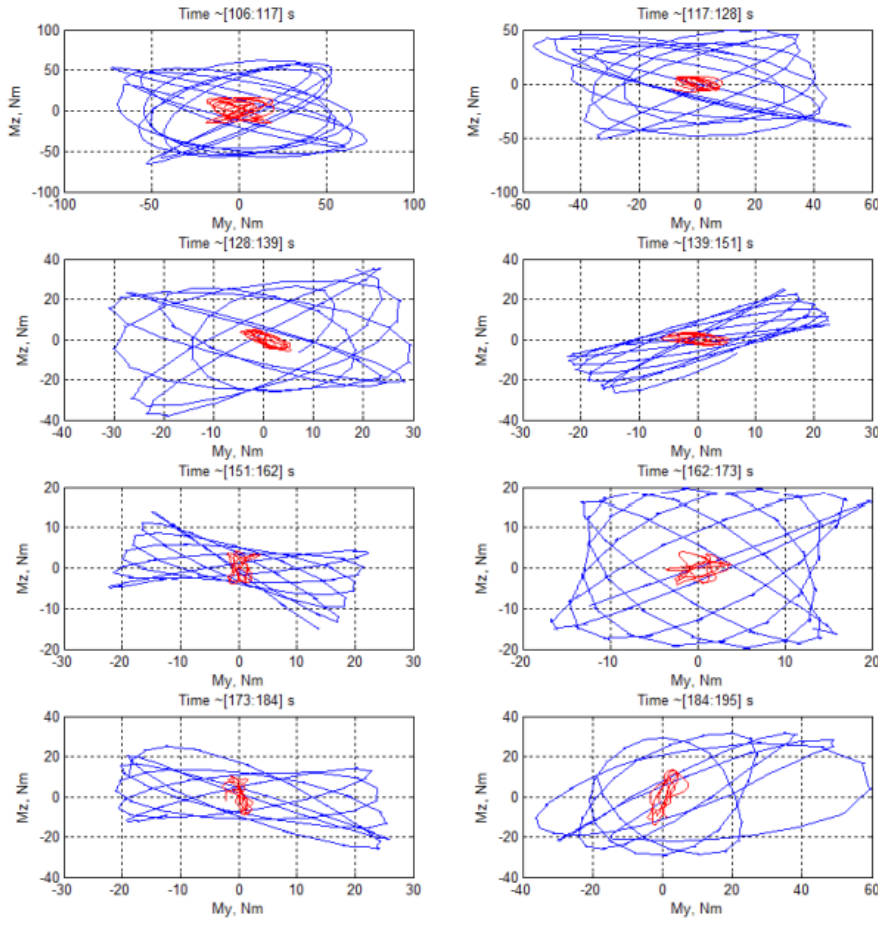


Fig 26. Yaw and pitch moments: comparison between most likely (blue) and reconstructed (red) [5]

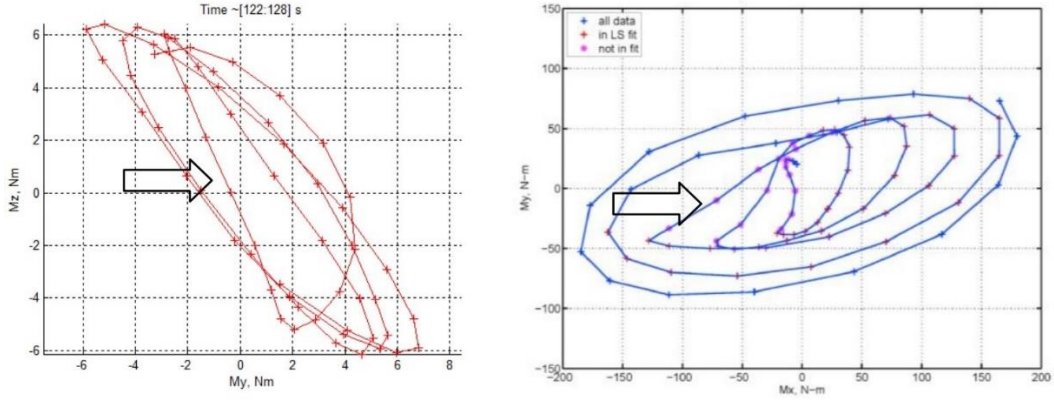


Fig 27. Yaw and pitch moments: reconstructed (red, left) and MER (blue, right) [6]

Table 4 shows the details of Timeline for Schiaparelli Related to centre of Gravity State variables for Nominal and Real Trajectory.

Table 4: Timeline details for Schiaparelli Related to centre of Gravity State variables for Nominal and Real Trajectory [5]

Event	Parameter	Nominal	Real
Pre-SEPERATION (SEP-)	Heading (deg)	82.31031	0
	Inertia Position X-coordinates (km)	0	895532.96382677
	Inertia Position Y-coordinates (km)	0	145317.73820200
	Inertia Position Z-coordinates (km)	0	-101350.44321325
EIP (RADIUS 120+3396km)	Body Roll rate X-body (deg/s)	15.71391	15.71307
	Body pitch Rate Y-body(deg/s)	-0.05567	-0.01507
	Body yaw Rate Z-body(deg/s)	0.17103	0.20302
	X COG (Centre of Gravity)-From nose(m)	-0.59390	0
	Y COG (Centre of Gravity)- (m)	-0.00120	0
	Z COG (Centre of Gravity)- (m)	0.00780	0
Parachute Deployment PDD (MOTOR FIRING)	Body roll rate X-body (deg/s)	16.52461	116.48696
	Body pitch rate Y-body (deg/s)	-2.76833	-0.65209
	Body yaw rate Z-body (deg/s)	1.23176	3.23130
	X- COG (Centre of Gravity) after deployment (From Nose) (m)	-0.59514	0
	Y- COG (Centre of Gravity) after deployment (m)	-0.00121	0
	Z- COG (Centre of Gravity) after deployment (m)	0.00784	0
Front-Shield Jettison	Body roll rate X-body (deg/s)	16.58646	17.53771
	Body pitch rate Y-body (deg/s)	-5.37218	-21.97286
	Body yaw rate Z-body (deg/s)	0.72743	-10.04831
Back-shell Release	Body roll rate X-body (deg/s)	16.59099	17.46116
	Body pitch rate Y-body (deg/s)	-3.05107	-14.71465
	Body yaw rate Z-body (deg/s)	-2.54363	3.27344
Powered Landing Start	Planetocentric Latitude(deg)	0	-2.06956
	Planetocentric Longitude (deg)	0	353.7824
Touchdown	Planetocentric Latitude(deg)	-2.05954	-2.06958
	Planetocentric Longitude (deg)	-89.29640	-87.60318

CHAPTER 2

HYPOTHESIS OF THE FAILURE

After the initial aerobraking against the Martian atmosphere at Mach No M=2, the parachuting effects are modelled at the spacecraft's speed, although several uncertainties have led to several uncontrollable elements. Unexpected angular motions are produced by the parachute's inflation and deployment. As a result of some non-gravitational accelerations, the saturation of the IMU (Inertial Measurement Unit) occurred, however a post processing analysis on the state of the spacecraft, including speed, angular rate, altitude, etc has been possible.

The saturation lasts for an unexpectedly long period of time, causing an error in the GNC unit. The parachute was prematurely disconnected when the module was 3.7 kilometres above the surface of Mars, and the retro rockets were started and immediately turned off (after three seconds) because of the (erroneous) reading of the attitude as if the capsule was up-side-down. Of course, this produced the crash on the Martian surface.

A key point in the mission failure was the duration of the IMU's saturation persistence, which was assumed to be 15 ms, however it wasn't tested when the hardware was supplied by the related subcontractor. The chapter gives a summary of other alternative hypotheses (as indicated in Fig 28) and the reasons why a re-entry parachute could fail [1].

2.1 Different hypothesis according to the ESA Report

ESA has been reported the different hypothesis by understanding the causes of IMU Saturation and high dynamic phenomenon is depicted as an anomaly tree as shown in Fig 28.

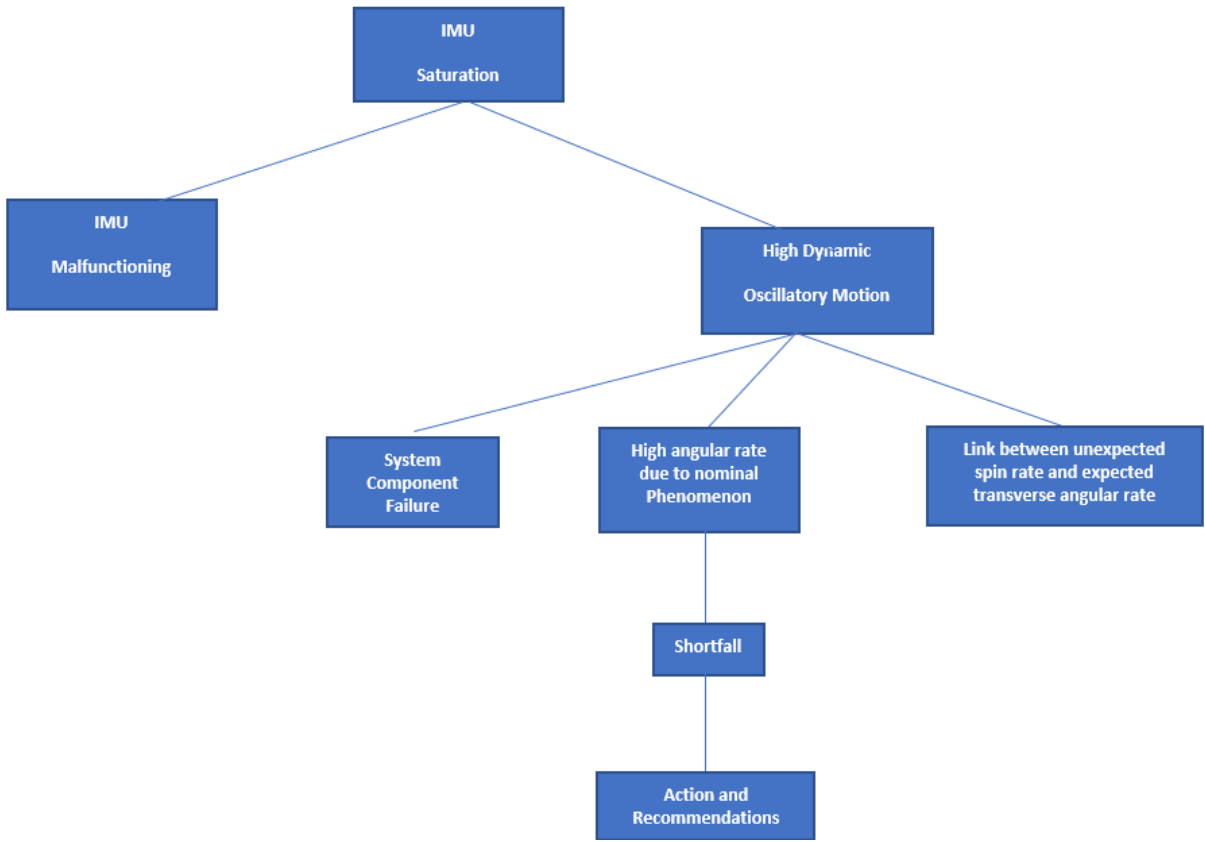


Fig 28. Description about Hypothesis of an EDM failure in Factor tree diagram [1]

2.1.1 IMU Malfunctioning

IMU malfunction is brought about by incorrect measurements made in a demanding environment when a parachute was being deployed, or by sensitivity to greater angle acceleration and IMU internal component failure. Some additional analysing and testing have been conducted to identify the malfunctioning of IMU in a demanding situation.

- When angular rates exceed its measurements capability.
- When it suddenly experiences high angular acceleration and linear jerk environment in which IMU was not previously tested.

Above all these activities, it was discovered that IMU performance degrades when subjected to jerk and angle of attack. However, the errors discovered during the tests were never so high to justify the gyro saturation [1].

2.1.2 High Dynamic oscillatory motion

The following were found to be the primary contributing factors to the re-entry parachute's high dynamic oscillatory motion:

- a) Higher angular rates were generated by the failure of some hardware component during the deployment of the parachute.
- b) Higher angular rates are due to unforeseen aerodynamic phenomena that is brought on by a combination of significant factors but is unrelated to a particular failure.

As for point a), no unusual behaviour during the periods before or after the parachute deployment might suggest any system or component faults have been found. The inquiry of requests for devotions and waivers (RFDs, RFWs) and Non-Conformance Reports (NCRs) of the hardware determined that the high dynamics motion observed during parachute deployment is not the result of any system or component failure.

As for point b), it is known that the hypersonic parachute deployment is a very complex phenomenon affected by several uncertainties (winds, wake, etc.) Therefore, it is difficult to predict the model. The following aspects have been identified as potentially contributing to the higher angular rates during parachute deployment:

- AOA is higher than estimated due to presence of winds or gusts in atmosphere, inertia values and position of evolution/COG and Evolution during descent in line with charge of EDL configuration.
- Additional torques at parachute mortar firing and inflation due to mortar axis not aligned with Centre of Gravity (COG)
- Bridles asymmetry

- Incorrect modelling of parachute riser angle at inflation
- Parachute oscillation force along the river due to parachute area oscillation.
- Large canopy motion due to unsteady wake dynamics causing large riser angle variation including bridle shaking asymmetric canopy inflation [1].

Simple planar oscillation wrist mode modelling agrees with Monte Carlo simulations in a significant number of cases where angular rates are above the EDM-IMU saturation levels, according to NASA/Monte JPL's Carlo simulations of the Schiaparelli parachute deployment using their high-fidelity model.

Post-fight analysis was used to reconstruct the parachute riser angles based on the angular rates and linear acceleration of the EDM. This analysis revealed that significant riser force and angle fluctuations after parachute inflation were possible to predict but not taken into account in the phase of the project of the mission.

The Canopy's performance demonstrates that high parachute dynamics were to be expected when compared to similar Mach number wind tunnel experiments carried out in the context of NASA missions with their fighting experience [1].

2.1.3 Links between unexpected spin rate and transverse angular rates

The planar oscillations model does not consider the spin rotation of the parachute and the possible coupling of the spin dynamics with the planar oscillations at high attitude energy dynamics. So, it is important to investigate if some link between spin rate and transverse rate was possible.

During Entry and descent, the EDM spin rate showed an unexpected behaviour between EIP and PDD triggering spin rate increased from 16 to 18 deg/s before PDD and decreases to 12 deg/s before PDD. After PDD triggering, the spin rate decreased up to almost zero before Front Shield Jettisoning.

These spin rate variations were also observed during NASA's mars exploration rover mission. A possible explanation of the phenomenon was given by the inspection

performed by the rover Opportunity on the surface of Mars revealing the existence of several remaining thermal blanket elements. The unexpected spin rate during entry could be due to uneven disintegration of thermal blankets and associated hardware.

In the Schiaparelli mission, this potential effect was limited to a small spin rate due to transonic speeds ($M = 0.75$ to 2.5): the spin energy could not be transferred to transversal oscillations due to high dynamics. The angular acceleration around the spin axis has been recharged and there became slight twist in a parachute riser after parachute deployment. The SIB (Schiaparelli Inquiry Board) considered there is no link between the unexpected spin rate behaviour and transverse angular rates that saturated the IMU due to high dynamic oscillatory motion of Re-entry Parachute [1].

2.1.4 Riser angle

Riser angle inflation is one of the main parameters that drives the angular rates of the parachute riser, which should aligned to parachute drag force with respect to longitudinal vertical axis at end of inflation. Angular transverse rates are different from 0 to PDD which increasing and decreasing limit of maximum angle of attack depending on the direction of an initial angular transverse rate [1].

Fig 29 shows a sensibility analysis of the raiser angle at the EIP with respect to the landing site [5]. The Monte Carlo Analysis is based on 5000 shots in full stage dispersions [5].

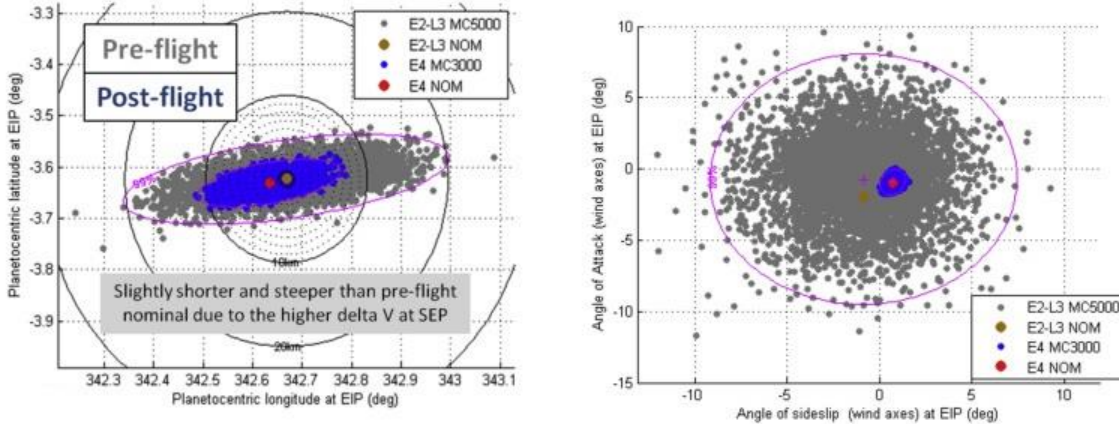


Fig 29. Pre-flight (grey, 5000 shots) and post-flight (blue, 3000 shots) dispersions at EIP.

Credit: DEIMOS Space [5]

It is evident from the post processing of the riser angle that the predictions by the used multibody simulation did not provide its real behaviour. This is supported by JPL7NASA model which indicates the position of the canopy as it begins inflating does not correlate with the altitude of the vehicle at mortar fire as it assumed in EDM modelling.

Moreover, EDM parachute models also do not account for the large non-linear and non-stationary parachute forces that occurs when parachutes deployed at supersonic conditions which increases above $M=1.4$ and becomes severe above $M=2$ [5].

2.1.5 Inadequate persistent time of IMU Saturation flag by GNC

The IMU indicates an exceedance by setting a bit when angular rates exceed the saturation limit (Rate Flag Bit): 150 deg/s. It was discovered that the mission's so-called persistence flag for IMU saturation (1s) was too high. The GNC created a bias error on the attitude as it integrated such a rate throughout the course of the whole IMU saturation persistence duration. If the persistence period had been chosen at a lower value (15ms) as planned in the initial phase of the IMU procurement, the attitude knowledge mistake brought on by IMU saturation would not have put the mission in danger [1].

From IMU data it was possible to extract the time profiles of non-gravitational accelerations and capsule angular rates. The following Fig 30 shows the important events, such as the firing of the mortar, the full inflation of the parachute, and the release of the front shield (Fig 30) [5].

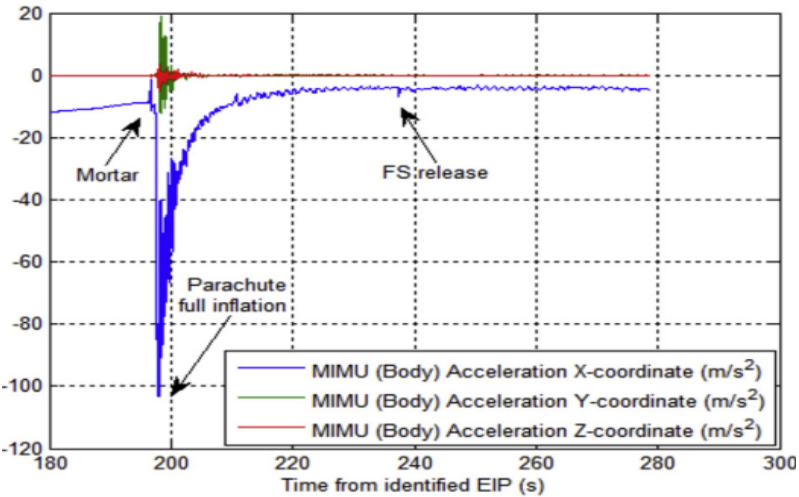


Fig 30. Body axes non-gravitational accelerations: key descent phase events. Credit: DEIMOS Space [5]

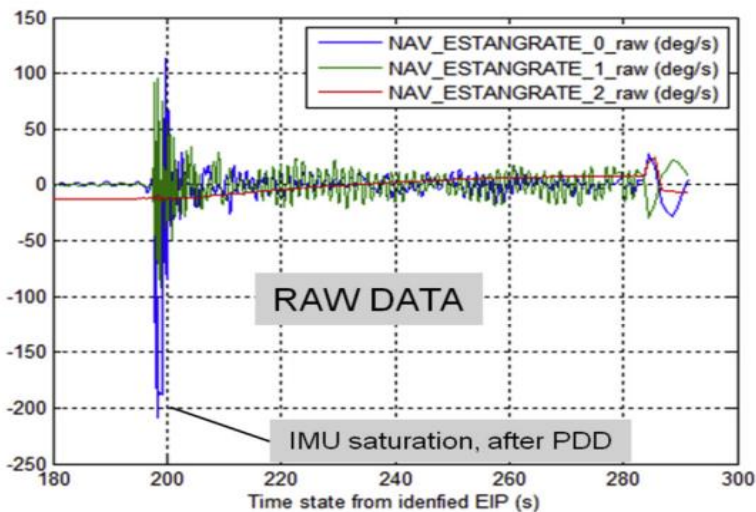


Fig 31. IMU navigation: angular rates and saturation. Credit: DEIMOS Space [5]

Fig 31 shows that the yaw angular rate sensor's saturation at -187 deg/s continued for 1s (instead of the anticipated 15ms). Of course, this persistence generates a relevant

error in the yaw angle, shown in Fig 32. In particular, the Euler's angle and the on-board estimation of the capsule in the X-Direction were both incorrectly estimated because of this bias's impact on the navigation solution during the descent phase [5].

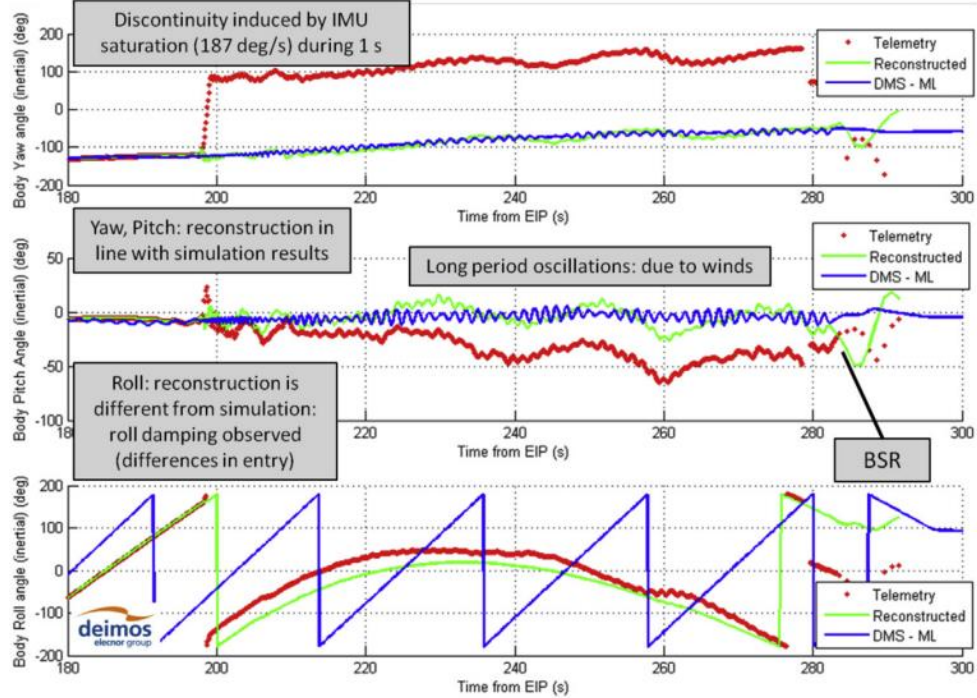


Fig 32. Inertial Euler's angles (red: OBT, green: reconstructed by DEIMOS, blue: most likely trajectory). Credit: DEIMOS Space [5]

This wrong attitude produced a series of wrong commands after the parachute deployment, such as the anticipated cut of the parachute and the shutdown of the retrorockets [5].

2.2 The failure due to areal oscillations

An asymmetry in canopy would explain both forces on transversal Y and Z axes and force magnitude oscillations. This is a highly non-linear problem observed in wind tunnel tests of DGB parachutes in the supersonic region of Mach numbers around the IMU saturation and is understood to be the result of interactions between the capsule shockwave and the parachute canopy and lines, see Fig 33.

In the experimental tests “The mechanism discovered is the turbulent wake coupling to the parachute’s bow-shock causing it to change shape and standoff distance, resulting in depressurization of the canopy and resultant partial collapse” [5]. Images of the supersonic instability known as “area oscillations” (from left to right) at Mach 2.0, 2.2, and 2.5 for a 0.8-m DGB parachute ExoMars 2016 are in Fig 33[5].

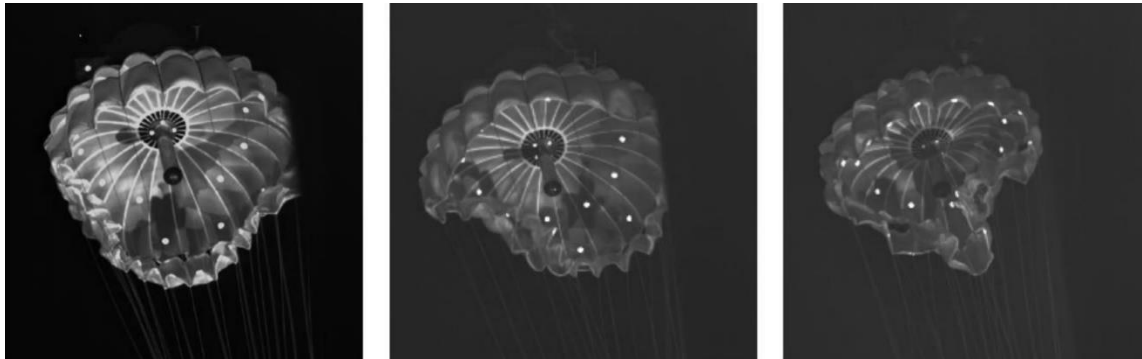


Fig 33. Images of the supersonic instability known as “area oscillations” (from left to right) at Mach 2.0, 2.2, and 2.5 for a 0.8-m DGB parachute [5]

A simple planar oscillation model was introduced during the SIB investigation [8] considering the capsule and parachute body system having the same attitude, as if they were a single rigid body with transversal inertia moment I_y with value approximated to

$$I_y = 5760 \text{ kg m}^2$$

From the attitude reconstruction, see Fig 34, the anomalous kick of the yaw angular rate occurs at the interval of time ΔT starting from 1.5s and ending with 2.0s. The corresponding variation $\Delta\Omega_y$ of yaw angular rate is about 180deg/s:

$$\Delta\Omega_y = 180 \text{ deg/s} = \pi \text{ rad/s} \quad (6)$$

$\Delta T = 0.5\text{s}$,

i.e., the related angular acceleration can be approximated by

$$\frac{\Delta \Omega_y}{\Delta T} = 2\pi \text{ rad/s}^2 \quad (7)$$

The torque M necessary to generate such a variation of angular rate is approximated by

$$I_y \frac{\Delta \Omega_y}{\Delta T} = M \quad (8)$$

In both equations (7) and (8) the term $(I_z - I_x) \Omega_z \Omega_x$ of the yaw dynamics is neglected, since the averaged angular velocities Ω_z, Ω_x in the interval of time ΔT are small and their product is approximated to zero [8].

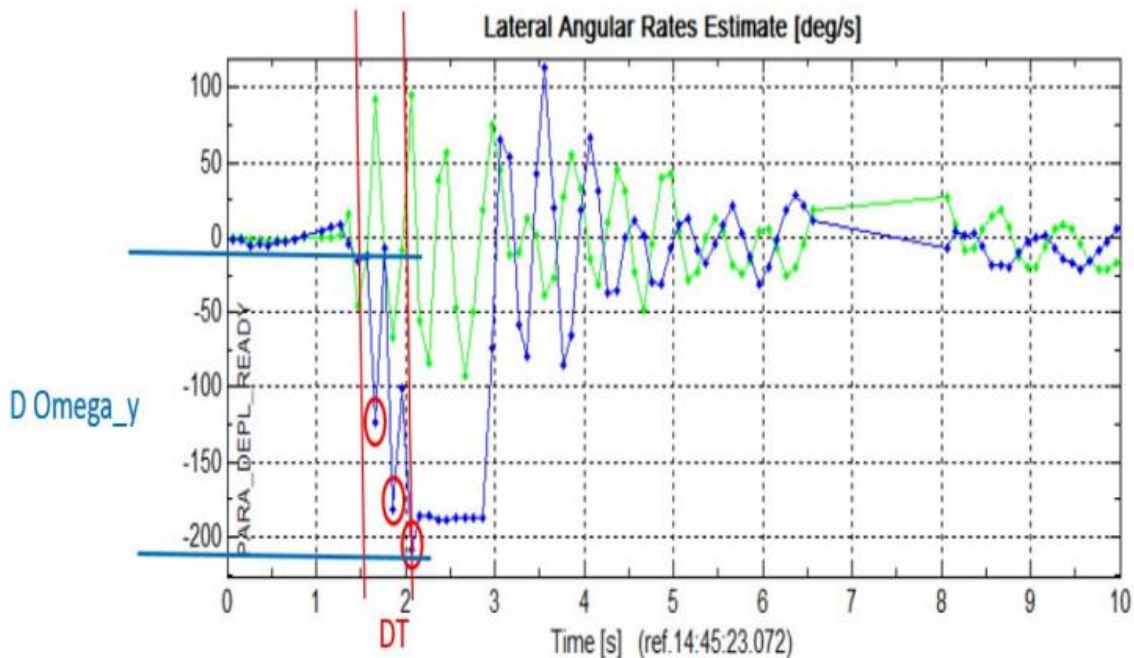


Fig 34. The angular rates Ω_y, Ω_z during the parachute inflation and stabilization [8]

Then torque on the system in the yaw component is equal to

$$M_{kick} = \frac{\Delta \Omega_y}{\Delta T} I_y = 2\pi I_y = 36191\text{Nm} \quad (9)$$

The Aerodynamic Torque produced by the parachute is

$$M_{aero} = qSL_{tot}C_z \quad (10)$$

Where,

q is dynamic pressure = 800Pa,

S is the parachute reference surface, set to 113 m²,

L_{tot} is the distance between the parachute centre of pressure and the system centre of mass= 27.6m.

Then

$$M_{aero} = (2.495e^{06})C_z \text{ Nm} \quad (11)$$

The high value of coefficient in equation (11) shows the importance of aerodynamic lateral coefficient C_z (depending on angle of attack and Mach number): in fact, C_z coefficients compatible with the equality $M_{kick} = M_{aero}$ are possible.

If the kick torque M_{kick} is equal to the aerodynamic torque,

$$M_{kick} = 36194 \text{Nm} = M_{aero} = (2.495e^{06})C_z \text{ Nm}$$

the values of the aerodynamic coefficient C_z is obtained:

$$(C_z)_{kick} = 0.0145$$

This value is marked by a black line in Fig 35. The figure shows the computed aerodynamic coefficients C_z , maximum (in red), minimum (in green) and nominal (in blue) values as function of the angle of attack (α). For angle of attack $\alpha < 12\text{deg}$ the nominal C_z coefficient is below the value of $(C_z)_{kick}$, and the maximum C_z exceeds the value $(C_z)_{kick}$ for α in the range of 2deg and also from 5deg to 16deg. There is a decrease in the value $(C_z)_{kick}$ for α in the range of 3deg to 4deg [8].

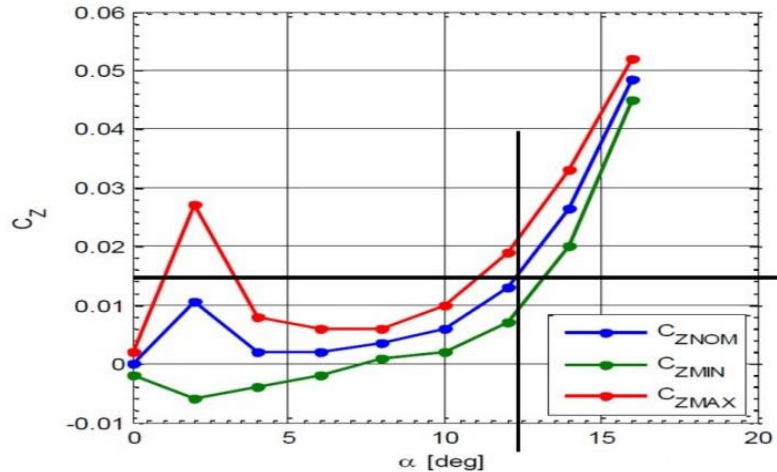


Fig 35. The lateral aerodynamic coefficient of the parachute [8]

The reported expected value of α before the inflation was $\alpha = 6^\circ$ corresponding to a small C_z also in the case of $C_{Z\max}$. However, the inflation of the parachute can be subjected to the different anomalies [8].

The different peaks in the Fig 34 (underlined by red circles) can be related to the uneven parachute inflation. In particular asymmetries in the shape of the parachute due to the partial inflation of the parachute can increase the value of the lateral force coefficient. Fig 36 shows that the symmetry of the aerodynamic pressure on the canopy produces no lateral force. On the other hand, asymmetry due to non-zero angle of attack or to a not symmetric canopy geometry (due to partial inflation) can produce large C_z [8].

The asymmetries in the Schiaparelli mission were probably due to areal oscillations and the asymmetry of the canopy during inflation produced the large C_z . Note that also in the Schiaparelli mission, at the end of the inflation process the symmetry of the canopy is established and the strong lateral oscillations are damped, see Fig 34 after time $t=3$ s [8].

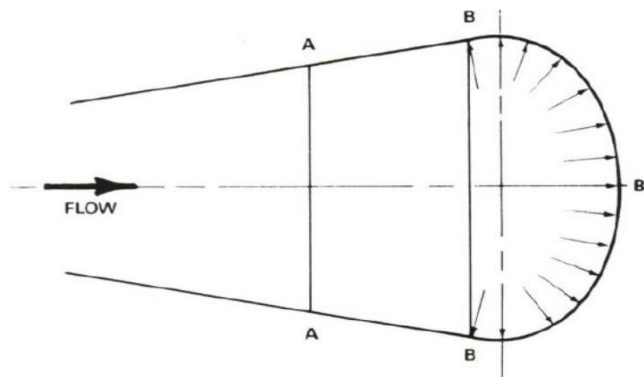


Fig 36. The symmetry of the pressure on the canopy that produces no lateral force [8]

CHAPTER 3

MARS ENVIRONMENT

In the mission design of Mars entry trajectories, the different elements of the Mars environment are relevant for the different phases of the mission. During the arrival arch of the hyperbolic trajectory the gravity effect is by far the most relevant, whereas the aerodynamic drag becomes prevalent in the terminal phase of the entry trajectory. The entry corridor and the parachute deployment depend strongly on the Mars atmosphere model, this model, together with the gravitational model are now sufficiently accurate after the measurements performed by different Mars missions.

3.1 Mars gravity Field

The Mars gravity field map has been created by tracking Mars gravitational pull on the three NASA spacecraft Mars Global Surveyor (MGS), Mars odyssey and Mars Reconnaissance orbiter (MRO). The new gravity solution includes the information the Martian tides, crustal thickness and CO₂ Cycle which leads to a better understanding of Mars interior and Climatic Evolution.

The new gravity map combined with topography allowed us to derive more accurate crustal thickness map of mars with the resolution of ~120km. New gravity field also provided to information on Martian tides that confirmed the pressure of Mars liquid outer core of molten rock. Overtime changes in the gravity of mars have been measured to monitor the polar ice caps. For the first time, it was possible to use MRO data to continue monitoring the planet mass. Variations of the polar caps mass over an entire solar cycle have been computed showing the consistent results with numerical predictions from Mars global reference atmospheric model 2010 [10].

3.1.1 Mars orbital Missions

MGS, Mars odessy and MRO have been contributed to NASA's Mars Exploration Program, that makes use of orbiters, landers and rovers to investigate and monitor this Planet. MGS was designed to provide global mapping of the atmosphere surface and interior. One of mapping the fine measurements on board was the Mars Orbiter Laser Altimeter (MOLA) operated until July 2001. The ranging measurements from the MGS Space craft to the Martian atmosphere surface resulted in high-resolution topographic maps of the planet, they are still the most geodetically accurate. The MOLA topography resolution is 1km in latitude and 2km in longitude at the equator as shown in Fig 37. MGS Executed its mapping mission between 1999 and 2006 in frozen sub-synchronous near circular, polar orbit with their periapsis at 370km and dayside equatorial crossing at 2pm Local Solar Time (LST) [10].

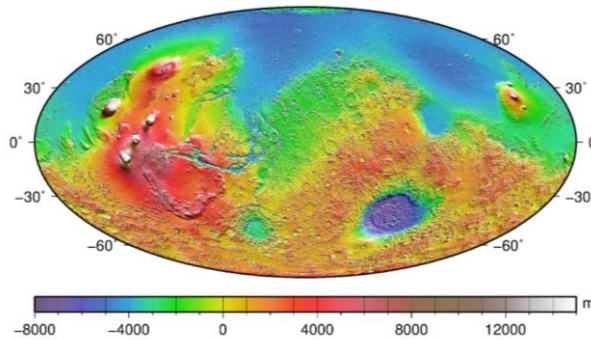


Fig 37. Map of the global topography of Mars. The projection is Mollweide centered at 0° longitude [10]

Mars odessy and MRO are still orbiting mars in two different sun-synchronous near polar orbits with periapsis altitude at ~390km and ~250km respectively. The descending node of MRO is at 3pm LST. Both spacecraft have collected the measurements at lower altitudes (approximately 220km) during orbit transition phases that preceded the mapping missions. In 2002, Mars odessy has been stared to mars with three measurements that were focussed on studying about past and present water and ice, geology and radiation environment. In 2006, MRO was in a low-altitude orbit around Mars. The Engineering instruments of this which included Gravity field

investigation packages that has been dedicated to measurement variation in the gravitational field of Mars through determination of spacecraft orbit [10].

3.1.2 Data of NASA-DSN with solution of Gravity

The NASA-Deep Space Network (DSN) have acquired X-band tracking data from these three-space craft that provide information on the static and time varying gravity field of Mars. The continuity of the radio tracking data, which covers more than entire solar cycle is an unique opportunity to characterize the temporal variability of the Gravity field relevant to internal dynamics of planet and Dynamics and structure of an atmosphere.

The Gravity solution of Mars depends significantly on the geodetic altitude and latitude coverage of the radio tracking data. Lower orbital altitudes provide better sensitivity to short- wavelength signals and improved gravity solution. MRO low-altitude orbit was designed to determine the high accurate gravity maps with spatial resolution of ~90km corresponds to 110° in spherical harmonic expansion [10]. The Gravitational Constant on Mars is 6.68×10^{-11} Nm²kg⁻²[11].

Table 5: Planetary Parameters for Each Planet including Mars [9]

Planet	Equatorial Radius (Re) in Meters	Gravitational Parameter (GM) in m ³ /s ²	Zonal Harmonic Coefficients (J Values)
Earth	6378.1363e3	3.986004415e ¹⁴	[0.0010826269(J1) -0.0000025323(J2) -0.0000016204 (J3)]
Jupiter	71492e3	1.268e ¹⁷	[0.01475(J1) 0 (J2) -0.00058(J3)]
Mars	3397.2e3	4.305e ¹³	[0.001964(J1) 0.000036(J2)]
Mercury	2439.0e3	2.2032e ¹³	0.00006(J1)
Moon	1738.0e3	4902.799e ⁹	0.0002027(J1)
Neptune	24764e3	6.809e ¹⁵	0.004(J1)
Saturn	60268e3	3.794e ¹⁶	[0.01645(J1) 0(J2) -0.001(J3)]
Uranus	25559e3	5.794e ¹⁵	0.012(J1)
Venus	6052.0e3	3.257e ¹⁴	0.000027(J1)

3.2 Mars Atmosphere

Martian atmosphere composed of 96% of Carbon di-oxide (CO₂), 1.9% of Nitrogen (N₂) and 1.9% of Argon (Ar) and remaining 1.2 % of trace gases (O₂, CO, H₂O) which is over 100 times thinner than that of earth as shown in Fig 38. Table 5 Shows the

Comparison of planetary parameters for Mars along with earth and other planets. The atmospheric pressure at the Martian surface is 6.35mbar which is 100 times than earth. The humans cannot breathe Martian air because it is oxidised with dust particles were kicked up from the surface of Mars that fills the atmosphere turning Mars skies a rusty tan colour. Water exists on Mars surface, but the atmosphere is too thin for its last long on the surface in the liquid state.

Early in history Mars had a thick enough atmosphere for water to run on its surface. According to NASA, some surface features suggest that mars experienced huge floods about 3.5 billion years ago.

Orbital pictures show vast river plains and possible ocean boundaries, while several mars rovers have found evidence of water soaked rocks on surface such as hematite or clay. So, the Martian surface has got thinner.

Mars is much colder than earth due to the thin atmosphere and it is far away from the sun. The average temperature on Mars is about 80°F (-60°C), although it can vary from -195°F (-125°F) near the poles during the winter to as much as a comfortable 70°F (20°C) at midday near the equator [11].

According to NASA results, the planet also has four seasons like earth but due to red planet's eccentric orbit, the length of each season varies more than on earth [12].

Mars ice caps made up of water, ice, and Carbon di-oxide (CO₂) shrink and grow in response to the seasons. These seasonal changes to ice caps affect Mars atmosphere that responds as one large interconnected system. The lower and middle level of Mars atmosphere appear to be coupled to the upper levels: there is a clear link between them throughout the years of Mars [11].

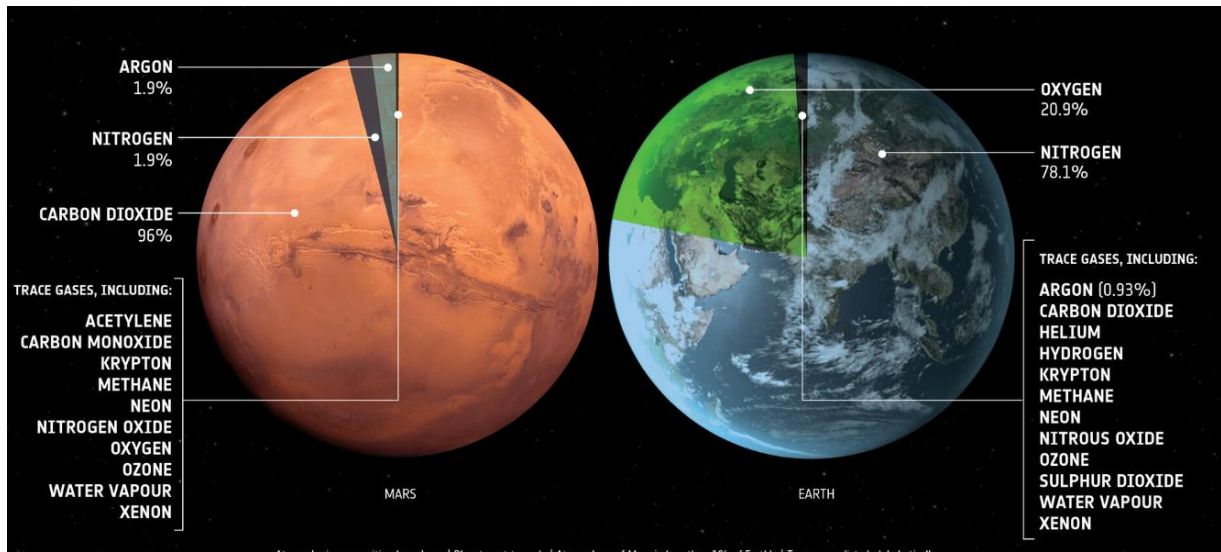


Fig 38. Atmospheric Composition of Mars and Earth [11]

ESA studies state that Mars atmosphere condenses up to third of mass to form an icy layer at each of the planet poles in every winter whereas some of the mass within these caps sublimes to re-join the atmosphere and the caps visibility shrinks in every summer [11].

Giant dust devils in Mars routinely kicks up the oxidized iron dust that covers mar's surface. Dust is also a permanent part of the atmosphere with huge amount of it in the northern fall and winter whereas lower amounts in northern spring and summer. The dust storms of mars are the largest in the solar system, capable of blanking the entire planet and lasting for months which usually take place in the spring or summer. These dust storms can play havoc with mars exploration mission can even ground flights [11].

The dust storms can grow so big on mars starts with air borne dust particles absorbing sunlight, warming the Martian atmosphere in their vicinity. Warm packets of air flow towards colder regions generating winds. Strong winds lift more dust of the ground which in turn heats the atmosphere raising more winds and kicks up more dust.

The snowflakes of Mars contain carbon dioxide (CO_2) rather than water are thought to be very small particles that create fog effects rather than appearing as falling snow.

The north and south pole regions of Mars are capped by ice made from Carbon dioxide (CO_2) and Water [11].

3.3 Statistical Models of the Mars atmosphere

SPICAM is one of the instruments which is used in Mars to observe its middle atmosphere. It also observes continuously a selected star while the space craft moves around the planet. So that star can be observed setting or rising the atmosphere when the star is high above the horizon, the light spectrum of star is recorded free from any atmospheric absorption whereas when it is seen through the atmosphere, the atmospheric constitutions integrated over a line of sight from the instrument of star. By analysing such variation in 110-310mm wavelength range with a 1.5mm resolution. SPICAM provides information about profile of aerosols, ozone, and CO_2 . The location of tangential points move only by a few tens of km during observation [12].

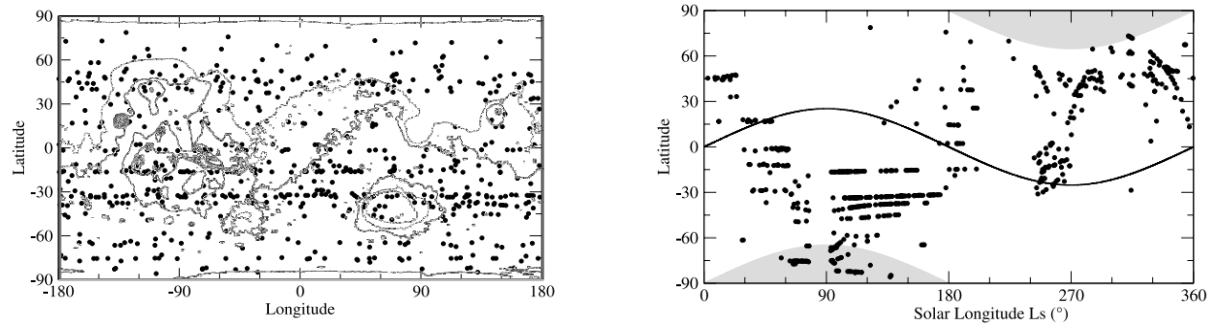


Fig 39. The spatial and seasonal distribution of the 616 SPICAM solar occultations. (a) Locations of the occultations superimposed on a topography map of Mars. (b) The latitudinal distribution of the occultations as a function of season (L_s , areocentric longitude of the sun, with $L_s = 0$ at northern spring equinox). The black solid line shows the latitude of the subsolar point. Shaded areas illustrate the extension of the polar nights [12]

The data are analysed from 616 usable stellar occupation profiles obtained over more than one Martian year in 2004, 2005 and Early 2006. After one early profile obtained at beginning of the mission during orbit 17 (14 Jan 2004, $L_s=332.8^\circ$) data were recorded regularly starting on orbit 134 (22 Feb 2004, $L_s=353.4^\circ$) until orbit 2779 (12 Mar

2006, $L_s=23.3^\circ$) with one late single profile obtained during stellar oscillations and their seasonal distribution covers the entire planet although the latitudinal coverage depends on the season with significantly more observation during fall and winter in each atmosphere as shown in Fig 39. These results are obtained from the concentration of hot UV stars along the galactic plane combined with the Mars Express orbit variations with its periapsis latitude slowly varying over time and the fact that observation were preferentially performed might side where solar light scattered by Aerosols and reflected by the surface could not affect the measure. The variation of Physical parameters and some thermal properties has been below in this section [12].

3.3.1 Variation in Density along with altitude

CO_2 is the main constituent of the Martian atmosphere absorbs the UV light emitted by the occulted star between 120nm and 190nm only hot stars emit enough UV to be used for CO_2 absorption, amount of CO_2 that present between SPICAM and star can be detected. The amount of slant density which is integral of the load density by performing a mathematical inversion. The forward radiative transfer model has been improved using Onion Peeling approach with a Tikhonov regularization method which used a model resolution of 1.5nm to match the SPICAM spectral. However, the transmission computed with such averaged cross section can differ from the average of the transmission obtained with infinite spectral resolution. Radiative transfer calculations are performed at the highest possible resolution which is provided by the spectroscopic database (0.005nm). The slant density profile in atmosphere were initially smoothed by using a running average function with a vertical width of 110km applied to logarithm on slant densities lower than 20%. The typical CO_2 profiles which are retrieved a various seasons shown in Fig 40(a) - Fig 40(c). The errors have been combined to improve the noise related error is averaged by smoothing the slant densities during retrieval and including instrumental noise that was now taken into account in our error bars with typical contribution from instrument noise around 3 to 8% between 70km and 120km [12].

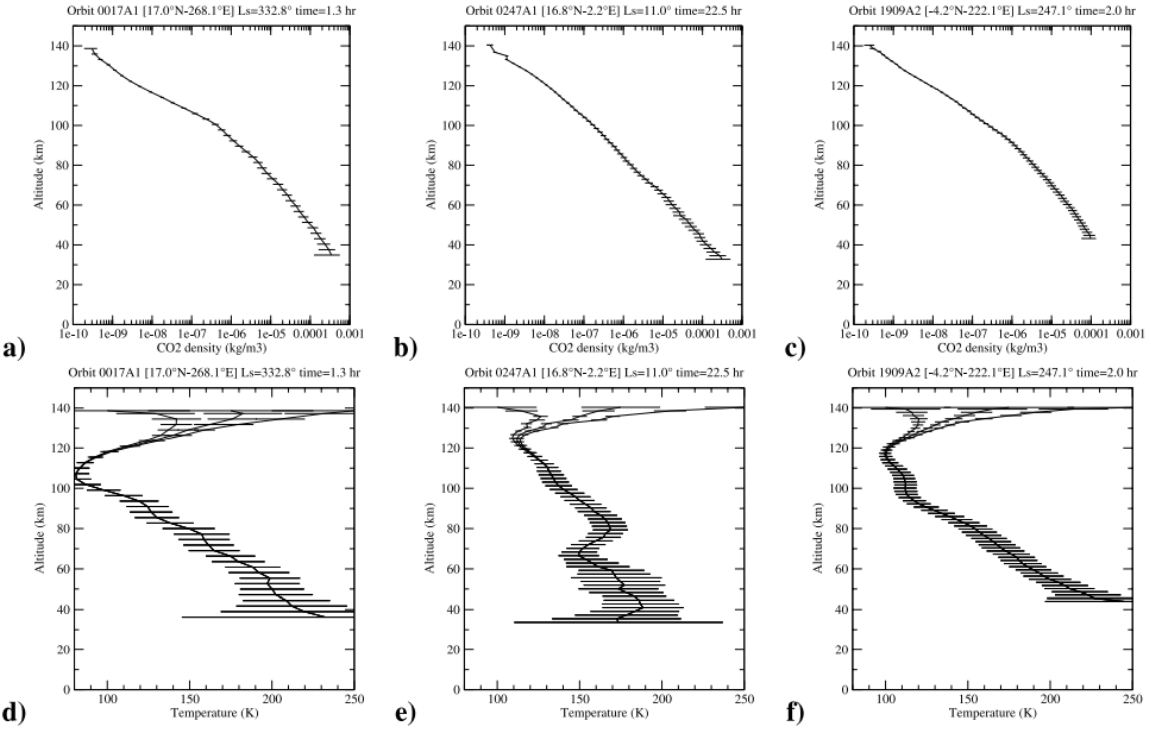


Fig 40. Examples of (top) three typical SPICAM CO₂ density profiles and (bottom) the corresponding derived temperature profiles. The error bars illustrate the instrumental and retrieval model errors and a possible bias due to uncertainties on CO₂ cross sections. In each case, three temperature profiles retrieved with top temperatures of 100, 175, and 250 K are shown [12]

The error bars are symmetric to represent a possible bias due to uncertainties in the spectroscopic data due to variations with temperature. The cross section of CO₂ is available only at 195K and 295K. The impact of temperature is stronger when observing largest slant densities because the absorption of CO₂ cross sections sensitivity to temperature is mostly significant at wavelength larger than 160nm as shown in Fig 40. The retrieval is sensitive to this part of the spectra only for slant densities the effect is small with an average difference of 7% between retrievals performed with 195K and 295K data set. Above 10¹⁹cm⁻², difference increases linearly with the log of slant density and reaches 50% for slant densities equal or larger than 10²² cm⁻² to extrapolate this sensitivity below 195L may be hazardous but 5% bias for slant densities lower than 10¹⁹cm⁻² and 20% error above 10²²cm⁻² with linear translation with the log of slant density for taking account to typical Martian Atmosphere.

Because the CO₂ absorption decrease with temperature and because the upper atmosphere is observed by SPICAM is colder than 195K, corresponds to density underestimation. Below 60km, due to presence of air borne dust there is difficult to estimate absorption by dust is limiting factor of the method at lower altitude whereas at higher altitude CO₂ slant density is the limiting factor. So, the density is retrieved by SPICAM below 50km are often strongly underestimated [12].

3.3.2 Variation in Temperature along with altitude

Temperature profiles can be derived from the densities profiles assuming that the atmospheric is in hydrostatic Equilibrium. To avoid amplification of Errors resulting from the decrease of density when going upwards, the integration is performed from the top of the density profile to the bottom. The temperature profiles retrieved assumption of top temperatures 100K, 175K and 250K compare with density Profile at 140km which is unknown as shown in Fig 40(d) - Fig 40(f), but the three curves are superimposed below 120km. It is safe to assume that the retrieved temperature profile is insensitive to the assumed boundary temperature below this level. The error bars account for the instrumental noise typically 3 to 6K at 115km, 7 to 15k at 70km and the possible bias resulting from the underestimation of density due to spectroscopic data uncertainties which was estimated by adding bias mentioned above the density profile and use the resulting profile to retrieve temperature. If the associated shift remains below 3K between 6km and 110km, the dust may affect the quality of the results. SPICAM temperatures below 0.1 Pa (or 70 km) which are unreliable are often strongly overestimated [12].

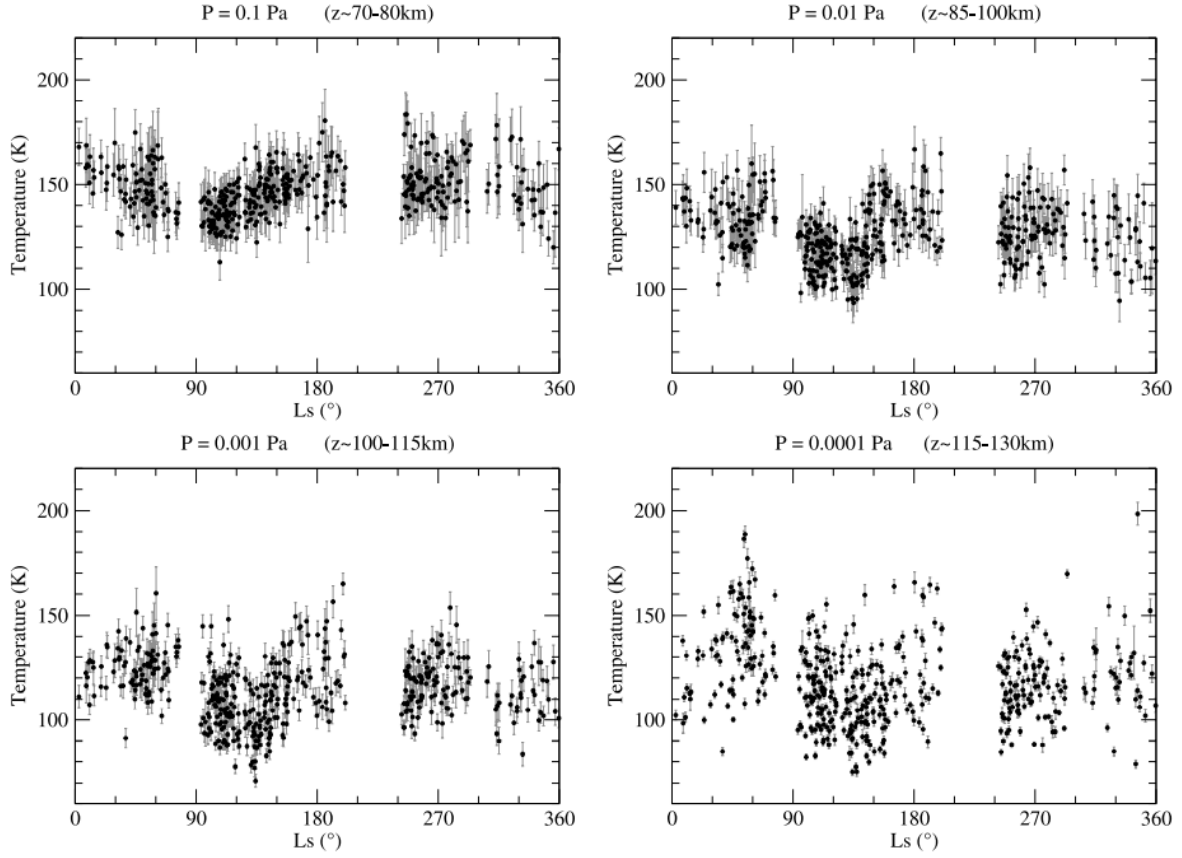


Fig 41. Temperature retrieved between 50°S and 50°N plotted as a function of season (L_s) and interpolated at four pressure levels. The absolute error bars shown are large, but we believe that the relative variations are meaningful. Depending on the season, 0.1 Pa corresponds to altitudes around 70–80 km, 0.01 Pa to 85–100 km, 0.001 Pa to 100–115 km, and 0.0001 Pa to 115–130 km [12].

3.3.3 Latitudinal and Longitudinal variations

Latitudinal Variations of Atmospheric density are observed by SPICAM between 70 and 120km which are primarily reflect the variations in lower atmospheric temperature. The density is observed to systematically decrease in the winter mid and high altitudes [12].

The distribution of SPICAM temperature retrieved at various atmospheric levels shortly after southern winter solstice ($L_s = 90^\circ\text{--}120^\circ$) as a latitude function as shown in Fig 42. Despite the spread of data 0.1 and 0.01Pa Temperature are characterised by 20 to 30K south polar warming such warming has been predicted by General circulation models. It is a result obtained from adiabatic compression in descending windows

induced by a convergence of Mass in the upper atmosphere, primarily forced warming forced warming has been observed in north polar night around 100-130km by the mars odyssey spacecraft during its aerobraking period as shown in Fig 41. In the southern hemisphere, there is less clear in Aerobraking observations. These data are obtained by Mars Global Surveyor and MRO which are detected a cooling at 120-130km, but MRO measured a 10K warming at 110km on the night side as shown in Fig 41 (d). When plotted altitude co-ordinate consistent with this observation and suggested that if MRO has been able to make measurements at 90km and 80km, it would have been detected at high side a polar warming larger than 20K [12].

In longitudinal Variations, Densities measured around 100-130km by the aerobraking mars Global surveyor accelerometer at fixed local time and latitude were often characterized by interesting longitudinal variations which are first interpreted as possible stationary planetary waves later attributed to eastward propagating waves of the diurnal and semi diurnal frequencies as shown in Fig 42. On this basis, the similar structures in SPICAM data obtained at similar local time season but no clearance could be identified at different altitude [12]. Table 6 shows the atmospheric density variation values of Mars environment with respect to Altitude from 1km to 50km. The Atmospheric surface density of Mars is approximately 0.020kg/m^3 compared to earth [12].

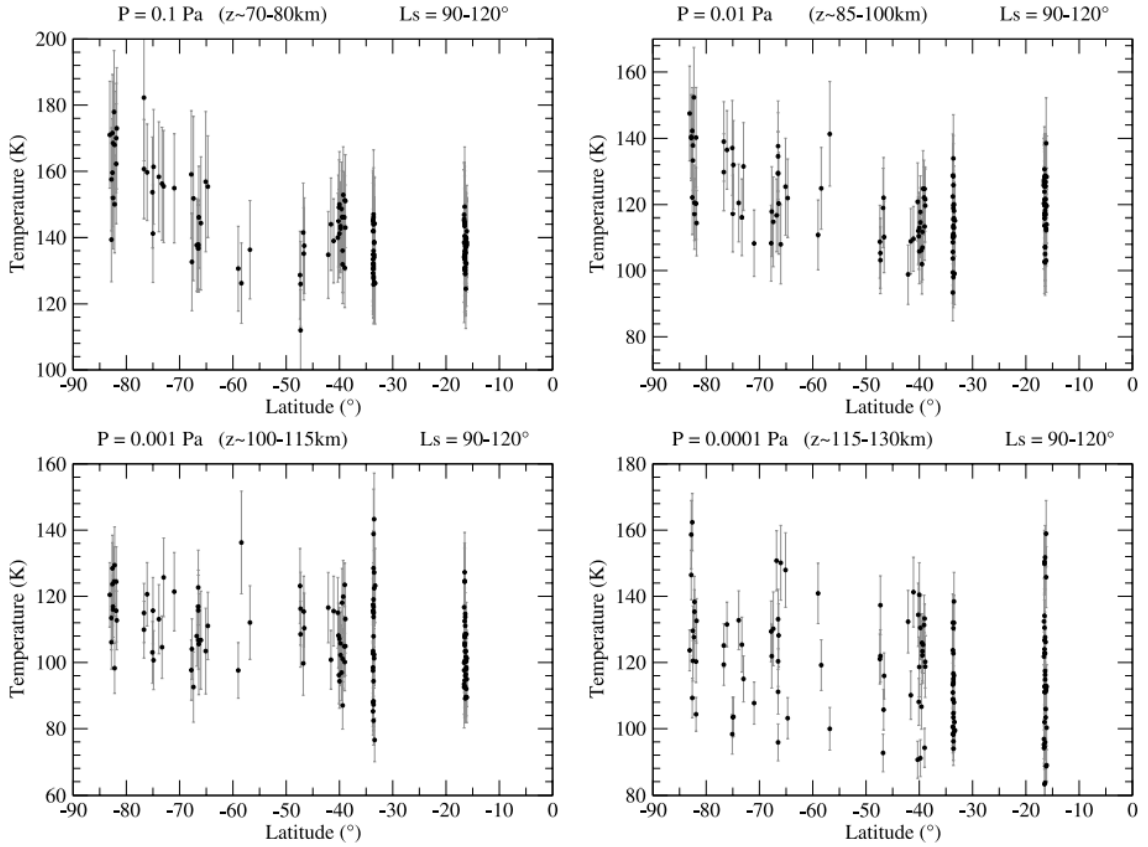


Fig 42. Latitudinal temperature variations in early southern winter ($L_s = 90^{\circ}\text{--}120^{\circ}$) interpolated at four pressure levels. Note the 30 K polar warming above the 0.01 Pa (90 km) level [12]

Despite of the different effects producing variations of the Mars atmospheric density, a standard model is assumed for the mission design, at least in a preliminary phase.

The exponential model [13] is used as

$$\rho = \rho_0 e^{-\frac{h}{H_{den}}} \quad (12)$$

where ρ_0 is the reference density which have been updated at the different altitudes from the Mars surface according to Table 6 first two columns, and H_{den} is the scale factor updated with the altitude according to the columns 1 and 4 of the Table 6.

Table 6: Table of standard Mars atmospheric density with respect to Altitude [13]

ht, km	d, kg/m ³	T, K	Hden, km	c, m/s
0	1.5500E-02	214	11.6	233.6
10	6.4700E-03	205	11.73	228.5
20	2.6300E-03	188.3	10.68	218.8
30	9.8000E-04	175	9.77	211
40	3.4000E-04	162.4	9.06	203.6
50	1.0800E-04	152.2	8.42	197
60	3.1800E-05	144.2	7.93	191.6
70	8.7300E-06	139.5	7.53	188.4
80	2.2900E-06	139	7.47	187.9
90	6.0100E-07	139	7.51	188.2
100	1.5900E-07	139	7.38	188.1
110	4.1400E-08	149.4	7.75	195.5
120	1.1900E-08	159.7	8.34	202.5
130	3.7600E-09	170	9.58	208.6
140	1.0900E-09	245.1	9.65	251.9
150	4.7300E-10	288.6	9.7	275.5

CHAPTER 4

ANALYSIS OF TRAJECTORY

In this chapter are reported the results obtained reconstructing the Schiaparelli capsule trajectory and attitude by the telemetry data as well as from the backward propagation of the impact point with estimated impact velocity updated to match the conditions after SEP (filtering process). This “most likely real” trajectory is compared with the nominal one and with two other trajectories obtained by TAS-I and DEIMOS Space (DMS) based on updated real (and not exactly nominal) initial conditions at SEP propagated with nominal conditions after SEP [5].

Therefore, four set of data will be compared:

- a) The Schiaparelli telemetry data
- b) The data obtained by the TAS-I propagation of the trajectory starting from the real initial data at SEP and nominal parameters and commands after SEP
- c) The data obtained by the DEIMOS propagation of the trajectory starting from the real initial data at SEP and nominal parameters and commands after SEP
- d) The data obtained by the DEIMOS most likely reconstruction of the real trajectory

4.1 Description of the real re-entry trajectory

The Schiaparelli EDM performed off-nominal trajectory during descent and landing phases. Deimos company was charged by ESA to identify the actual timeline for different mission events in identify large discrepancies with respect to nominal design. Table 7 shows the events in UTC time, as declared by OBSW (On-Board Software). It shows that red marking is related to the off-nominal flight events and the declared by OBSW. It shows that events and the declared touch down corresponds to

pre-scheduled trigger of the GNC-SW (Guidance Navigation Control Software) to declare symbolical touchdown up to 4s after thruster switch off. The results are observed by comparing the OBT (On-Board Telemetry) events lists with the Entry to Entry(E2E)-loop3 prediction analysis [5].

Table 7: Telemetry events by OBSW [5]

EVENTS detected in PACKETHISTORY	Telemetry OBT (UTC)
POSTHIB_RSTRT_CMPLT	14:17:26.778
EIP_DETECT	14:42:22.074
PARA_DEPL_READY	14:45:23.072
PARA_DEPL_CMD_NOM	14:45:23.972
FSH_REL_READY	14:46:00.071
FSH_REL_CMD_NOM	14:46:04.972
	PDD + 41 s
RDA_USE_TIMEOUT	14:46:46.025
NAV_TRANSR_RDA_VEL	14:46:51.224
BEP_SEP_CMD_NOM	14:46:49.973
BAM_NO_NEED	14:46:50.073
CL_CNTRL_START	14:46:50.773
BAM_START_NOM	14:46:53.675
	BSR + 0.8 s
PRESWOFF_STRT_NOM	14:46:53.773
RCS_OFF_NOM	14:46:53.872
TOUCH_DOWN	14:46:57.925
	RRI + 3.1 s

After PDD (Parachute Deployment), Front Shield Release (FSR) was commanded 41s which is in the line with 40s interval considered in the phases E2 loop 3 prediction analysis whereas Back shell Release (BSR) command was given 86s after PDD but in nominal condition this should occurred 129s after PDD [5].

Retro-rockets Ignition (RRI) was commanded 0.8s after BSR which is the line with 1s expected time interval between the two events whereas Retro-rockets Cut-off (RRC) was command 3.1s after Retro-rockets Ignition (RRI) but it occurred 29.5s after RRI in

nominal conditions. In particular, the BSR, occurred 45s earlier than expected and RCS were active only 10% of the expected duration. Then all landing phases events were compromised [5].

Deimos company produced a numerical trajectory, called E4-0 predicted trajectory, with the nominal simulations run executed based on updated and real initial conditions. That is, the following assumptions were considered:

- Nominal vehicle properties (MCI, AEDB and ATDB, nominal environment(atmosphere) and nominal EDL events: all as pre-flight design.
- Updated Separation (SEP) performance with respect to phase E2E-loop3 prediction [5].
 1. Pre-SEP position and velocity from post-SEP OD.
 2. Delta-V at SEP as considered by ESOC for post-SEP trajectory simulations.

The Table 8 reports the comparison between the events timeline declared by the OBT, and the post-SEP trajectory simulated by DEIMOS Space [5].

Table 8: Mission Timelines comparison: OBT, post-SEP TAS-I prediction and E4-0 DEIMOS prediction [5]

Phase	Event	Mission Timeline (UTC)		
		Telemetry OBT (EVENTS detected in PACKET HISTORY)	TAS-I OBT	DEIMOS Space E4-0 Prediction
Coasting	Separation	2016-10-16- 14:42:00.000	2016-10-16- 14:42:00.000	2016-10-16- 14:42:00.000
Entry	EIP-GNC_EIP	2016-10-19- 14:42:22.074	2016-10-19- 14:42:21.800	2016-10-19- 14:42:07.032*
	Peak heat flux	n/a	n/a	2016-10-19- 14:43:25.832
Descent	PDD-Parachute deployment	2016-10-19- 14:45:23.972	2016-10-19- 14:45:26.200	2016-10-19- 14:45:26.288
	FSR-FS Jettison	2016-10-19- 14:46:04.972	2016-10-19- 14:46:07.700	2016-10-19- 14:46:06.288
Landing	BSR-Back shell release	2016-10-19- 14:46:49.973	2016-10-19- 14:47:30.500	2016-10-19- 14:47:34.695
	RRI-Retro rockets Ignition	2016-10-19- 14:46:50.773	2016-10-19- 14:47:31.500	2016-10-19- 14:47:35.695
	FF-Free fall (RCS off)	2016-10-19- 14:46:53.872	2016-10-19- 14:47:59.700	2016-10-19- 14:48:05.180
	Touch down	2016-10-19- 14:46:57.925	2016-10-19- 14:48:00.220	2016-10-19- 14:48:05.995

The results often indicates that the timeline of OBT shows an anticipation of the PDD events of 2.3 s with respect to the nominal condition that suggest a parachute opening at a Mach number higher than the 1.95 target.

Table 9 shows the simulation of reconstructed descent phase timeline to support the understanding about the occurrence of nominal flights by comparing nominal and OBT events [5].

Table 9: Reconstructed descent phase timeline for occurrence of Nominal Flight [5]

Event	Nominal Design	Derived from OBT
PDD-Parachute Deployment	Mach 1.95	Mach >1.95
FSR-FS Jettison	PDD + 40s	PDD + 41s
BSR-Back shell release	Altitude ~ 1.1km (PDD+129s)	PDD+ 86s
RRI-Retro Rockets Ignition	BSR+1s	BSR+0.8s
FF-Free fall (Retro Rockets Cut off)	Altitude~1.5m	RRI+3.1s

FSR commands 41s after PDD is confirmed also by TAS-I simulation. BSR occurs 40.5s earlier that TAS-I prediction and 44.7s earlier than DEIMOS prediction.

RRE occurs 40.7s earlier that TAS-I prediction and 44.9s earlier than Deimos prediction.

Free fall occurs at 71.7s earlier than DEIMOS prediction.

To simulate the real re-entry trajectory, it was necessary to identify additional conditions from registered data or by propagating in backward time the impact point plus filter analysis. The filtering process allowed to generate a trajectory that represents the mostly likely simulated flight of Schiaparelli capsule. Table 10 and Table 11 shows the most likely trajectory timeline compared to nominal entry after

SEP [5]. AGL is known as Altitude at Ground Level which is calculated and measured around the earth surface [5].

Table 10: Mission Timelines Comparison: OBT vs post-SEP DEIMOS prediction vs DEIMOS most Likely [5]

Phase	Event	Mission Timeline (UTC)		
		Telemetry OBT (EVENTS detected in PACKET HISTORY)	DEIMOS Space E4-0 Prediction	DEIMOS Space E4 Most likely
Coasting	Separation	2016-10-16- 14:42:00.000	2016-10-16- 14:42:00.000	2016-10-16- 14:42:00.000
Entry	EIP-GNC_EIP	2016-10-19- 14:42:22.074	2016-10-19- 14:42:07.032*	2016-10-19- 14:42:06.806*
	Peak heat flux	n/a	2016-10-19- 14:43:25.832	2016-10-19- 14:43:26.449
Descent	PDD-Parachute deployment	2016-10-19- 14:45:23.972	2016-10-19- 14:45:26.288	2016-10-19- 14:45:23.469
	FSR-FS Jettison	2016-10-19- 14:46:04.972	2016-10-19- 14:46:06.288	2016-10-19- 14:46:04.469
Landing	BSR-Back shell release	2016-10-19- 14:46:49.973	2016-10-19- 14:47:34.695	2016-10-19- 14:46:49.469
	RRI-Retro rockets Ignition	2016-10-19- 14:46:50.773	2016-10-19- 14:47:35.695	2016-10-19- 14:46:50.269
	FF-Free fall (RCS off)	2016-10-19- 14:46:53.872	2016-10-19- 14:48:05.180	2016-10-19- 14:46:53.369
	Touch down	2016-10-19- 14:46:57.925	2016-10-19- 14:48:05.995	2016-10-19- 14:47:27.924

Table 11: Mission timeline of EDL for Real re-entry trajectory compared to nominal post SEP-Prediction [5]

Phase	Event	DEIMOS Space E4-0 Prediction				DEIMOS Space E4 Most Likely			
		Time from EIP(s)	Mass (kg)	AGL (km)	Velocity (m/s)	Time from EIP(s)	Mass (kg)	AGL (km)	Velocity (m/s)
Coasting	separation	-72 h	576.30	9.1E+05	64378.34	-72h	575.98	9.09e+ 05	64378.44
Entry	EIP-GNC_EIP	0	576.30	122.58	5786.33	0	575.98	122.64	5786.35
	Peak heat flux	78.80	570.94	45.45	5069.43	79.64	573.98	44.56	5089.89
Descent	PDD-Parachute deployment	199.26	563.63	11.15	463.70	196.66	569.28	11.17	492.52
	FSR-FS Jettison	239.26	460.57	7.42	87.60	237.66	460.66	7.50	85.53
Landing	BSR-Back shell release	327.66	300.25	1.08	65.00	282.66	299.93	4.14	70.73
	RRI-Retro rockets Ignition	328.66	300.25	1.01	68.31	283.46	299.93	4.09	73.39
	FF-Free fall (RCS off)	358.15	274.02	0.00134	0.13	286.56	296.56	3.88	62.56
	Touch down	358.96	274.02	0	3.16	321.12	296.56	0	151.34

The touch down point of the most likely trajectory is 7.1km from design target ($6.1^{\circ}\text{W}, 2.05^{\circ}\text{S}$) distance from reconstructed lander impact point is about 1.1km. The entry was within design range, a bit sleeping than nominal: Most likely entry FPA is about -12.48° , PDD occurred at Mach at 2.08 with full inflation at Mach 2.05. Front shield jettison occurred 41s after PDD (40s design) at 7.5km altitude vs 7.42km design. Backside released upto 47s earlier at altitude 4.1km in 1.08km design. Retrorockets are activated 1s later and switched off very early, after only 3.1s (2.9s design), at an altitude of about 3.88km vs 1.34m of design. The EDM has slowed 11m/s. The surface platform started a free-fall for about 34.5s, impacting with the planet surface at a velocity of about 545km/h (151.3m/s vs 3.16m/s)[5].

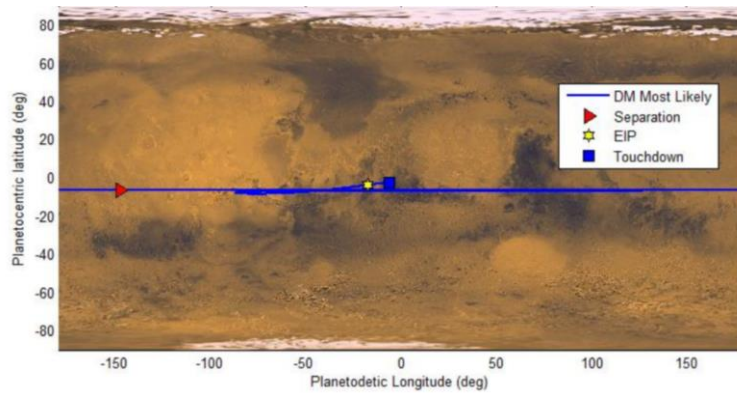


Fig 43. E2E Real Re-entry trajectory, ground track (from separation to touchdown) based on Planetocentric Latitude and Longitude [5]

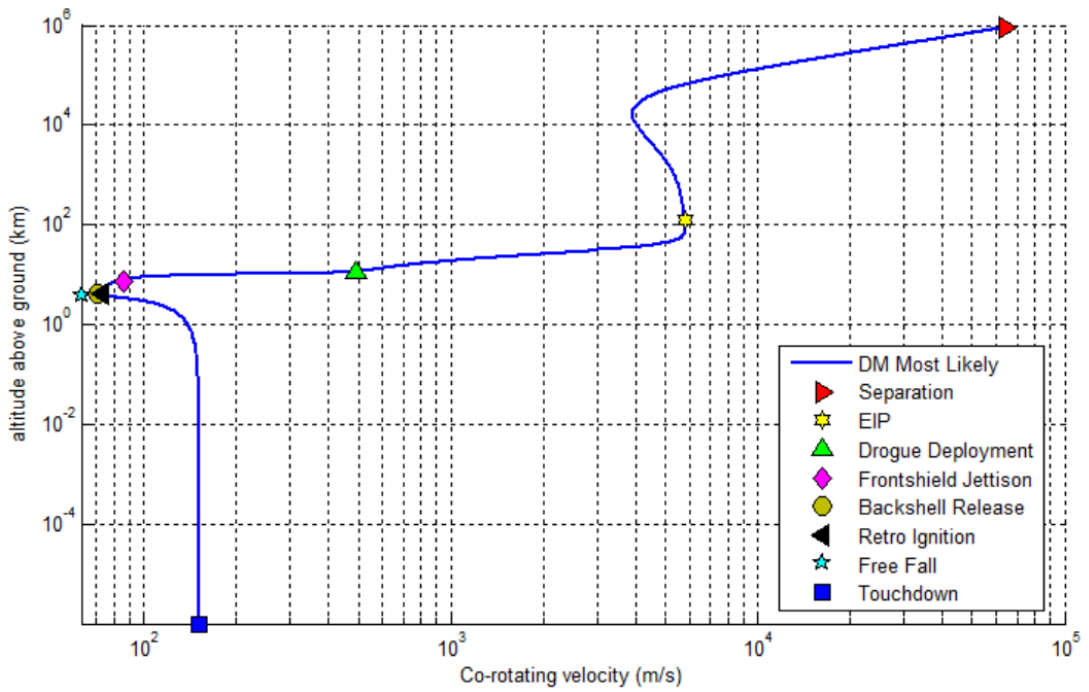


Fig 44. E2E Real Re-entry trajectory, ground track (from separation to touchdown) based on Altitude above ground level vs Co-rotating Velocity [5]

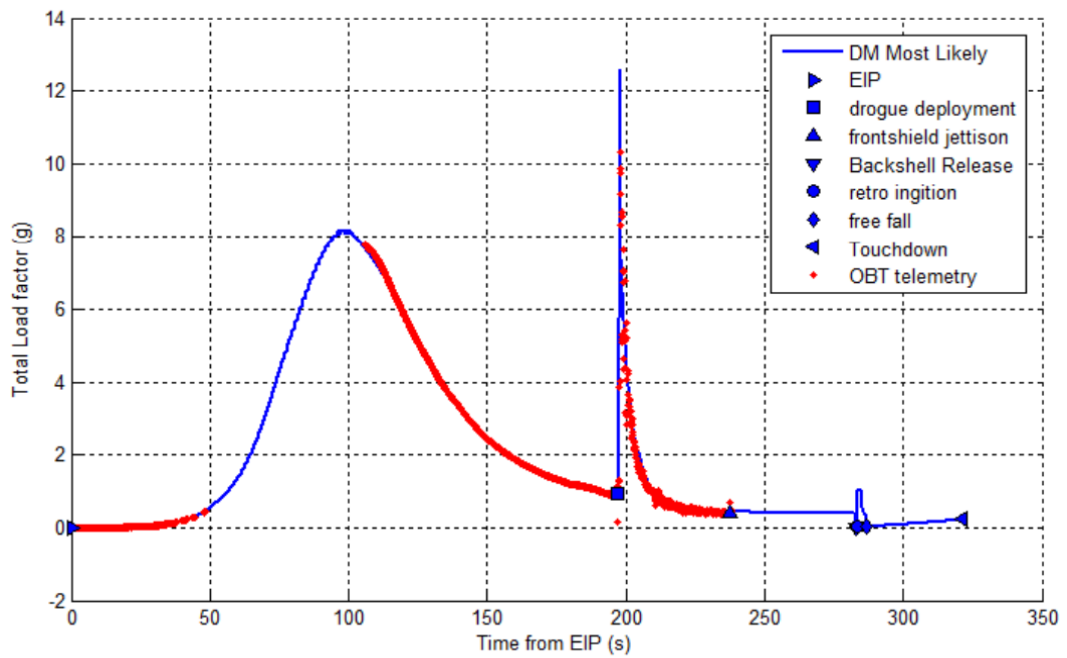


Fig 45. Most Real Re-entry trajectory, total Load factor as function of time (from EIP to touchdown) [5]

The inertial state vector at the different events is provided in MMED (Mars Mean Equator of Date) reference frame at the ground track from separation to touch down of a trajectory as shown in Fig 43. Fig 44 shows the graph of altitude lags the co-rotating velocity from same separation to touch down related to Table 12. The load factor from EIP to touch down, also reporting the estimated load factor from OBT as shown in Fig 45[5].

The most likely trajectory reproduces very well measured G-load. Also, the PDD event is perfectly aligned in time.

Fig 46 -Fig 51 shows the main EDL parameters like total heat flux, total heat load, total heat flux, dynamic pressure altitude above ground, Flight path angle, mass, plotted from EIP to touch down. Fig 52 shows the touch down point of real re -entry trajectory with respect to the predicted footprint. The most likely represented with a red star while lander impact yellow star which shows real re-entry trajectory path-line [5].

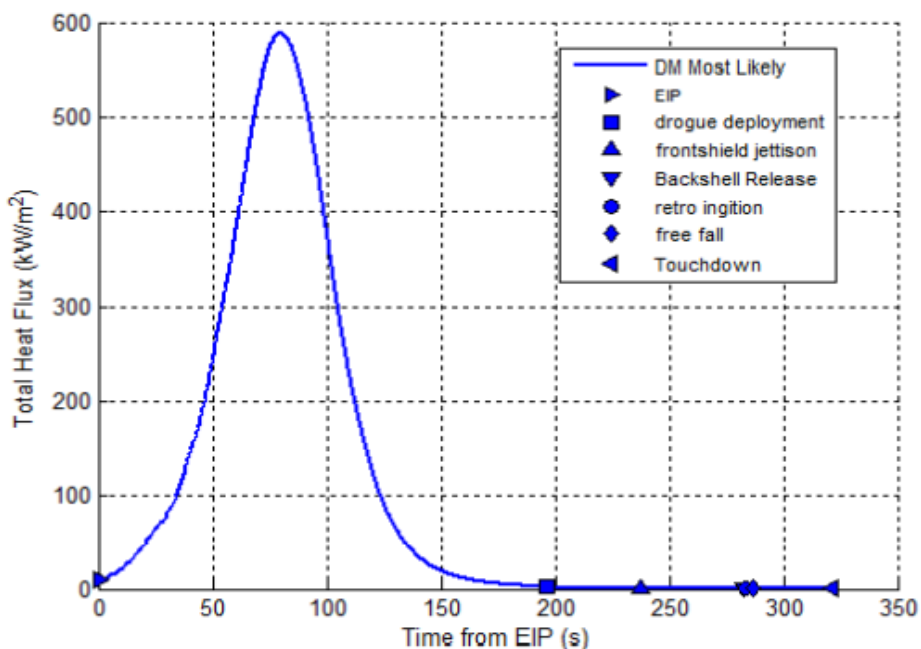


Fig 46. Real Re-entry trajectory, total Heat flux at stagnation as function of time (from EIP to touchdown) [5]

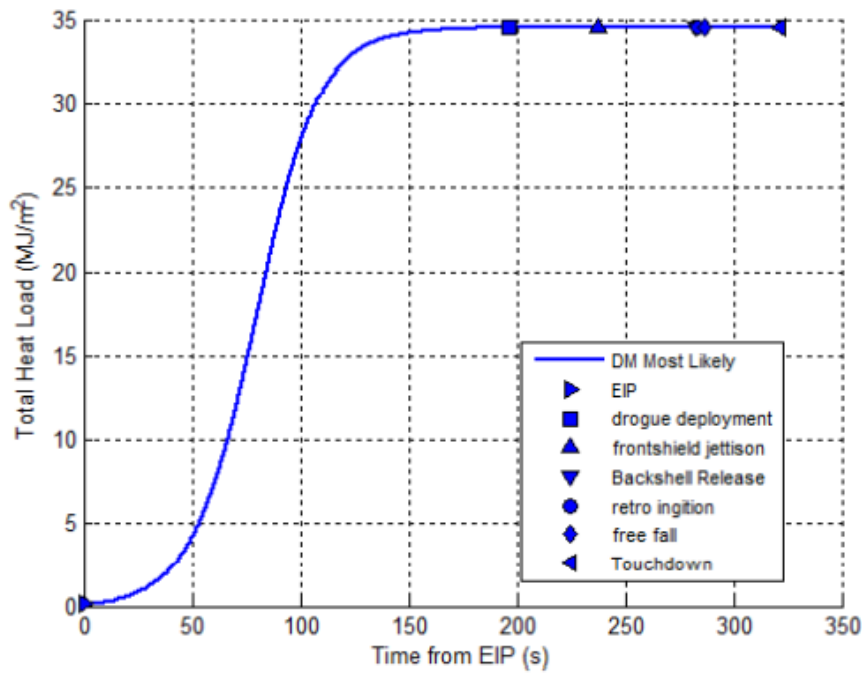


Fig 47. Real Re-entry trajectory, total Heat load as function of time (from EIP to touchdown)

[5]

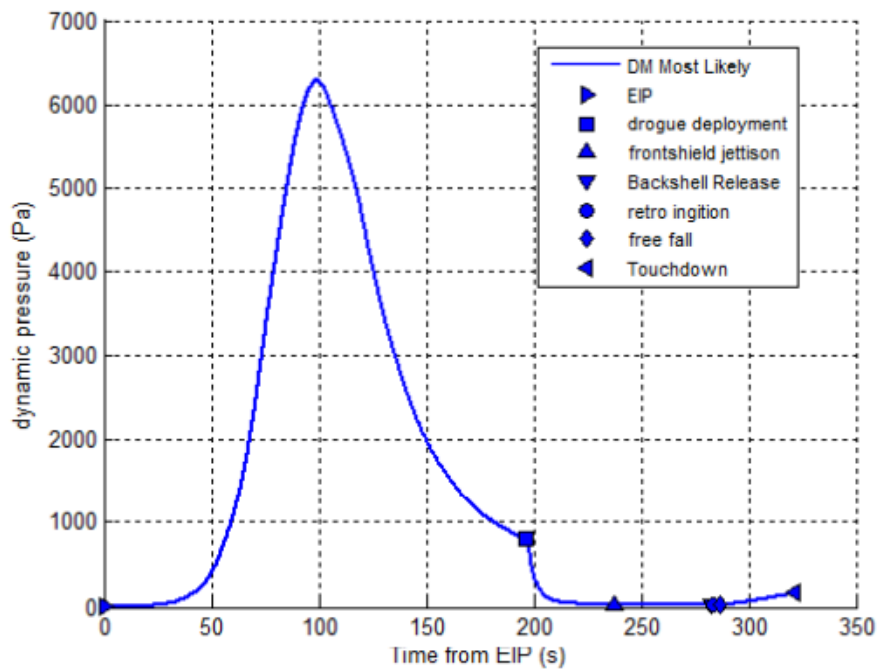
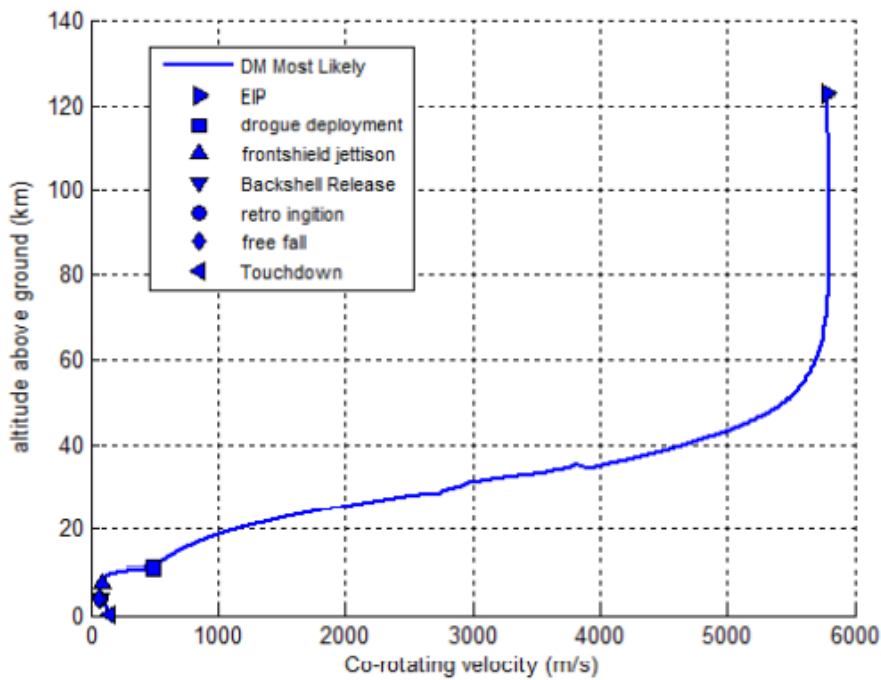


Fig 48. Real Re-entry trajectory, dynamic pressure as function of time (from EIP to touchdown) [5]



*Fig 49. Real Re-entry trajectory, altitude above ground as function of co-rotating velocity
(from EIP to touchdown) [5]*

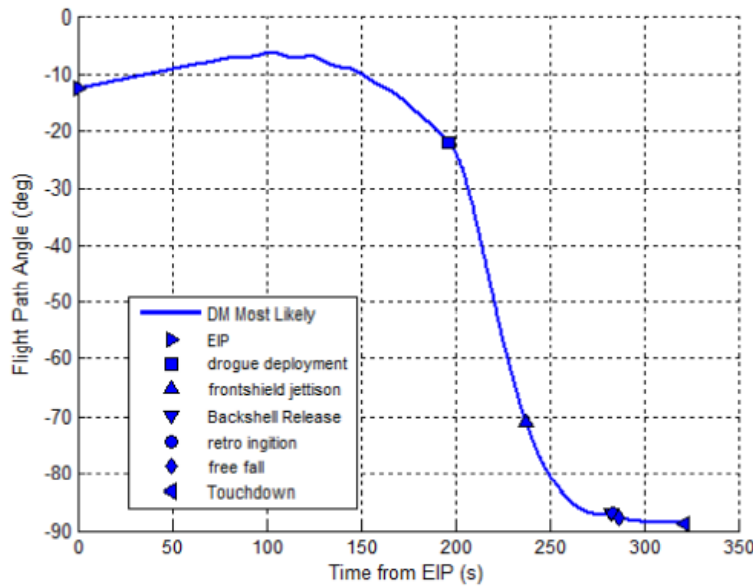


Fig 50. Real Re-entry trajectory, co-rotating flight path angle as function of time (from EIP to touchdown) [5]

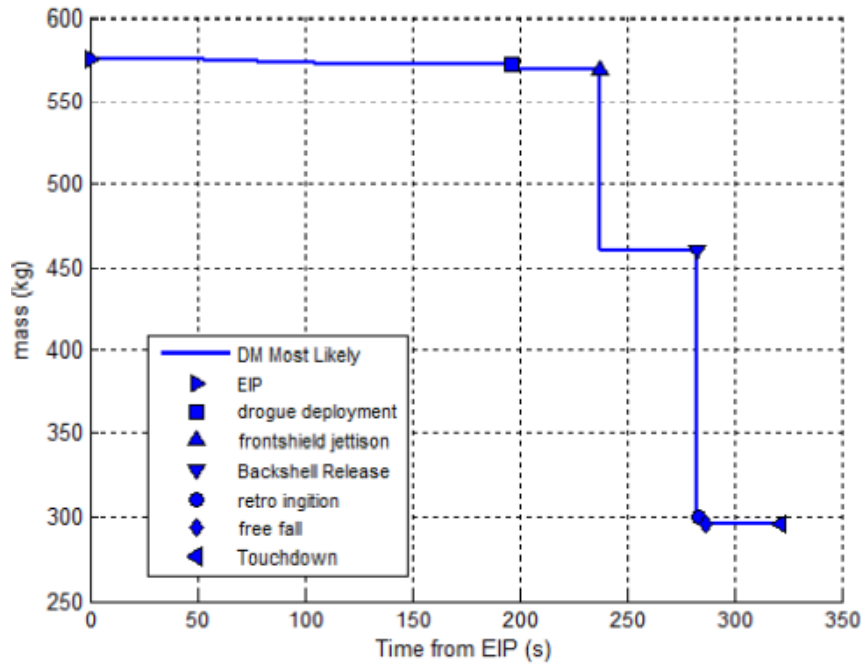


Fig 51. Real Re-entry trajectory, EDM mass as function of time (from EIP to touchdown) [5]

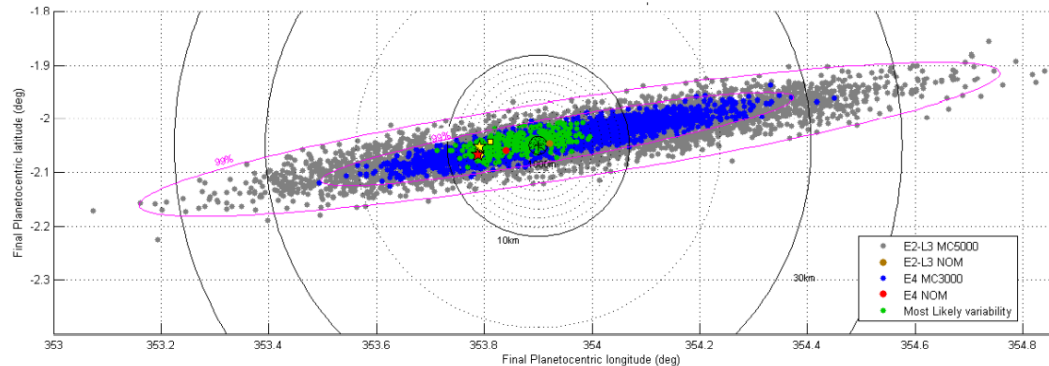


Fig 52. Real Re-entry trajectory, identification of the most likely touchdown position [5]

4.2 Reconstruction of the real attitude motion

The real-altitude motion is reconstructed in two methods in coasting phases.

- Separation Event: MSA (Main Separation Assembly) Performance
- Separation Event: Coasting Phase Initial Conditions

SEP(Separation) Analysis is fundamental to assess the mission performance during the complete EDL (Entry, Descent and Landing) the SEP occurs three days before EIP: the altitude at separation determined the Delta-V Vector applied by the MSA mechanism on the EDM that propagated during 3 days of casting, highly affects the target of the FPA and Capsule altitude at the EIP with the following assumptions.

- Separation occurred at more than 90000km of altitude and at the distance disturbances on the altitude motion due to atmosphere and gravitational field are negligible.
- Rigid body dynamics are assumed in the minutes following separation, but any fuel sloshing or other non-rigid body are neglected.
- SEP is an instantaneous event.

Based on above assumptions, the observed EDM altitude motion after SEP can be modelled as a Poinsot motion which depends only on the initial conditions and the inertial properties of the body. The angular accelerations can be obtained using Euler's Equations of Rigid boy dynamics forcing a null External Torque are [5]:

$$\dot{\omega}_x = (I_{xx}(\dot{\omega}_y - \omega_x \omega_z) + I_{xz}(\dot{\omega}_z + \omega_x \omega_y) - (I_{zz} - I_{yy})\omega_y \omega_z + \frac{I_{yz}(\omega_y^2 - \omega_z^2)}{I_{xx}}) \quad (13)$$

$$\dot{\omega}_y = (I_{yz}(\dot{\omega}_z - \omega_y \omega_x) + I_{xy}(\dot{\omega}_x + \omega_y \omega_z) - (I_{xx} - I_{zz})\omega_z \omega_x + \frac{I_{xz}(\omega_z^2 - \omega_x^2)}{I_{yy}}) \quad (14)$$

$$\dot{\omega}_z = (I_{xz}(\dot{\omega}_x - \omega_z \omega_y) + I_{yz}(\dot{\omega}_y + \omega_z \omega_x) - (I_{yy} - I_{xx})\omega_x \omega_y + \frac{I_{xy}(\omega_x^2 - \omega_y^2)}{I_{zz}}) \quad (15)$$

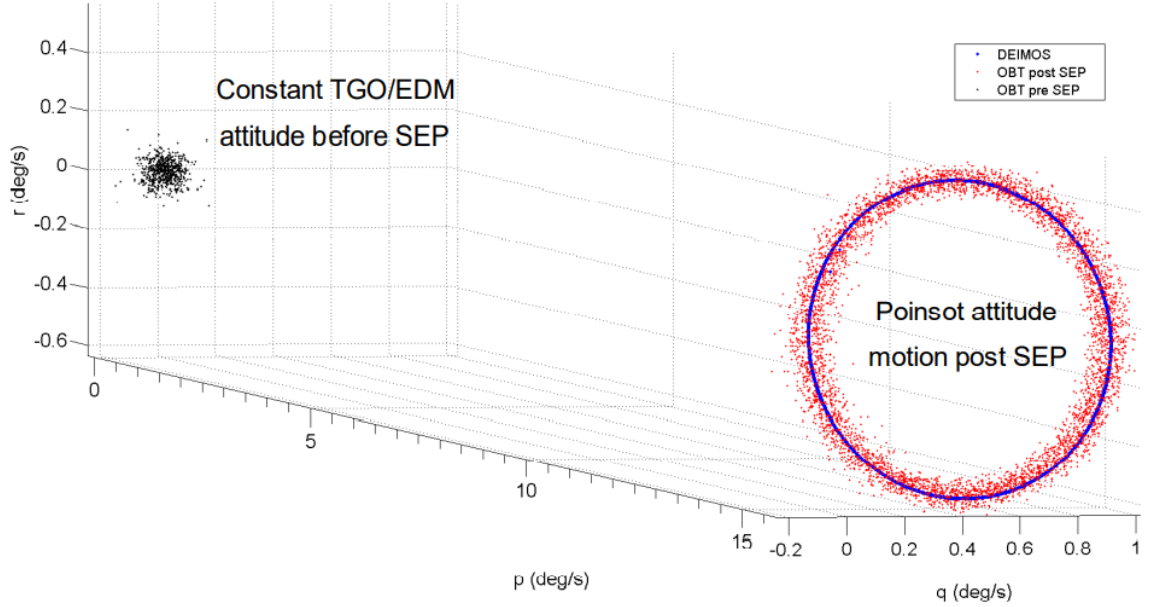


Fig 53. Post-SEP attitude reconstruction, reconstructed Poinsot motion vs measured attitude rates [5]

Through time integration of angular acceleration, the history of angular rates and inertial yaw pitch and roll angles can be obtained by multiple solutions. The p,q,r rates form OBT before (black points, two pointing mode) and after (red points, Poinsot motion) the separation event is shown in Fig 53. The reconstructed Real altitude motion based on EDM inertia properties are shown in Table 12.

It is noticed that a gap of about 170s is present in OBT around SEP on the top of the gap. The results of simulated precession motion is obtained with inertia properties is shown as blue line in Table 12 which perfectly matches with OBT data [5].

Table 12: Re-constructed EDM inertia [5]

Element	Reconstructed value	Reference value for design		Difference wrt REF
		REF	3 σ Range	
$I_{xx}(\text{kgm}^2)$	259.9	263.4	2.7	-3.5
$I_{yy}(\text{kgm}^2)$	168.20	157.2	10	+11
$I_{zz}(\text{kgm}^2)$	179.8	168.8	10	+11
$I_{xy}(\text{kgm}^2)$	-2.35	1.9	10	-4.25
$I_{xz}(\text{kgm}^2)$	0.03	1.7	10	-1.67
$I_{yz}(\text{kgm}^2)$	6.00	3.1	10	+9.1

The main inertia terms (I_{xx}, I_{yy}, I_{zz}), the reconstructed values exceed the range assumed for designed validation. Different inertia solutions could be found that reproduced the poinsot motion observed.

The reconstructed MSA performance in terms of real attitude rate at post-SEP is shown in Table 13.

The altitude rate profiles pre- and post-SEP are estimated from OBT and simulated by DEIMOS with the reconstructed inertia properties and altitude rates of post-SEP as shown in Fig 54.

Table 13: MSA performance: reconstructed Real EDM attitude rate in at post-SEP [5]

Element	Reconstructed value	Reference value for design		Difference w.r.t REF
		REF	3 σ Range	
Roll Rate (deg/s)	15.7148	16.2	0.852	-0.4852
Pitch Rate (deg/s)	-0.1011	0	1.283	-0.1011
Yaw Rate (deg/s)	-0.1651	0	1.283	-0.1651

Table 14: MSA performance: reconstructed EDM delta V at post-SEP

Element	Reconstructed value	Reference value for design		Difference w.r.t REF
		REF	3 σ Range	
EDM delta V, X axis (mm/s)	335.1	320	8.4	+15.1
EDM delta V, Y axis (mm/s)	4.1	0	8.1	+4.1
EDM delta V, Z axis (mm/s)	-0.7	0	8.1	-0.7

Table 15: TGO pointing performance: reconstructed EDM attitude at post-SEP

Element	Reconstructed value	Reference value for design	Difference wr.t REF
Right ascension (deg)	260.1657	260.1240	-0.0417
Declination (deg)	-12.9294	-12.9457	0.0237
Roll (deg)	141.4	N/A	N/A

The Reconstructed MSA performance in terms of EDM Delta-V shown in Table 14 which was performed by TAS-I and understood to be a based on lower frequency telemetry data from the EDM and considered as an input for DEIMOS computations.

The input shows the Axial Delta-V generated by the MSA Mechanism onto the EDM is out of 3 σ range assumed with design closed to 6 σ value performance in terms of FPA at EIP is attached and steeper entry is expected.

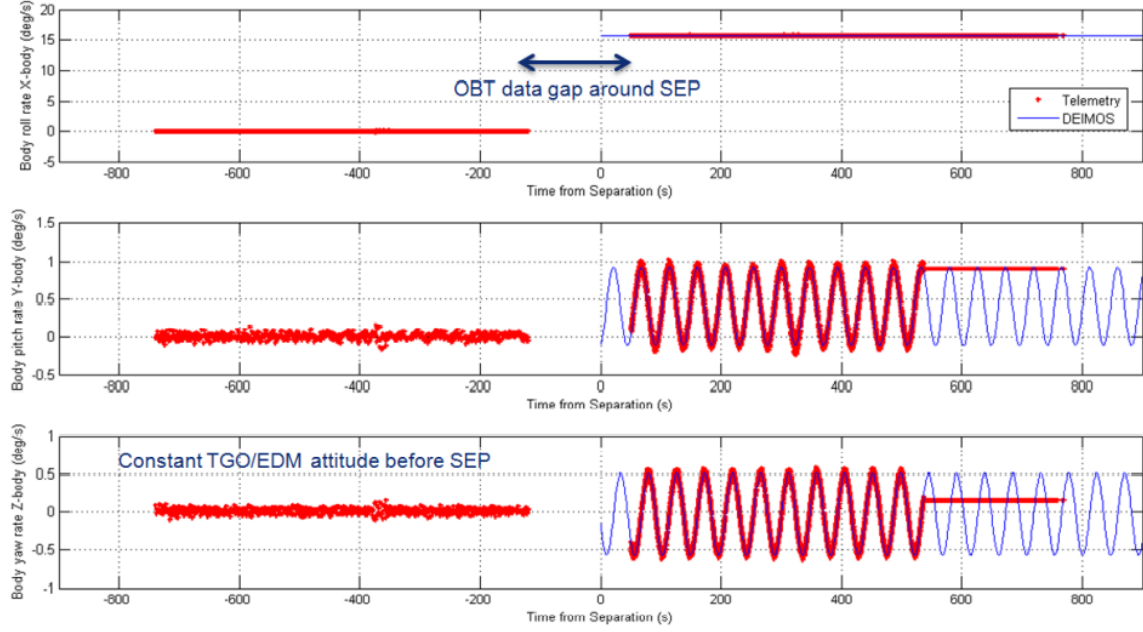


Fig 54. Post-SEP attitude reconstruction, reconstructed vs measured attitude rates profiles [5]

Finally, the reports of reconstructed altitude angles at post SEP are shown in Table 15. The declination and right ascension of the EDM x-axis in EME2000 have been reconstructed by DEIMOS form the OBT altitude inertial angle. The comparison with commanded altitude inertial angle. The comparison with commanded altitude shows that pointing of the TGO at the moments of separation was really accurate. The DEIMOS has simulated the altitude rate profiles pre and post-SEP which are estimated from OBT is shown in Fig 55(a) - Fig 55(c).

There is an OBT data gap around SP from -100s to 50s in Time of Separation and Yaw angle -147° at inertial at body with the red curve indicates from -700 to 100s and 50s to 700s at telemetry curve and at DEIMOS curve at OBT data gap around SEP and at -146° to 147.5° body yaw angle as shown in 55(a).

In Fig 55(b), At constant TGO/EDM altitude before SEP the same lags behind the body pitch angle from 8° to -10.5° at telementary curve and also in DEIMOS curve.

At Fig 55(c) same as previous two curves from -750s to 50s at 130° body roll angle with EIP Time 50s to 700s at -150° to -50° body roll angle and it increases the peak level of 150° at telemetry line [5].

It starts from 0 to 800s EIP by increasing and decreasing the angle from 120° to -120° .

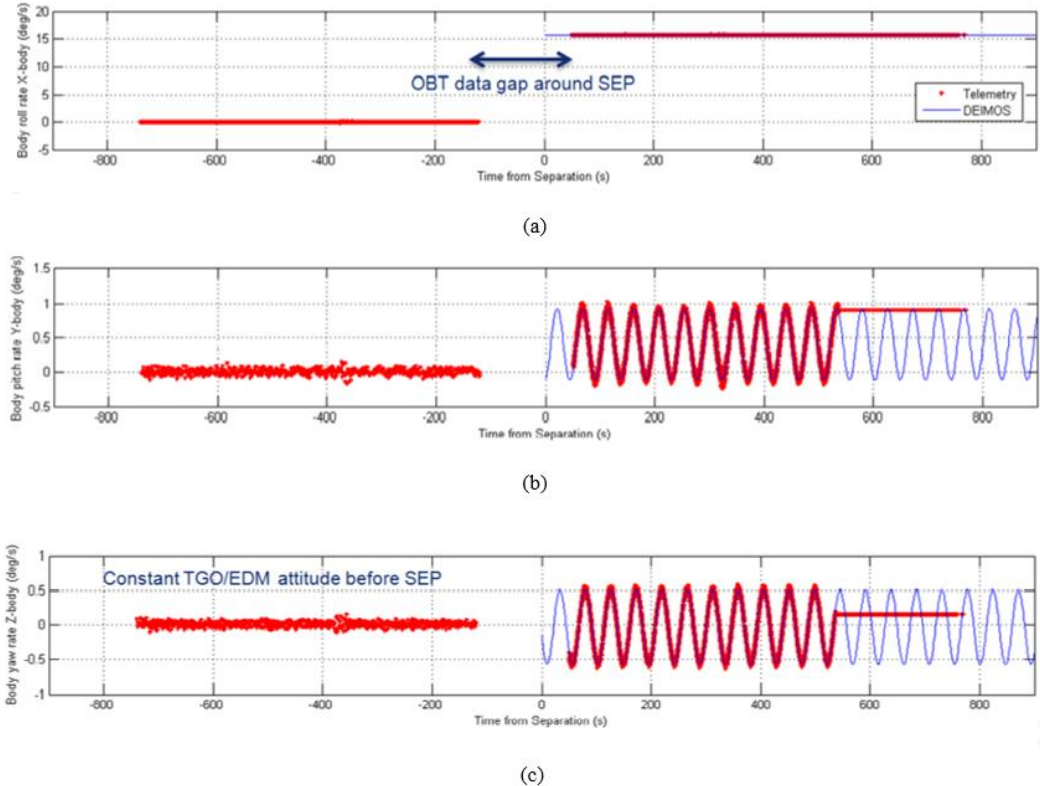


Fig 55. Post-SEP attitude reconstruction, reconstructed vs measured attitude angles profiles [5]

From the analysis of the MSA performance and the reconstruction of the altitude at separation in coasting phase initial conditions, it is possible to derive the completer state vector to be assumed as reference Pre-SEP initial conditions for EDL post flight analysis Table 15 shows the report of state vector at Pre-SEP, as obtained by the latest orbit determined. Table 16 shows the delta received by EDM reconstructed in Table 12.

Table 16: State Vector at EDM pre-Separation

Variable	Reconstructed Value
Time (UTC)	2016-10-16T14:42:00.000
Px (EME2000 Mars Centered) (km)	472260.9351
Py (EME2000 Mars Centered) (km)	781212.5874
Pz (EME2000 Mars Centered) (km)	6896.3995
Vx (EME2000 Mars Centered) (km/s)	-1.811014487
Vy (EME2000 Mars Centered) (km/s)	-2.957809338
Vz (EME2000 Mars Centered) (km/s)	-0.014266967
Right Ascension (EME2000) (deg)	260.16568757
Declination (EME2000) (deg)	-12.92935141
Delta-V Module (m/s)	0.335125812

Based on the above initial conditions 3 days coasting phase has been propagated in 6 DOF as a part of the E2E nominal flight Prediction which is based on real altitude motion. No Oscillation in the pitch and yaw is observed from analysis of the altitude rate which concerns only the coasting phase. The Poinsot motion is reconstructed right after the SEP is damped by the RCS fuel sloshing acting during three days of wasting [5].

This leads to small difference that are observed due to assumption of the body dynamics in the 6 DOF Simulations performed as shown in Fig 56 which is based on the real altitude comparison with EIP timings with body roll rate X-body (deg), Body pitch rate Y-body (deg) and Body Yaw rate Z-body (deg).

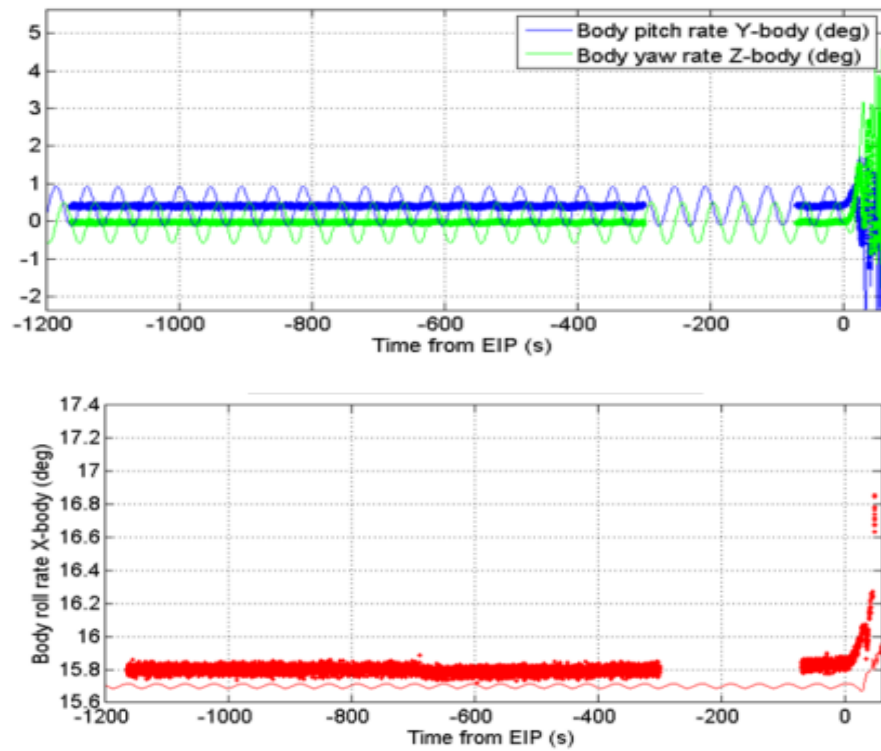


Fig 56. Real Altitude rate comparision (dots: OBT, lines:simulation) [5]

CHAPTER 5

NUMERICAL SETUP FOR RE-ENTRY SIMULATIONS

This chapter gives a short description of the theory behind Computational Fluid Dynamics (CFD) and combustion modelling. The governing equations are described as well as the numerical methods of solving them.

In every numerically solved problem, the selection and modelling of governing equations play an important role because of the internal flow physics are greatly affected by the flow governing equations.

The foundations of fluid mechanics have been known for more than a century. The equations, originating in Newton's equations of motion, are named Navier-Stokes equations. These equations are non-linear and also cannot be solved analytically, with the exception of a small number of elementary cases.

Theoretical models for a given fluid-mechanical problem thus generally consist of a system of partial differential equations, which cannot be solved analytically, therefore resulting in the need for numerical methods. Numerical methods imply that the space and time are discretized in many computational cells and short timesteps, over which the solution of the equations are then iterated. In most practical applications the flows are mainly turbulent, i.e., almost random in the sense that the velocity of a flow cannot be predicted for a certain point at a certain time. The turbulent nature of a flow is basically ruled by a dimensionless number, the Reynolds number. At high Reynolds numbers there is a large gap between the large scales, where energy is supplied, and the so-called Kolmogorov scale, where energy dissipation occurs [14].

In addition, the solution must be iterated over time since the solution varies, not only from one point to another, but also with time. The available computing capacity therefore limits how many computational cells and time steps can be used to simulate a certain problem. With the computer capacity accessible today only flows at low Reynolds numbers and in simple geometries can be directly simulated. If flow at high Reynolds numbers and in complex geometries is of interest, which it usually is in most engineering and scientific applications, some form of model simplification must be introduced. The most common way of accomplishing this so far is by utilizing what is known as Reynolds-averaged Navier-Stokes models (RANS) [15]. These are based on a statistical treatment of the fluctuations of a stationary or very slowly varying flow.

Turbulence models like those described above thus provide a way of making very complex equation systems manageable. Another method of technological interest is Large Eddy Simulation (LES). In LES the large energy containing eddies are simulated and only the small-scale turbulence is modelled. This method has on several occasions proved more accurate in resolving different observed phenomena. The computational cost of LES is still very high, largely owing to its requirement of a very fine computational mesh. Although expensive, the method is fast becoming feasible with massive computer clusters [15].

5.1 The flow around capsules during the re-entry phase

5.1.1 Governing Equation

Mathematical modelling of turbulent reacting flow is a central conception since it is coupled by fluid dynamics and chemical kinetics. This section outlines the equations governing the flow, on tensor form, as they appear when they have been complemented with models for thermodynamics and chemical reactions. The unit vectors in x-, y- and z-directions are denoted \mathbf{i} , \mathbf{j} and \mathbf{k} [14]. The position vector \mathbf{r} is written as

$$\mathbf{r} = x\mathbf{i} + y\mathbf{j} + z\mathbf{k} \quad (16)$$

and the operator ∇ is defined as

$$\nabla \equiv \mathbf{i} \frac{\partial}{\partial x} + \mathbf{j} \frac{\partial}{\partial y} + \mathbf{k} \frac{\partial}{\partial z} \quad (17)$$

When operating on a scalar function of position φ , it generates the gradient of φ .

$$\nabla = \mathbf{i} \frac{\partial \varphi}{\partial x} + \mathbf{j} \frac{\partial \varphi}{\partial y} + \mathbf{k} \frac{\partial \varphi}{\partial z} \quad (18)$$

whereas the divergence of a vector field v is defined as the scalar,

$$\nabla \cdot v \equiv \frac{\partial v_1}{\partial x} + \frac{\partial v_2}{\partial y} + \frac{\partial v_3}{\partial z} \quad (19)$$

The velocity vector \mathbf{u} is given by

$$\mathbf{u} = u(x, y, z, t) \mathbf{i} + v(x, y, z, t) \mathbf{j} + w(x, y, z, t) \mathbf{k} \quad (20)$$

where u , v and w are the velocity components in directions of x , y , z and t is time.

The mathematical models implemented in this study include the well-known Navier-Stokes equations for mass, momentum, and energy conservation, supplemented by models for thermodynamic and chemical processes [14,16].

Three differential equations describe a Newtonian compressible media. The continuity equation for the species m is

$$\frac{\partial \rho_m}{\partial t} + \nabla \cdot (\rho \mathbf{u}) = \nabla \cdot \left[\rho D \nabla \left(\frac{\rho_m}{\rho} \right) \right] + \frac{\dot{\rho}_m}{\rho} \quad (21)$$

Where,

ρ_m is the density of species m ,

ρ is the total density,

\mathbf{u} is the flow velocity vector and

D is the diffusion coefficient (Fick's law-based) [16].

Summing (21) across all species involved in the process yields the global continuity equation describing mass conservation. The rate of mass flow into a control volume per unit time equals the rate of mass growth contained inside the volume per unit time, according to this equation.

$$\frac{\partial \rho}{\partial t} + \nabla \cdot (\rho \mathbf{u}) = 0 \quad (22)$$

The momentum equation, describing the conservation of momentum in three dimensions, for the mixed flow is

$$\frac{\partial \rho \mathbf{u}}{\partial t} + \nabla \cdot (\rho \mathbf{u} \cdot \mathbf{u}) = -\frac{1}{a^2} \nabla p - A_o \nabla \left(\frac{2}{3} \rho k \right) + \nabla \cdot \boldsymbol{\sigma} + \varphi \mathbf{f} \quad (23)$$

where

p is the pressure,

k is the turbulent kinetic energy,

A_o is a constant related to the turbulence model and

\mathbf{f} is the total external force exerted on the volume.

The viscous stress tensor $\boldsymbol{\sigma}$ is defined by

$$\boldsymbol{\sigma} = \mu (\nabla \mathbf{u} + (\nabla \mathbf{u})^T + \lambda \nabla \cdot \mathbf{u} I) \quad (24)$$

where μ and λ are the viscosities of the gas mixture and I is the identity matrix. [15]

The last partial differential equation that governs the flow is the energy equation (25). This equation is derived from the first law of thermodynamics. It states that the increase in energy per unit time in a fluid element equals the net rate of heat added per unit time and the net rate of work exerted on the fluid element per unit time.[15]:

$$\frac{\partial(\rho i)}{\partial t} + \nabla \cdot (\rho \mathbf{u} i) = -p \nabla \cdot \mathbf{u} + (1 - A_o) \boldsymbol{\sigma} \otimes (\nabla \mathbf{u}) - \nabla \cdot \mathbf{J} + A_o \rho \varepsilon + \dot{Q}_c \quad (25)$$

where i is the internal energy, not including chemical energy and ε the turbulent energy dissipation per unit time. The heat flux vector \mathbf{J} is the sum of the contributions from heat conduction and enthalpy diffusion and \dot{Q}_c is a chemical source term.

5.1.2 Finite Volume Method

The Navier-Stokes equations can, as already concluded, only be solved analytically for the simplest of flows. To obtain solutions for real flows a numerical approach must be adopted, where the equations are replaced by algebraic approximations that can be solved with a numerical method.

First, the flow domain is divided into several small volumes, so called control volumes or computational cells. After having divided the domain into a grid of computational cells, the governing equations are integrated over each finite volume [14].

Following [16], all governing equations can be said to be of the same form as the following general transport equation.

$$\frac{\partial \rho\phi}{\partial t} + \nabla \cdot (\rho\phi u) = \nabla \cdot [D(\nabla\phi)] + S_\phi \quad (26)$$

where,

ρ is the density of fluid,

\mathbf{u} is the velocity of the Vehicle,

$\nabla\phi$ is a fluid characteristic,

D denotes the diffusion coefficient, and

S_ϕ denotes a source or sink of ϕ

When this equation is applied to a three-dimensional control volume (CV), The generic transport equation transforms into

$$\int_{cv} \frac{\partial \rho\phi}{\partial t} dv + \int_{cv} (\rho\phi u) dv = \int_{cv} \nabla \cdot [D(\nabla\phi)] dv + \int_{cv} S_\phi dv \quad (27)$$

By relating a volume integral to a surface integral, Gauss's divergence theorem then gives

$$\int_A n \cdot (\rho\phi u) dA = \int_A n \cdot [D(\nabla\phi)] + \int_{cv} S_\phi dv \quad (28)$$

where n is the outward unit normal vector. This applies to steady state flow, for transient flow the transient term must be included, i.e.

$$\frac{\partial}{\partial t} \left(\int_{cv} \rho\phi dv \right) + \int_A n \cdot (\rho\phi u) dA = \int_A n \cdot [D(\nabla\phi)] dA + \int_{cv} S_\phi dv \quad (29)$$

This equation is also integrated over time and the general transport equation becomes [17]

$$\int_{\Delta t} \frac{\partial}{\partial t} \left(\int_{cv} \rho\phi dv \right) dt + \iint_{\Delta A} n \cdot (\rho\phi u) dAdt = \iint_{\Delta A} n \cdot [D(\nabla\phi)] dAdt + \int_{cv} S_\phi dv dt \quad (30)$$

This conservation equation applies to each control volume in the computational domain. Thus, by summing the equations for all control volumes global conservation automatically apply. Since the integrand is not known over the entire control volume surface, the integrals need to be approximated. This is often done in a two-level approximation, where the integral is first approximated in terms of the variable value at one or more locations on the cell face over which the integral is evaluated. The cell face value is in turn assumed to be the same as the value in the computational node, which is defined as the center of the control volume. Depending on which differencing scheme is being used, this is done in various ways. In the upwind differencing scheme, for example, the value of the fluid property variable is approximated as the nodal value of the upstream control volume. This scheme is accurate to the first order and will always be stable. A drawback is that it suffers from numerical diffusion, which tends to smear out sharp gradients.

5.1.3 Turbulence modelling

Turbulence modelling is the key part in numerical modelling problems for the analysis of dissipation and development of internal thermal energy in a flow stream.

The accuracy of all the physical flow parameters is dependent on the accuracy of turbulence modelling. Turbulence consists of fluctuations in the flow field in space and time. It is a very complex and poorly understood process, mainly because it is three-dimensional, unsteady and occurs on many scales. Turbulence occurs when the inertial force in a fluid becomes considerable relative to the viscous forces and is characterized by a high Reynolds number [18].

As already discussed in the beginning of this chapter, a direct simulation of the turbulent flow in a scramjet engine would require a far more detailed computational grid than manageable with present computing power. A way of modelling the turbulent effects of the flow is needed. The most common turbulence modelling approach and the one used in this thesis is the Reynolds-averaged Navier-Stokes models. As stated before, RANS is based on a statistical treatment of the flow. More precise, this means that some of the variables that govern the flow are divided into a time-averaged component of the flow and a fluctuating component that represents the deviation from the mean flow. The governing RANS equations are obtained as the mean of equations (22)-(29). The resulting equations are on the same form but with a few extra terms describing the fluctuations 'influence on the mean flow [15].

A very successful and widely employed turbulence model is the so-called k- ε model. It is a two-equation model meaning that it includes two extra transport equations to represent the turbulent properties of the flow. This allows the model to account for certain historic effects, such as convection and diffusion of turbulent energy. The transported variables are the turbulent kinetic energy (k) and its dissipation per unit time (ε) [16].

The equations for k and ε are

$$\frac{\partial(\rho k)}{\partial t} + \nabla \cdot (\rho u k) = -\frac{2}{3} \rho k \tau \nabla \cdot u + \sigma \otimes \nabla u + \nabla \cdot \left[\left(\frac{\mu}{P_{r_k}} \right) \nabla k \right] - \rho \varepsilon \quad (31)$$

and

$$\frac{\partial(\rho\varepsilon)}{\partial t} + \nabla \cdot (\rho u \varepsilon) = -\left(\frac{2}{3}c_{\varepsilon_1} - c_{\varepsilon_3}\right)\rho\varepsilon\nabla \cdot u + \nabla \cdot \left[\left(\frac{\mu}{P_{r_\varepsilon}}\right)\nabla\varepsilon\right] + \frac{\varepsilon}{k}(c_{\varepsilon_1}\sigma \otimes \nabla u - c_{\varepsilon_3}\rho\varepsilon) \quad (32)$$

These are the standard $k-\varepsilon$ equations with some extra terms. The quantities $C_{\varepsilon_1}, C_{\varepsilon_2}, C_{\varepsilon_3}, P_{r_k}$ and P_{r_ε} are experimentally determined constants. An advantage with RANS is that it is fast and readily available in most commercial CFD tools. The predominant disadvantage is that all turbulent flows are unstable, and it is practically impossible to extract any detailed information about such a flow from its mean flow. However, since it has proven to be stable and numerically robust, the $k-\varepsilon$ model offers a good compromise between accuracy and robustness for simulation of supersonic flow. In the cold flow investigation, $k-\varepsilon$ model is considered.

However, for the reacting flow in this study, the widely used shear stress turbulence (SST) model has been considered for more accurate prediction of boundary layer separation and vortices development region. SST turbulence model has an important feature which combines the both $k-\varepsilon$ and $k-\omega$ turbulence model such that $k-\varepsilon$ model is used in free shear flow and switches to the $k-\omega$ model used in the inner region of the boundary layer. The turbulent kinetic energy k and the specific dissipation rate ω can be obtained by the following turbulence governing equations [19, 20].

$$\frac{\partial}{\partial t}(\rho k) + \frac{\partial}{\partial x_i}(\rho k u_i) = \frac{\partial}{\partial x_j}\left(\Gamma_k \frac{\partial k}{\partial x_j}\right) + \widetilde{G}_k - Y_k + S_k \quad (33)$$

and

$$\frac{\partial}{\partial t}(\rho\omega) + \frac{\partial}{\partial x_i}(\rho\omega u_i) = \frac{\partial}{\partial x_j}\left(\Gamma_\omega \frac{\partial \omega}{\partial x_j}\right) + \widetilde{G}_\omega - Y_\omega + D_\omega + S_\omega \quad (34)$$

Here G_k and G_ω reflect the growth of turbulent kinetic energy owing to mean velocity gradients and the formation of Γ_ω and Γ_k denotes the diffusivity of ω and k ,

respectively. Y_k and Y_ω represent the turbulence-induced dissipation of k and ω . The cross-diffusion term is represented by D_ω , which is expressed as follows,

$$D_\omega = 2(1 - F_t)\rho_{\omega,2} \frac{1}{\omega} \frac{\partial k}{\partial x_j} \cdot \frac{\partial \omega}{\partial x_j} \quad (35)$$

where F_t is the blending function and is defined as

$$F_t = \tanh(\arg_1^4) \quad (36)$$

where,

$$\arg_1^4 = \min \left[\max \left(\frac{\sqrt{k}}{C_\mu \omega'_y}, \frac{500\vartheta}{y^2 \omega} \right), \frac{4\rho \sigma_{\omega,2}}{CD_{k\omega} y^2} \right] \quad (37)$$

and where $CD_{k\omega}$ is the positive portion of the cross-diffusion term and y represents the normal distance to the wall.

Handling near-wall flow is a key difficulty in most CFD applications. Many CFD tools model such flows using a logarithmic law of the wall. The tangential velocity of the flow near the wall is related to the wall shear stress by a logarithmic relationship in the log-law region. Turbulent flows near a no-slip wall are not affected by the freestream flow speed; only the wall distance y , fluid density, viscosity, and wall shear stress are essential. The near-wall tangential velocity relationship is provided by

$$u^+ = \frac{u_t}{u_\tau} \frac{1}{k} \ln(y^+) + C \quad (38)$$

Where,

$$y^+ = \frac{\rho \Delta y u_\tau}{\mu} \quad (39)$$

and

$$u_\tau = \left(\frac{\tau_\theta}{\rho} \right)^{1/2} \quad (40)$$

Here u_+ is the near-wall velocity, u_τ is the friction velocity, U_t is the known velocity tangent to the wall at Δy from the wall, κ is the von Karman constant and C is a log-layer constant related to the wall roughness [17].

5.1.4 Chemical Kinetic Model

In order to address the real gas effects, the Martian atmosphere has been considered as a reacting gas mixture of nine species (Ar, CO₂, N₂, O₂, CO, NO, N, O) involved in 49 forward and backward chemical reactions [21-23]. Table 17 summarizes the reaction mechanism and related chemical kinetics taken into consideration in the current nonequilibrium CFD calculations, where M is the responding partner (third body) that can be any of the nine reacting species. The reaction mechanism and kinetics are obtained from the work of Park et al. in [18]. It is noted that this reaction scheme excludes ionic reactions since the degree of ionization is likely to be low in the environment of interest (e.g., entry below 9km/s) due to the existence of CO₂, N₂, and Ar in the Martian atmosphere, as stated by Park et al. in [21].

Table 17: Reaction's mechanism and rate parameters [24]

Reaction	Third body M	Ar (cm ³ mol ⁻¹ s ⁻¹)	β_r	T_d (K)
$CO_2 + M \rightarrow CO + O + M$	CO ₂ , CO, N ₂ , O ₂ , NO	6.9×10^{21}		
	Ar	6.9×10^{20}	-1.5	63275
	C, N, O	1.4×10^{22}		
$CO + M \rightarrow C + O + M$	CO ₂ , CO, N ₂ , O ₂ , NO	2.3×10^{20}		
	Ar	2.3×10^{19}	-1.0	129000
	C, N, O	3.4×10^{20}		
$N_2 + M \rightarrow N + N + M$	CO ₂ , CO, N ₂ , O ₂ , NO	7.0×10^{21}		
	Ar	7.0×10^{21}	-1.6	113200
	C, N, O	3.0×10^{22}		
$O_2 + M \rightarrow O + O + M$	CO ₂ , CO, N ₂ , O ₂ , NO	2.0×10^{21}		
	Ar	3.0×10^{21}	-1.5	59750
	C, N, O	3.0×10^{22}		
$NO + M \rightarrow N + O + M$	CO ₂ , C, N, O, NO	1.1×10^{17}		
	Ar	5.0×10^{15}	0.0	75500
	CO, N ₂ , O ₂	5.0×10^{15}		
$C_2 + M \rightarrow C + C + M$	All	2.0×10^{21}	-1.5	59750
$NCO + M \rightarrow CO + N + M$	All	6.3×10^{16}	-0.5	24000
$NO + O \rightarrow N + O_2$		8.4×10^{12}	0.0	19450
$N_2 + O \rightarrow NO + N$		6.4×10^{17}	-1.0	38370
$CO + O \rightarrow C + O_2$		3.9×10^{13}	-0.18	69200
$CO_2 + O \rightarrow CO + O_2$		2.1×10^{13}	0.00	27800

The mass rate of production of species i per unit volume is expressed as

$$\omega_i = M_i \sum_{i=1}^{nr} (\beta_{ri} - \alpha_{ri}) \left[k_{f,r} \prod_{i=1}^{ns} \left(\frac{\rho_i}{M_i} \right)^{\alpha_{ri}} - k_{b,r} \prod_{i=1}^{ns} \left(\frac{\rho_i}{M_i} \right)^{\beta_{ri}} \right] \quad (41)$$

where nr denotes the number of reactions, ns denotes the number of species, α_{ri} and β_{ri} denotes the stoichiometric coefficients for reactants and products in the r reaction, $k_{f,r}$, $k_{b,r}$ denote the forward and backward rate coefficients for the r reaction, and M_i denotes the molecular weight of species i .

The Arrhenius form gives the forward rate coefficient of chemical processes, while the equilibrium constants give the backward rate coefficient [17].

$$K_{b,r} = \frac{k_{f,r}}{k_{eq(T_d)}} \quad (42)$$

and

$$K_{b,r} = C_{f,r} T_d^{n_{f,r}} \exp\left(-\frac{E_{f,r}}{T_d}\right) \quad (43)$$

where $C_{f,r}$, $n_{f,r}$, $E_{f,r}$ are the reaction parameters, $T_d = T \cdot T_v$ stands for the control temperature of chemical reactions, and K_{eq} is the equilibrium constant [17].

5.2 Validation of the numerical algorithm by literature results

In this section, the validation of numerical algorithm has been performed by comparing these results with those available in the literature.

5.2.1. Aerodynamic Analysis for manned space vehicles for mission to mars

The Aerodynamic analysis of Apollo shaped MSV, performed for flight conditions compatible for manned mission entering mars, has been done using ANSYS Fluent 19.0. Comparison with the Antonio Viviani's results has been done using ICEM-CFD toolbox in Ansys 10.1. The capsule travels in trajectory path which is from surrounded by Chemical components in Martians Atmosphere like Carbon dioxide 95.7%, Argon 1.6% and Nitrogen 2.7% along with remaining gases like CO, HCO, C, N, O. The design of MSV Capsule is done using ANSYS Fluent is shown in Fig 57.

5.2.1.1 Design and Meshing of the MSV Capsule

The primary design consideration of entry capsule requires large spherical nose radius of their fore body that gives high aerodynamic drag and a short body length for reducing the total structural weight and the ballistic coefficient. The MSV configuration, under investigation in this work, is shown in Fig 57. It consists of a blunt body close to an Apollo-shaped capsule measuring about 5 m in diameter, with a nose radius of 6.05 m, a sidewall angle of 33°, and an overall height of 3.8 m [24].

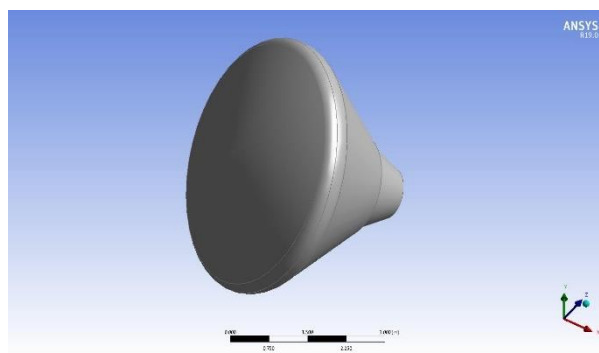


Fig 57. MSV Capsule

The meshing of this capsule is done in ANSYS Fluent with 1.12 million nodes as shown in Fig 58. This simulation undergoes based on Navier-Stokes equation and Range-Kutta method. A laminar model along with species transport using Chemkin file has been implemented as shown in Table 17. The angle of attack of MSV ranges from 0 to 28 and Mach number ranges from 5 to 20 is shown in Fig 18 [24].

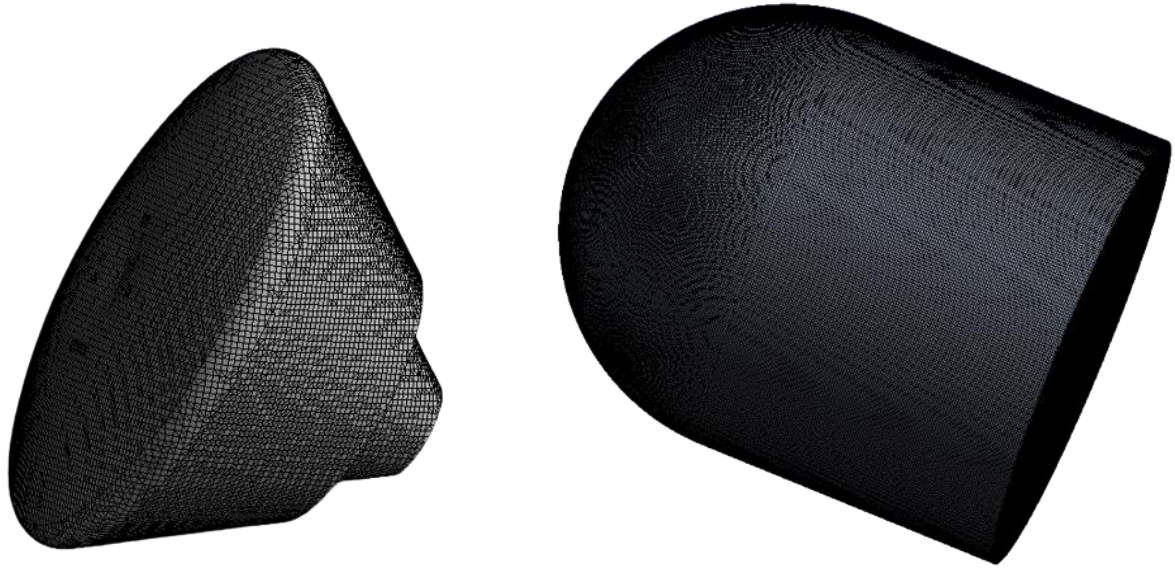


Fig 58. Meshing of (a) MSV Capsule and (b) its 80m domain

5.2.1.2 Boundary conditions

Fully three-dimensional CFD simulations both for perfect and chemically reacting gas have been computed. Free-stream conditions are shown in Table 18 which have been taken from [24]. Different angles of attack α have been investigated and compared. For the perfect gas case, the Mars atmosphere is characterized by a specific heat ratio γ (e.g., $\gamma = 1.3755$) very close to that of Earth (e.g., $\gamma = 1.4$). Therefore, it follows that force coefficients are nearly independent of CO₂ concentration and are essentially the same as those obtained using air [24]. The computational model has been investigated using the following conditions as indicated in Table 19.

Table 18: Free stream conditions [24]

Mach Number	Pressure(pa)	Temperature(k)	Angle of attack
5	1400	560	5°
10	1400	560	10°
20	1400	560	20°
20	1400	560	28°

Table 19: Boundary conditions for Simulation of MSV Capsule in Fluent

Zone	Type	Parameters
Inlet	Pressure far field	Mach number(M)=10,20 Temperature(T)=560K Pressure(P)=1400Pa
Pressure far field	Wall	-

MBS's aerodynamic analysis is presented in terms of lift (C_L), drag (C_D), and pitching moment (C_{M_y}) coefficients, which are derived using the following formulas [24]:

$$C_i = \frac{F_i}{(1/2)\rho_\infty v_\infty^2 S_{ref}}, i = L, D \quad (44)$$

$$C_{M_j} = \frac{M_j}{(1/2)\rho_\infty v_\infty^2 L_{ref} S_{ref}}, j = Y \quad (45)$$

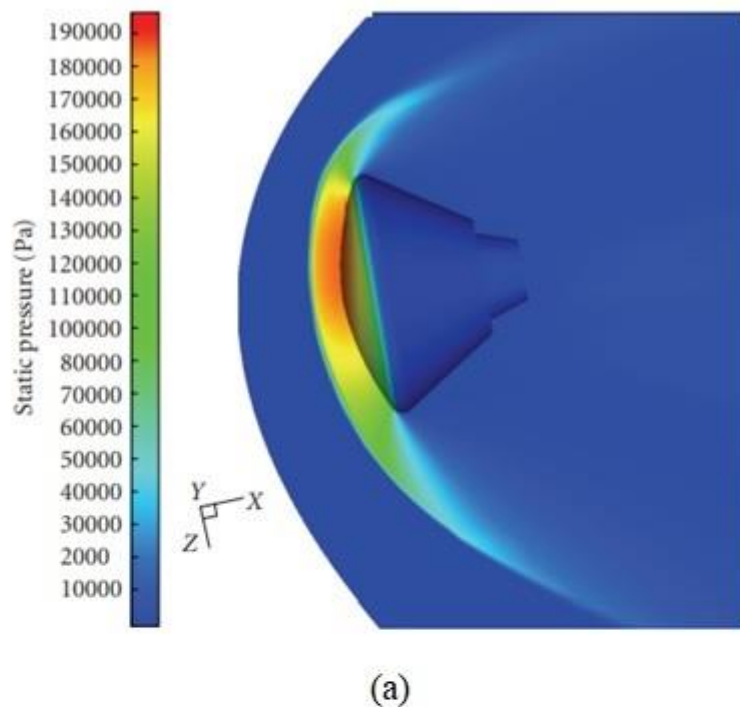
The reference parameters that have been chosen for the definition of the aerodynamic forces and moment nondimensional coefficients are the longitudinal reference length ($L_{ref} = D = 2R_b$), equal to the capsule diameter (e.g., 5.0 m), and the reference surface ($S_{ref} = \pi R_b^2 = 19.6 \text{ m}^2$), that is the maximum cross-section area of the MBS. The pitching moment was computed from the nose of the Capsule [24].

The evaluations of the vehicle aerodynamic database (AEDB) have been performed by means of engineering tools and CFD (Computational Fluid Dynamics) computations to focus on some critical design aspects not predictable with simplified tools as, for example, real gas effects [24-31].

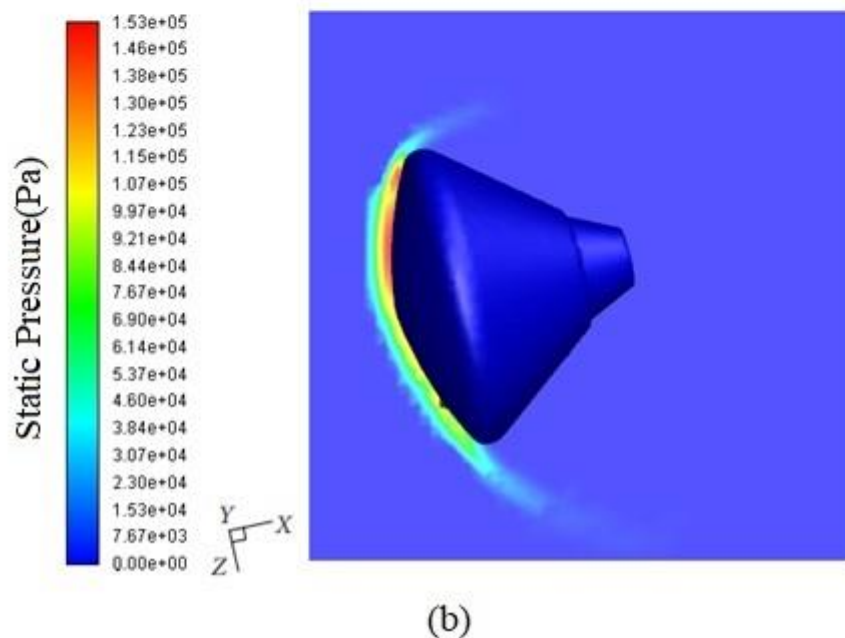
5.1.1.3 Validation of Results

The hypersonic flow around the capsule has a strong compressible effect due to the wide range of the vehicle's nose causing a strong detachment of the bow shock that is in front of the capsule which in turn has a drastic effect of increasing pressure and temperature with maximums within the bow shock region up to the capsule surface. The shock wave still extends over the shoulder of the capsule deflecting the wide-range stream. The immediate drop in the pressure is observed at the leeside of the afterbody. The Fig 59 shows the pressure contours of a symmetric plane all along the domain length along with the surface pressure of the capsule at Mach number 10 ,20 and $\alpha= 10^\circ$ and 20° [24].

At the angle of attack $\alpha=10^\circ$, $M=10$, the maximum pressure in [25] is about 190000 Pa due to the strong bow shock detached at 0.21 m from the front end of the capsule as shown in Fig 59 (a) [25]. The maximum pressure in the current work is 153000 Pa due to the strong bow shock detached at 0.15m from the front end of capsule, as shown in Fig 59 (b).



(a)

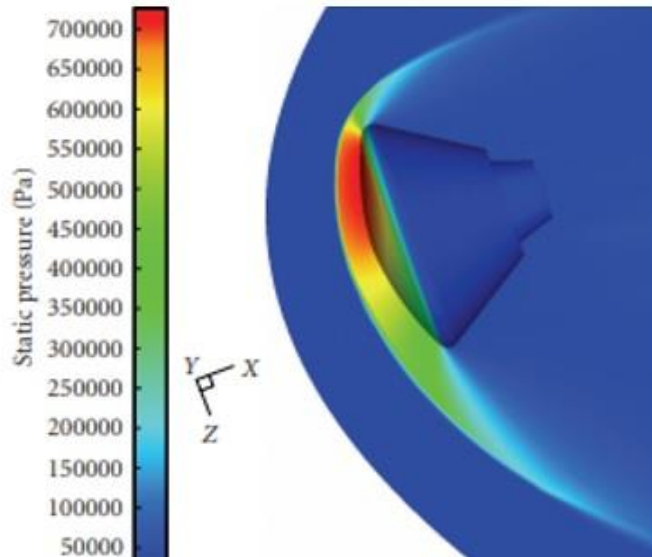


(b)

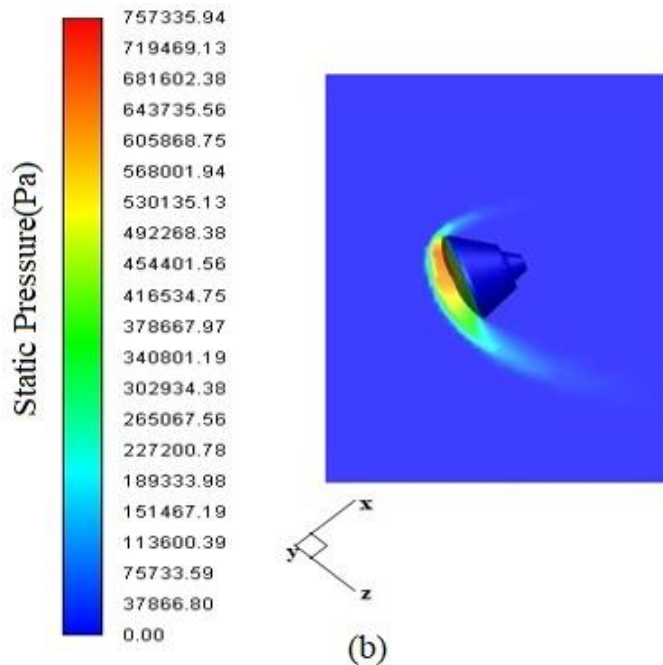
Fig 59. Static Pressure contour for MSV capsule at $\alpha=10^\circ$ and $M=10$ (a). [24], (b). Current work

At the angle of attack $\alpha=20^\circ$, $M=20$, the maximum pressure in [25] is 700000 Pa at 0.21 m from the front end of the capsule as shown in Fig 60 (a). The maximum pressure

observed in this work is 757335.94 Pa, and the bow shock is detached at 0.2 m from the front end of capsule (Fig 60(b)). As the angle increases from 10° to 20° , the maximum pressure increases.



(a)



(b)

*Fig 60. Static Pressure contour for MSV capsule at $\alpha = 20^\circ$ and $M=20$ (a). [24], (b).
Current work*

When the MBS flies at a higher Mach number, a stronger bow shock detaches in front of the entry vehicle and dominates the flow field of the front body. In particular, the higher the number of Mach and α , the narrower the shock layer. Fig 61 and Fig 62 shows the effect of hypersonic flow with different angle of attack of the re-entry capsule. The shock layer at the wind side of forebody is thicker than leeside. After the shoulder, the flow begins to expand because of the large deflection angle of afterbody.

The expansion waves intersect at back of the capsule, and recompression waves are generated. Due to the negative pressure gradients and viscous effect, the flow is separated at the leeside of afterbody, and recirculating flow is generated at rear of the vehicle. The recirculating flow can be seen even at 57.5 m from the centre of the capsule. When compared the contour images of $\alpha=10^\circ$ and $\alpha=20^\circ$, the shock layer in $\alpha=20^\circ$ is wider than $\alpha=10^\circ$. When analysed numerically considering the boundary conditions of Table 19, the hypersonic flow velocity drops dramatically from Mach 10 to subsonic flow (i.e., less than Mach 1). Due to recirculation, the flow rate increases within a sonic to supersonic range independently of α [14, 24].

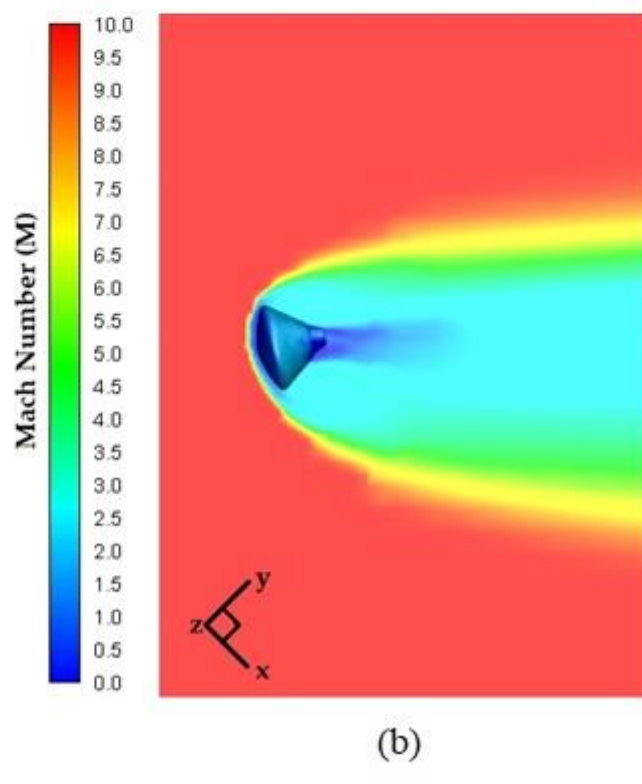
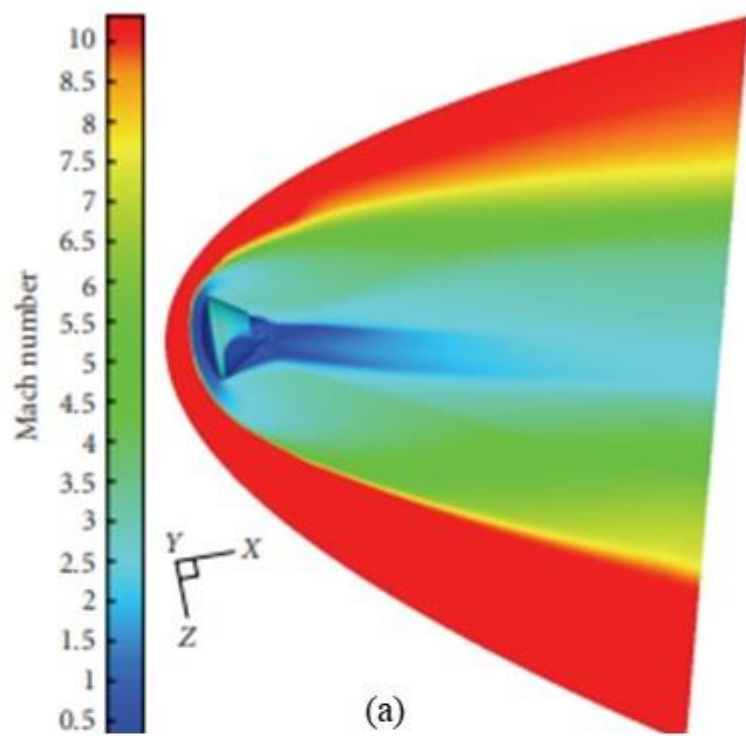


Fig 61. Velocity-Mach number contour for MSV at $\alpha = 10^\circ$ and $M= 10$ (a). [24], (b). Current work

At the angle of attack $\alpha=10^\circ$, $M=10$, a strong bow shock at 0.3 m from the front end the capsule is shown in Fig 61(a) [24], while, in Fig 61(b) these results show that it is predicted at 0.45 m from the front end the capsule. The shockwaves are narrower is shown in Fig 61(b).

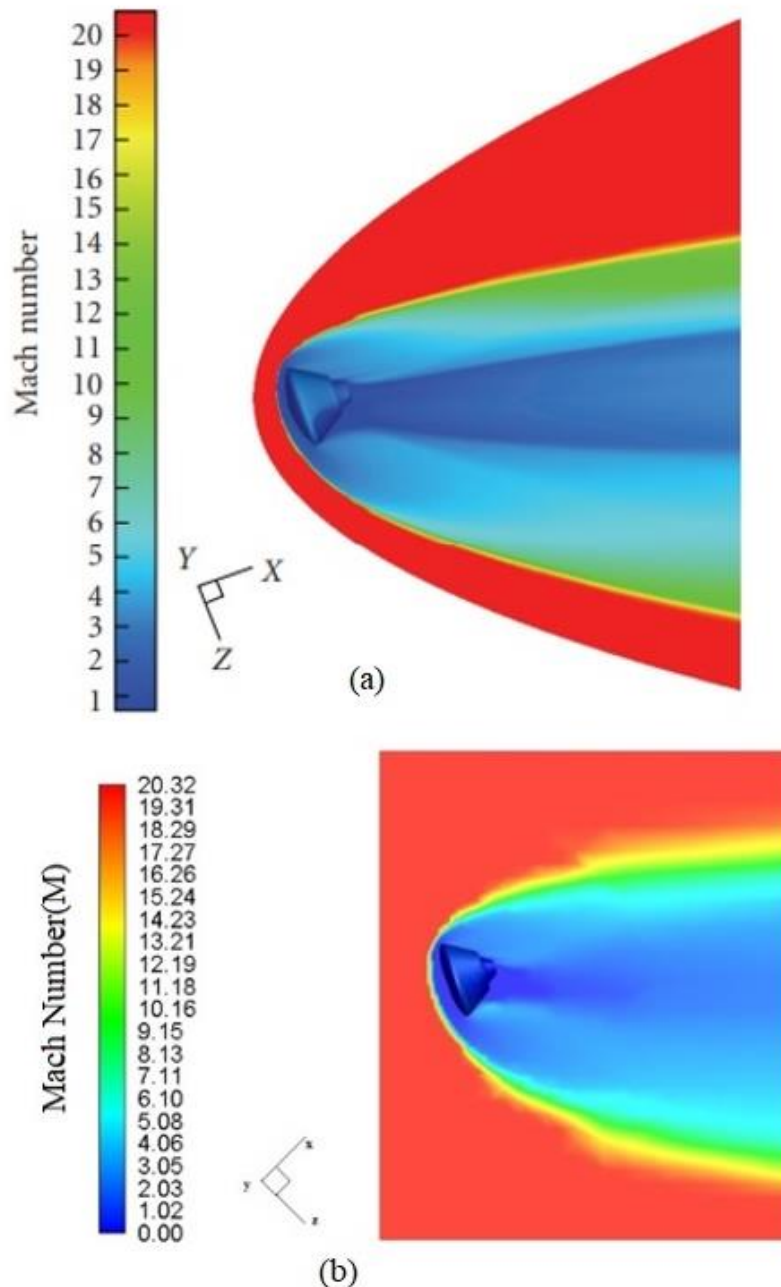
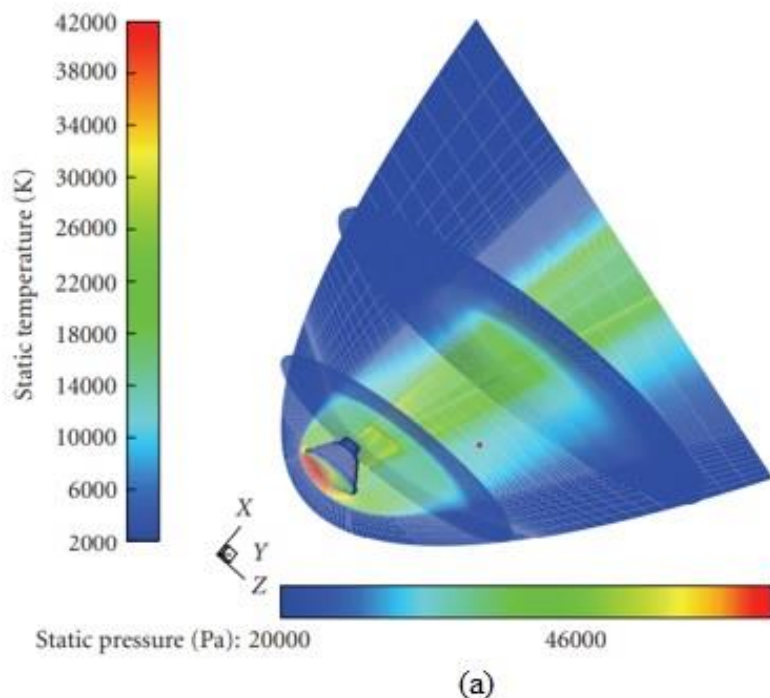


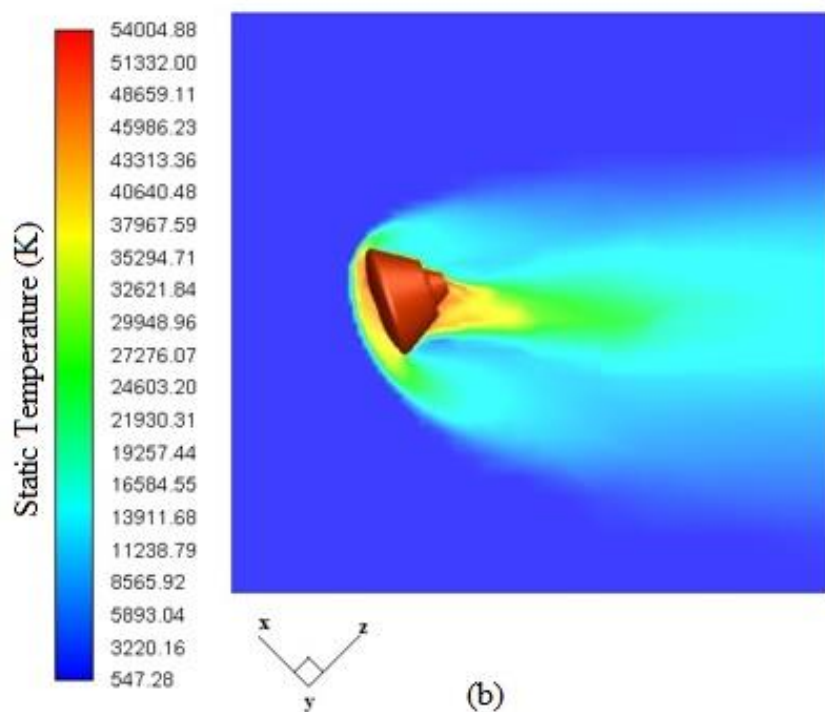
Fig 62. Velocity - Mach number contour for MSV at $M = 20$, and $\alpha = 20^\circ$ (a). [24],
(b). Current work

At the angle of attack $\alpha=20^\circ$, $M=20^\circ$, the shock waves get wider before the front body as shown in Fig 62 (a), i.e., it is at 0.2 m in [24] and 0.35m in the current work (see Fig 62 (b)).

The three-dimensional flow field occurring beyond the input capsule at $M = 20$ and $\alpha = 20^\circ$ is shown in Fig 63(a). The maximum temperature was estimated at [24] in 42000K at 0.1 m from the front end of the capsule (see Fig 63(b)) and 45986.23K at the front end of the capsule and 54004.88K on the capsule body. The minimum temperature observed around the capsules is 2000K [24] and 547.28K (in Fig 63).



(a)



(b)

Fig 63. Static Temperature contour for MSV at $M = 20$ and $\alpha = 20^\circ$ (a). [24], (b). Current work

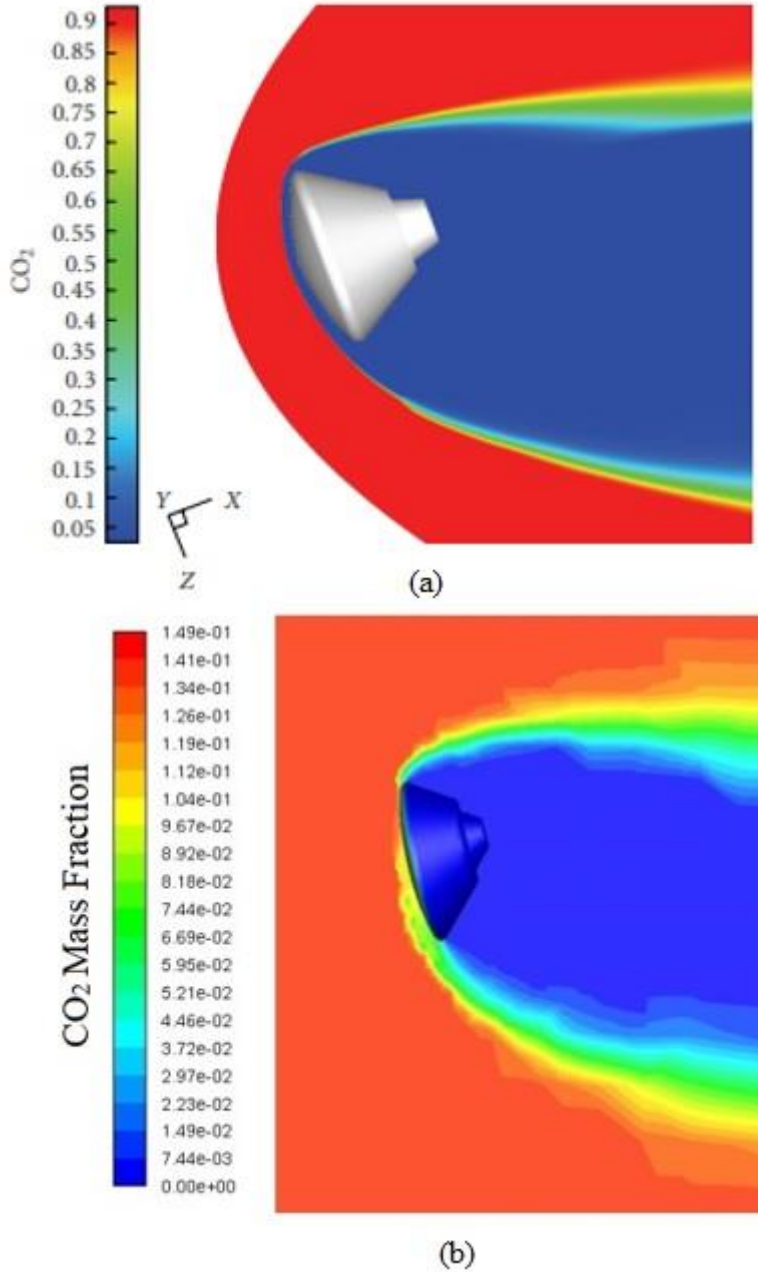


Fig 64. CO₂ Mass fraction contour for MSV at $M = 20$ and $\alpha = 20^\circ$ (a). [24], (b). Current work

The chemical dissociation of the flow in the shock layer can be recognized in Fig 64(a)-Fig 64(b) where contour of both CO₂ mass fraction on MBS pitch plane for $M = 20$ and $\alpha = 20^\circ$ is reported. Fig 64(a) shows that the strong bow shock arises at 0.2m from front end of Capsule and 0.1m from front end of Capsule as shown in Fig 64(b). Therefore, flow dissociation determines a large density ratio ϵ across the strong bow shock compared with a flow of the same gas where no dissociation takes place [24]. This

results in a thinner shock layer around the entry vehicle (e.g., lower stand-off distance). Under conditions where dissociation exists, the aerodynamics of vehicle depends primarily on shock density ratio. In fact, the change of aerodynamic characteristics is the result of change in surface pressure acting on the vehicle forebody.

As matter of fact, the level of pressure at the vehicle stagnation point (e.g., C_{pmax}) reads:

$$C_{pmax} = C_{pt2} = \frac{p_{t2} - p_\infty}{q_\infty} = \left(\frac{P_{t2}}{P_{t\infty}} - 1 \right) \frac{2}{\gamma M_g} \cong 2 - \varepsilon \quad (46)$$

instead of the classical Newtonian value (e.g., $C_{pmax} = 2$). Moreover, the density ratio across the bow shock wave, ε , in the hypersonic limit is:

$$\varepsilon = \lim_{M_\infty \rightarrow \infty} \frac{\rho_1}{\rho_2} = \frac{\gamma-1}{\gamma+1} \quad (47)$$

So, ε changes as γ depends on the number of active degrees of freedom of the gas mixture species. The reason for the discrepancy at afterbody of the capsule is the constant specific heat ratio γ . As shown in Fig 64(b), most molecules of carbon dioxide (CO_2) dissociate in the shock layer due to the high temperature. At forebody of the capsule, the flow is nearly chemical equilibrium, the specific heat ratio calculated by equation (47) is appropriate. At afterbody of the capsule, the flow expands and the temperature decreases, and the dissociated atoms recombine to molecules. The specific heat ratio increases with the temperature descending and the atoms recombining. A constant specific heat ratio calculated by the flow properties in the shock layer is utilized for perfect gas model, while it is lower than the real gas model at afterbody of the capsule. The smaller specific heat ratio results in stronger compressibility. The difference of specific heat ratio or the flow compressibility between the two gas models induces the discrepancy at afterbody of the vehicle [14,24-26].

$$\gamma = \frac{\eta + 1}{\eta - 1} - \frac{2\eta}{(\eta - 1)Ma^2} \quad (48)$$

In [25], the effect of the real gas model with respect to the perfect gas model has been investigated. The authors found that for $M=20$ and $\alpha =20^\circ$, in real gas model the bow shock is located at 0.6m ahead of the capsule and the maximum pressure observed is 79900 Pa approximately, while in the perfect gas model, the bow shock arises at 0.6 m ahead of the capsule and the maximum pressure observed is 170000 Pa approximate.

5.2.2. Aerothermodynamic Analysis of Ducted re-entry vehicles

5.2.2.1 Design and Meshing

In this paper, the comparison of the pressure for an Orion CEV re-entry vehicle is done according to Mach number between 0 and 7 (see Fig 65 [32]). The meshing is done in design modeler with 1.17 million elements using ANSYS Fluent Meshing 19.0 by hexagonal method and converted into polyhedral method in Fluent as shown in Fig 66.

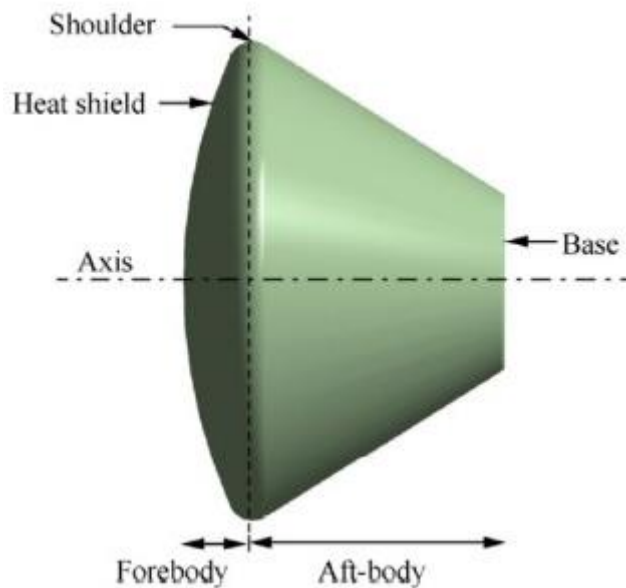


Fig 65. Design of Orion capsule

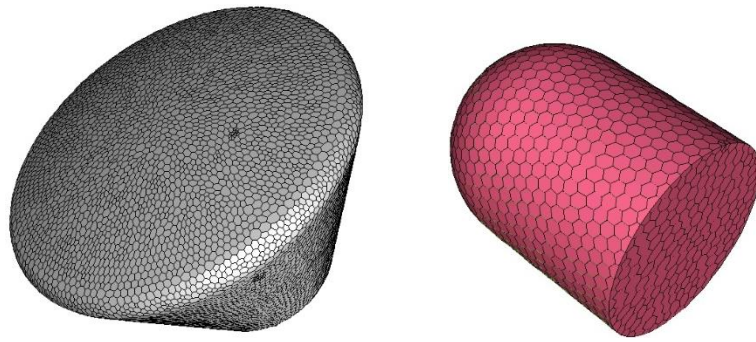


Fig 66. Mesh of numerical domain for the Orion CEV Re-entry vehicle

5.2.2.2 Method of Simulations

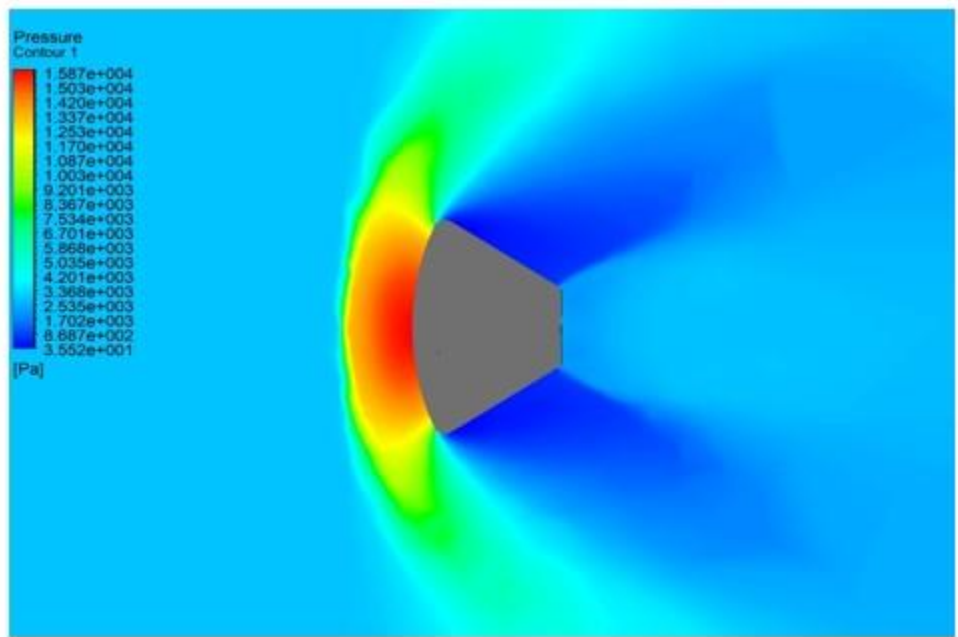
RANS simulations have been performed implementing the SST k- ω turbulence and air at ideal gas and Sutherland's Law of Viscosity. This simulation also undergoes based on Navier-Stokes equation and Range-Kutta method. Boundary conditions are shown in Table 20.

Table 20: Boundary conditions for Ducted Re-entry vehicles [32]

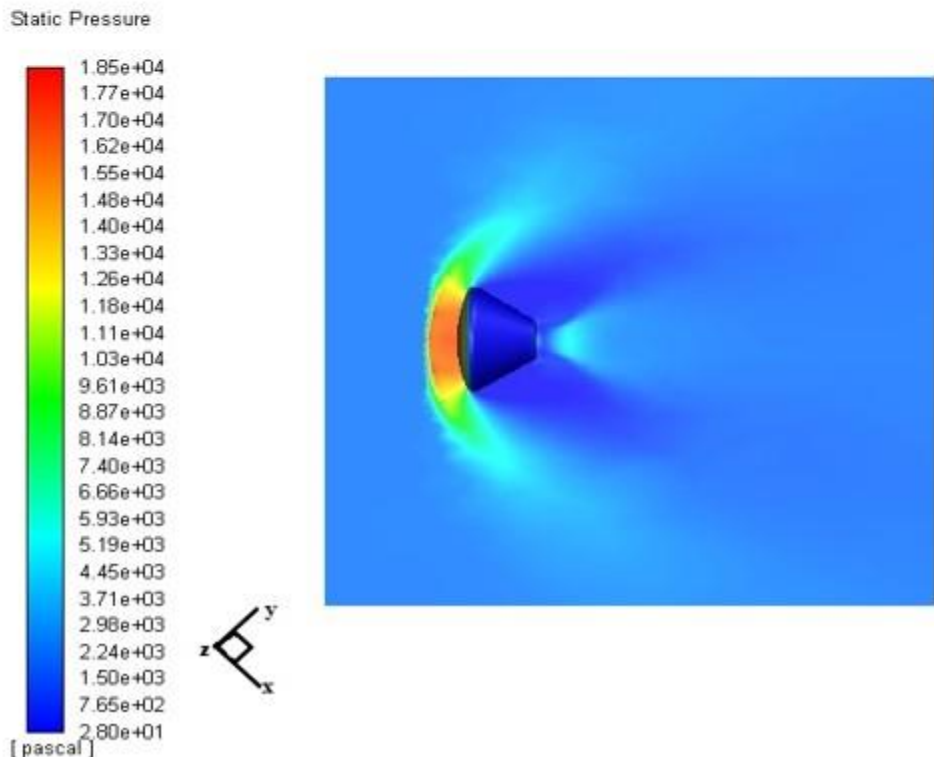
Zone	Type	Parameters
Pressure far field	Pressure far field	Pressure: between 1000 and 7500pa Mach Number: between 0.5 to 6 Temperature: between 110 and 300
Space Capsule	Interior wall	-

5.2.2.3 Validation of Results

The static pressure contours are obtained for Mach 2 and 5 as shown in Fig 67 and Fig 68 [32].



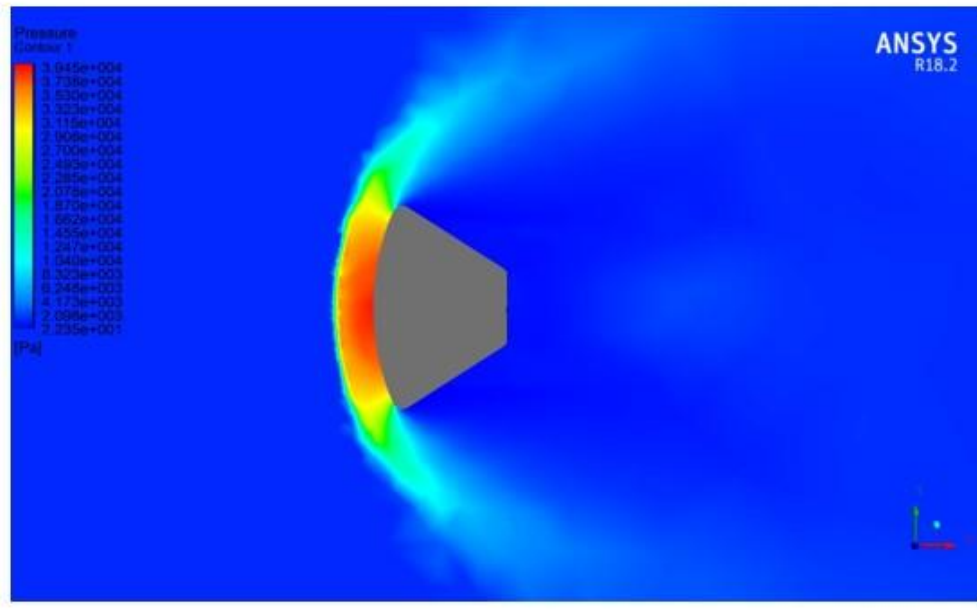
(a)



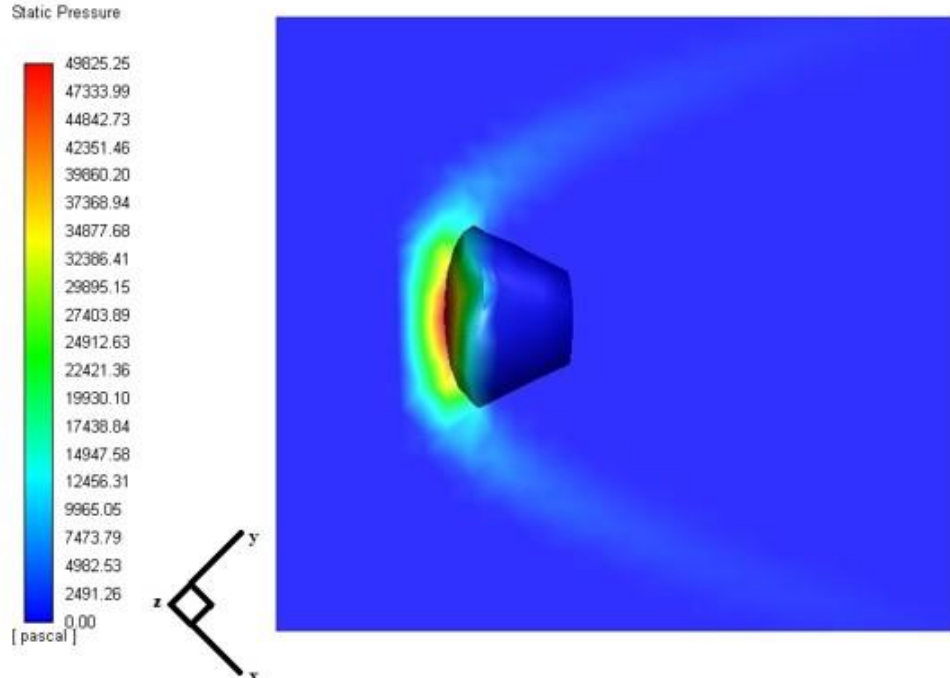
(b)

Fig 67. Comparison of the Baseline re-entry vehicle pressure at $M = 2$, (a).[32],
(b). current work

Fig 67 shows that at $M=2$ but the bow shock arises at 0.3m from front end of the capsule, and the pressure increases at a maximum of $1.85 \times 10^4 \text{ Pa}$.



(a)



(b)

Fig 68. Comparison of the Baseline re-entry vehicle pressure at $M = 5$, (a).[32],
(b). current work

Fig 68 shows that at $M=5$ but the bow shock arises at 0.3m from front end of the capsule, and the pressure increases at a maximum of 49825.25Pa.

5.2.3. MSV capsule at Mach number 1.94 and 10

5.2.3.1 Design and Meshing of MSV Capsule at $\alpha = 2^\circ$

The actual model of MSV space capsule has been created in Ansys design modeler for $\alpha = 2^\circ$ as shown in Fig 69 using the same length of the capsule [24]. The domain has been created for this capsule as shown in Fig 70.

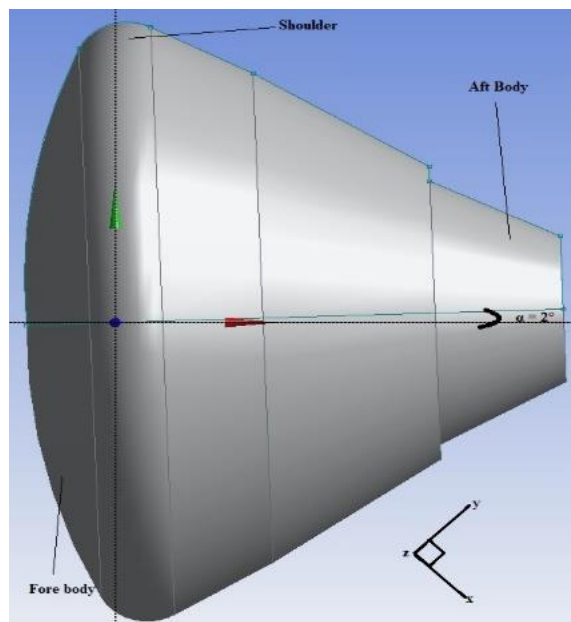


Fig 69. Design of MSV capsule at $\alpha = 2^\circ$

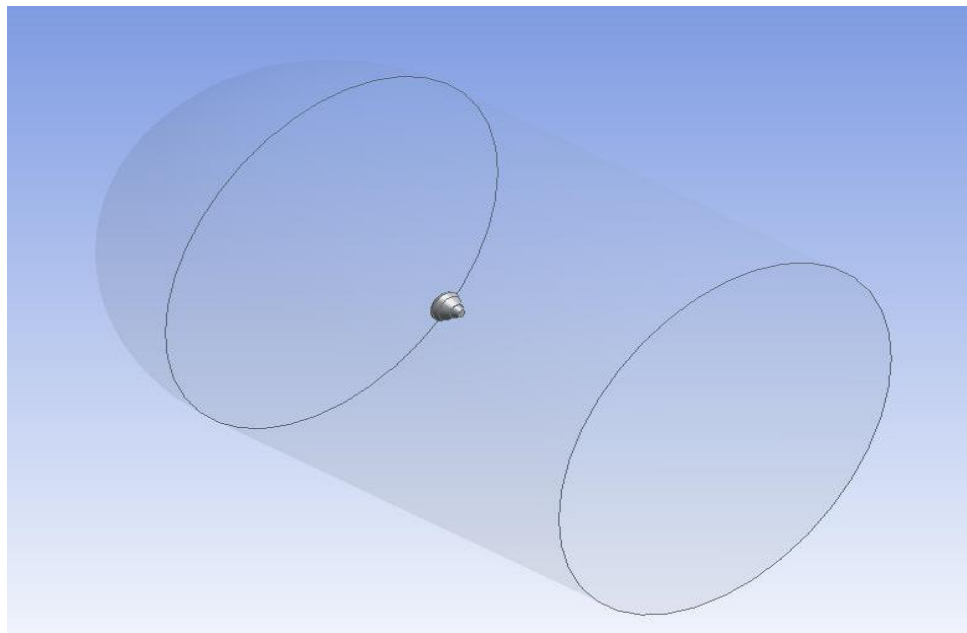


Fig 70. Domain length of 100m

The meshing for this capsule has been shown in Fig 71 and for domain in Fig 72 by the method of cut cell meshing that contains 1198724 nodes. It has been done by sizing length of body edge and face of both domain and capsule as shown in Table 21.



Fig 71. Mesh image of Re-entry capsule



Fig 72. Mesh of computational domain with 100m length

Table 21: Details of mesh definition

Type of Sizing	Size of the Element (m)	Normal Angle (in degrees)	Size function
Body sizing for enclosure	1.5	9°	Curvature
Body sizing for Space capsule	1.0	5°	Curvature
Face sizing for enclosure	0.5	-	Uniform
Face sizing for Space capsule	0.5	-	Uniform
Edge sizing for enclosure	0.25	-	Uniform
Edge sizing for Space capsule	0.25	-	Uniform

5.2.3.2 Method of Simulation

Simulations are performed using the following boundary conditions based on free flow, as shown in Table 22. The SST k- ω turbulence model for viscosity and the Sutherland's law for molecular viscosity has been implemented. The gas has been assumed ideal. The courant number which is set to 0.8 for simulation. The simulation can be calculated from the input and performed calculations per 100000 iterations.

Table 22: Boundary conditions for Simulation of MSV Capsule

Zone	Type	Parameters
Inlet	Pressure far field	For Case(i): Pressure = 1400pa Temperature = 560K Mach number = 1.94 For Case(ii): Pressure = 1400pa Temperature = 560K Mach number=10
Wall	Wall	-

5.2.3.3 Validation of Results

The hypersonic flow around the capsule has a strong compressible effect due to the large nose radius of the vehicle causing a strong bow shock detachment ahead of the capsule. Fig 73 shows that there is a drastic increase in pressure at the beginning of the capsule. The shockwave become extend till the shoulder of the capsule. The immediate drop in the pressure is observed at the leeside of the afterbody. The Fig 73

and Fig 75 shows the pressure contours of a symmetric plane all along the domain length along with the surface pressure of the capsule at $\alpha = 2^\circ$ and $M=1.94, 10$.

The samples are drawn from five different axial directions (L1(0 m), L2(0.5 m), L3(1m), L4(-0.5 m) and L5(-1 m) equally spaced from the centre in the direction of flow as shown in the Fig 74 and Fig 75. The results show that the pressure of the flow continues to be constant until it reaches the forebody of the capsule. Due to the detachment of the bow shock, the pressure is raised to the approximate value of 7550.432 Pa (approx.) at the centre of the capsule surface and the bow shock as well. Amidst the peak value at the surface centre, the surface pressure decreases gradually reaching an approximate value of 4530.239 Pa as the peak pressure at the shoulder. With the increase in the α from 0° to 20° , a slight variation in the peak values is observed. Irrespective of the α , a drastic drop in the pressure is seen reaching an average approximate value of 755.043 Pa (see Fig 73) at the leeside of the body, which then gradually matches the given freestream value after few body diameters. At $M=1.94$ and $\alpha = 2^\circ$, the peak value of pressure observed in the line L1 is 7310 Pa which is the maximum pressure among all the lines L2, L3, L4 and L5. The peak value of pressure observed in the line L2 is observed as 6930 Pa. The peak value of pressure is observed in the line L3 is 6130 Pa. The peak value of pressure is observed in the line L4 is 6840 Pa. The peak value of pressure is observed in the line L5 is 6030 Pa (see Fig 74).

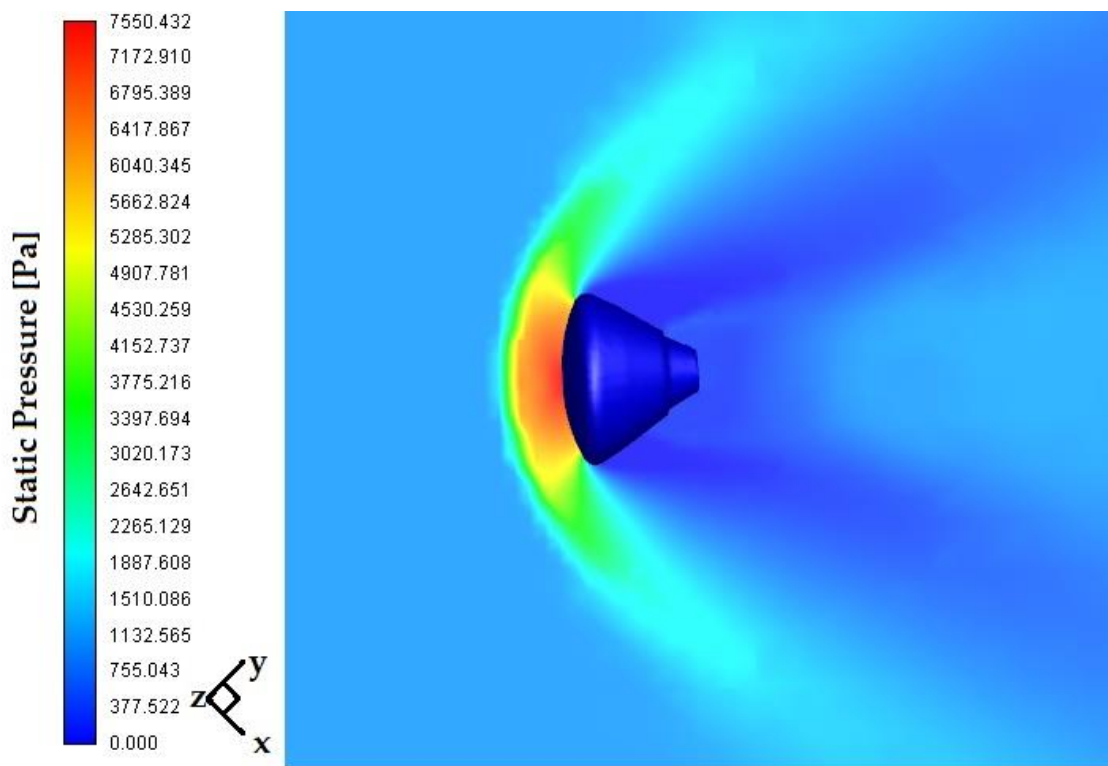


Fig 73. Static pressure contour for MSV capsule at $\alpha = 2^\circ$ and $M = 1.94$

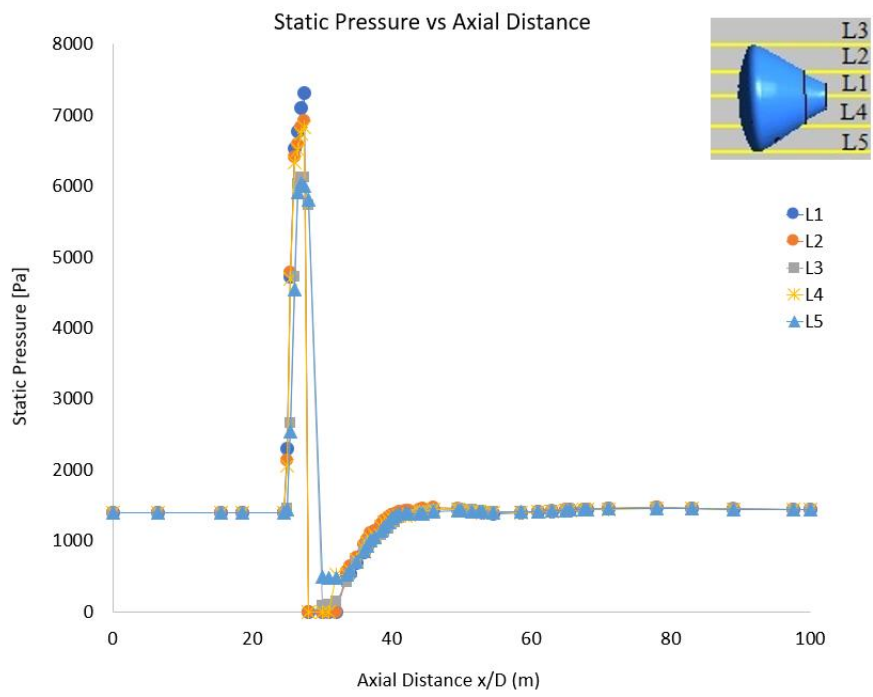


Fig 74. Static pressure along the domain axial distance at $\alpha = 2^\circ$, $M = 1.94$ for domain length = 100m

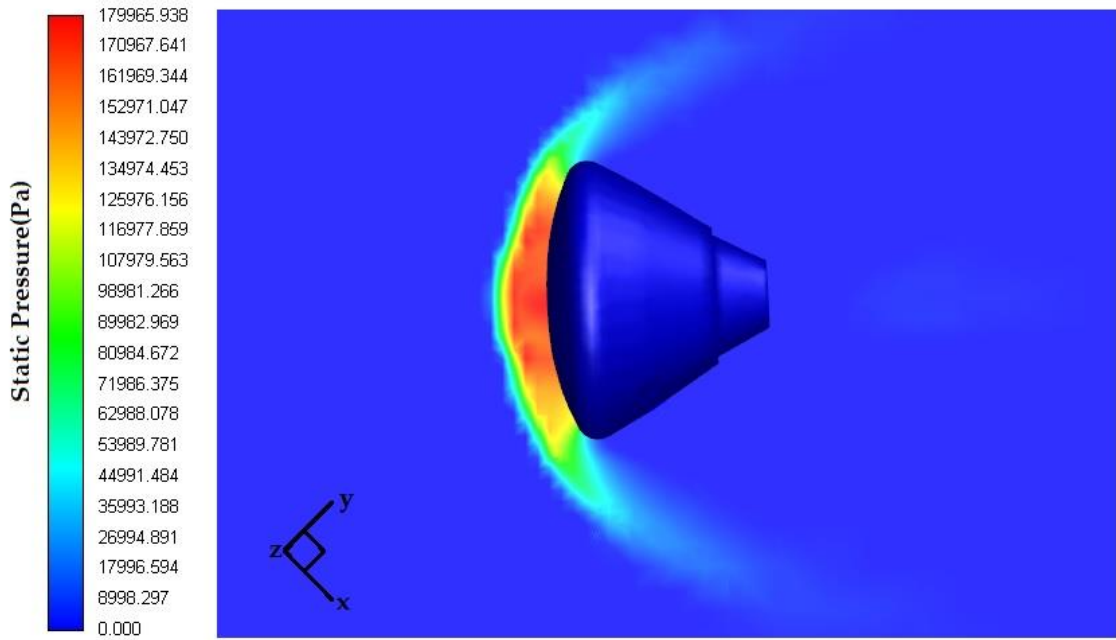


Fig 75. Static pressure contour for MSV capsule at $\alpha = 2^\circ$ and $M = 10$

The bow shock wave is greater at $M = 1.94$ in the distance of 0.45 m than the bow shock at $M = 10$ at 1.2 m from the front end of the capsule. There is an increase in pressure at the front end of the capsule due to strong shock waves for both Mach numbers as shown in Fig 73 and Fig 75.

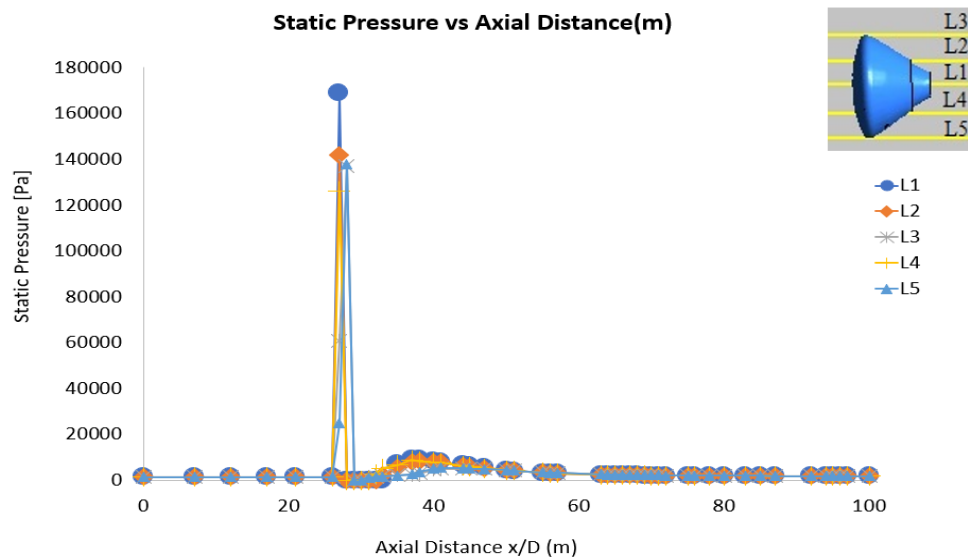


Fig 76. Static pressure along the domain axial distance at $\alpha = 2^\circ$, $M = 10$ for domain length = 100m

Fig 76 shows a drastic increase in pressure at the beginning of the capsule. The pressure decreases drastically downstream of the capsule, then starts increasing slightly and becomes constant as shown in Fig 76. At $M=10$ and $\alpha = 2^\circ$, the peak value of pressure observed in the line L1 is 169000 Pa which is the maximum pressure among all the lines L2, L3, L4 and L5. The peak value of pressure observed in the line L2 is observed as 142000 Pa. The peak value of pressure is observed in the line L3 is 137000 Pa. The peak value of pressure is observed in the line L4 is 126000 Pa. The peak value of pressure is observed in the line L5 is 138000 Pa (see Fig 76).

The density contour gives an insight view about the changes in the gas phase of a hypersonic flow when compressed due to the interaction with the blunt body vehicle. Due to drastic increase in density of the gas, the strong bow shock detaches at 1.5 m from the front end of the Re-entry vehicle and dominates flow body forefield. The density of the gas is observed maximum at the front end of the Capsule due to there is drop of density at the lee side of aft body where the shockwave is narrower. The flow gets deflected after the shoulder due to the wide deflection angle. The flow is recirculated until several body diameters. The flow and recirculation can be observed even at 60 m distance from the afterbody. The contours of density at $\alpha = 2^\circ$ and $M = 1.94$ are shown in Fig 77 and Fig 79.

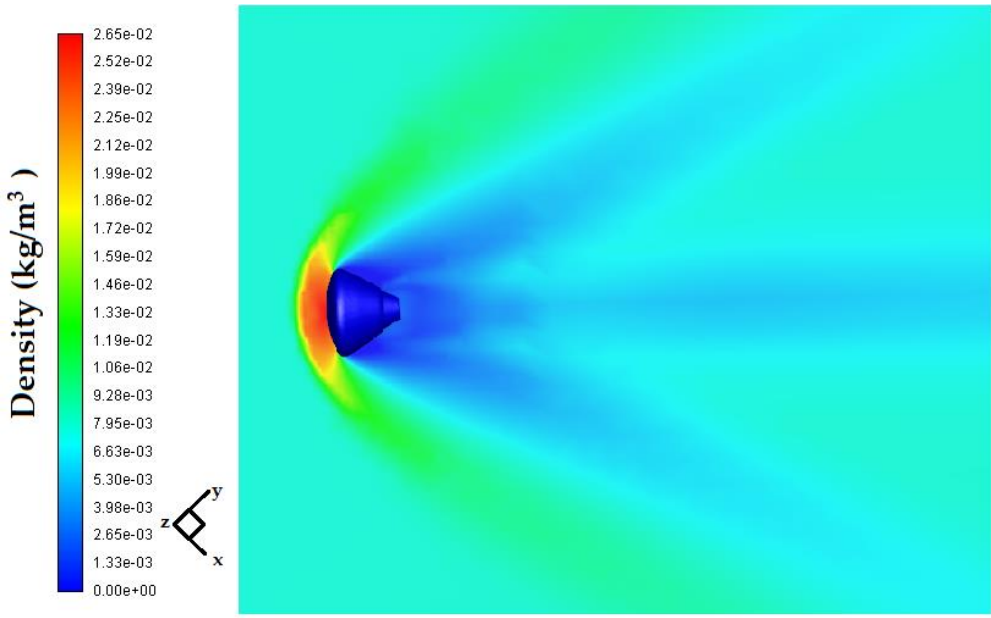


Fig 77. Density contour for MSV capsule at $\alpha = 2^\circ$ and $M = 1.94$

The numerical investigations undergone at various phases of MSV Space Capsule is shown in Fig 78 and Fig 80. At $M=1.94$ and $\alpha = 2^\circ$, the peak value of density is obtained in the line L1 is 0.026 kg/m^3 which is higher among all the lines (see Fig 78). The peak value of density obtained in the line L2 is $0.024962194 \text{ kg/m}^3$. The peak value of density obtained in the line L3 is 0.0231 kg/m^3 . The peak value of density obtained in the line L4 is 0.0247 kg/m^3 . The peak value of density obtained in the line L5 is 0.0228 kg/m^3 (see Fig 78). At $M=10$ and $\alpha = 2^\circ$, the peak value of density obtained in the line L1 is 0.0511 kg/m^3 which is higher among all the lines L1, L2, L3, L4, L5 (see Fig 80). The peak value of density obtained in the line L2 is 0.045 kg/m^3 . The peak value of density is obtained in the line L3 is $0.04365021 \text{ kg/m}^3$. The peak value of density obtained in the line L4 is $0.039908785 \text{ kg/m}^3$. The peak value of density obtained in the line L5 is 0.0443 kg/m^3 (see Fig 80).

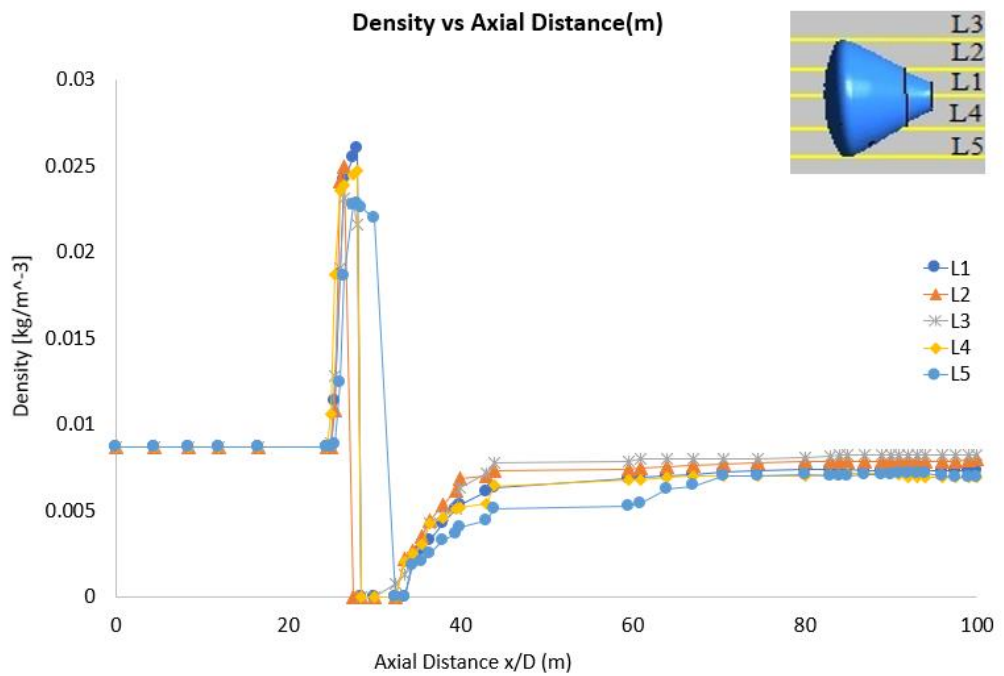


Fig 78. Density along the domain axial distance at $\alpha = 2^\circ$, $M = 1.94$ for domain length = 100m

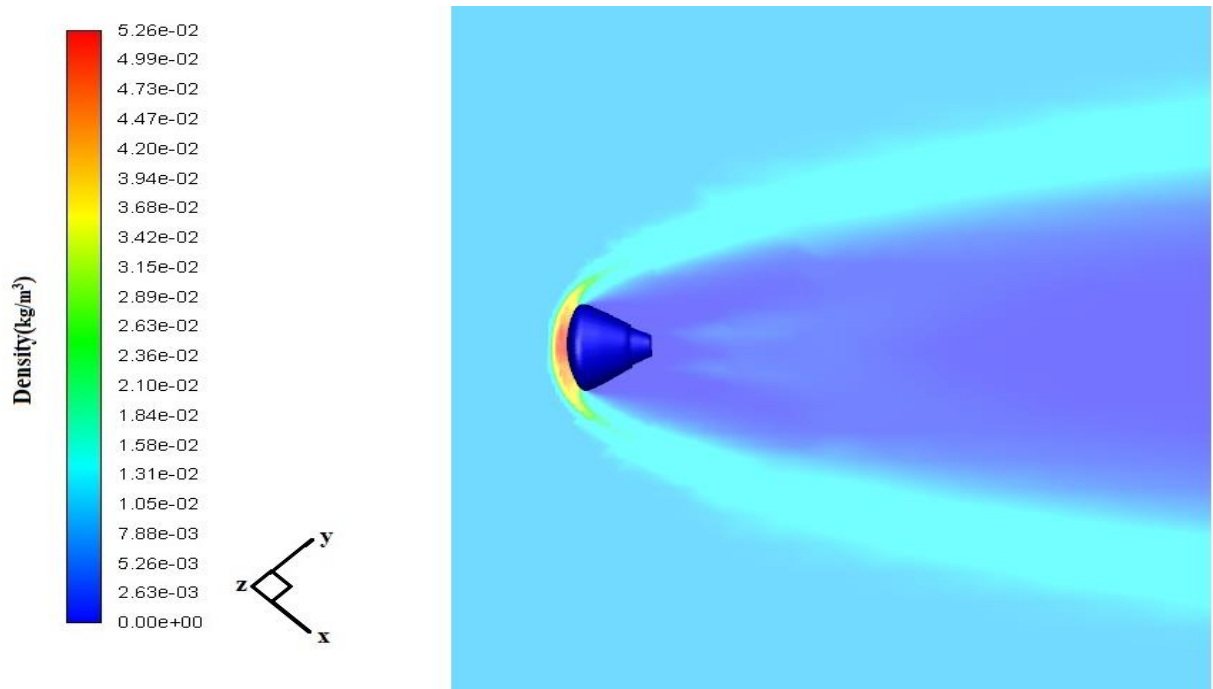


Fig 79. Density Contour for MSV capsule at $\alpha = 2^\circ$ and $M=10$

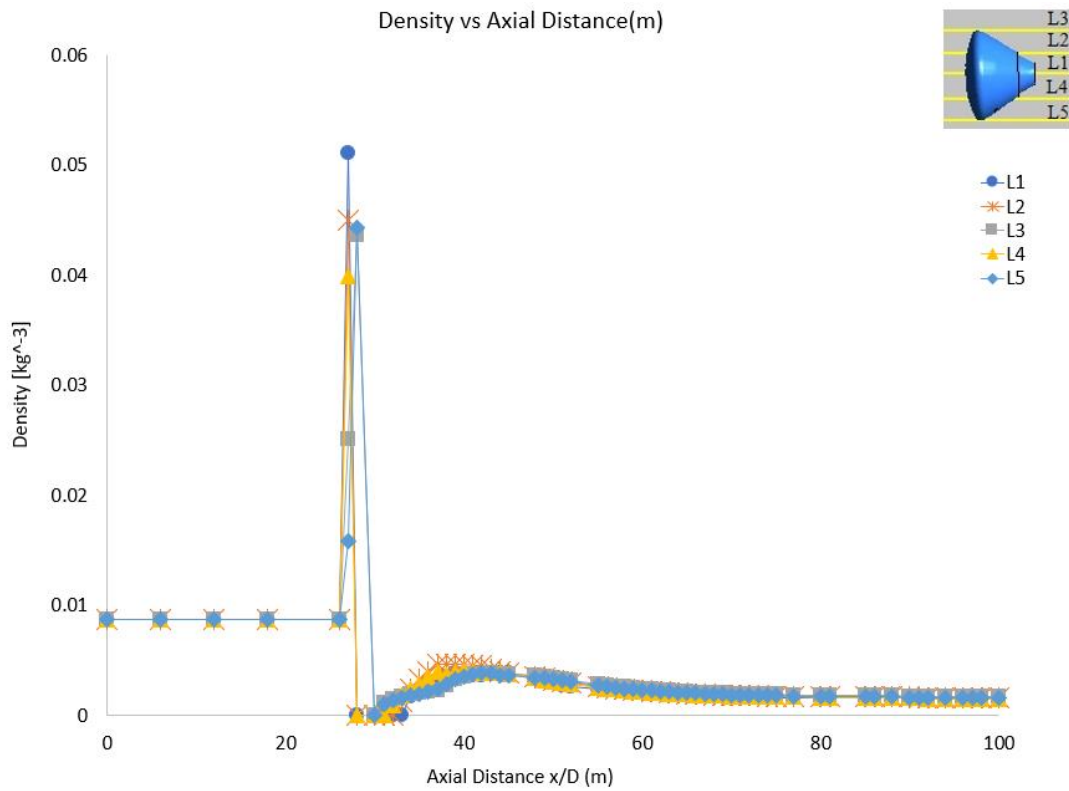


Fig 80. Density along the domain axial distance at $\alpha = 2^\circ$, $M = 10$ for domain length = 100m

At $M=1.94$ and $\alpha = 2^\circ$, the bow shock is at 0.5 m from front end of the capsule (see Fig 81) where at $M=10$, the shockwave at 0.4 m from front end of the capsule at same angle of attack (see Fig 83), the temperature is increases at 980.84K (see Fig 81). At $M=10$, the shock layer is wider than $M=1.94$ at the rear end of the capsule at the same angle of attack (see Fig 83) and the maximum temperature observed is 20059.72K (see Fig 83).

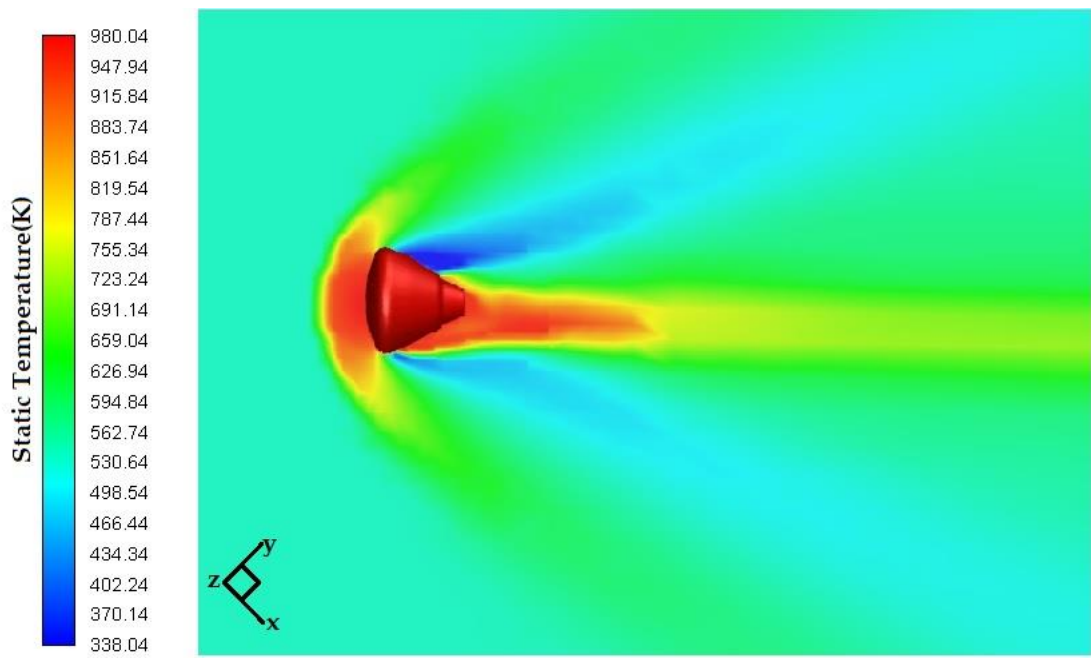


Fig 81. Static Temperature contour for MSV Capsule at $\alpha = 2^\circ$ and $M = 1.94$

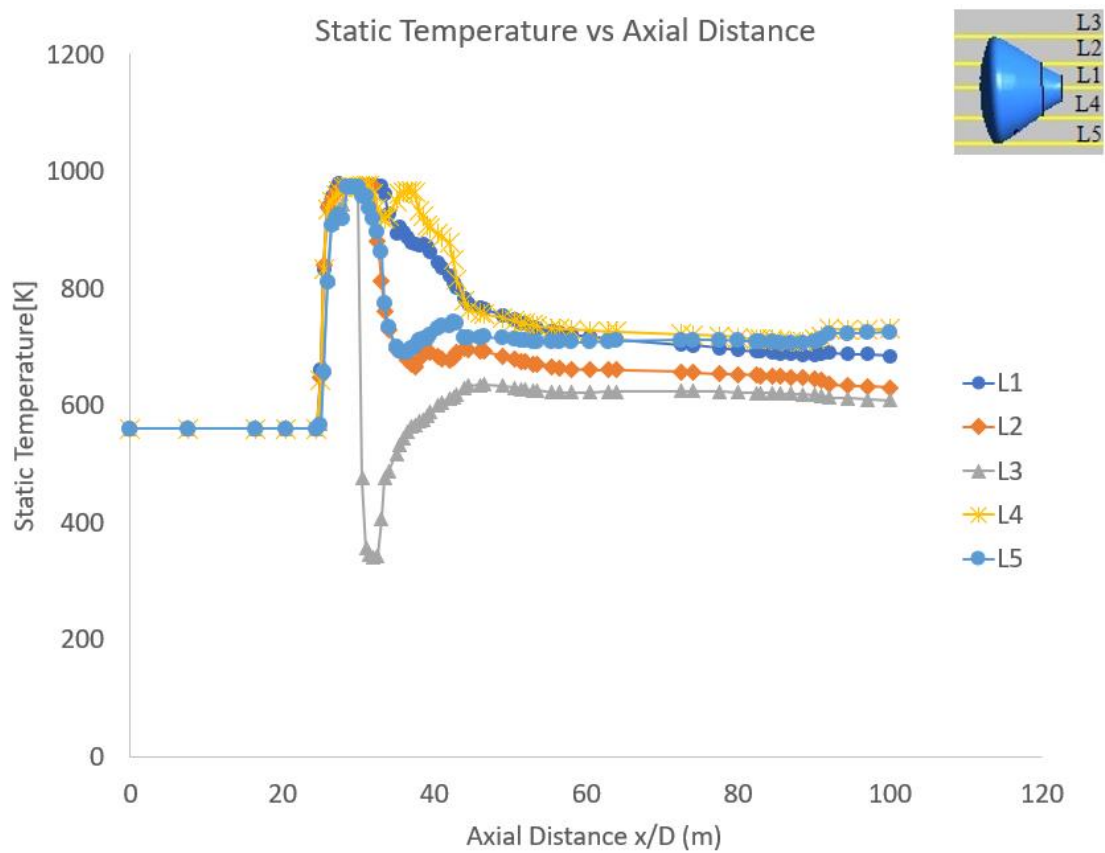


Fig 82. Static Temperature along the domain axial distance at $\alpha = 2^\circ$, $M = 1.94$ for domain length = 100m

There is a drastic increase in temperature at the beginning of the Capsule. After the capsule, the temperature decreases and again increases as shown in Fig 82. At $M=1.94$ and $\alpha = 0^\circ$, the peak temperature is observed in the line L1 is 979 K which is maximum among all remaining direction of lines (see Fig 82). The peak temperature is observed in the line L2 is 975 K. The peak temperature is observed in the line L3 is 972 K. The peak temperature observed in the lines L4 and L5 is 973K (see Fig 82).

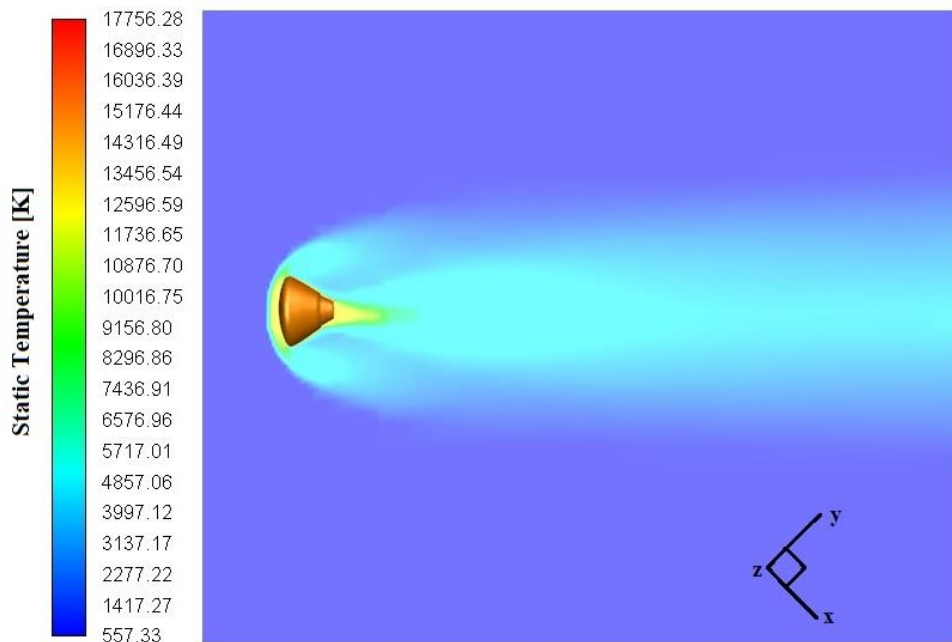
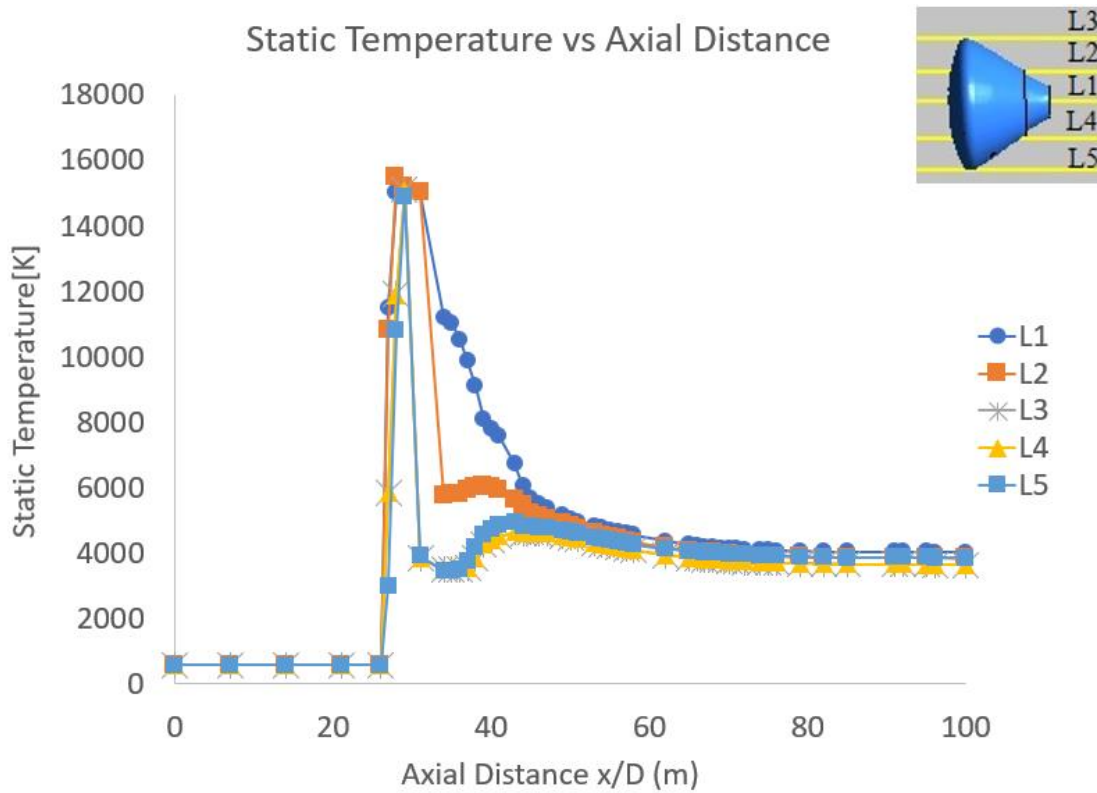


Fig 83. Static Temperature contour for MSV Capsule at $\alpha = 2^\circ$ and $M=10$



*Fig 84. Static Temperature along the domain axial distance at $\alpha = 2^\circ$,
 $M = 10$ for domain length = 100m*

Fig 84 shows that at $M=10$ and $\alpha = 2^\circ$, the peak temperature is observed in the lines L1 and L3 is 15100 K. The peak temperature is observed in line L2 is 15500 K which is maximum among all remaining direction of lines (see Fig 84). The peak temperature is observed in the line L4 is 15065K. The peak temperature observed in the line L5 is 14500K (see Fig 84).

As the strong bow shock arises before 1m from the front end of the capsule at $M=1.94$ and $\alpha = 2^\circ$, the temperature difference 2389.38 is observed is shown in Fig 85. So, DT/Dx is constant till 25m in all lines of directions (L1 (0 m), L2 (0.5 m), L3 (1.5 m), L4 (-0.5 m) and L5 (-1 m)) is shown in Fig 86. Afterwards, L3 will go to peak level at value of 3277.14 and goes down till 31m and then increases till 50m and then become constant till 100m. In line L5, the peak value at negative direction is observed as - 3260.9.

The line L1 has maximum DT/Dx peak value of 341 and minimum peak value of 522.3. The line L2 has highest peak value of 798.15 and lowest peak value of 450.6. The line L4 has the peak value of -2289.14 is in negative direction. Thus, Fig 86 shows that the temperature difference of lines L4 and L5 travels in negative direction due to there is some oblique shocks arise at aft body of the capsule as shown in Fig 85.

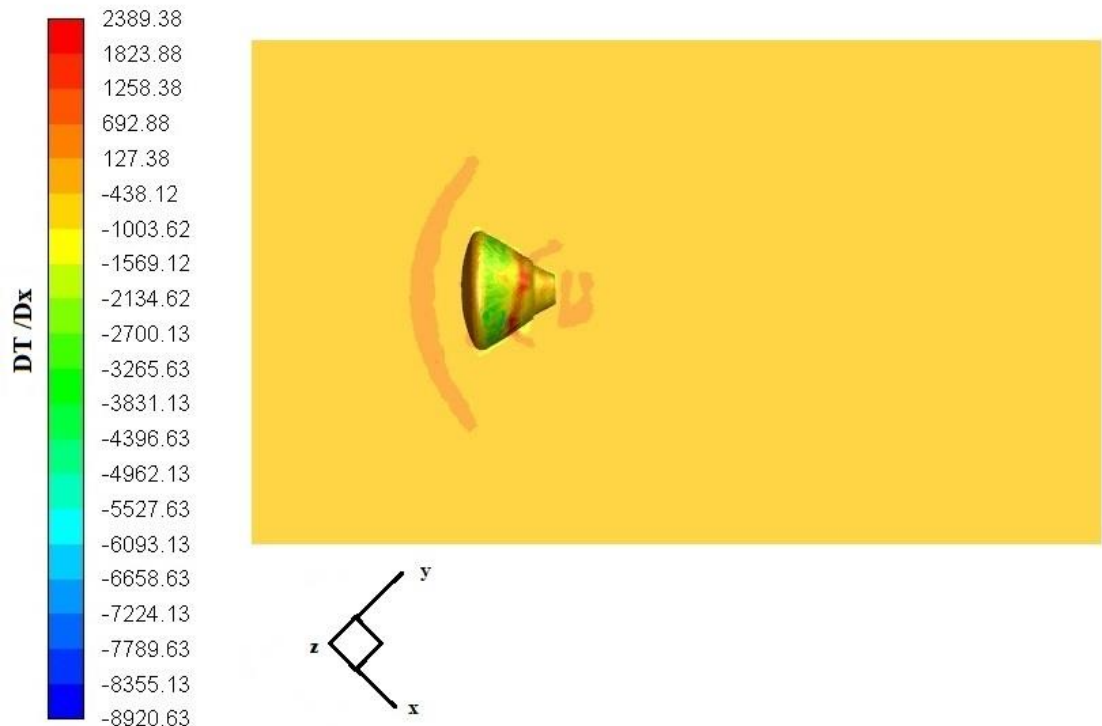


Fig 85. DT/Dx contour for MSV Capsule at $\alpha = 2^\circ$ and $M = 1.94$

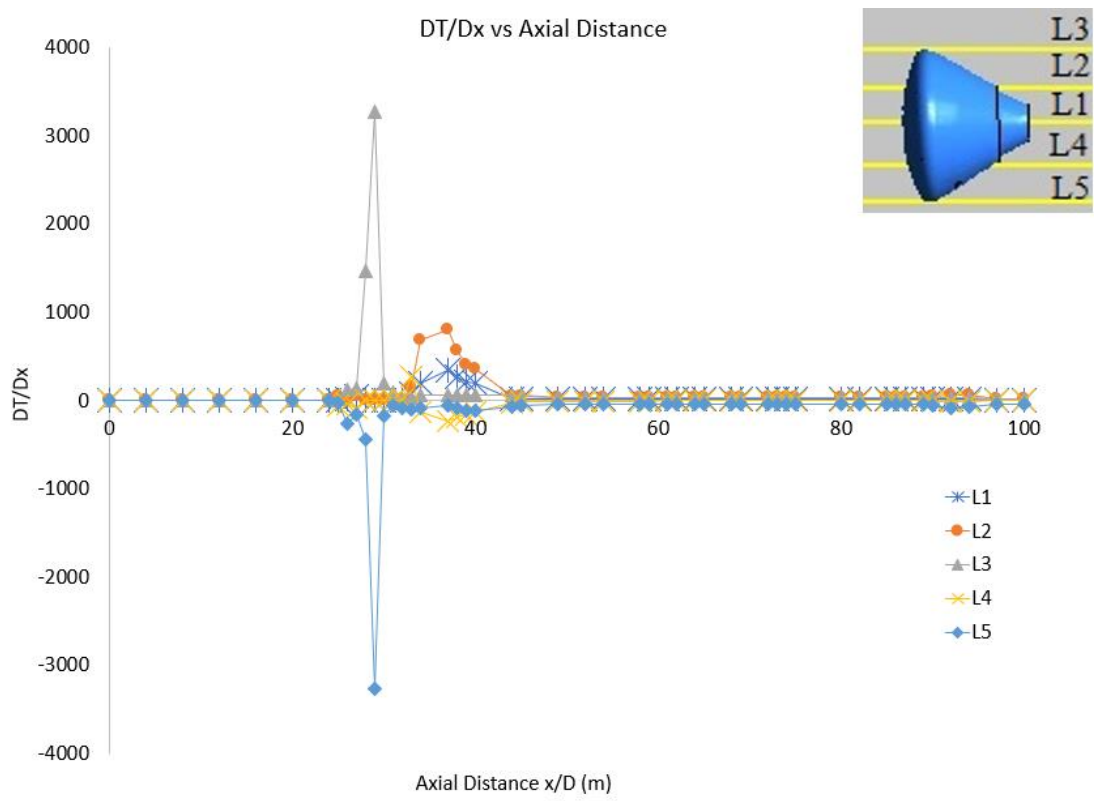


Fig 86. DT/Dx along the domain axial distance at $\alpha = 2^\circ$, $M = 1.94$ for domain length = 100m

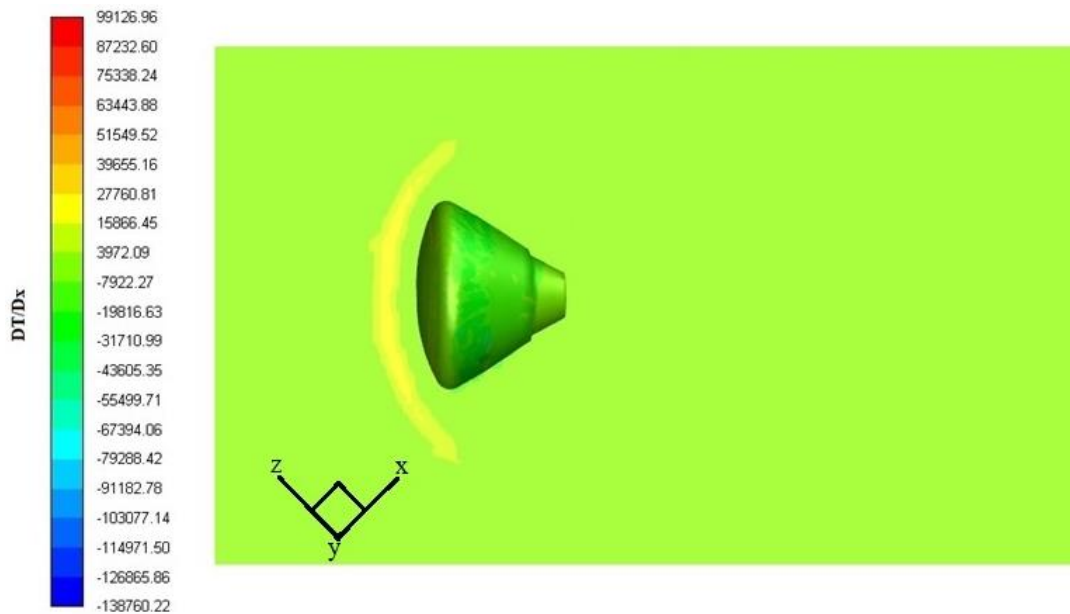


Fig 87. DT/Dx contour for MSV Capsule at $\alpha = 2^\circ$ and $M=10$

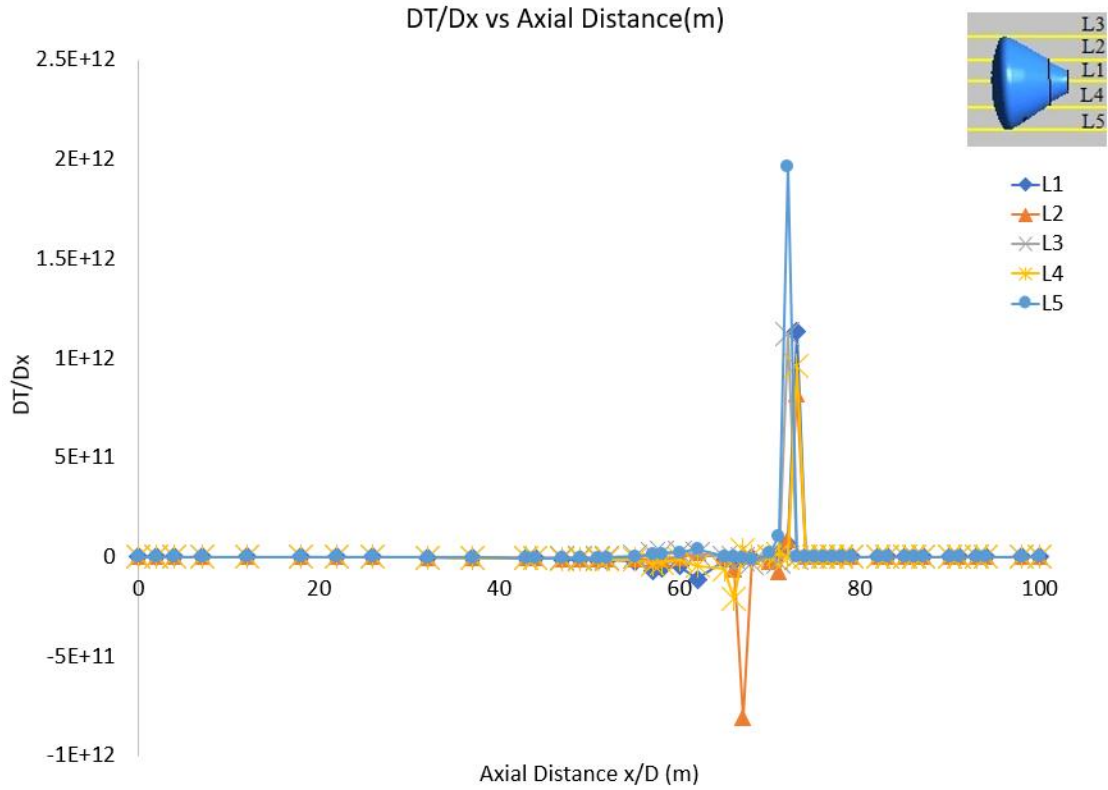


Fig 88. DT/Dx along the domain axial distance at $\alpha = 2^\circ$,

$M = 10$ for domain length = 100m

As the strong bow shock arises before 1m from the front end of the capsule at $M=10$ and $\alpha = 2^\circ$, the temperature difference is 99126.96 (see Fig 87). In line L1, the maximum positive peak value is observed as 13894.27 and the maximum negative value is observed as -99.543. In line L2, the maximum positive peak value is observed as 13997.45 and maximum negative value is observed as -2301.44. In line L3, the maximum positive peak value is observed as 12550.39 and negative value is observed as -8148.95. In line L4, the maximum positive peak value is observed as 13401.37. In line L5, the maximum positive peak value is observed as 19462.11 and minimum negative value is observed as -10568.23 (see Fig 88).

Fig 89 shows that at $M=1.94$ the strong bow shockwave detaches after 1m from the forebody of the capsule and in the sides of forebody of the capsule (From Fig 89).

Dx_v/Dx is constant from 0 to 22m in the direction of lines (L1(0m), L2(0.5m), L3(1.5m), L4(-0.5m) and L5(-1m)) as shown in Fig 90.

The peak values are observed in this direction of these lines are $(Dx_v/Dx)_{L1(-ve)} = -651.91 s^{-1}$, $(Dx_v/Dx)_{L1(+ve)} = 154.875 s^{-1}$, $(Dx_v/Dx)_{L2(-ve)} = -673.83 s^{-1}$, $(Dx_v/Dx)_{L2(+ve)} = 211.75 s^{-1}$, $(Dx_v/Dx)_{L3(-ve)} = -444.42 s^{-1}$, $(Dx_v/Dx)_{L3(+ve)} = 1897.91 s^{-1}$, $(Dx_v/Dx)_{L4(-ve)} = -664.581 s^{-1}$, $(Dx_v/Dx)_{L4(+ve)} = 142.03975 s^{-1}$, $(Dx_v/Dx)_{L5(-ve)} = -760.35 s^{-1}$ and $(Dx_v/Dx)_{L5(+ve)} = 1919.52 s^{-1}$ (see Fig 90). From 45m to 100m Dx_v/Dx becomes constant in all the directions (shown in Fig 89) because wake region is slightly arised at end of the capsule is shown in Fig 89.

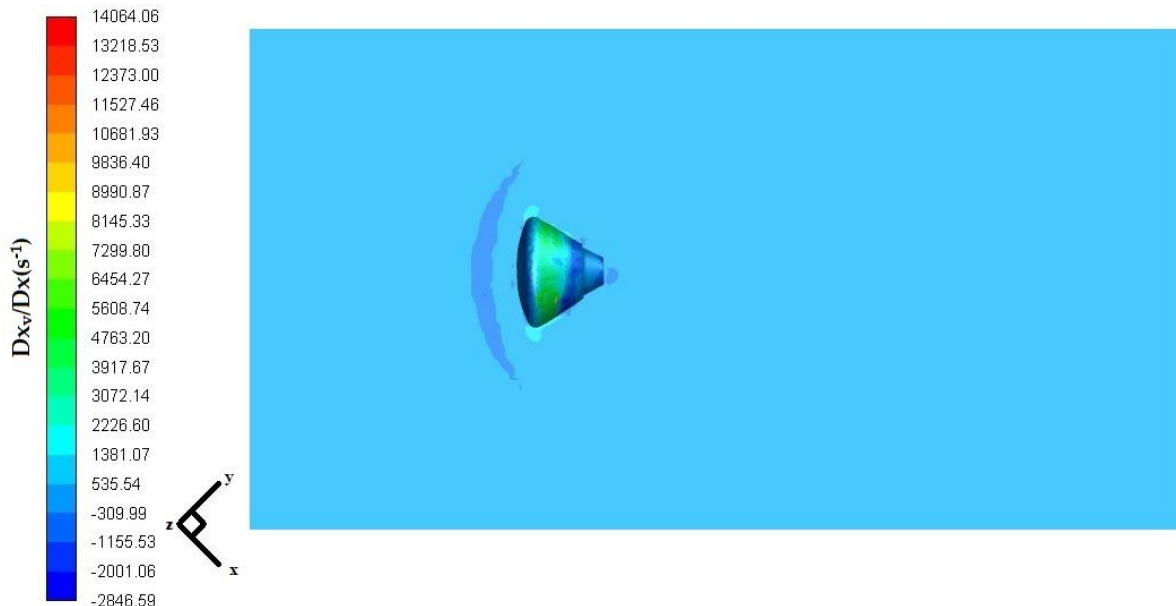
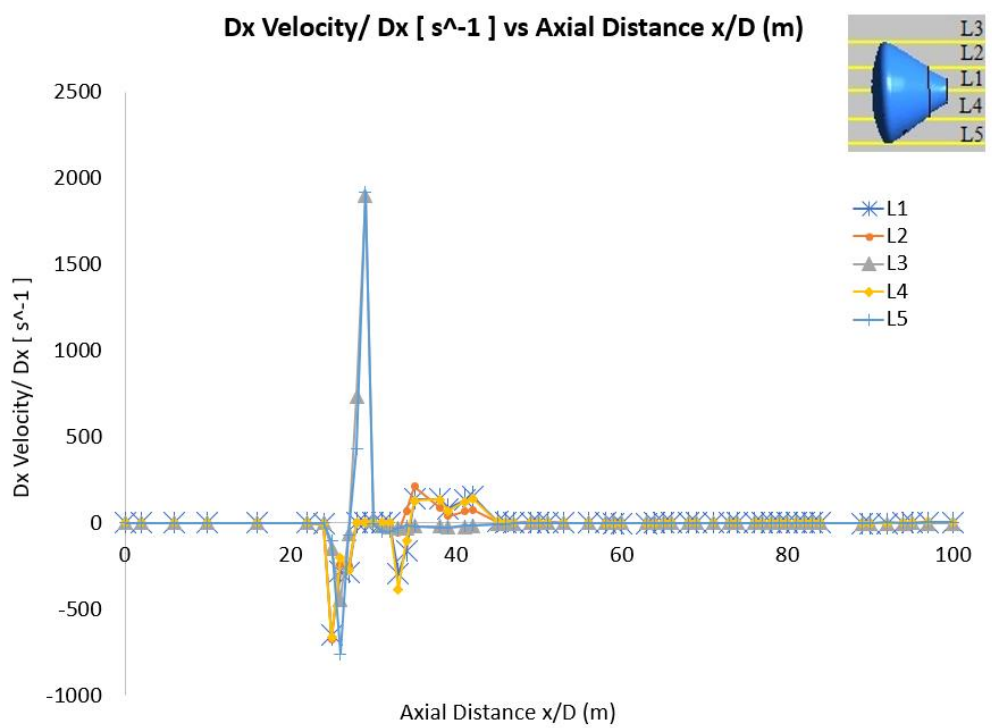


Fig 89. Dx_v/Dx contour for MSV Capsule at $\alpha = 2^\circ$ and $M=1.94$



*Fig 90. Dx_v/Dx along the domain axial distance at $\alpha = 2^\circ$,
 $M = 1.94$ for domain length = 100m*

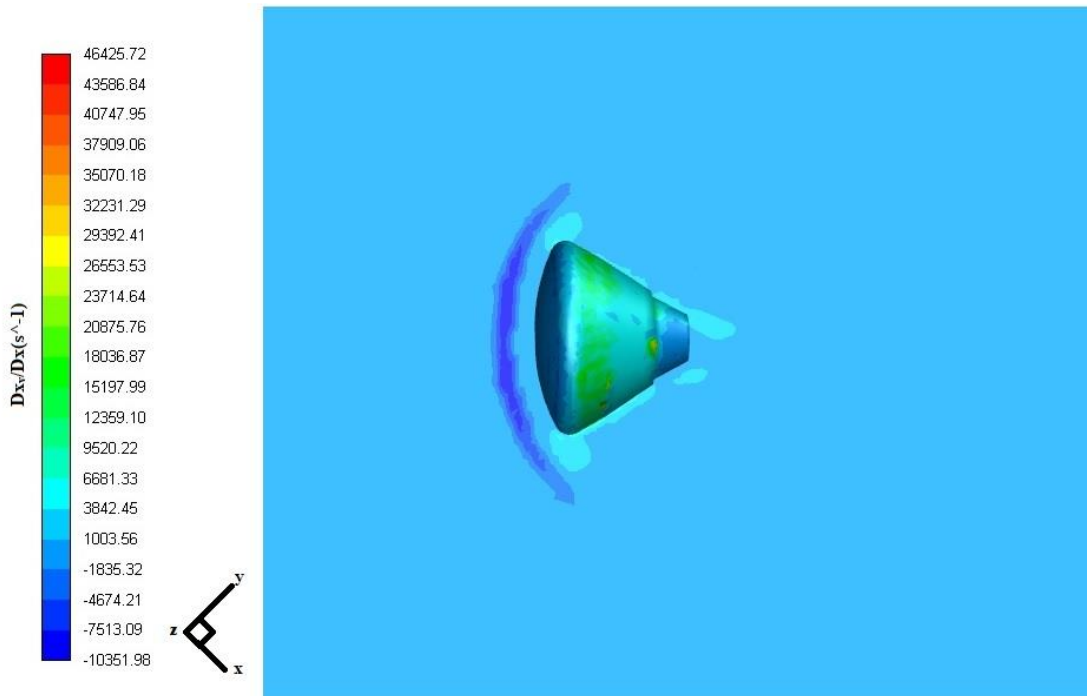


Fig 91. Dx_v/Dx contour for MSV Capsule at $\alpha = 2^\circ$ and $M=10$

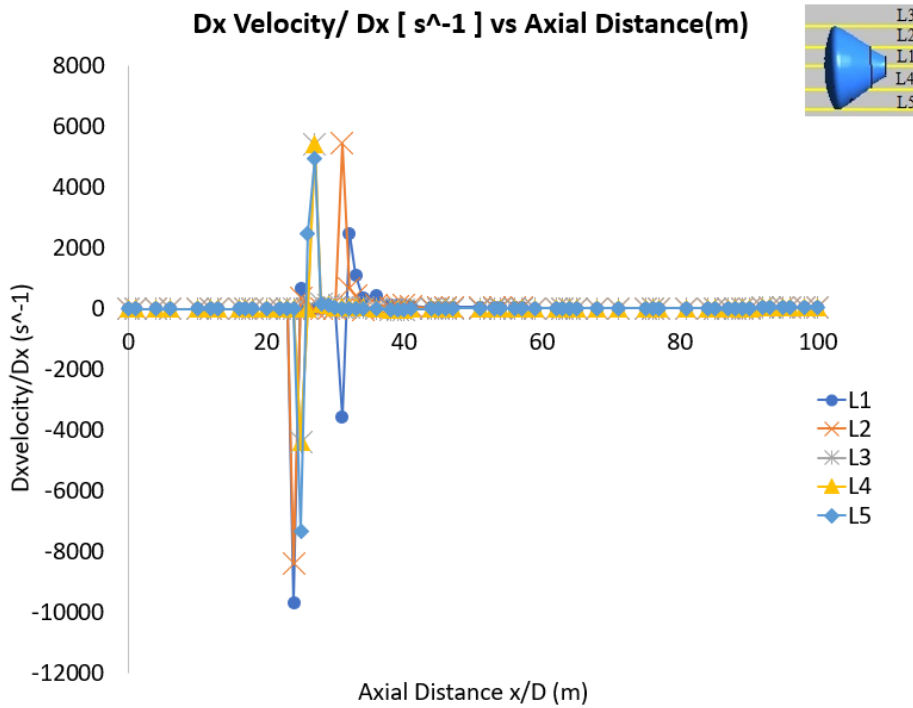


Fig 92. Dx_v/Dx along the domain axial distance at $\alpha = 2^\circ$, $M = 10$ for domain length = 100m

At $M=10$, Dx_v/Dx is constant from 0 to 25m in the Direction of Lines (L1(0 m), L2(0.5 m), L3(1 m), L4(-0.5m) and L5(-1m)) as shown in Fig 92.

The peak values of Dx_v/Dx are observed in this direction of these lines are $(Dx_v/Dx)_{L1(-ve)} = -4496.48 \text{ s}^{-1}$, $(Dx_v/Dx)_{L1(+ve)} = 2947.05 \text{ s}^{-1}$, $(Dx_v/Dx)_{L2(-ve)} = -3298 \text{ s}^{-1}$, $(Dx_v/Dx)_{L2(+ve)} = 986.41 \text{ s}^{-1}$, $(Dx_v/Dx)_{L3(-ve)} = -5097.03 \text{ s}^{-1}$, $(Dx_v/Dx)_{L3(+ve)} = 2850.25 \text{ s}^{-1}$, $(Dx_v/Dx)_{L4(-ve)} = -3429.53 \text{ s}^{-1}$, $(Dx_v/Dx)_{L4(+ve)} = 731.33 \text{ s}^{-1}$, $(Dx_v/Dx)_{L5(-ve)} = -7308.44 \text{ s}^{-1}$ and $(Dx_v/Dx)_{L5(+ve)} = 3607.04 \text{ s}^{-1}$.

From 47m to 100m, Dx_v/Dt becomes constant in all the directions (see Fig 92) because the wake region is slightly arised at end of the capsule is shown in Fig 91.

For instance, when MSV flies at high Mach number, a strong bow shock detaches in front of the entry vehicle and dominates the forebody flow field. In particular, the higher the Mach number and Angle of Attack (α), shock layer is narrower (see Fig 95) whereas lowers the Mach number, the shock layer is less narrow (see Fig 93). There is a strong bow shock wave detaches at the 1.5m from front end of the MSV due to increase in Mach number. The shock waves are wider at sides of the MSV at Mach

number between 1.94 and 10 At $\alpha=0^\circ$. The bow shock is wider at the front end of the capsule. At the rear end of the capsule shock wave is narrow.

The numerical data is analysed by taking samples from five different locations of space capsule as shown in Fig 94.

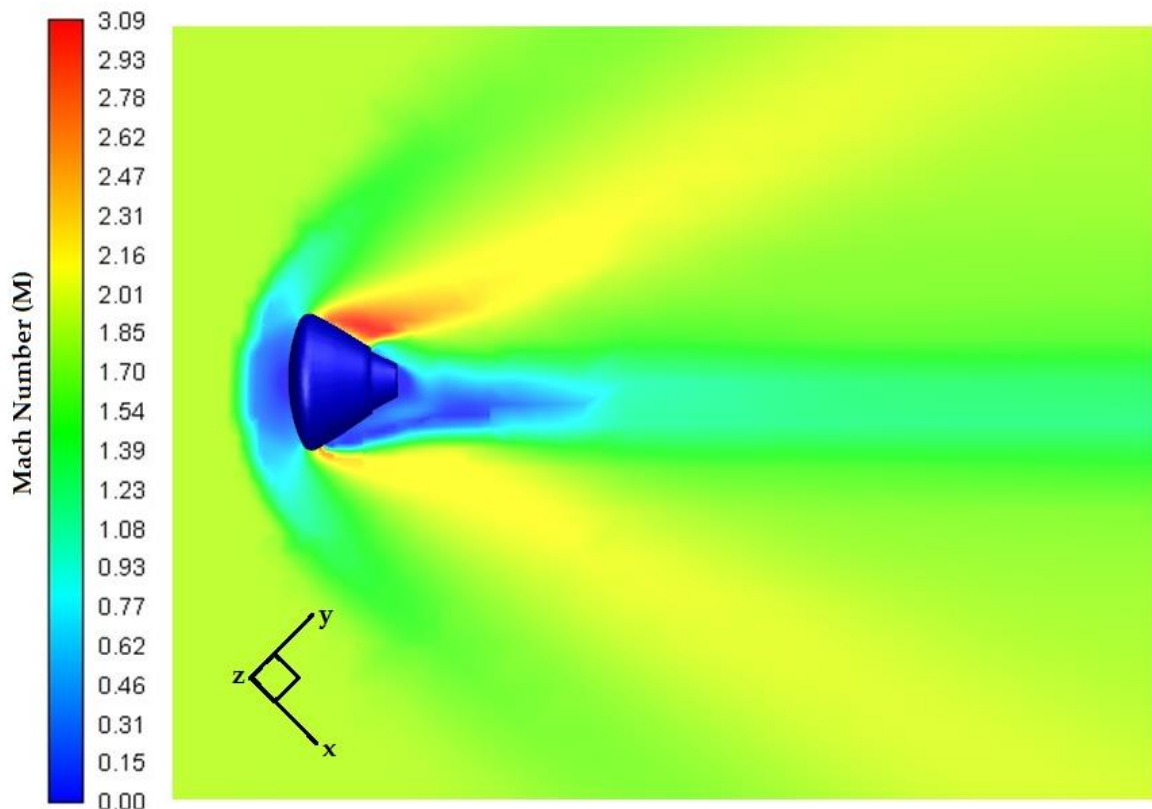


Fig 93. Velocity-Mach number contour for MSV Capsule at $\alpha = 2^\circ$ and $M=1.94$

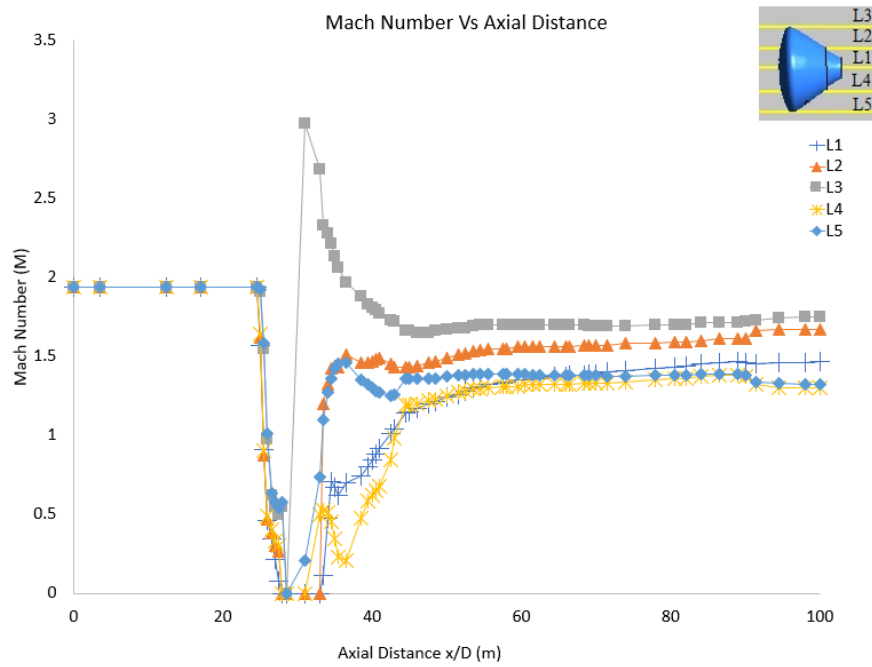


Fig 94. Velocity-Mach number along the domain axial distance at $\alpha = 2^\circ$, $M = 1.94$ for domain length = 100m

There is a drastic decrease in Mach Number at the beginning of the capsule. The Mach Number increases at the end of the capsule due to strong bow shock as shown in Fig 95.

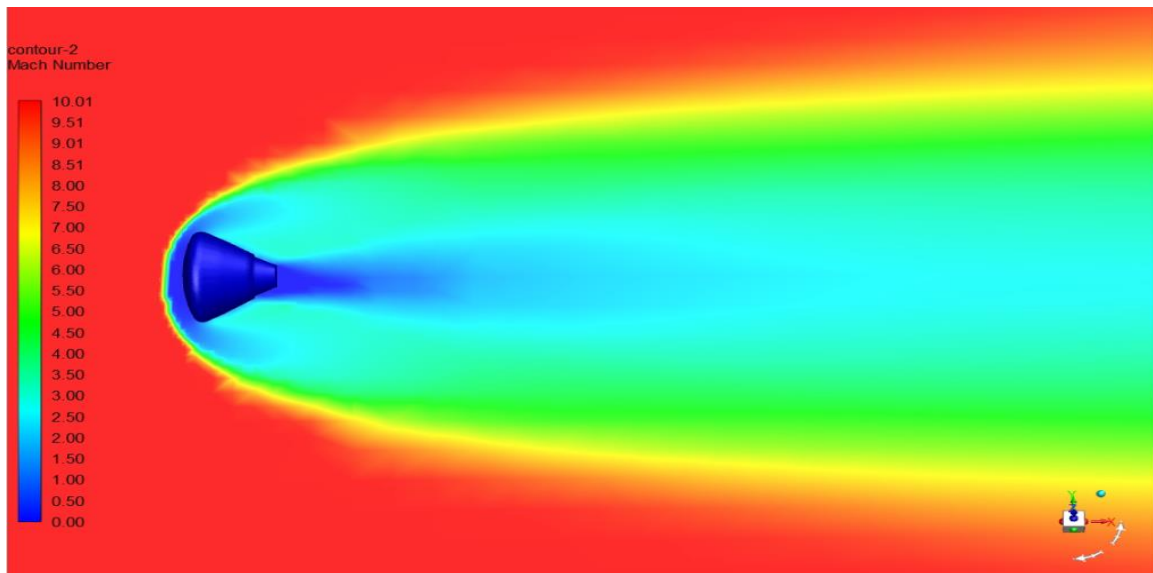


Fig 95. Velocity-Mach number contour for MSV Capsule at $\alpha = 2^\circ$ and $M=10$

The shockwave is wider at front end in the range of $M=10$ whereas the shockwave is narrow at $M=1.94$ as shown in Fig 93 and Fig 95.

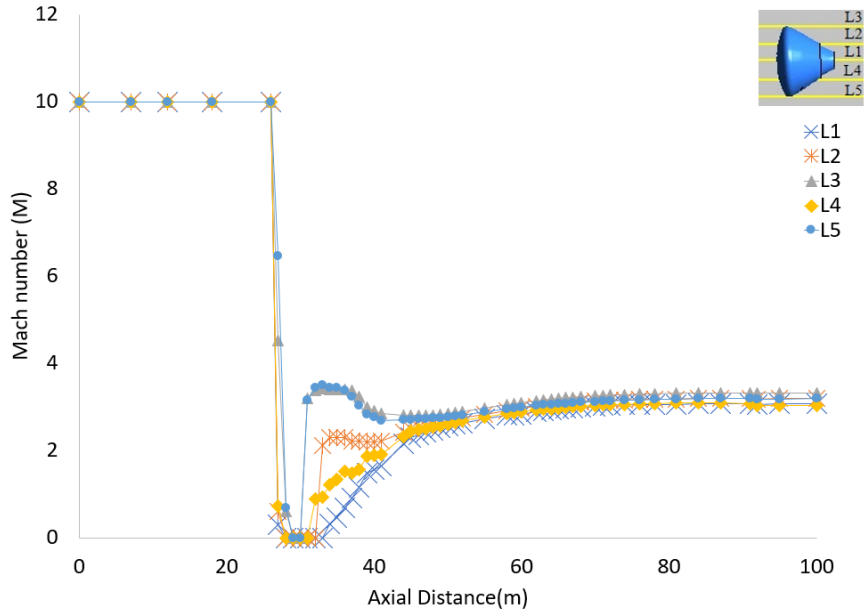


Fig 96. Velocity-Mach Number along the domain axial distance at $\alpha=2^\circ$,

$M = 10$ for domain length = 100m

There is a drastic decrease in Mach number at the beginning of the capsule as shown in Fig 96. The Mach number increases at the end of the capsule due to strong bow shock as shown in Fig 95.

We have the shockwaves from -0.5m to +2.8m in X axis and -6m to +6m in Y-axis for this MSV capsule [25]. In both cases at $\alpha=2^\circ$, the bow shock and oblique shock waves in fore body and also in aft body are arises due to high number of pressures, Mach number, density, and temperature. So, it has been identified as the space capsule travels in right direction with these cases. There all shockwaves are narrower at the rear end of capsule at $M=10$.

CHAPTER 6

THE WAKE AND PARACHUTE DYNAMICS

6.1 Flow around the Schiaparelli Capsule and Parachute

6.1.1 Schiaparelli Capsule

6.1.1.1 Design and Meshing

The 3D model of the Schiaparelli anomaly is shown in Fig 97 which has been designed using the dimensions shown in Fig 1 from Chapter 1. The dimension of domain is 100 m x 20 m x 10 m (see Fig 98). The domain was discretized with a mesh of 1.675 million nodes, as shown in Fig 99.

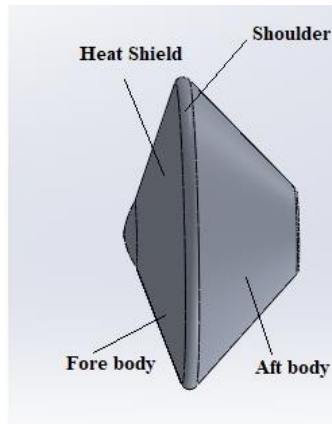


Fig 97. Design of a Schiaparelli EDM

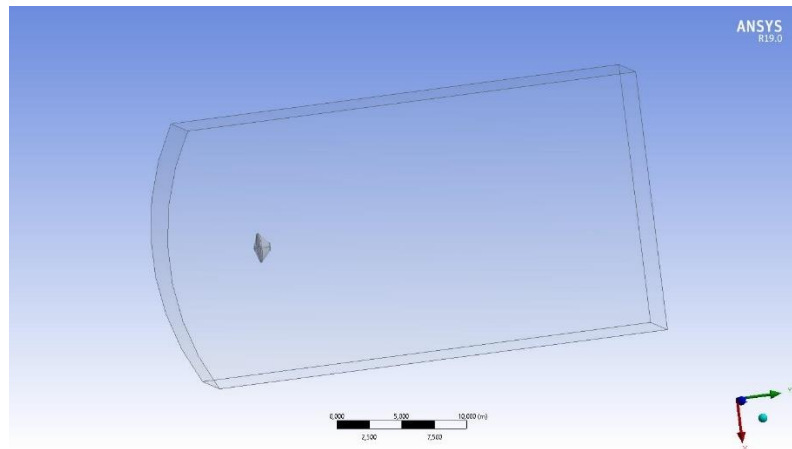


Fig 98. 3D Design of Schiaparelli anomaly with enclosure booleaned

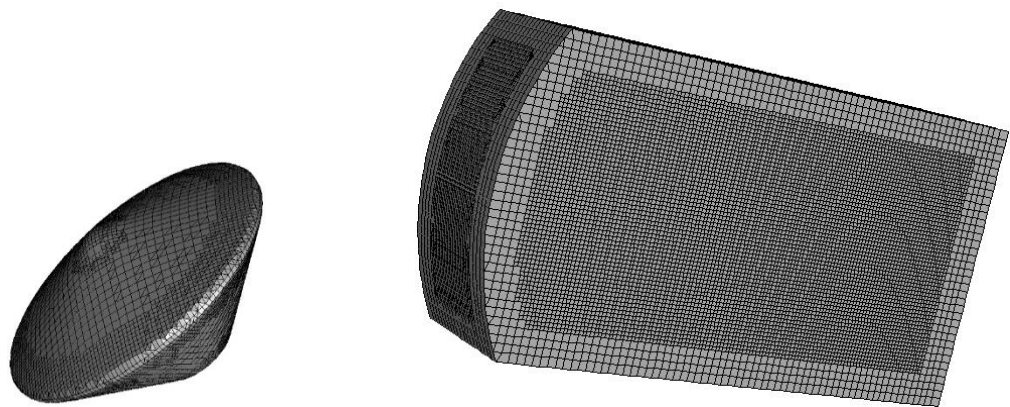


Fig 99. Mesh of the Schiaparelli EDM (a)Capsule (b) Domain at 100m length

6.1.1.2 Boundary Conditions

The simulations of Schiaparelli capsule are done using the boundary conditions based on free stream at H=10km as shown in Table 23.

The SST k- ω method for the turbulent viscosity has been implemented, Sutherland's law of viscosity and ideal gas, courant number is set to 0.5 for simulation.

Table 23: Boundary conditions for Schiaparelli EDM

Zone	Type	Parameters
Inlet	Pressure Far field	At H=10km, $M=2.04814$ $P=250\text{Pa}$ $T=205\text{K}$ (For H= 20km and 50km refer to the values at Table 24) For chemical composition, Species transport Mass fractions: $\text{CO}_2 = 0.9532$ $\text{O}_2 = 0.00174$ $\text{N}_2 = 0.0028$ $\text{CO} = 0.000747$ $\text{H}_2\text{O} = 0.0003$ $\text{Ar} = 0.0017$
Wall	Wall	-

6.1.1.3 Validation of Results

The Supersonic flow around the capsule has a strong compressible effect due to the small blunt nose radius of the vehicle causing a strong bow shock detachment ahead of the capsule. which in turn has a drastic effect in the rise of pressure and temperature with the maxima inside the bow shock region till the surface of the capsule. There is a

strong bow shock wave detaches at the front end of the Schiaparelli EDM due to increase in Pressure. The shock wave extends till the shoulder of the capsule deflecting the flow at wide radius. The immediate drop in the pressure is observed at the leeside of the aft body. The pressure contours of a symmetric plane all along the domain length along with the surface pressure of the capsule at $H = 10\text{km}$ above mars is shown in Fig 100.

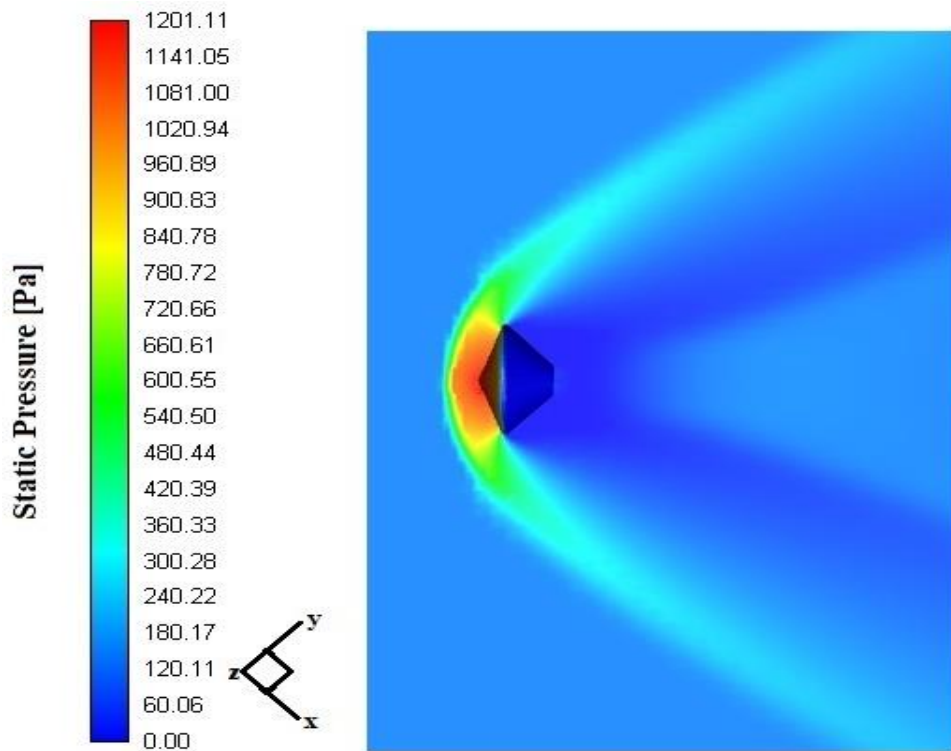


Fig 100. Static pressure contour of Schiaparelli EDM at $H = 10\text{km}$ (from Table 24) above mars at $\alpha = 0^\circ$

To analyse the effect of the hypersonic compressible flow in terms of static pressure, a numerical investigation with the freestream conditions described in Table 23 is carried out all along the length of the computational domain. The samples are drawn from five different locations (L1, L2, L3, L4 and L5) equally spaced from the centre in the direction of flow as shown in the Fig 101. The results show that the pressure of the flow continues to be constant until it reaches the forebody of the capsule. Due to the detachment of the bow shock at $H=10\text{km}$ and $\alpha = 0^\circ$, the pressure is raised to the

approximate value of 1201.11 Pa and decreased to 780.72 Pa at the centre of the capsule surface and the bow shock as well is shown in Fig 100. Amidst the peak value at the surface centre, the surface pressure decreases gradually reaching an approximate value of 180.17 Pa (see Fig 100).

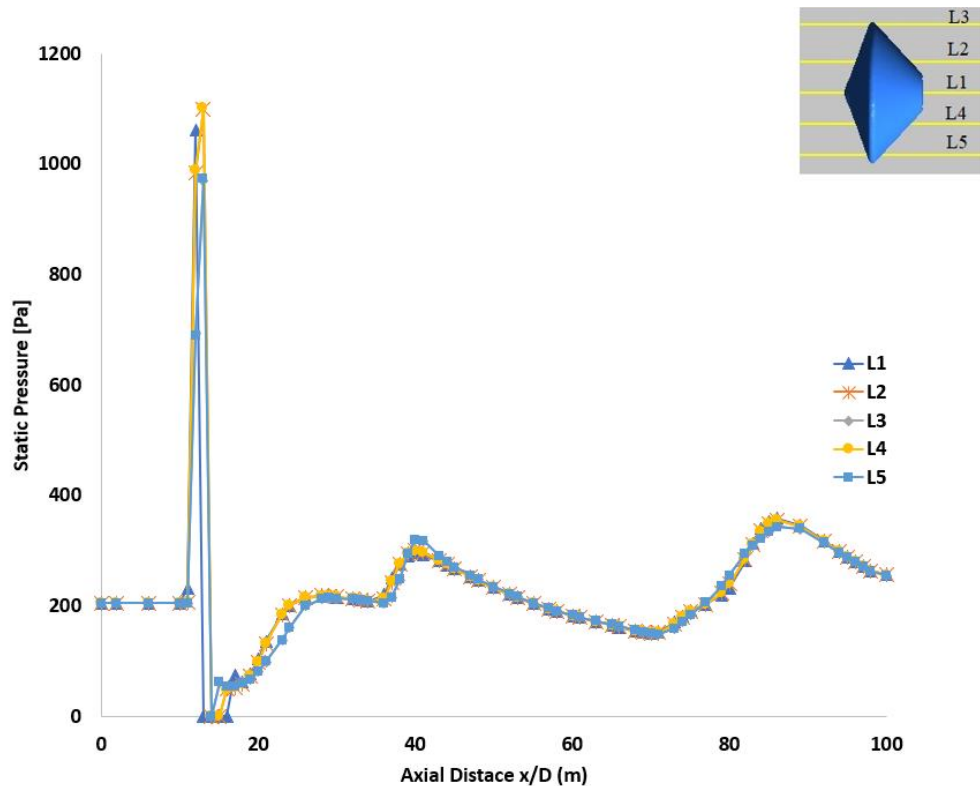


Fig 101. Static pressure along the domain axial distance at H= 10km above mars, $\alpha = 0^\circ$

for domain length = 100m

Fig 101 shows that there is a drastic increase in pressure at the beginning of the capsule. The Pressure become zero after the capsule. The pressure again increases slightly and becomes constant. At $H=10\text{km}$ and $\alpha = 0^\circ$, the peak value of pressure observed in the line L4 is 1101.57 Pa which is the maximum pressure among all the lines L1, L2, L3 and L5. The peak value of pressure observed in the line L1 is observed as 1061.41 Pa. The peak value of pressure observed in the line L2 is 1098.24 Pa. The peak value of pressure is observed in the line L3 is 969.05 Pa. The peak value of pressure observed in the line L5 is 973.497 Pa (see Fig 101).

The density contour gives an insight view about the changes in the gas phase of a supersonic flow when compressed due to the interaction with the blunt body vehicle. The shock wave detached due to the vehicle's resistance towards the high velocity flow causes a change in the density of the gas around it. There is a strong bow shock detaches at the front end of the Schiaparelli EDM, there is increase in density. The shockwave is wider at the rear end of the capsule. The density of the gas is observed maximum at the nose portion of the vehicle which immediately drops at the leeside of the afterbody. The flow gets deflected after the shoulder due to the wide deflection angle. The flow is recirculated until several body diameters. The flow and recirculation can be observed even at 57.5 m distance from the afterbody. Fig 102 shows the density contour at 10km above mars for varying domain length.

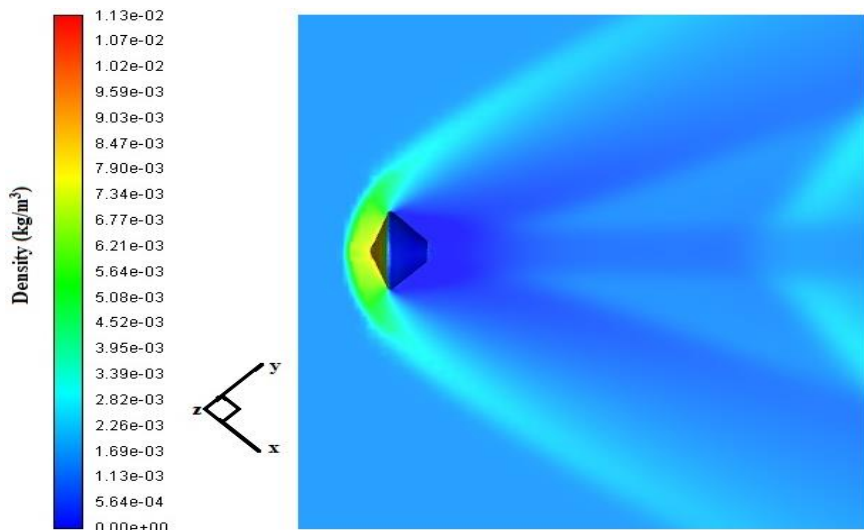


Fig 102. Density contour of Schiaparelli EDM at $H = 10\text{km}$ (from Table 24) above mars at $\alpha = 0^\circ$

The numerical data is analysed by taking the samples from five different locations equally spaced from centre as shown in the Fig 103.

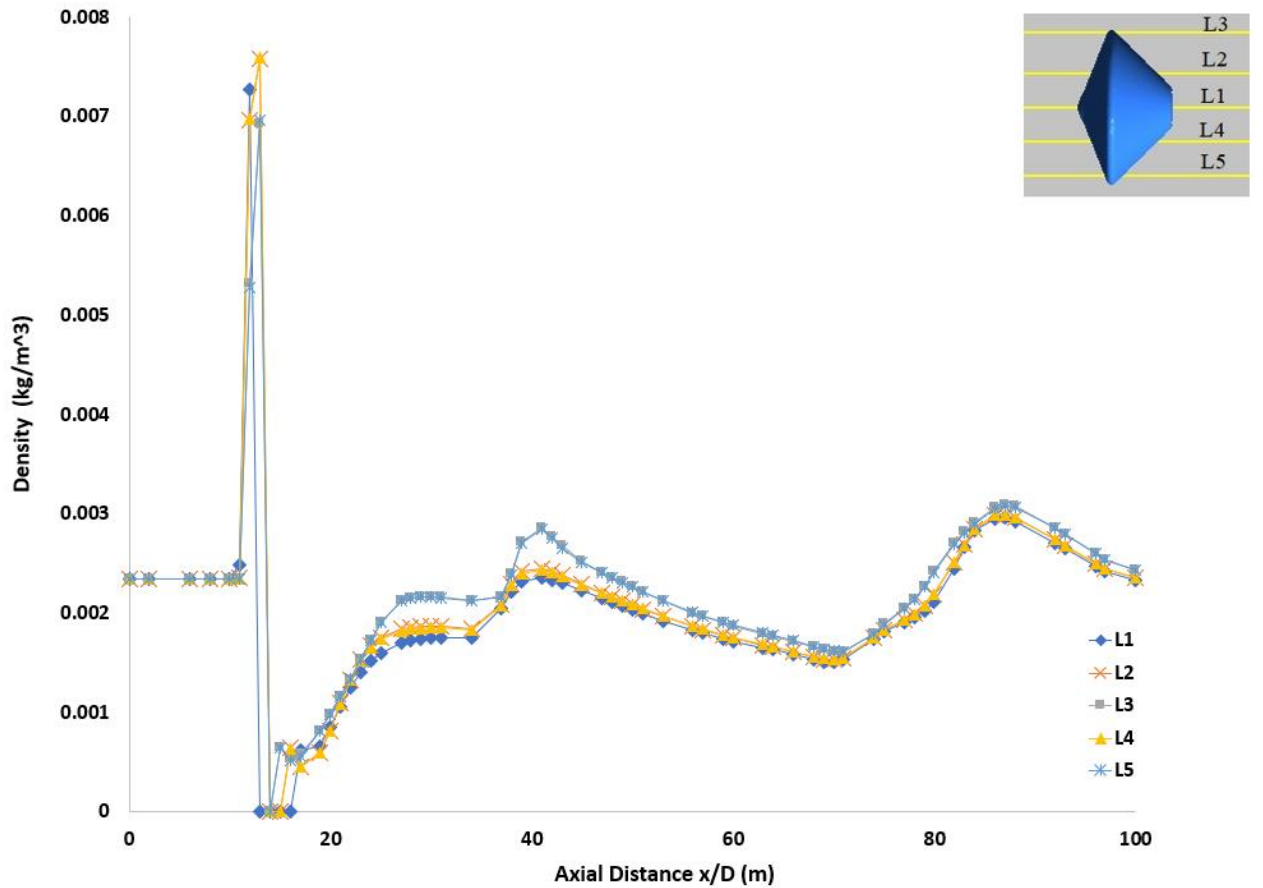


Fig 103. Density along the domain axial distance at $H= 10\text{km}$ above mars, $\alpha = 0^\circ$

for domain length = 100m

Although the details of the flow vary with Mach numbers and angle of attacks in freestream conditions, the general features remain the same. For instance, when the Schiaparelli flies at low Mach number, a strong bow shock detaches in front of the entry vehicle and dominates the forebody flow field. In particular, the lower the Mach number and Angle of attacks, the narrower the shock layer. It shows the Schiaparelli travels in straight path.

At $H= 10\text{km}$ and $\alpha = 0^\circ$, The peak value of density is obtained in the line L4 is 0.007587 kg/m^3 which is higher among all the lines of directions L1, L2, L3 and L5 (see Fig 103). The peak value of density is obtained in the line L1 is 0.007276 kg/m^3 . The peak value of density obtained in the line L2 is 0.007585 kg/m^3 . The peak value of

density is obtained in the line L3 is 0.006921 kg/m^3 . The peak value of density is obtained in the line L5 is 0.006958 kg/m^3 (see Fig 103).

Fig 104 shows the effect of supersonic flow in the computational domain of different lengths and with different angle of attacks of the Re-entry capsule. There is a bow shock wave detaches at the 1.5m from front end of the Schiaparelli EDM due to decrease in Mach number. The shock waves are wider at lee side of the Schiaparelli EDM at high Mach number. At the rear end of the capsule shock wave is narrow. The numerical data is analysed by taking samples from five different locations of space capsule as shown in Fig 105 that Mach numbers at all locations are decreases till 25m and varied till 100m.

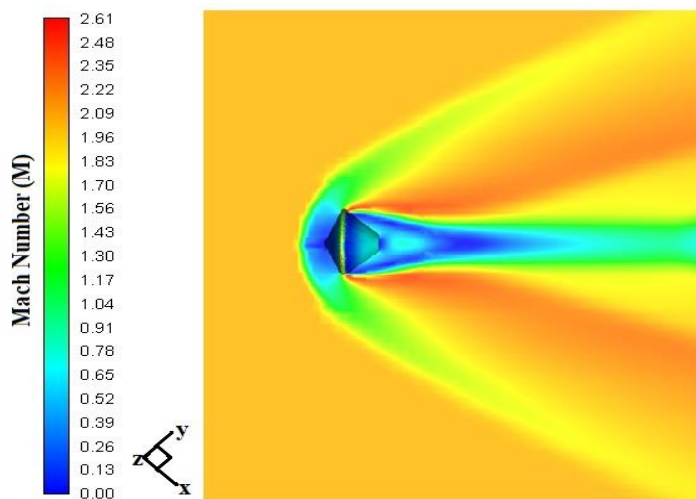


*Fig 104. Velocity-Mach number contour of Schiaparelli EDM at $H = 10\text{km}$ (from Table 24)
above mars and $\alpha = 0^\circ$*

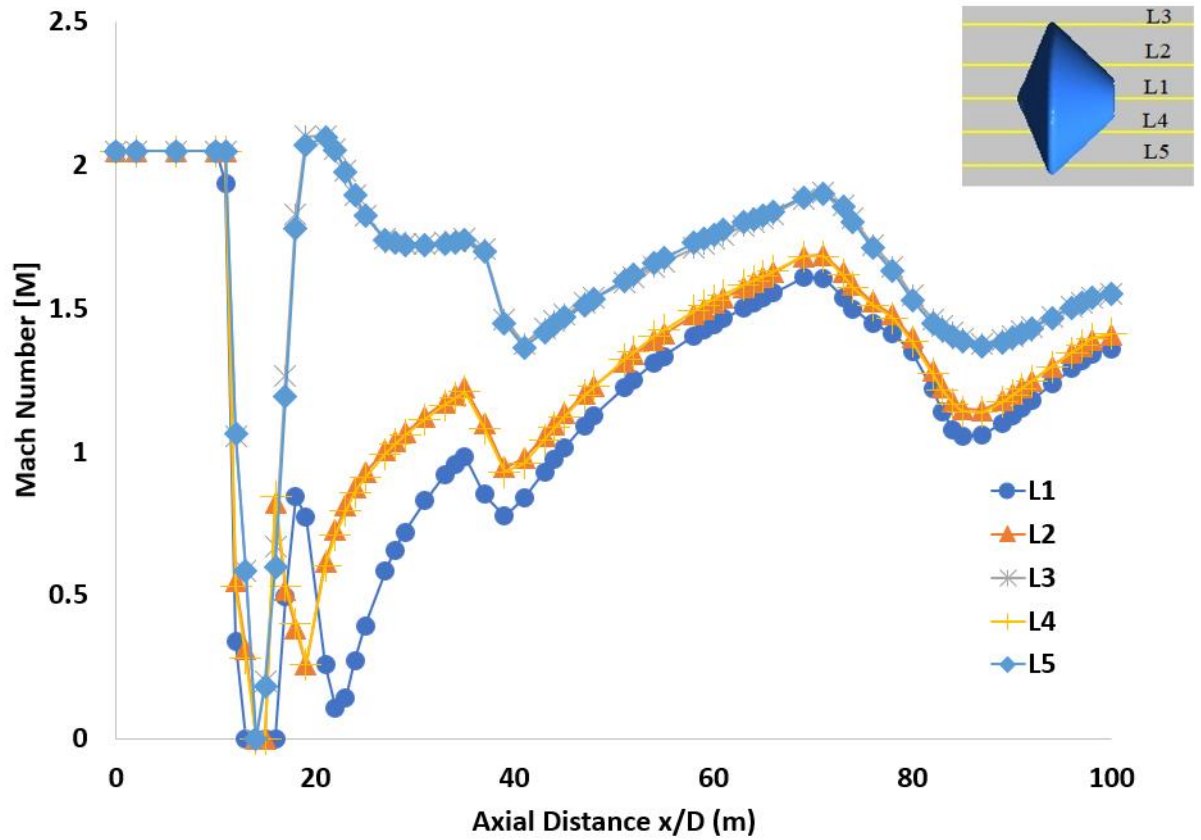


Fig 105. Velocity -Mach Number along the domain axial distance at $H= 10\text{km}$ above mars,
 $\alpha = 0^\circ$ for domain length = 100m

Even though the capsule flows at straight path, the shock layer is narrower at rear end of the capsule and the detachment of bow shock is wider at front end of the capsule due to increase in temperature from as 316.36K to 346.87K is shown in Fig 106.

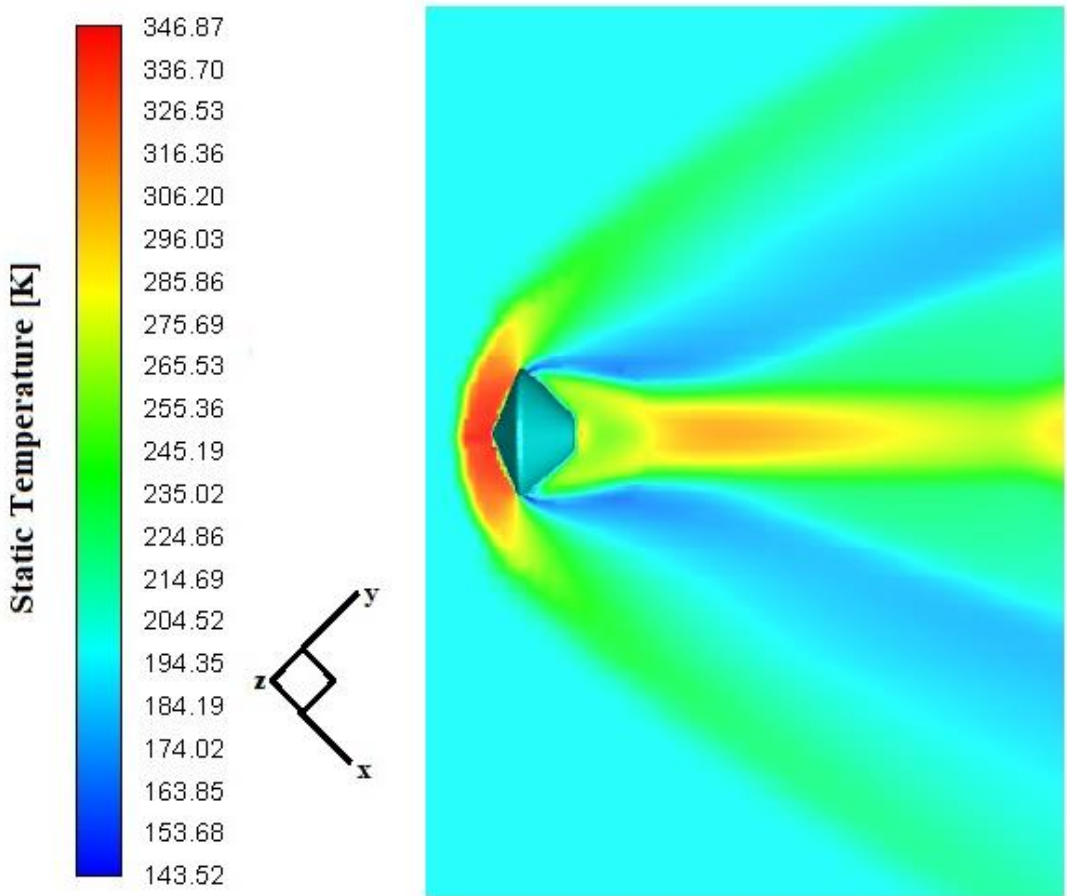


Fig 106. Static temperature contour of Schiaparelli EDM at H=10km (from Table 24) above mars and $\alpha=0^\circ$

The numerical investigation of the temperature at the various portions of the space capsule is shown in Fig 107. At H =10km There is increase in temperature at peak level of 1098.24 K(T_1) at L2 among all line of directions L1, L3, L4 and L5 (see Fig 107). The temperature at peak level is 342.06 K at the line L1. The peak temperature is observed in the line L3 is 328.205 K. The peak temperature is observed in the line L4 is 340.33 K. The peak temperature observed in the lines L5 is 327.95 K (see Fig 107).

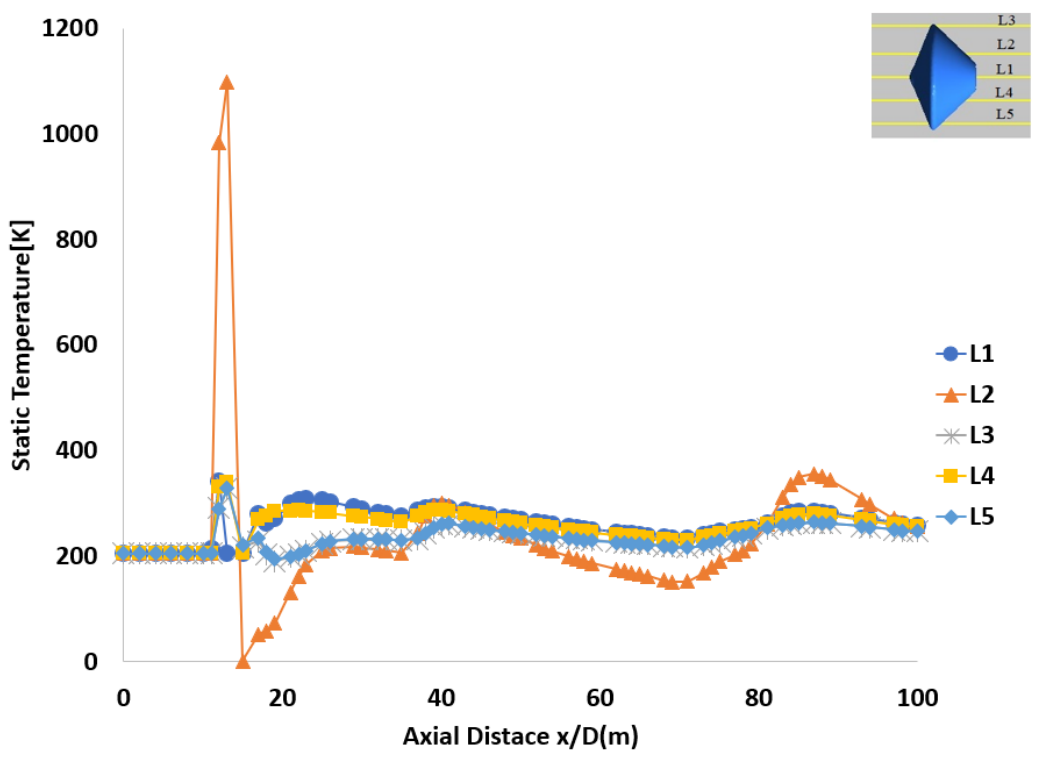


Fig 107. Static Temperature along the domain axial distance at $H= 10\text{km}$ above mars, $\alpha=0^\circ$ for domain length = 100m

6.1.2 Parachute of Schiaparelli

6.1.2.1 Design and Meshing

The parachute of a Schiaparelli Re-entry anomaly has been modelled using Ansys design modeler software with a given dimensions as shown in Fig 1 and Table 2 is shown in Chapter 1. The domain is 100 m length and 50m diameter (see Fig 108).

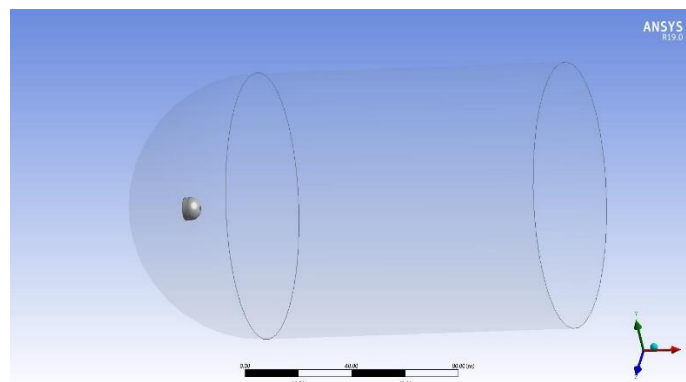


Fig 108. Design of the parachute

The parachute of a Schiaparelli EDM has been meshed with nodes of 113000 million mesh count using tetrahedral mesh and converted into polyhedral mesh using Fluent is shown in Fig 109.

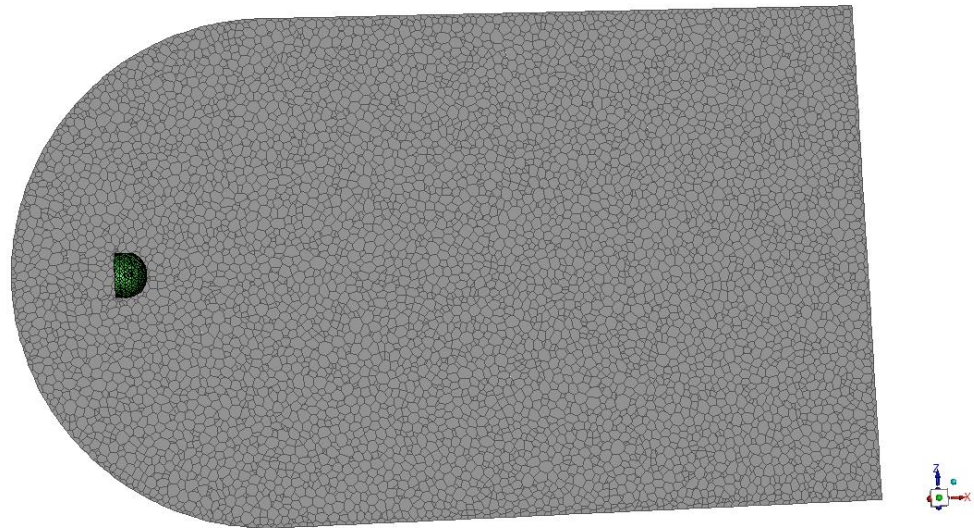


Fig 109. Mesh of the parachute

6.1.2.2 Validation of Results

The supersonic flow around the parachute of a Schiaparelli has a strong compressible effect causing a strong bow shock detachment ahead of the parachute which in turn has a drastic effect in the rise of pressure and temperature with the maxima inside the bow shock region till the vent hole of the parachute. There is a strong bow shock wave detaches at the front end of the parachute due to increase in pressure. The shock wave extends till the shoulder of the capsule deflecting the flow at wide radius. The immediate drop in the pressure is observed at the sides and aft body of a parachute as same as capsule due to pulsation. The pressure contours of a symmetric plane all along the domain length along with the surface pressure of the capsule at $H = 10$ km above mars is shown in Fig 110. The maximum pressure observed is 5545.86 Pa in shockwave at front end of parachute whereas the minimum pressure is observed as 277.29 Pa at sides and aft body of parachute.

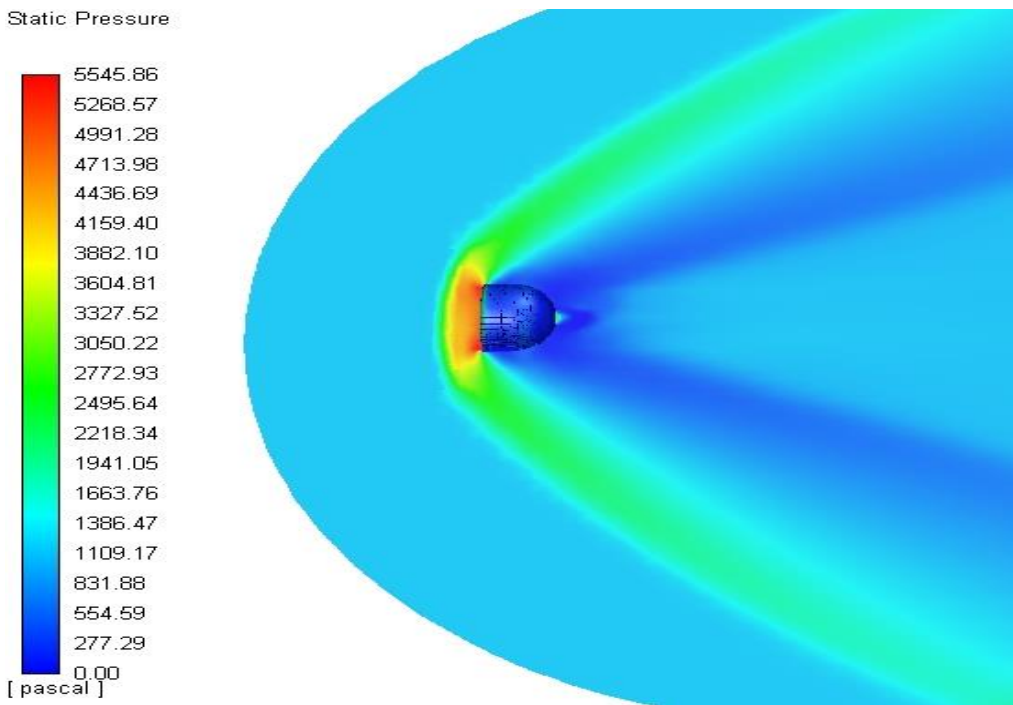


Fig 110. Static pressure contours of the parachute at $\alpha=0^\circ$, $H = 10$ km above mars

The lines are drawn from five different locations ($L1(0m)$, $L2(0.5m)$, $L3(1m)$, $L4(-0.5m)$, $L5(-1m)$) equally spaced from the centre in the direction of flow as shown in the Fig 111. The results show that the pressure of the flow continues to be constant until the parachute deploys. Due to the detachment of the bow shock at $H=10$ km and $\alpha = 0^\circ$, the pressure is raised to peak level at the approximate value of 7175.26 Pa (see Fig 111) in the front of the parachute and the bow shock as well. The pressure at approximate value of 2000 Pa at the vent hole of the parachute at Amidst the peak value at the surface centre, the surface pressure decreases gradually reaching an approximate value of 3000 Pa as the less pressure at the shoulders. At $H=10$ km and $\alpha = 0^\circ$, the peak value of pressure observed in the line $L4$ is 7175.261 Pa which is the maximum pressure among all the lines $L1$, $L2$, $L3$ and $L5$. The peak value of pressure observed in the line $L1$ is observed as 7074.088 Pa. The peak value of pressure observed in the line $L2$ is 6998.202 Pa. The peak value of pressure is observed in the line $L3$ is 4882.974 Pa. The peak value of pressure is observed in the line $L5$ is 6447.49 Pa (see Fig 111).

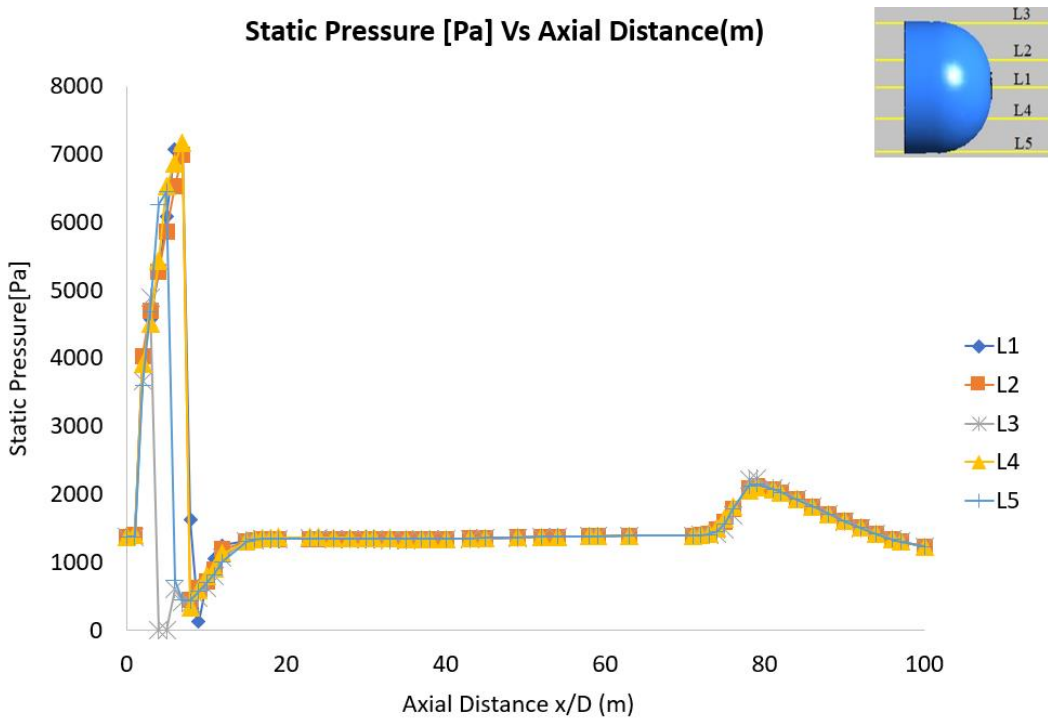


Fig 111. Static Pressure along the domain axial distance at H= 10km above mars at $\alpha=0^\circ$ for domain length = 100m

The density contour gives an insight view about the changes in the gas phase of a supersonic flow when compressed due to the interaction with the annular parachute of Schiaparelli EDM. The shock wave detached due to the parachute's resistance towards the high velocity flow causes a change in the density of the gas around it. There is a strong bow shock detaches at the front end of the parachute, there is increase in density. The shockwave is wider at the rear end of the parachute. The density of the gas is observed maximum at the front of the parachute which immediately drops at the leeside of the afterbody. The flow gets deflected after the shoulder due to the wide deflection angle. The flow is recirculated until several body diameters. The flow of recirculation and deployment can be observed even at 80 m distance from the afterbody. Fig 112 shows the density contour at H=10km above mars for varying domain length.

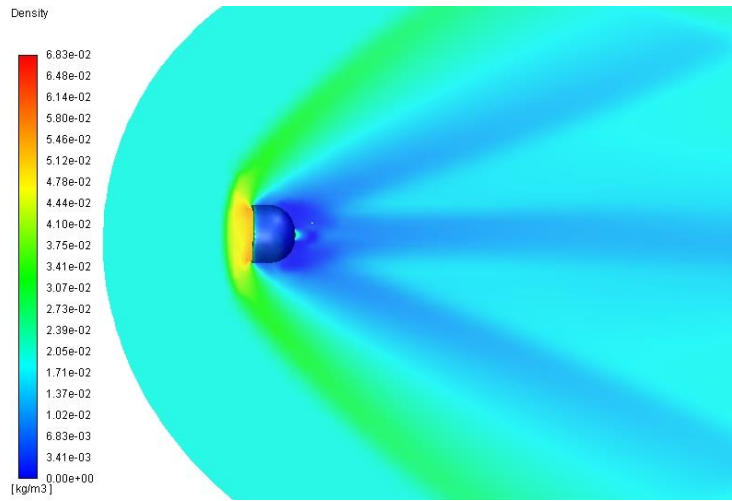


Fig 112. Density Contours of the Parachute at $\alpha = 0^\circ$, $H = 10\text{km}$ above mars

The numerical data is analysed by taking the samples from five different locations equally spaced from centre as shown in the Fig 113.

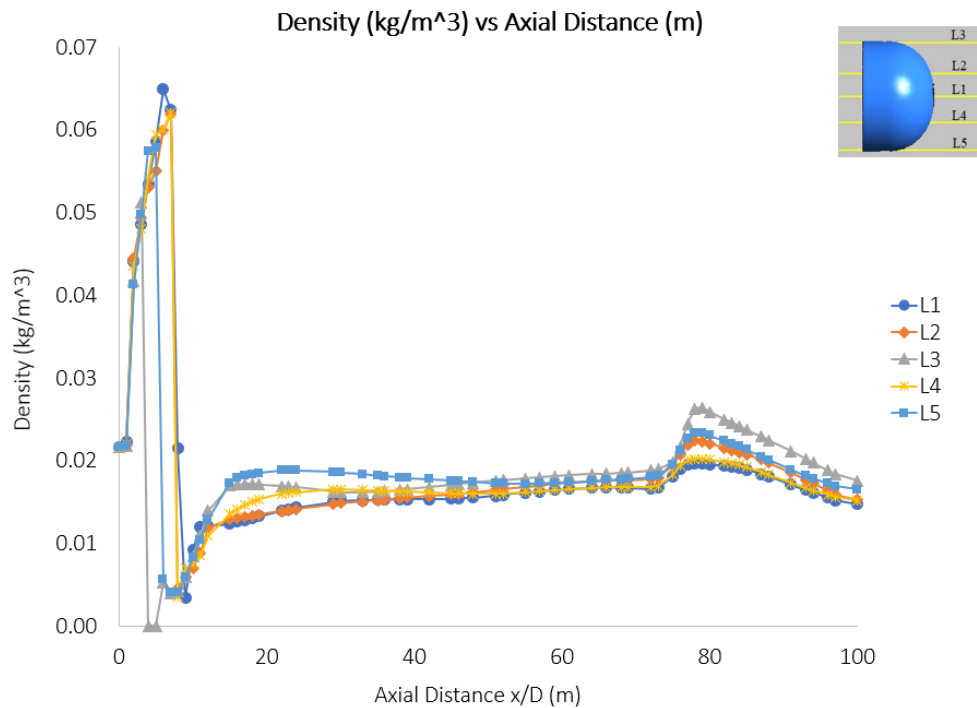


Fig 113. Density along the domain axial distance for at $H = 10\text{km}$ above mars, $\alpha = 0^\circ$ for domain length = 100m

Although the details of the flow vary with angle of attacks and freestream conditions, the general features remain the same. For instance, when the parachute pulsates at 10km altitude, a strong bow shock detaches in front of the entry parachutes and

dominates the forebody flow field. In particular, the lower the Mach number and angle of attack, the narrower the shock layer. It shows the parachute pulsates in straight path.

Fig 113 shows the effect of hypersonic flow in the computational domain of different lengths and with different angle of attacks of the Re-entry parachutes. There is a strong bow shock wave detaches at the 1.5m from front end of the parachute EDM due to supersonic flow. The shock waves are wider at canopy of the parachute at high Mach number. The bow shock is wider at the front end of the parachute. The shockwave is narrower after the vent hole of the canopy. At $H = 10\text{ km}$ and $\alpha = 0^\circ$, The peak value of density is obtained in the line L1 is 0.064909 kg/m^3 which is higher among all the lines of directions L2, L3, L4 and L5 (see Fig 113). The peak value of density is obtained in the line L2 is 0.06189 kg/m^3 . The peak value of density is obtained in the line L3 is 0.05125 kg/m^3 . The peak value of density is obtained in the line L4 is 0.06202 kg/m^3 . The peak value of density is obtained in the line L4 is 0.05778 kg/m^3 (see Fig 113).

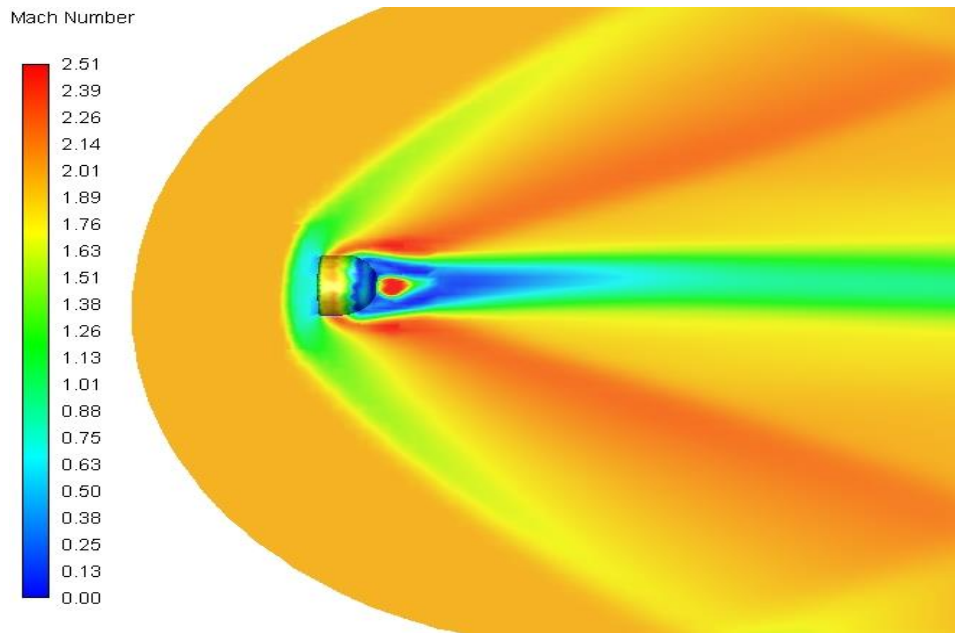


Fig 114. Velocity-Mach Number Contours of the Parachute at $\alpha=0^\circ$, $H = 10\text{km}$ above mars

At $H=10\text{km}$ and $\alpha=0^\circ$, There is a strong shockwave detached at front end of the parachute at 2m distance is shown in Fig 114. There is a jet wave formed at the vent hole of the capsule and the turbulent wake at aft body of the parachute.

Fig 115 shows the velocity path lines of Re-entry Parachute shows the main topological flow structure of the annular parachute described by the flow pattern around the canopy of the parachute. The high speed of air release from inlet was directly flow toward the inflated parachute. As the air approaching the parachute's stagnation point, the velocity of air was gradually decreased. When the air entered the parachute domain, most of the airflow could not escape or get through the canopy due to solid and non-porous type of parachute. The air was directly passing through the vent hole at the apex while some went along the canopy's surface before separating and leaving at the skirt edge. This phenomenon resulted in a turbulence separation flow [35].

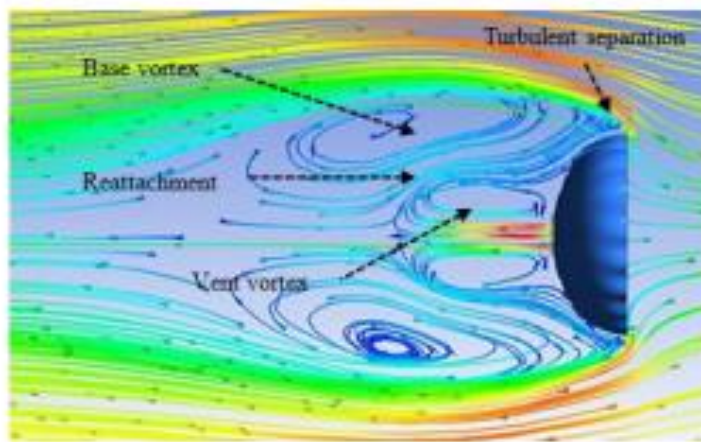


Fig 115. Velocity Pathlines of Parachute Taken from Reference [35]

The numerical data is analysed by taking samples from five different locations of Re-entry parachute as shown in Fig 116. The Mach number is observed as $M=3.42$ while analysing with conditions of $H = 10\text{km}$ at velocity (v)= 228.5m/s .

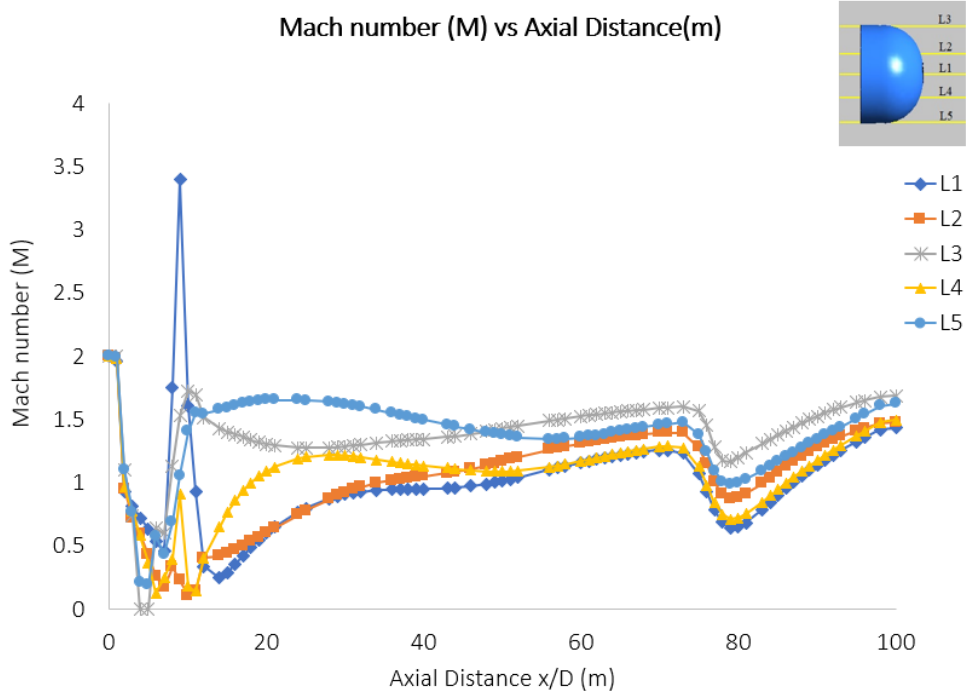


Fig 116. Mach Number along the domain axial distance at $H = 10\text{km}$ above mars, $\alpha = 0^\circ$
for domain length = 100m

Even though the parachute pulsates at straight path, the shock layer is narrower at canopy and bow shock is wider at front end of the parachute due to increase in temperature from as 342.35K to 438.41K is shown in Fig 117.

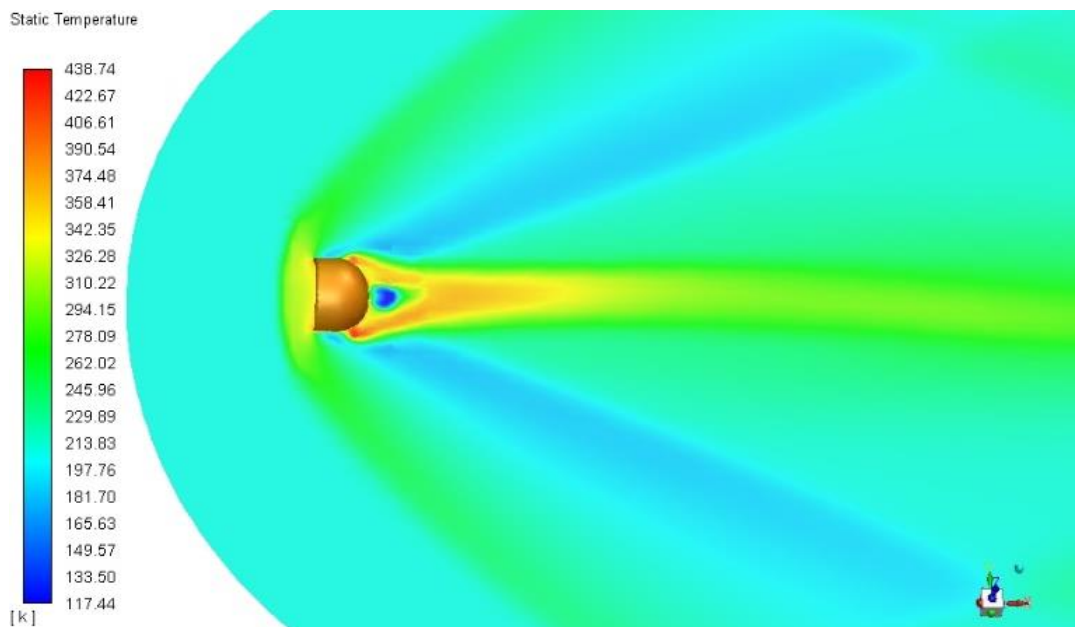


Fig 117. Static Temperature Contours of the Parachute at $\alpha=0^\circ$, H=10km above mars

The numerical investigation of the temperature at the various portions of the space capsule is shown in Fig 118. The observed temperature $H = 10\text{km}$ above mars is 400K above peak level. At $H = 10\text{km}$ and $\alpha = 0^\circ$, There is increase in Temperature at Peak level of 409.37 K at L4 among all line of directions L1, L2, L3 and L5 (see Fig 118). The temperature at peak level is 393.53 K at the line L1. The peak temperature is observed in the line L2 is 392.25 K. The peak temperature is observed in the line L3 is 377.324K. The peak temperature observed in the lines L5 is 385.54 K (see Fig 118).

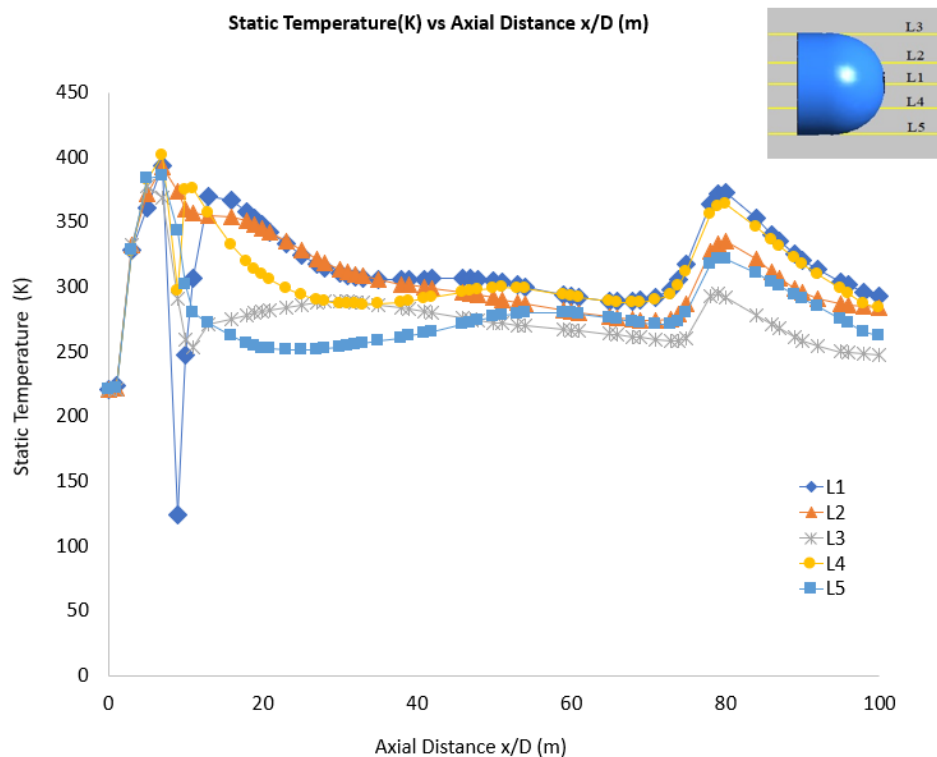


Fig 118 Static temperature along the domain axial distance at $H= 10\text{km}$ above mars, $\alpha = 0^\circ$ for domain length = 100m

6.2 Effect of chemical decomposition

The problematic issue with the design of atmospheric re-entry vehicles is the phenomena of actual gas behaviour, for which non-equilibrium simulations have been done. The activation of molecular modes of vibration, the breakdown of air molecules into their component atoms, and the recombination procedure that results in the creation of new chemical species are some examples of these chemical processes. For

instance, the shock wave created in forebody of vehicle which travels at hypersonic speeds, the temperature of the gas around it has been raised quickly.

It is obvious that the value of cannot be regarded as a constant as temperature rises since the ratio between the specific temperatures relies on the number of active degrees of freedom for the species (perfect gas hypothesis). The gas combination must thus be regarded as being in thermal and chemical nonequilibrium. The thermodynamics of the flow surrounding the vehicle considers the impacts of actual gas in a significant way. For instance, in a flowing gas, thermodynamic equilibrium takes a limited amount of time, known as relaxation time, to establish. The shock wave structure can be significantly impacted by departure from thermodynamic equilibrium, which in turn affects the flow field surrounding the vehicle.

When compared to the flow of the same gas where there is no chemical dissociation, the flow in the shock layer can have a high-density ratio ($\frac{\rho_1}{\rho_2}$) across the powerful bow shock. The shockwave ratio is the main factor that determines the capsule's aerodynamics. According to the forebody of the vehicle, a change in surface pressure leads to a change in aerodynamic properties.

When compared to a flow of the same gas where chemical dissociation doesn't occur, the flow in the shock layer's chemical dissociation can produce a significant density ratio across the powerful bow shock. The shock density ratio has a major role in the aerodynamics of capsules when dissociation is present. A change in the surface pressure pressing on the forebody of Schiaparelli causes the change in aerodynamic properties.

The major influence on the shock shape as well as the standoff distance. Because it varies the pressure at the stagnation point (for instance, C_{pmax}), the shock density ratio change affects the surface pressures:

$$C_{pmax} = C_{pt2} = \frac{P_{t2} - P_\infty}{q_\infty} = \left(\frac{P_{t2}}{P_\infty} - 1 \right) \frac{2}{\gamma M_\infty} \cong 2 - \varepsilon \quad (49)$$

instead of the classical Newtonian value of $C_{pmax} = 2$, where the density ratio across the bow shock wave, ε , in the hypersonic limit reads as

$$\varepsilon = \lim_{M_\infty \rightarrow \infty} \frac{\rho_1}{\rho_2} = \frac{\gamma - 1}{\gamma + 1} \quad (50)$$

These calculations were carried out to evaluate the aerodynamic performance of a Schiaparelli EDM by numerically investigating the flow field past the entering vehicle. In the completely three-dimensional error and Navier stokes equation, both perfect gas and reactive gas with finite rate chemistry modes are employed. All the findings are computed using SST-k- ω viscosity beginning at free stream conditions, which are presented in Table 23 as presumed initial boundary conditions. All simulations are run with the vehicle surface assumed to be a fully catalytic wall and its temperature (T) at radiative equilibrium. During the investigation, the wall temperature is calculated using the Stephen Boltzmann Law and each streamwise station is updated using the Newton Raphson approach. According to the energy balance at the surface of EDM with the Stephen Boltzmann constant(σ),

$$q_w = -\lambda \left(\frac{\partial T}{\partial n} \right) - \rho \sum_i \text{Dim } h_{Di} \left(\frac{\partial y_i}{\partial n} \right)_w = \sigma \varepsilon T_\omega^4 \quad (51)$$

Latter content is determined by the surface catalytic with heat shield transport coefficient for pure species, which is obtained from kinetic theory of semi-empirical principles such as mixing of and. For the diffusion coefficient of the i th species in the reacting mixture, the multicomponent diffusion coefficient is used [24,26,31].

The CFD study of Schiaparelli was preceded by an ESA code validation and been done using existing data with a combination of Ar, CO₂, O₂, N₂, CO, and H₂O found in the Martian atmosphere, but it was performed by adding these gases in ANSYS Fluent 19.0 in mixture species.

6.2.1 CO₂ Mass Fraction

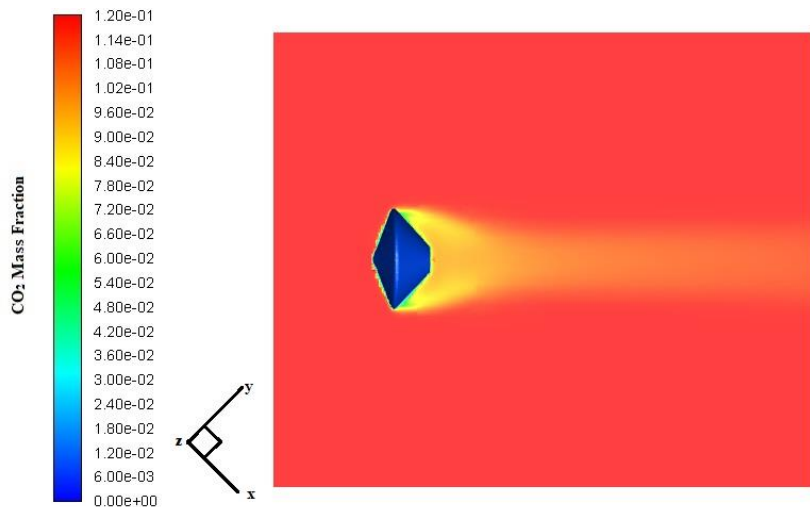


Fig 119. CO₂ mass fraction contour of Schiaparelli EDM at H=20km above mars and $\alpha=0^\circ$

At H = 20km above mars (From Table 24) and $\alpha=0^\circ$, there is a shockwave detached at aft body of the capsule is wider and front end at 0.02m. The whole atmosphere has observed CO₂ mass fraction is 0.12% which is higher, and the medium CO₂ mass fraction is observed is 0.0840 % is shown in Fig 119.

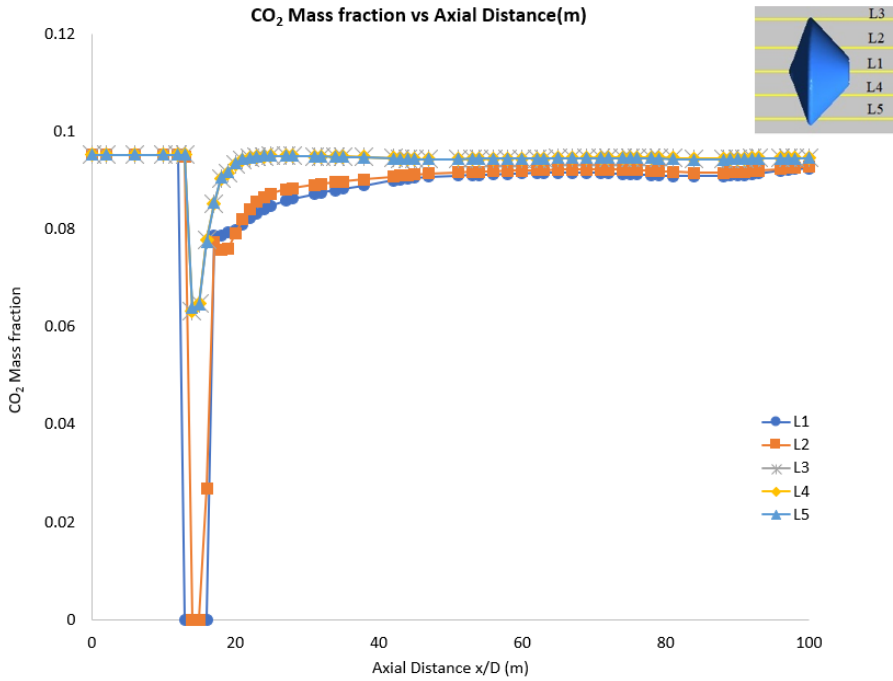


Fig 120. CO₂ mass fraction along the domain axial distance at H= 20km above mars, $\alpha = 0^\circ$ for domain length = 100m

At H = 20km above mars (From table 24) and $\alpha=0^\circ$, when the powerful bow shock detaches at the front end of the re-entry capsule at 0.02m (as shown in Fig 119), the mass fraction remains constant until 12m in L1, L2, L4 and until 13m in L3 and L5. The mass fraction will become zero in L1 from 13m to 16m and 14m to 15m in L2. Finally, the mass of CO₂ grows and drops until it reaches 100m in L3, L4, L5 and increases in L1 and L2 (as shown in Fig 120) as oblique shocks at 0.1m diameter from the sides of the capsule and the formation of a wake at the rear end of the capsule is narrower as shown in Fig 119.

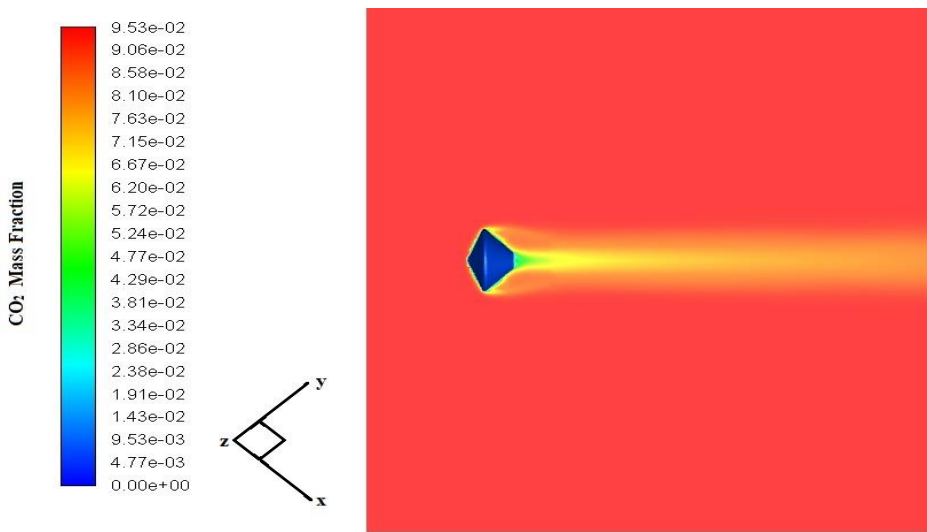


Fig 121. CO₂ mass fraction contour of Schiaparelli EDM at H=50km above mars and $\alpha=0^\circ$

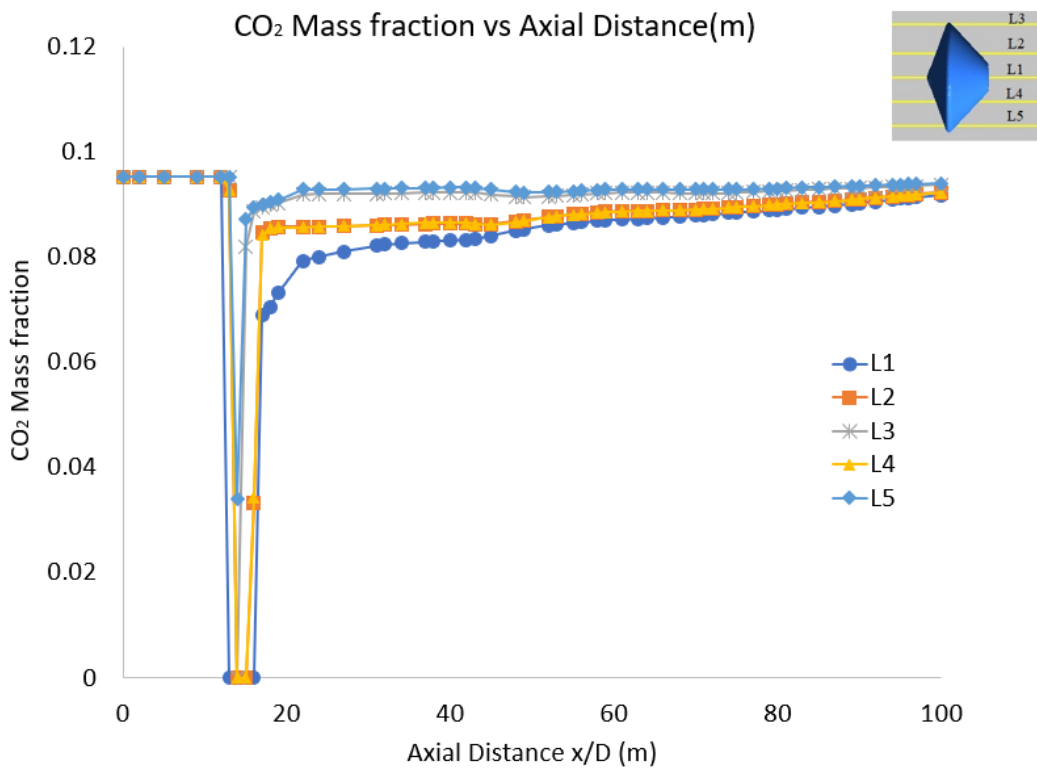


Fig 122. CO₂ mass fraction along the domain axial at H= 50km above mars, $\alpha = 0^\circ$
for domain length = 100m

At H = 50km above mars (From Table 24) and $\alpha=0^\circ$, the mass fraction of CO₂ remains constant until 12m in L1, L2, L4, and 13m in L3 and L5. It is zero from 13m to 16m in L1, 14m to 15m in L2 and L4, and 14m in L3. It expands from 17m to 100m (as seen in

Fig 122) when the wake area emerges at the back end of the capsule, indicating the flow direction in Fig 121.

6.2.2 N₂ Mass Fraction

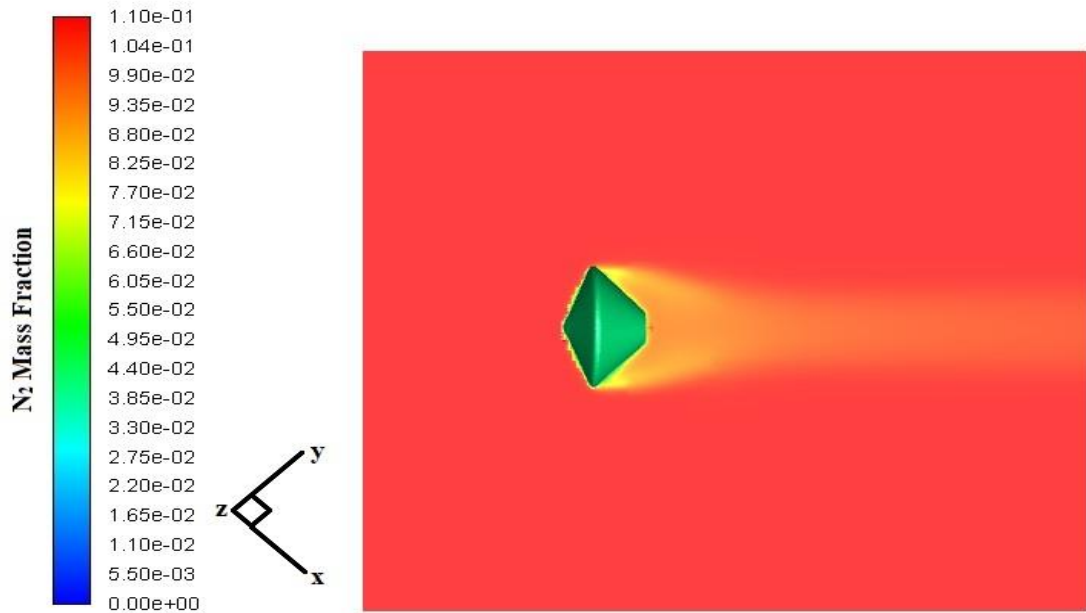


Fig 123. N₂ Mass fraction contour of Schiaparelli EDM at H=20km above mars and $\alpha=0^\circ$

At H = 20km above mars (From Table 24) and $\alpha=0^\circ$, There is a shockwave detached at 0.0013m from forebody of the capsule. The Wake at aft body of the Capsule is narrower. The whole atmosphere has observed N₂ mass fraction is 0.011 which is higher, and the medium N₂ mass fraction is observed is 0.0070 is shown in Fig 123.

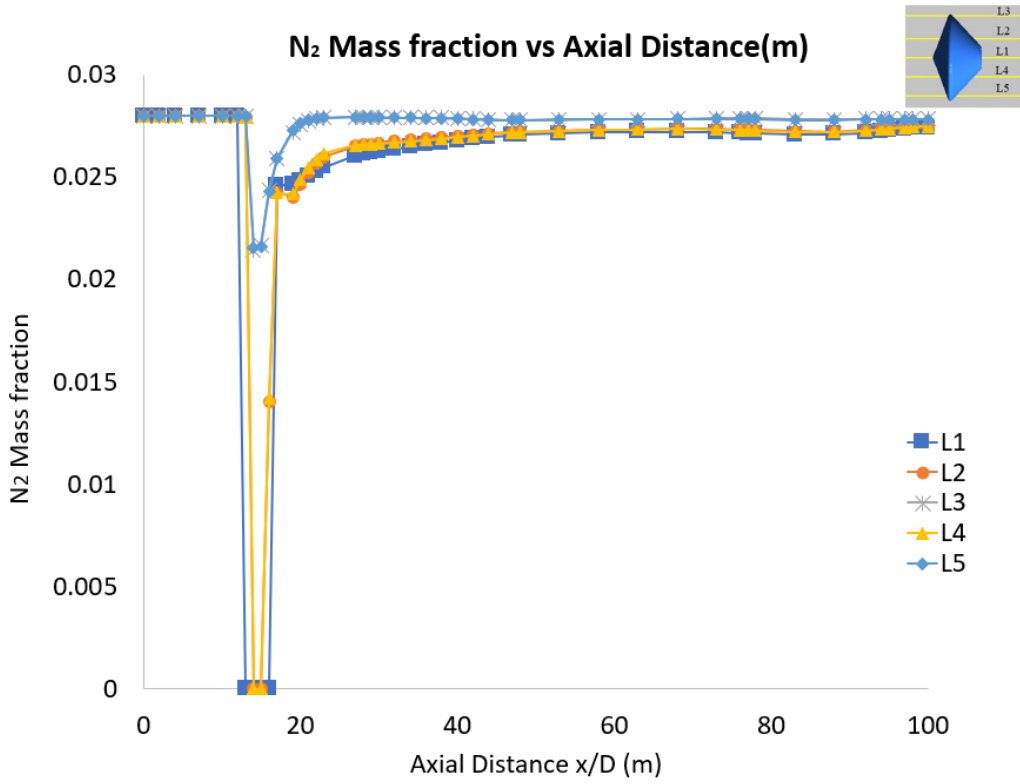


Fig 124. N_2 mass fraction along the domain axial distance at $H= 20\text{km}$ above mars, $\alpha = 0^\circ$ for domain length = 100m

At $H = 20 \text{ km}$ above mars (From Table 24) and $\alpha=0^\circ$, a shockwave rises 0.0001m from the front end of the capsule and extends to the centre of the capsule is shown in Fig 123. So, N_2 mass fraction is constant until 13m in L2, L3, L4, L5 and becomes constant until 12m in L1 before becoming zero from 13m to 16m in L1 whereas N_2 mass fraction is constant until 13m in L2, L3, L4, L5 and becomes constant from 14m to 15m in L2 and L4. Following that, the N_2 mass fraction in L5 grows from 14m to 100m (shown in Fig 124). The N_2 mass percentage only increases (shown in Fig 124) as the wake zone emerges at the back end of the capsule (shown in Fig 123).

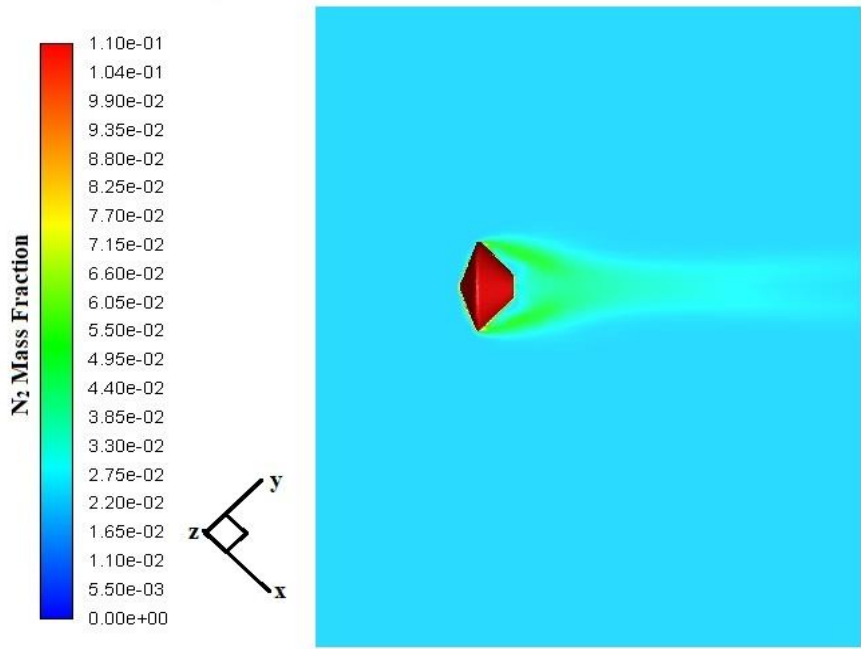


Fig 125. N_2 mass fraction contour of Schiaparelli EDM at $H=50\text{km}$ above mars and $\alpha=0^\circ$

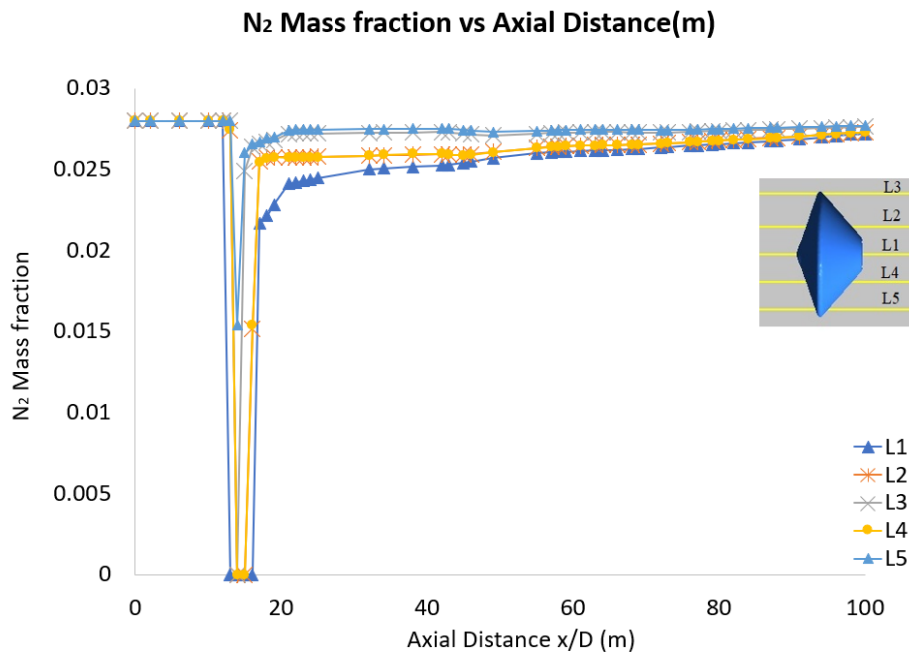


Fig 126. N_2 mass fraction along the domain axial distance at $H= 50\text{km}$ above mars, $\alpha = 0^\circ$ for domain length = 100m

At $H = 50\text{km}$ above mars (From Table 24) and $\alpha = 0^\circ$, when the shockwave gradually rises from the front end of the capsule to the sides (see Fig 125), the N_2 mass fraction

remains constant until 13m in L2, L3, L4, L5, and 12m in L1. It reaches zero between 13m and 16m in L1, 14m to 15m in L2 and L4, and 14m in L4. Because of the wake zone that forms at the rear end of the capsule, all these lines grow and become constant until 100m (as seen in Fig 126).

The observed level of N₂ mass fraction for 20km is 0.0028 (see Fig 126).

6.2.3 Ar Mass Fraction

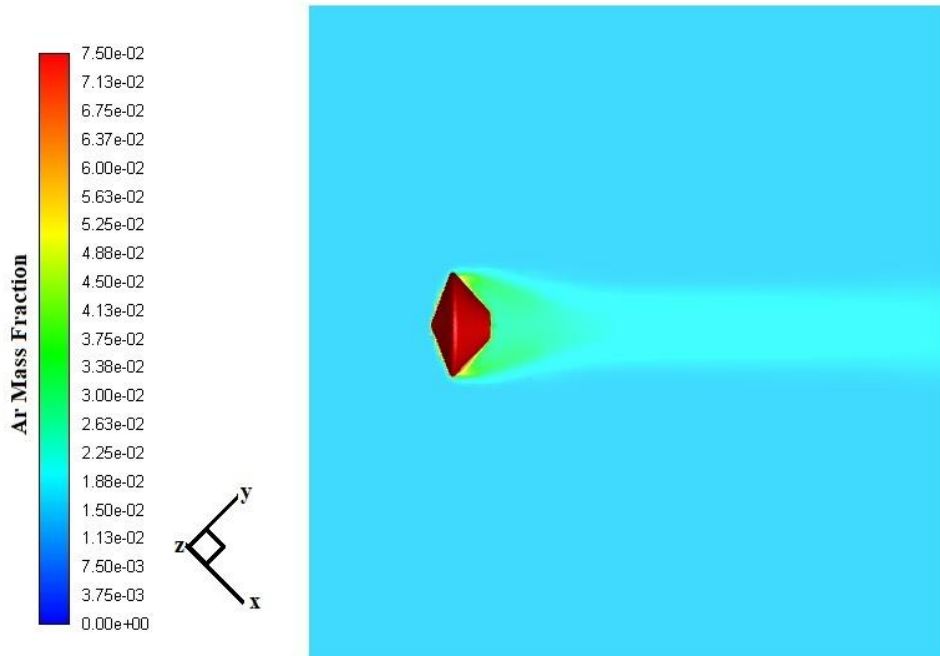


Fig 127. Ar mass fraction contour of Schiaparelli EDM at $H=20\text{km}$ above mars and $\alpha=0^\circ$

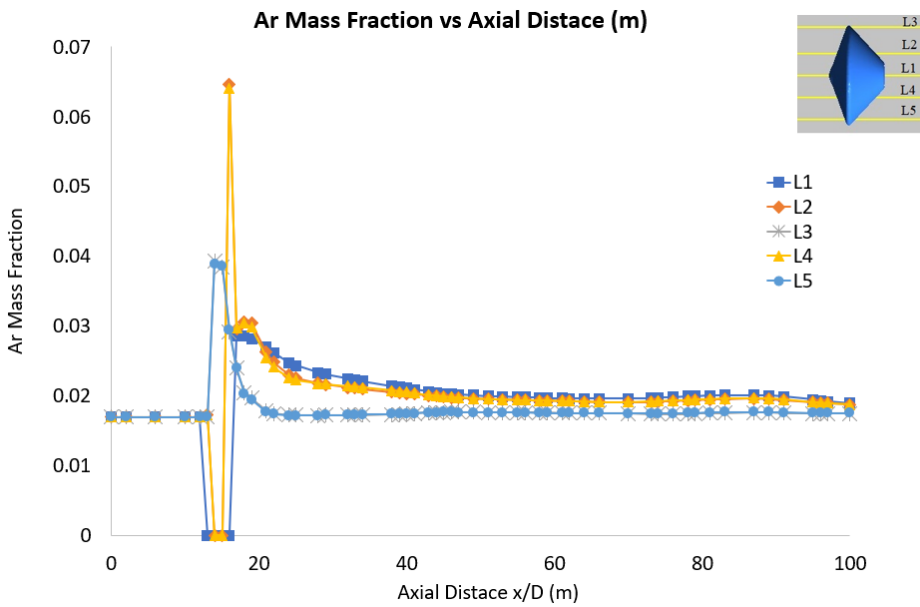


Fig 128. Ar mass fraction along the domain axial distance at $H=20\text{km}$ above mars, $\alpha = 0^\circ$ for domain length = 100m

At $H = 20\text{km}$ above mars (From Table 24) and $\alpha = 0^\circ$, as the powerful shockwave emerges at the sidewalls of the space capsule (as illustrated in Fig 127), the Ar Mass percentage remains constant until 12m in L1 and 13m in L2, L3, L4, and L5 (is shown in Fig 128). The observed level of Ar Mass fraction for 20km is 0.0647 (see Fig 128).

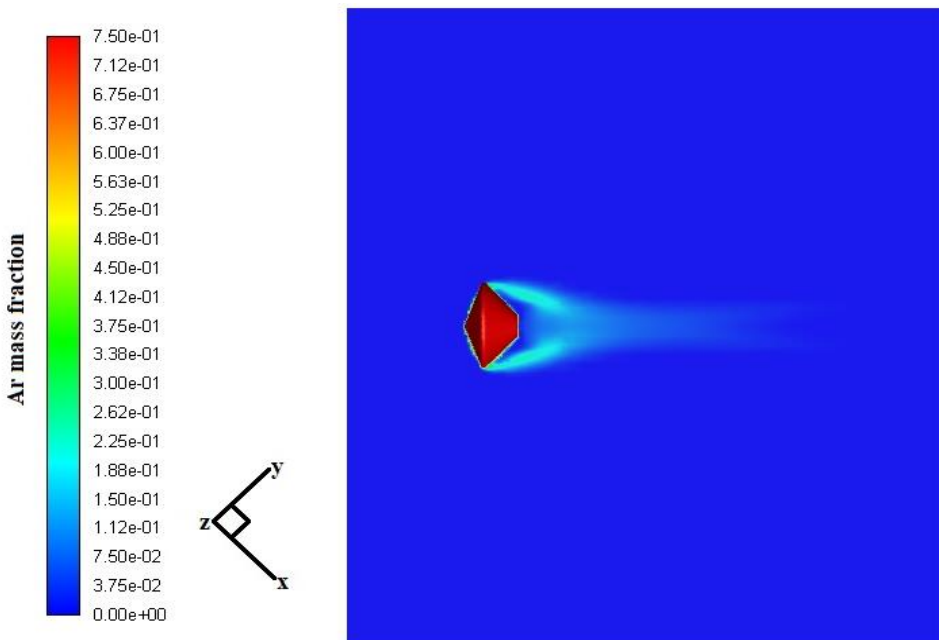


Fig 129. Ar mass fraction contour of Schiaparelli EDM at $H=50\text{km}$ above mars and $\alpha=0^\circ$

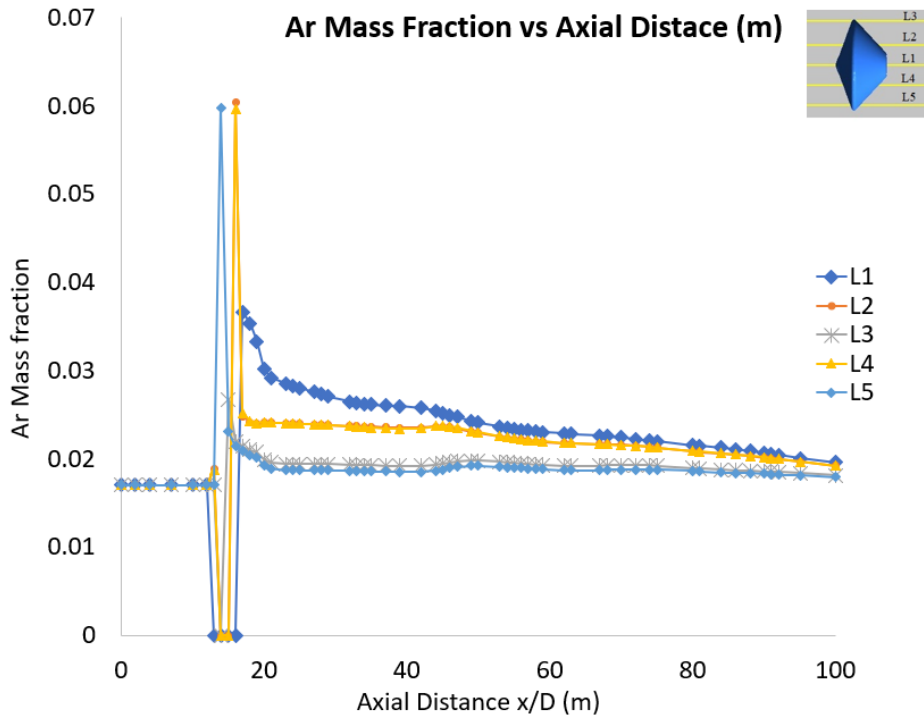


Fig 130.Ar Mass fraction along the domain axial distance at H= 50km above mars, $\alpha = 0^\circ$ for domain length = 100m

At $H = 50\text{km}$ above mars (From Table 24) and $\alpha = 0^\circ$, the Ar mass remains constant until 12m in the line of directions L1, L2, L4 and 13m in L2 and L5 (see Fig 130) when the powerful shockwave emerges at the front end of the capsule at 0.0001m (shown in Fig 129). Following that, the Ar Mass fraction grows and drops from 17m to 100m in L1, and then climbs and lowers again till 100m (shown in Fig 130) due to the formation of a significant wake zone behind the rear end of the capsule, as seen in Fig 129. The observed level of Argon Mass fraction for 50km is 0.0605 (see Fig 130).

6.2.4 CO Mass Fraction

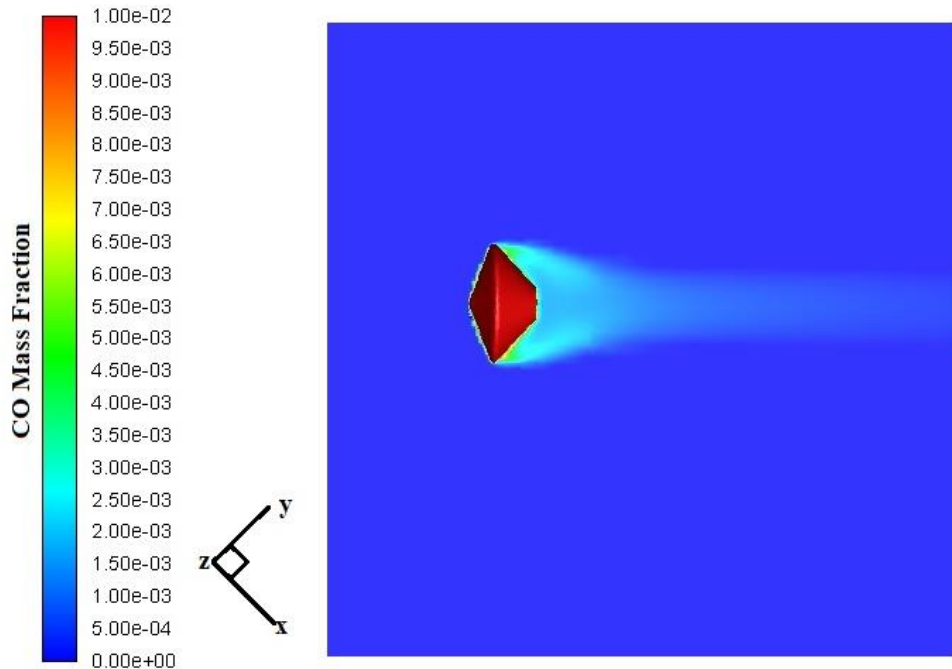


Fig 131. CO Mass fraction contour of Schiaparelli EDM at $H=20\text{km}$ above mars and $\alpha=0^\circ$

At $H = 20\text{km}$ above mars and $\alpha=0^\circ$, The small bow shock emerges at 0.0001m from the end of the capsule(see Fig 131),the mass fraction of CO ranges constant from 0to12m distance in Direction of lines L1,L2,L3,L4 and till13m distance in L5 Line direction is shown in Fig 132.The peak values are observed in the graph (see Fig 132) are $m_{fL1}=0.0150485$, $m_{fL2}=0.008241$, $m_{fL3}=0.001513203$, $m_{fL4}=0.008138$, $m_{fL5}=0.001268$ is observed. Due to the arise of turbulent wake from the sides and aft body of the capsule is shown in Fig 131, the mass fraction of CO at least decreases till 100m is shown in Fig 132.

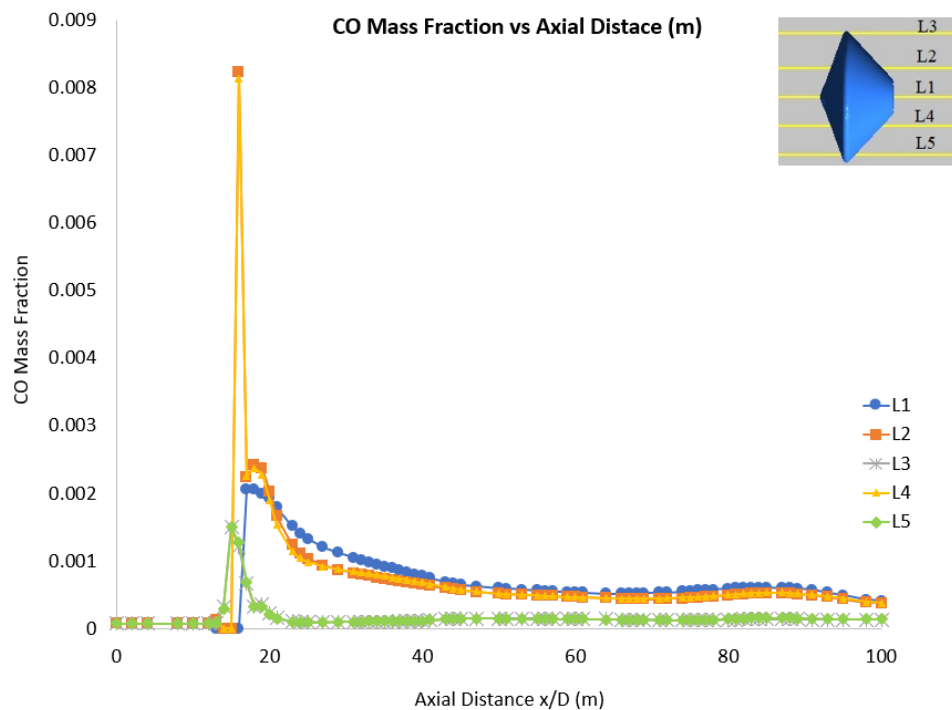


Fig 132. CO Mass fraction along the domain axial distance at $H= 20\text{km}$ above mars, $\alpha = 0^\circ$
for domain length = 100m

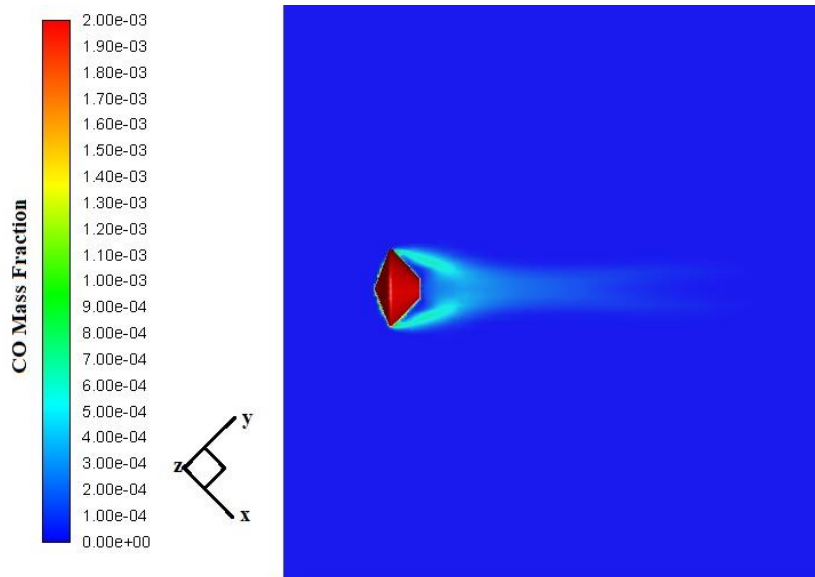


Fig 133. CO Mass fraction contour of Schiaparelli EDM at $H= 50\text{ km}$ above mars and $\alpha=0^\circ$

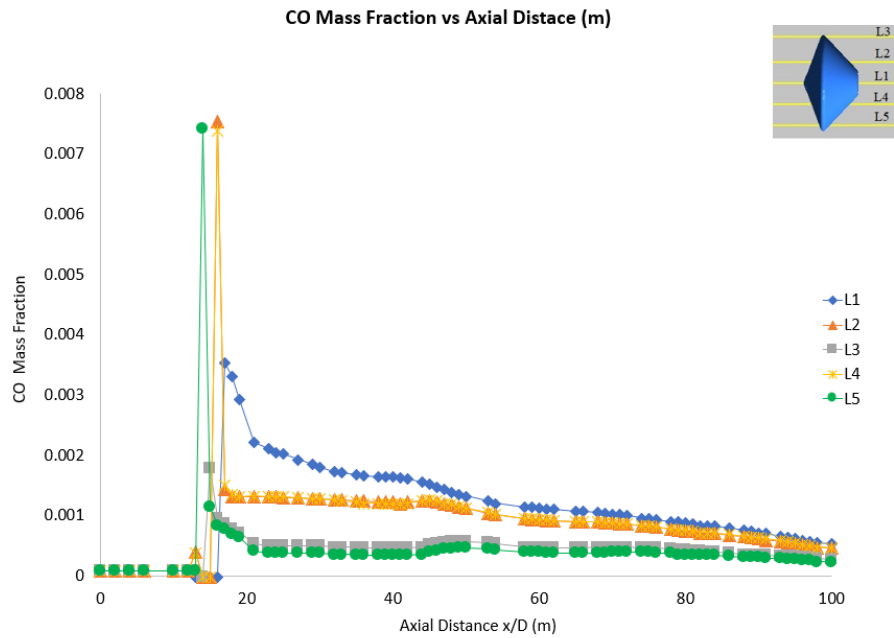


Fig 134. CO Mass fraction along the domain axial distance at $H= 50\text{km}$ above mars, $\alpha = 0^\circ$ for domain length = 100m

At $H = 50\text{km}$ above mars and $\alpha=0^\circ$, the shockwave emerges from the front end of capsule till the sides of the capsules in Fig 133, the CO mass fraction is constant till 12m is shown in Fig 134 in the lines L1, L2, L3, L4 and L5.

The peak values are observed in the graph (Fig 134) are $m_{fL1} = 0.0035332$, $m_{fL2} = 0.007592495$, $m_{fL3} = 0.0017801$, $m_{fL4} = 0.00740037$ and $m_{fL5} = 0.007409$. Finally, each line decreases till 100m length (shown in Fig 134) due to wake region arises at aft body of the capsule is shown in Fig 133.

6.2.5 O₂ Mass Fraction

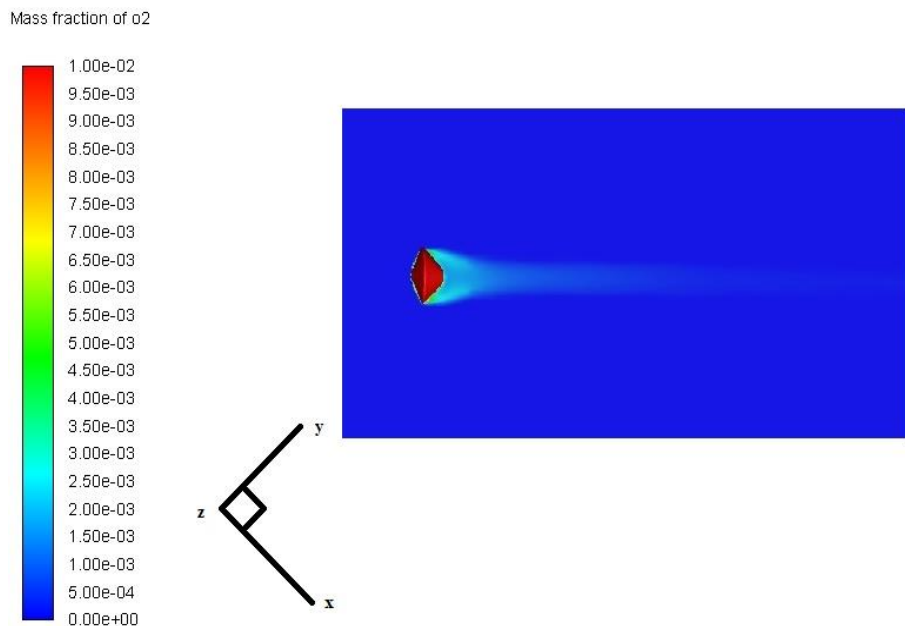


Fig 135. O₂ Mass fraction contour of Schiaparelli EDM at H=20km at $\alpha=0^\circ$

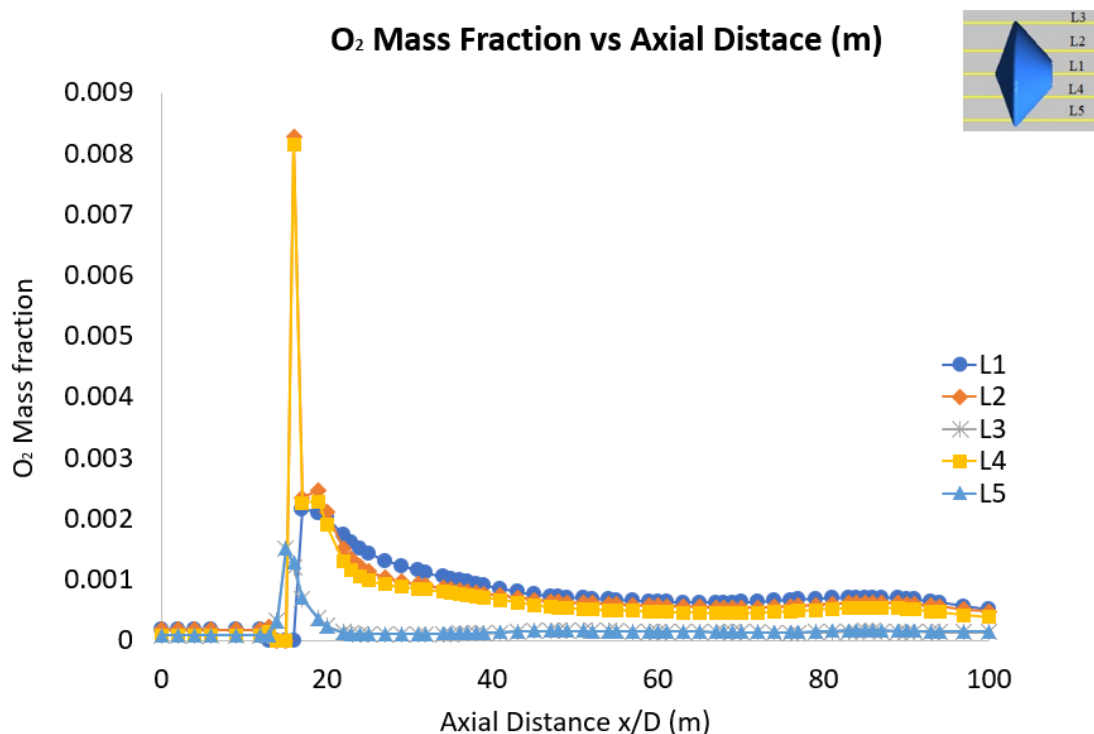


Fig 136. O₂ Mass fraction along the domain axial distance at H= 20km above mars, $\alpha = 0^\circ$
for domain length = 100m

At $H = 20\text{km}$ above mars and $\alpha=0^\circ$, the normal shockwave arises slightly at the distance of 0.000001m from the front end of the capsule is shown in Fig 135. So, the mass fractions of O_2 will be constant till 12m in the direction of lines L1, L2, L3, L4 and it will be constant till 13m in the line L5 is shown in Fig 136. The peak values of O_2 Mass fractions are observed in each line as follows: $m_{fL1}=0.002154638$, $m_{fL2}=0.00826607$, $m_{fL3}=0.00160649$, $m_{fL4} = 0.00816529$ and $m_{fL5}=0.001599257$ is shown in Fig 136. Finally, each line decreases till 100m due to the wake region arise in normal at rear end of capsule is shown in Fig 135.

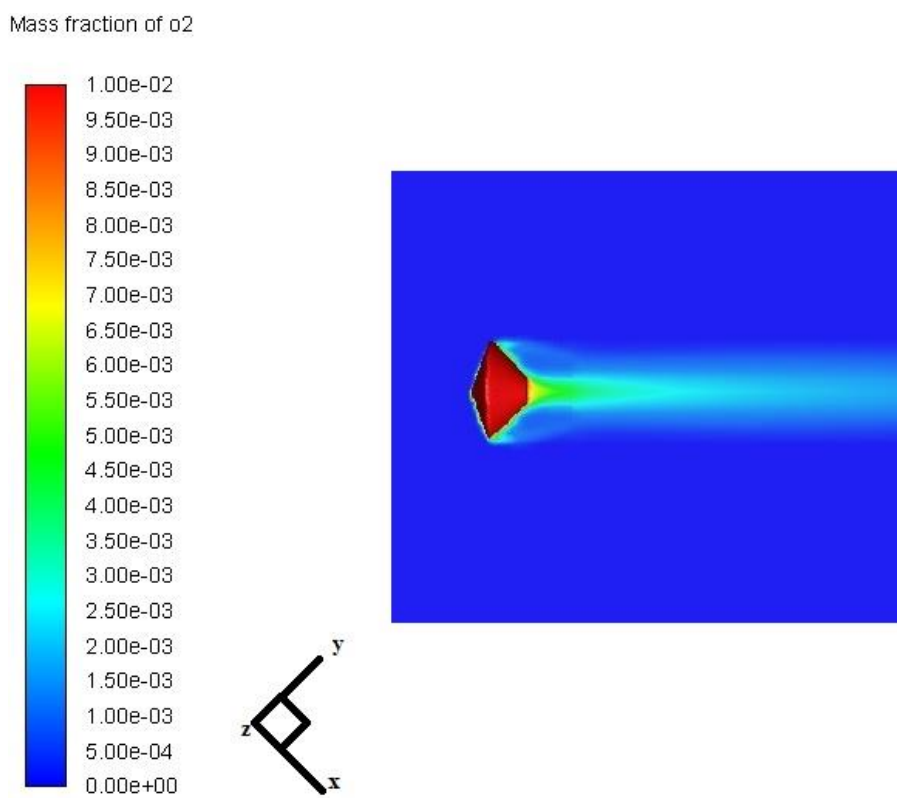


Fig 137. O_2 Mass fraction contour of Schiaparelli EDM at $H=50\text{km}$ at $\alpha=0^\circ$

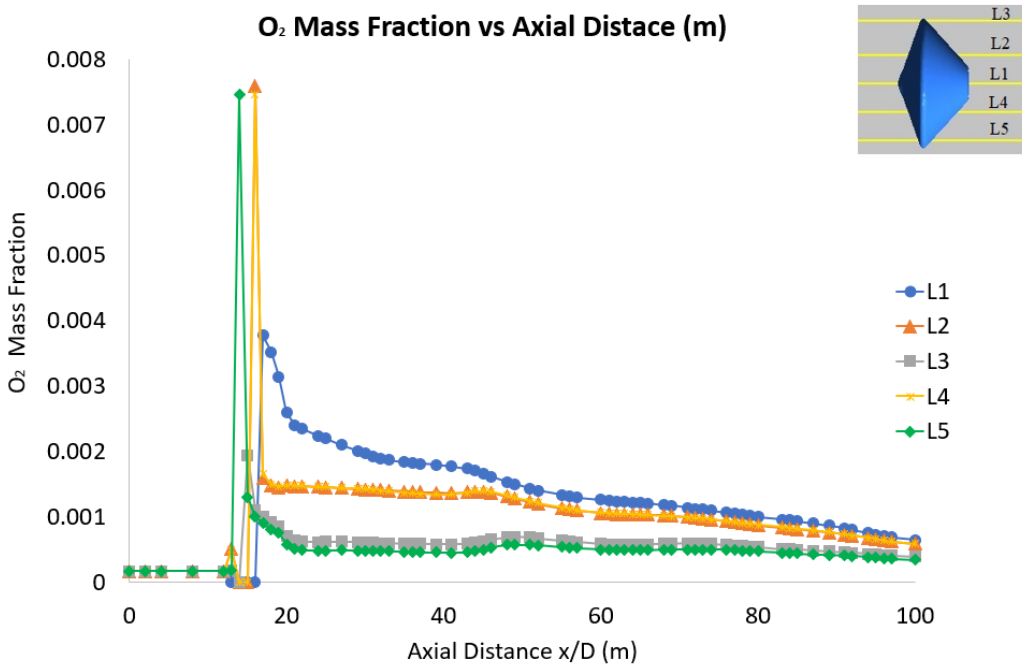


Fig 138 O₂ Mass fraction along the domain axial distance at H= 50km above mars, $\alpha = 0^\circ$ for domain length = 100m

At H = 50km above mars and $\alpha=0^\circ$, due to the arise of Shockwave at the distance of 0.0001m at the front end of the capsule is shown in Fig 137. The O₂ mass fraction remains constant till 12m in the direction of lines L1, L2, L3, L4 and also till 13m in L5 direction (shown in Fig 138). The observed peak values in each line are as follows: $m_{fL1}= 0.003778726$, $m_{fL2}= 0.007597269$, $m_{fL3}= 0.001942758$, $m_{fL4}= 0.007468477$ and $m_{fL5}= 0.007459029$ is shown in Fig 138. Finally, Mass fraction decreases till 100m position due to strong wake region arises at rear end of the capsule (see Fig 137).

When compared to the real gas model to the perfect gas in real gas model the bow shock is located at 0.3m ahead of the capsule and maximum pressure is observed at 450 Pa (capsule) and 7110Pa (canopy) while in perfect gas model the bow shock arises 0.5m ahead of the capsule and the maximum pressure observed is 550 Pa (capsule). The considered angle of attack (α) for this model is 0° at H= 20km and H = 50km above mars. Table 24 shows the implementation of various altitudes with thermal properties.

Table 24: Implementation of various altitudes above Mars[13]

Altitude (H) km	Density (ρ) kg/m ³	Temperature(T) K	Velocity -speed of sound(C) m/s	Mach Number (M)	Pressure(P) pa
0	1.5500e-02	214	233.6	2.0034	636.56
10	6.4700e-03	205	228.5	2.04814	254.54
20	2.6300e-03	188.3	218.8	2.13893	95.04
30	9.8000e-04	175	211	2.2180	32.91
40	3.4000e-04	162.4	203.6	2.2986	10.60
50	1.0800e-04	152.2	197	2.3756	3.1545e-02
60	3.1800e-05	144.2	191.6	2.4425	8.8001e-03
70	8.7300e-06	139.5	188.4	2.4841	2.3371e-03
80	2.2900e-06	139	187.9	2.4906	6.1087e-04
90	6.0100e-07	139	188.2	2.4867	1.6032e-04
100	1.5900e-07	139	195.5	2.4880	4.2414e-05
110	4.1400e-08	149.4	195.5	2.3938	1.1870e-05
120	1.1900e-08	159.7	202.5	2.3111	-
130	3.7600e-09	170	208.6	2.2435	-
140	1.0900e-09	245.1	251.9	1.857	-
150	4.7300e-10	288.6	275.5	1.6987	-

6.3 Flow at Different regimes during Re-entry

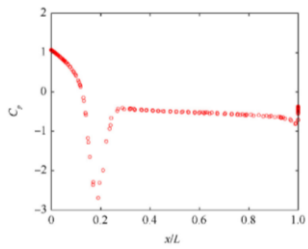
The drag coefficient obtained for the capsule model is plotted for various altitudes in Fig 141. The mass of the Schiaparelli re-entry vehicle is 577 kg and mass of parachute is to be 600kg. The ballistic coefficient (β), is calculated (in kg·m⁻²) using the formula (52) and (53) and plotted at various altitudes as shown in Fig 140,

$$\beta = \frac{m}{c_{DS}} \quad (52)$$

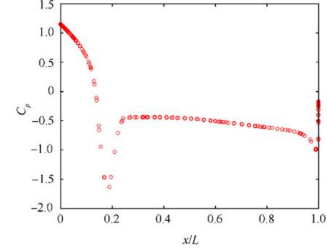
and with lift Coefficient,

$$\beta = \frac{m}{c_{LS}} \quad (53)$$

Upon observation of the drag coefficient plot, it is found that there is a decrease in C_D initially followed by a gradual decrease proceeding towards Mach number independence which is evident by the decrease in slope as Mach number increases. Upon observation of the lift coefficient plot, it is found that there is a decrease in C_L initially followed by a gradual decrease proceeding towards Mach number (M) independence which is evident by the decrease in slope as Mach number increases in Fig 142. The inverse proportionality of altitude to C_D is clear from Fig 141. The range of the ballistic coefficient(β) is found to lie between 170 kg/m^2 and 350 kg/m^2 [32].



(a) $M=0.5$



(b) $M=0.7$

Fig 139. Pressure coefficient C_p vs Axial distance (x/L) plotted along the sectional surface of baseline re-entry vehicle in subsonic regime [32]

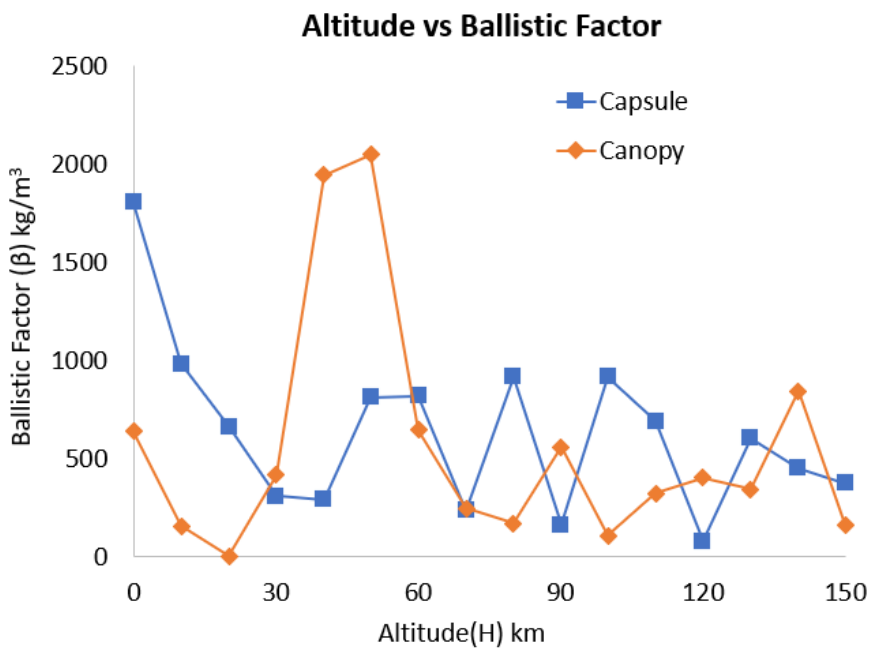


Fig 140. Ballistic Factor(β) Vs Altitude(H) of Re-entry capsule and its parachute (canopy)

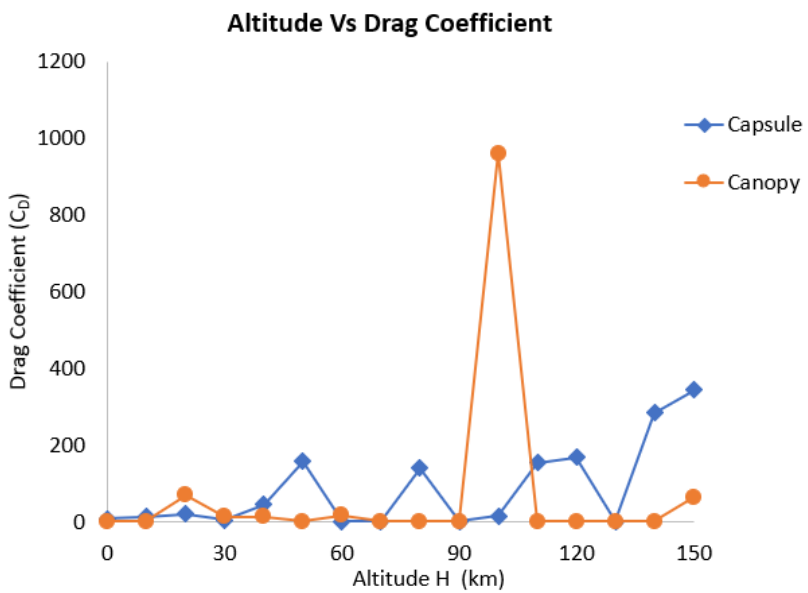


Fig 141. Drag coefficient (C_D) Vs Altitude(H) of Re-entry capsule and canopy

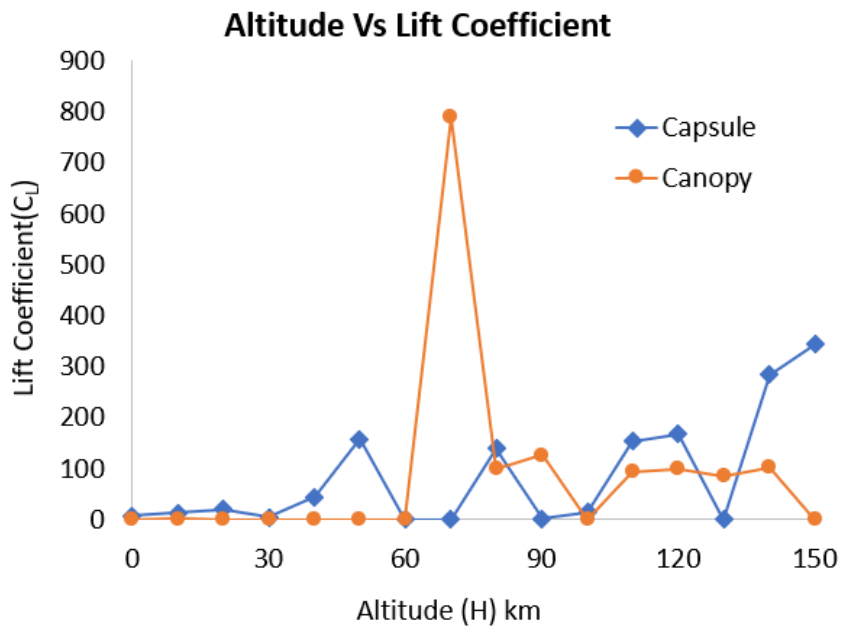


Fig 142. Lift coefficient (C_L) Vs Altitude(H) of Re-entry capsule and canopy

6.3.1 Subsonic Regime

In the subsonic regime (also known as transonic regime), Mach numbers 0.5, 0.7 were considered. The capsule model shows a significant increase in drag from $M= 0.5$ to $M= 0.7$. C_p distribution along the sectional surface of the re-entry vehicle is plotted against the axial position x/L of the capsule. When the freestream flow encounters the capsule, it stagnates at the centre of the heat shield, causing an increase in pressure, which can be seen as the peak C_p value at zero x/L , in Fig 139 [32]. The flow pattern over the re-entry capsule and Parachute was observed for subsonic regime using the streamline plots and the schematic is shown in Fig 143. The sudden drop in C_p near the shoulder of the capsule indicates strong flow acceleration, after which, the flow separates to create vortices symmetric about the axis of the capsule, recirculating over the aft body. This recirculation vortex is represented schematically in Fig 143. The pressure remains almost constant over the aft body indicating a separated flow. Near the base, another expansion region is observed, followed by an increase in C_p as we proceed towards the axis of the capsule and canopy. At $M= 0.7$, the strength of this expansion region

reduces, indicated by the rise in C_p value at the shoulder. Also, an increase in base pressure is seen at higher Mach number (M). The increase in pressure at the heat shield is evident from Fig 139 (a). It also elucidates the region of expansion with lower pressure near the base. From Fig 139 (b), the ballistic coefficient is very high in the subsonic regime. The mass and area of the baseline re-entry vehicle does not change the high value of β is due to the low drag coefficients [32].

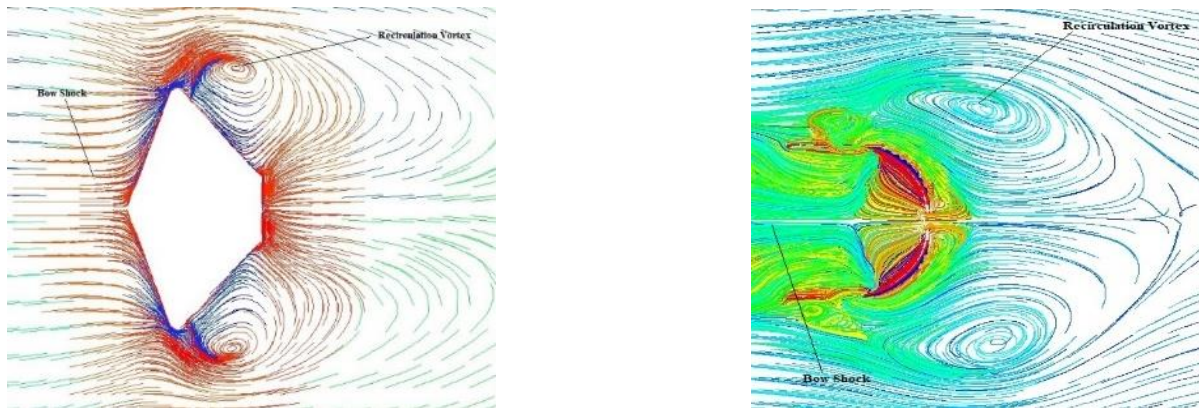


Fig 143. Sub sonic Regime of (a) Re-entry Capsule and (b) Canopy (Parachute)

6.3.2 Low Supersonic Regime

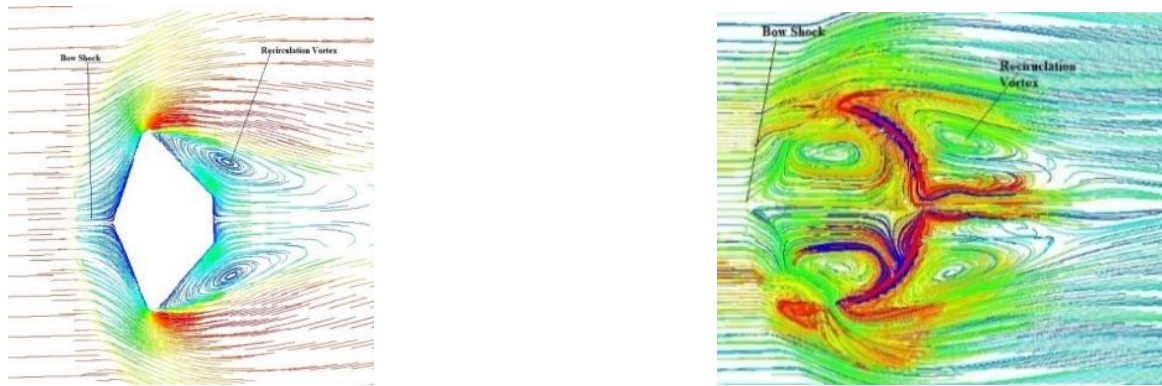


Fig 144. Low supersonic Regime of (a) Re-entry Capsule and (b) Canopy (Parachute)

The observed spike in C_D from $M=1.8$ to $M=2.5$ can be attributed to the presence of shock waves. Among the considered Mach numbers, the re-entry capsule attains maximum drag at $M= 2.13$ whereas Re-entry parachute attains drag at $M=2.4$ after which it decreases steadily. Generally, the supersonic flow over blunt re-entry vehicles

are characterised by the presence of a bow shock, as depicted in Fig 144 (b). The flow pattern over the Re-entry capsule and canopy was observed for low supersonic regime using the streamline plots and the schematic is shown in Fig 144 (a) and Fig 144 (b). The flow strongly decelerates downstream of the bow shock as Mach number (M) increases. On the other hand, the shock stand-off distance decreases, increasing the heat shield pressure steadily throughout the regime. At higher Mach number, the recirculating flow shrinks in size, eventually resulting in a partially attached flow over the aft body. From Fig 144 (a) and Fig 144 (b), compression shock over the base of the capsule, prominent from $M = 2$, redirects the flow again into the freestream direction. Considering the surface pressure coefficient and reveals that the aft-body and the base experience an overall rise in surface pressure, density, and velocity, in addition to the increase in peak pressure at the heat shield with respect to Mach number [32].

6.3.3 High Supersonic Regime

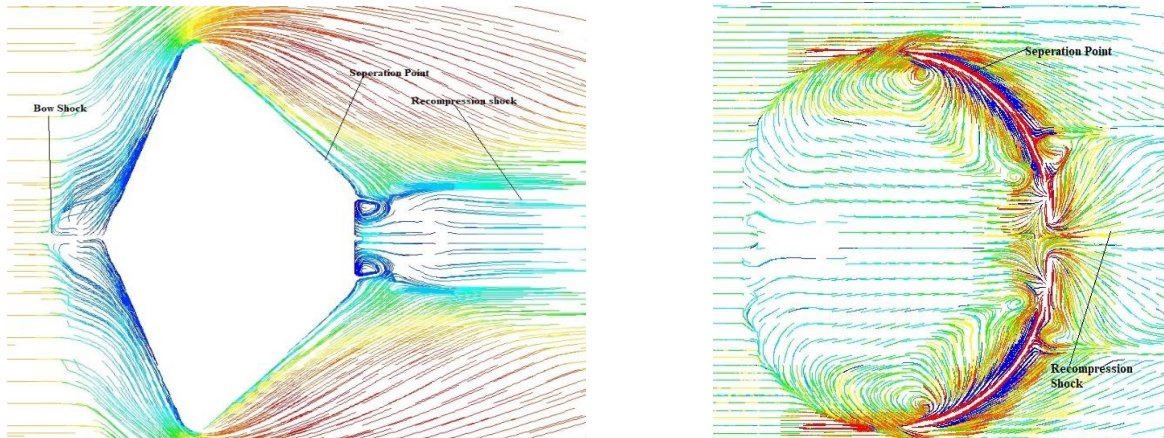


Fig 145. High supersonic Regime of (a) Re-entry Capsule and (b) Canopy (Parachute)

In this regime, the bow shock becomes stronger and moves in closer to the capsule raising the heat shield pressure attaining a constant value. The flow pattern over the Re-entry capsule and parachute was observed for high supersonic regime using the streamline plots and the schematic is shown in Fig 145 (a) - Fig 145 (b). Fig 145 (a) shows the flow over the aft body is partially attached, before separating to form a

smaller recirculating zone. In general, the drop in pressure difference across the parachute and reduction in the recirculation region explain the drop in drag with Mach number in the supersonic regime is shown in 145 (b) [32].

6.4 The possible oscillation regime occurring during Schiaparelli mission

Low supersonic Regime which operates from $M=1.8$ to $M= 2.5$ can be attributed to the presence of shock waves [32]. Among the considered Mach numbers, the re-entry capsule attains maximum drag at Mach number 2.13 whereas Re-entry parachute attains drag at 2.4. The fast oscillations at parachute opening exceeded the threshold of $187.5^\circ/\text{s}$ along X axis while they were well inside the design limit on Y axis. The X gyro saturation occurred 1 s after the PDD and lasted 1 s as shown in detail in Fig 146. The EDM oscillations during parachute inflation were linked to the parachute drag force applied along Z axis and measured on-board. The first peak on Z acceleration was about 0.6 s after PDD, from the acceleration decreased oscillating with a period of about 0.35 s. These oscillations are probably due to combined effects of canopy-bridle elasticity and canopy area oscillations that could occur when the parachute is deployed in supersonic regime (in this case around $M= 2$). The X gyro saturation is correlated with the second peak of the acceleration along Z, about 1 s after PDD (see Fig 146). This suggest that the second peak on the acceleration could have been combined with the probe tilt resulted from the first peak causing an increased angular rate [33].

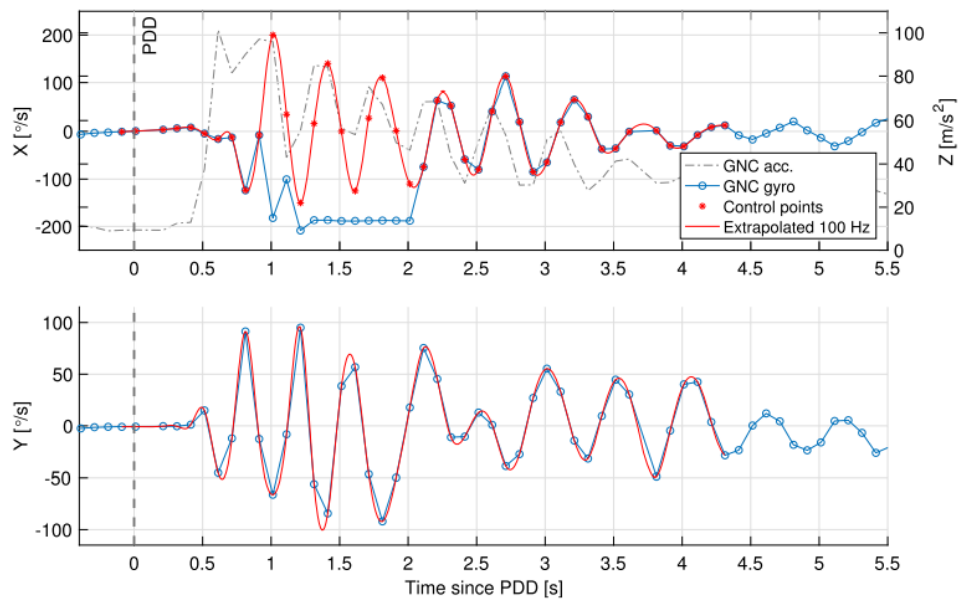


Fig 146. X-yaw and Y-pitch angular rate reconstructed after gyro saturation, interpolated using a cubic function and resampled at 100 Hz [33]

CHAPTER 7

SIMULATION OF SCHIAPARELLI FINAL ALTITUDE AND TRAJECTORY

7.1 Simulation of the Schiaparelli trajectory and attitude in the hypothesis failure due to areal oscillations

In this chapter, the simulations of the Schiaparelli attitude in the hypothesis of failure due to areal oscillations along the re-entry trajectory have been performed. The simulations involve the joint study of the interaction between capsule and parachute. The objective is to verify whether the coupling between the fluid dynamic field of the capsule and that of the parachute, can generate asymmetries in the distribution of pressure and velocity, then generate the known oscillations. The simulations were carried out for two different angles of attack.

7.1.1 Design of Schiaparelli Trajectory Anomaly with Various Angle of Attacks

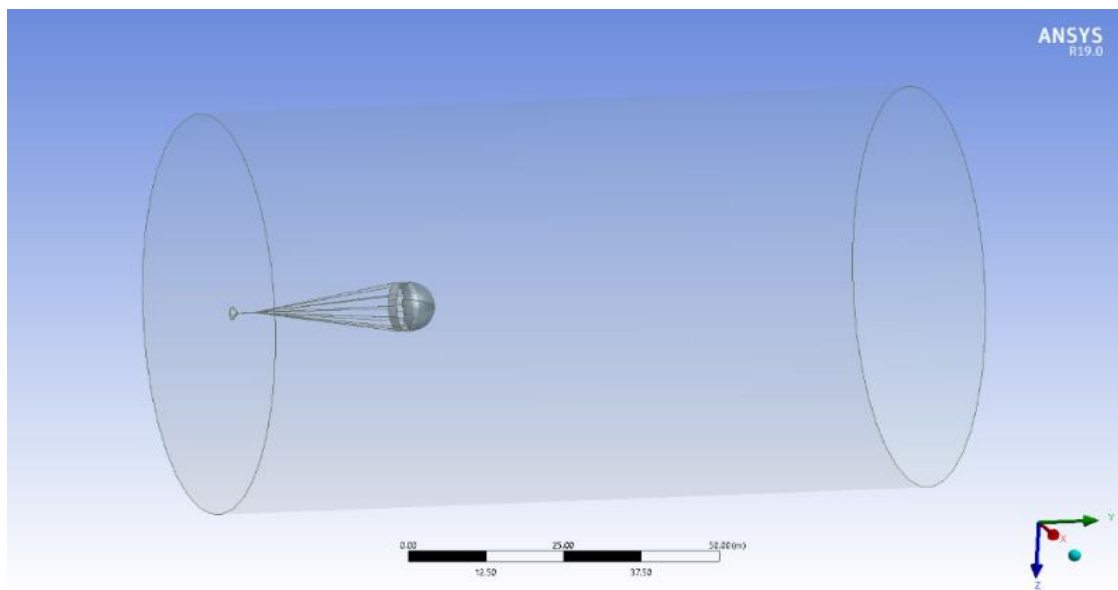


Fig 147. Design of a Re-entry Capsule with parachute at Angle of Attack(α)=0°

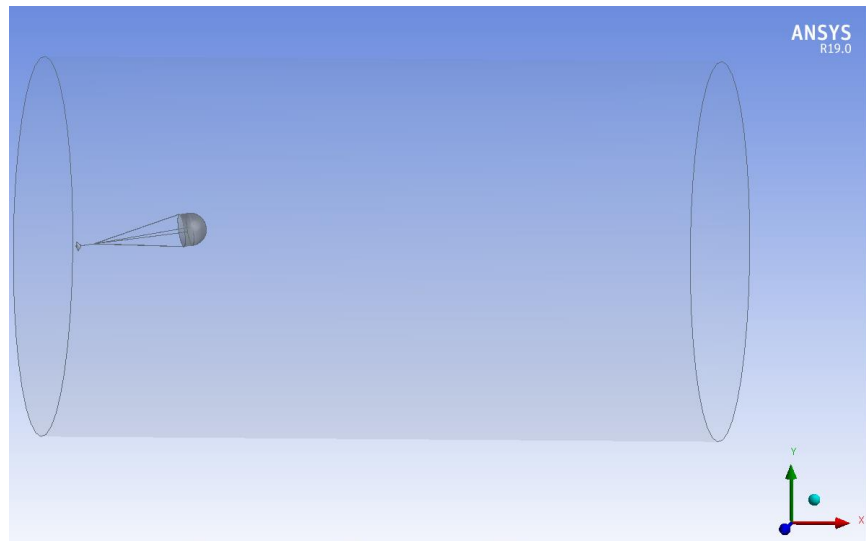


Fig 148. Design of a Re-entry Capsule with parachute at Angle of Attack(α)=20°

Fig 147 and Fig 148 show the design of capsule with parachute at $\alpha = 0^\circ$ and $\alpha = 20^\circ$ and $M=2.04814$. The geometry is shown in Fig 2 from Chapter 1.

7.1.2 Meshing and Grid Independence Test

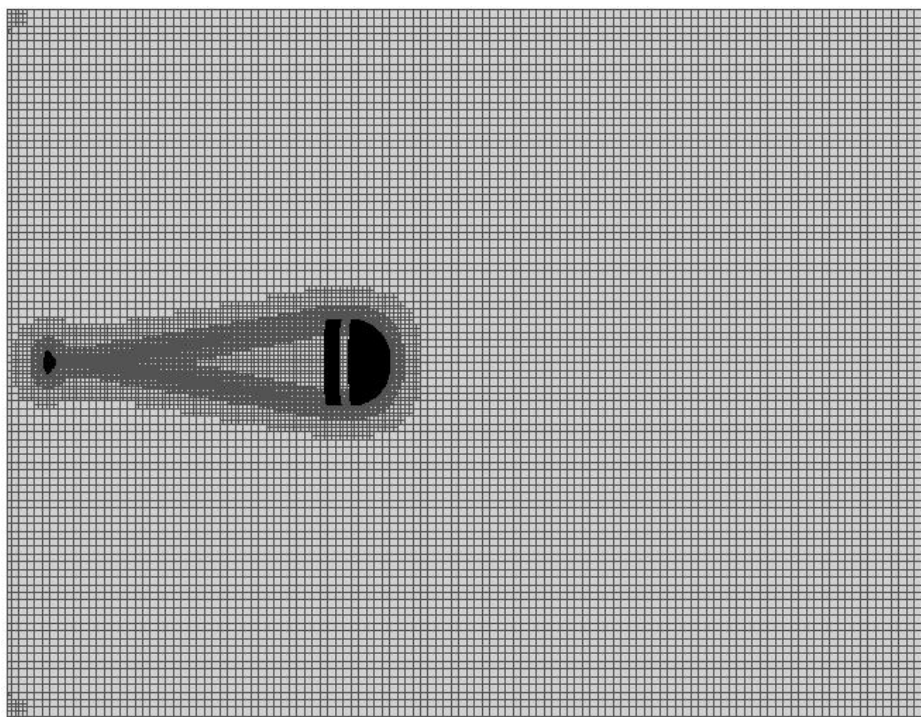


Fig 149. Mesh of the computational domain

The meshing of the capsule, done using cut cell method, is shown in Fig 149. Details are given in Table 25. Due to the asymmetrical configuration of the parachute-like

two-body system with DGB, the flow fields around the rigid and flexible parachute model were simulated using a single-block textured grid, which was created from a meridian plane [41-43,44 - 46,49,51-56]. 3D renderings of the grids and validity tests of the grid and temporal convergence were provided in [35-36].

Table 25: Mesh details

Angle of Attack(α)	Mesh type	No. of Elements	No. of nodes
0°	Coarse	308760	281767
	Medium	758489	737408
	Fine	1416103	1295970
20°	Coarse	281767	307860
	Medium	737408	758489
	Fine	1163920	1111666

7.1.3 Boundary Conditions

Large eddy simulations of parachute at H =10km have been performed by Fluent [34,39-40,47-48,50]. The composition of the Martian atmosphere was implemented, the gas has been assumed ideal, the Sutherland's viscosity law has been implemented. The boundary conditions are shown in Table 26.

Table 26: Boundary Conditions for Areal oscillation of a Schiaparelli Parachute

Zone	Boundary	Parameters
Inlet	Pressure Far Field	At Altitude 10km, Pressure (p) = 254.54 Pa, 538 Pa [34] Velocity (v)=228.5m/s Temperature (T)=205K Mach number(M)=2.04814,1.75[34]
Wall	Wall	-

7.1.4 Validation of Results for final Trajectory

The structure is placed in a supersonic flow going from the left to the right of Fig 150. Two bow shocks develop, one ahead of the capsule and one ahead of the canopy. The high Reynolds number of the present application results in the generation of a turbulent wake behind the capsule. This wake interacts with the bow shock ahead of the canopy and provides the main source of fluid dynamical unsteadiness. An analogous behaviour is observed during the interaction of vortical structures with subsonic parachutes [38]. The intensity of the turbulence carried by the wake is amplified as it is ingested by the canopy bow shock (due to turbulence-shock interaction). The amplified turbulence fluctuations lead to amplified pressure fluctuations. These, coupled with the structural dynamics of the canopy, induce large inhomogeneous pressure variations, leading to large canopy area oscillations in the Mach number range from 1.5 to 2.5. this is a form of oscillatory respiratory phenomenon that produces massive drag versions and giant stress fluctuations in the shape. This negatively affects the ability of the supersonic parachute to act as an effective decelerating device. In the present study, we consider cases in the Mach 2-2.5 range. The canopy is superimposed over Mach number isolevels at the plane through the centre of the domain at this instant. This composite view is a compromise among other visualization possibilities of the three-dimensional flow, and it highlights

the shape of the canopy over more detailed flow features rendering shown in the next figure. The compressible flow around the supersonic parachute can be decomposed into several canonical regions, as shown in Fig 150. Here, the capsule, canopy and suspension lines as well as colour is contour levels of the streamwise velocity- Mach number M and isolines of pressure at $t=57.5$ ms are shown in the central plane of the computational domain [37]. In Fig 150, the two bow shocks, BS_1 and BS_2 have been observed at ahead of the capsule and the canopy, respectively. These shocks are responsible for adjusting the supersonic flow conditions upstream to the solid boundaries of the rigid capsule and flexible canopy. A quite stable narrow turbulent wake develops behind the capsule, TW_1 , while a more irregular turbulent wake, TW_2 , is present behind the canopy. The latter experiences large variability due to the deformation of the canopy. The detached flow in the region immediately behind the capsule and the canopy is rectified by two recompression shocks, RS_1 and RS_2 , that reconcile the oblique flow direction just behind the blunt structures with the free-stream direction. The supersonic jet leaving the hole in the back of the canopy (the centre of the canopy is slightly off the centre plane at this instant, and therefore, the figure does not show a cut through the centre of the jet) is observed in Fig 149. As pointed out in the introduction, the main source of instabilities originates in the shock-turbulence interaction between TW_1 and BS_2 [40]. The bow shock is disturbed by the unstationarity and irregularities of the wake (since the wake is not instantaneously cylindrical) and its momentum and pressure fluctuations are amplified as the flow traverses the bow shock (turbulence ingestion by the shock). The resulting pressure fluctuations are now larger, and they enhance transmural forces across the canopy. These, in turn, induce large amplitude deformations of the canopy which feedback into the bow-shock location inducing large oscillations of BS_2 that further reinforce unsteady pressure forces in the region of the canopy, where the compressed flow resides. It is thought that this cycle maintains and generates the breathing phenomena observed in this supersonic parachute. The flexible canopy is not required for the bow

shock to develop unstationary (irregular) motion which is present regardless of the deformable structure [37,39].

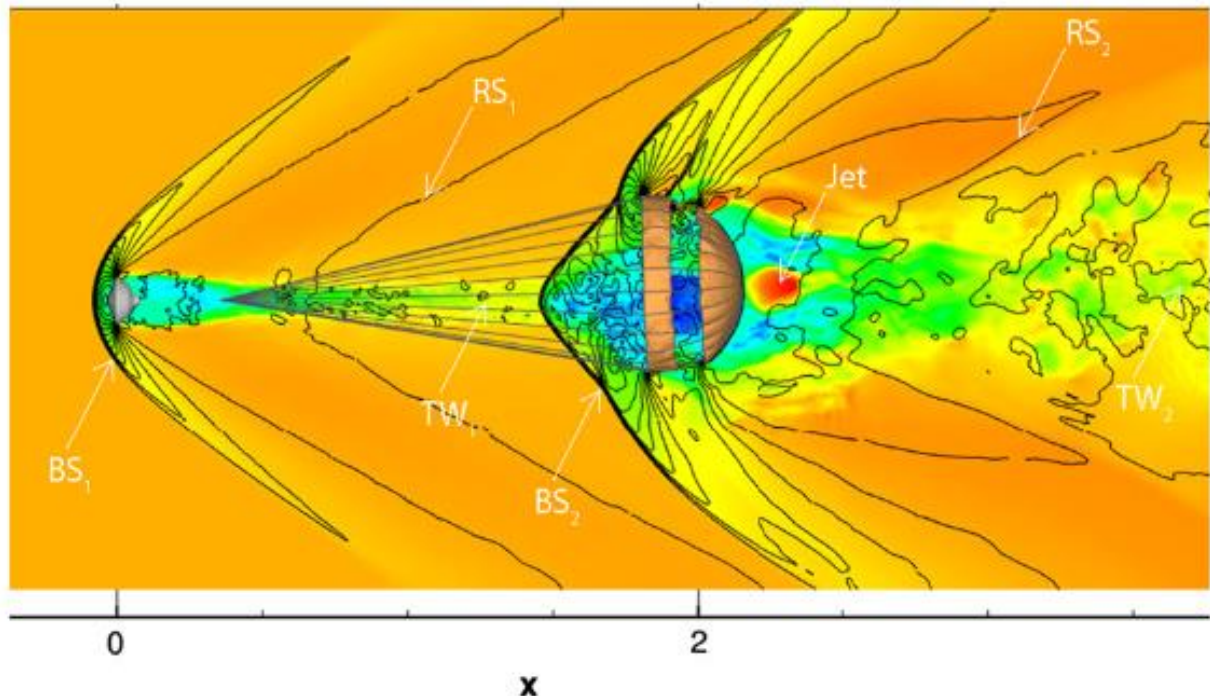


Fig 150. General flow features around the interacting surfaces. Iso-contours indicate streamwise velocity and isolines indicate pressure one instant [37]

7.1.4.1 Simulation of Parachute using SST k- ω at $\alpha = 0^\circ$ and $M = 2.04184$

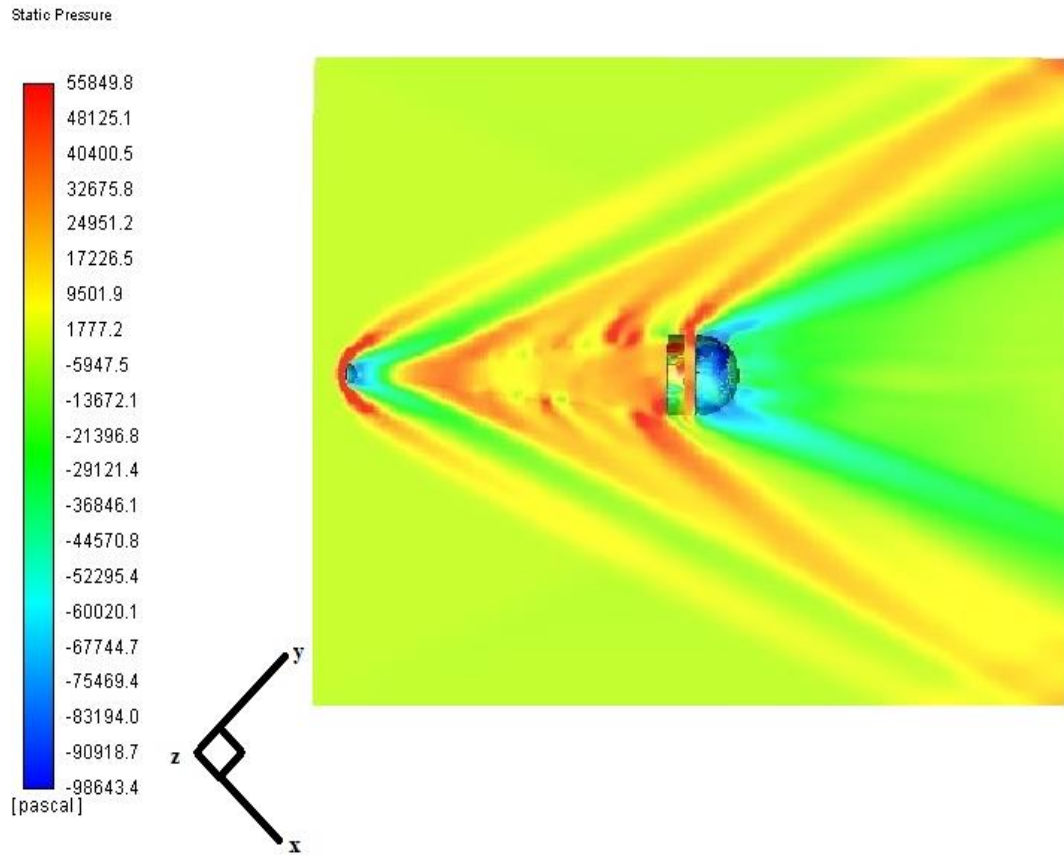


Fig 151. Static pressure contour for Re-entry parachute at $\alpha = 0^\circ$, $H=10\text{km}$ and $M=2.04814$

When Schiaparelli parachute with capsule at $H = 10\text{km}$ and $\alpha = 0^\circ$ with high Mach number, there is a strong bow shocks (BS₁ and BS₂) detaching in front end of re-entry capsule with high pressure and slightly at front end of the parachute with medium pressure and dominates flow body forefield. The re-compression shocks (RS₁ and RS₂) are formed between the capsule and canopy at high Pressure and also formed at backside of canopy at low pressure. At $M=2.04814$, the shock layer is wider at $\alpha = 0^\circ$. So, there is rise in pressure at 558849.8Pa due to the strong wake-shock interaction arises between the capsule and canopy in the stage of pulsation as shown in Fig 151.

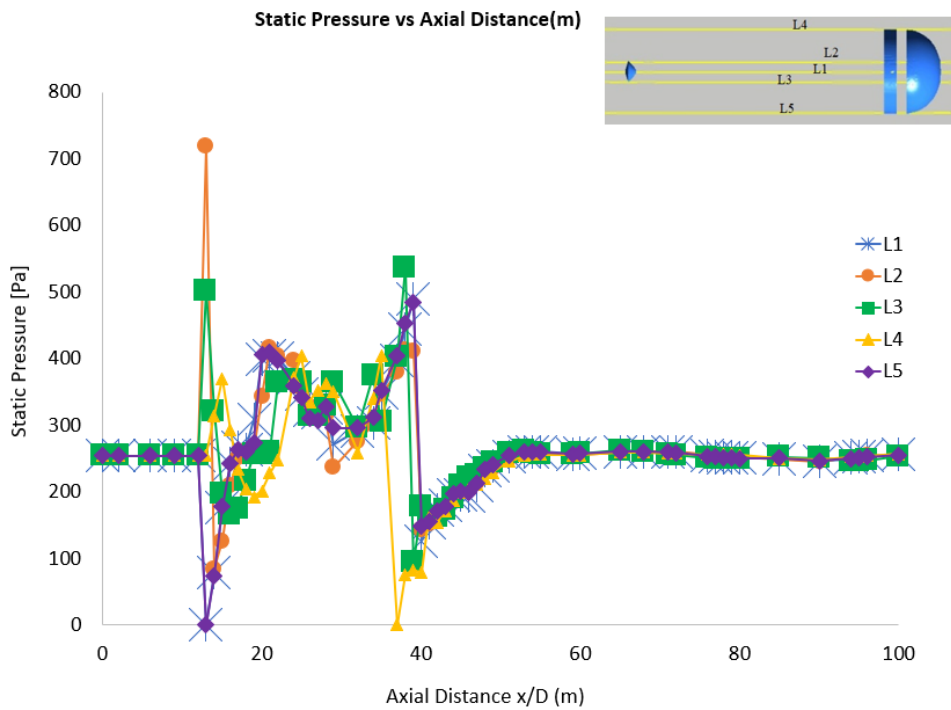


Fig 152. Static pressure along the domain axial distance at $\alpha = 0^\circ$, $H=10\text{km}$, $M=2.04814$ and domain length = 120m

Fig 152 shows, the pressure is constant from 0m to 12m. There is increase and decrease in pressure from 13m to 38m and increases from 40m to 55 m position due to the recompression shockwaves detached between capsule and canopy (see Fig 151). It becomes constant from 55m to 100m (see Fig 152) due to formation of re compression shock (RS_2) at parachute as shown in Fig 151. At 10km and $\alpha=0^\circ$, the peak pressure is observed in the Line L2 is 719.146 Pa which is maximum among all the lines. L1, L3, L4 and L5. The peak value of pressure observed in the line L1 is observed as 489.03 Pa. The peak value of pressure is observed in the line L3 is 537.09 Pa. The peak value of pressure is observed in the line L4 is 404.017 Pa. The peak value of pressure is observed in the line L5 is 484.876 Pa (see Fig 152).

Fig 153 reports the vector of the static pressure at $M=2.04814$ and $\alpha = 0^\circ$.

Flow field streamlines are also shown in order to highlight the vortex structures which arise at the lee side of the Capsule and Canopy.

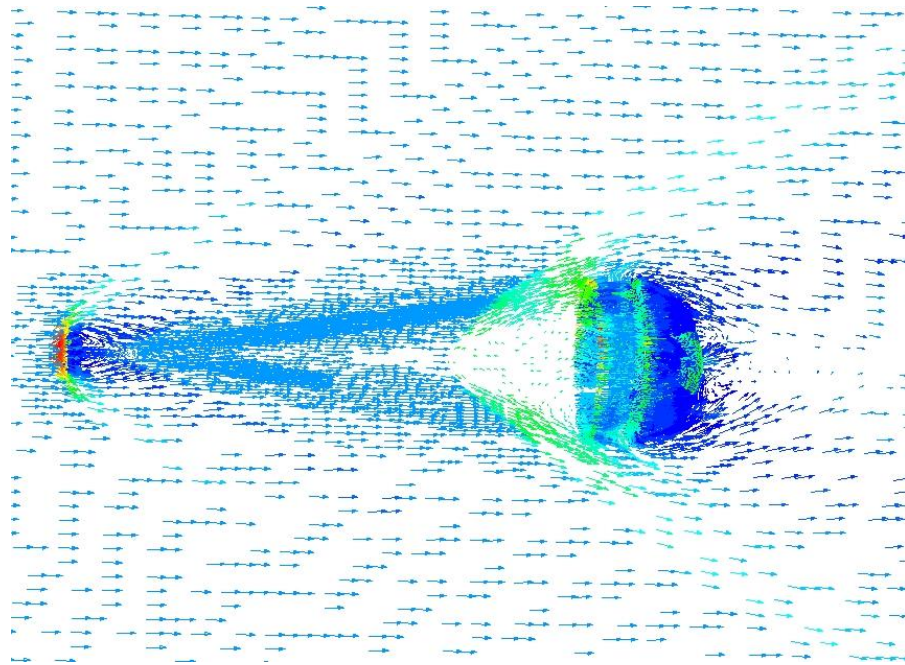


Fig 153. Static pressure vector for Re-entry parachute at $\alpha = 0^\circ$, $H=10\text{km}$ and $M=2.04814$

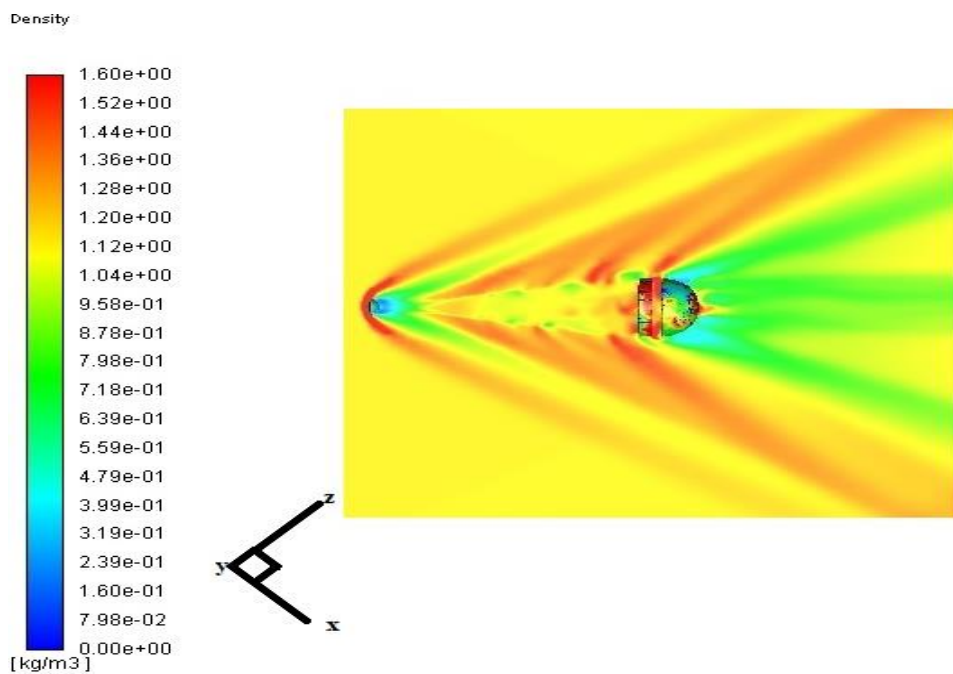


Fig 154. Density contour for Re-entry parachute at $\alpha = 0^\circ$, $H=10\text{km}$ and $M=2.04814$

Fig 154 shows the strong bow shocks (BS_1 and BS_2) in front of both the re-entry capsule and the parachute. There is an increase in density due to formation of a strong wake shock interaction and recompression shockwave (RS_1) between capsule and Parachute

and also backside of canopy (RS_2) is shown. The maximum density value observed at the front end of the capsule up to the sides of the gap in the canopy is 1.60 kg/m^3 .

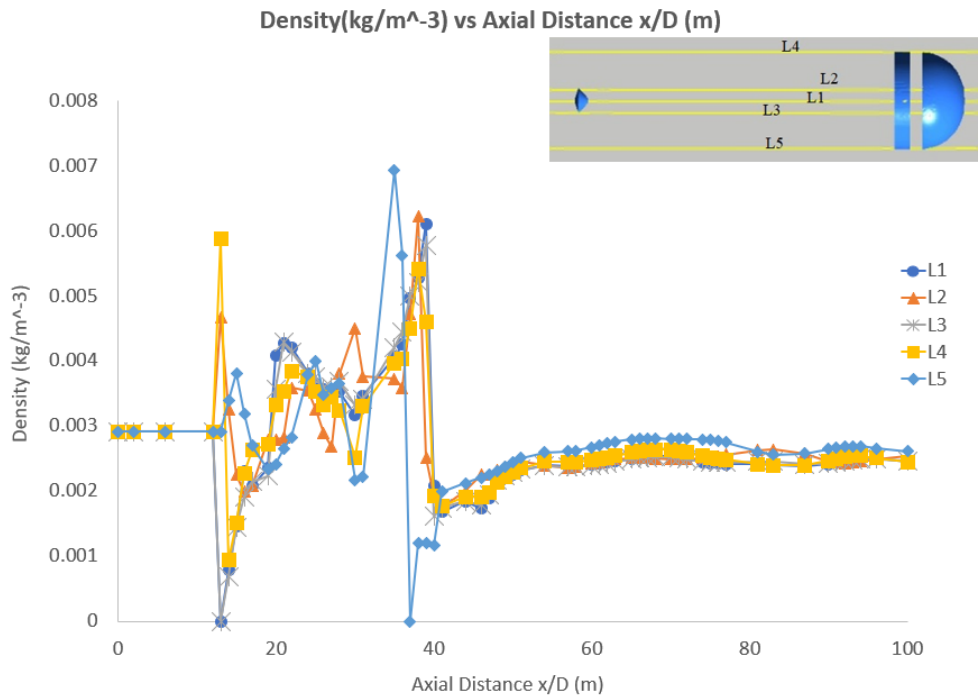


Fig 155. Density (kg/m^3) along the domain axial distance $\alpha = 0^\circ$, $H=10\text{km}$, $M=2.04814$ and domain length = 120m

Fig 155 shows the density is constant from 0 m to 12m. It increases and decreases till 39m distance and increases again from 39m to 52m (see Fig 155) due to formation of re compression shocks between capsule and parachute as shown in Fig 154. At 10km and $\alpha=0^\circ$, the peak density is observed in the Line L5 is 0.006932 kg/m^3 which is maximum among all the lines L1, L2, L3 and L4. The peak value of density observed in the line L1 is observed as 0.00610 kg/m^3 . The peak value of density is observed in the line L2 is 0.006215 kg/m^3 . The peak value of density is observed in the line L3 is 0.0055754 kg/m^3 . The peak value of density is observed in the line L4 is 0.0058743 kg/m^3 (see Fig 155).

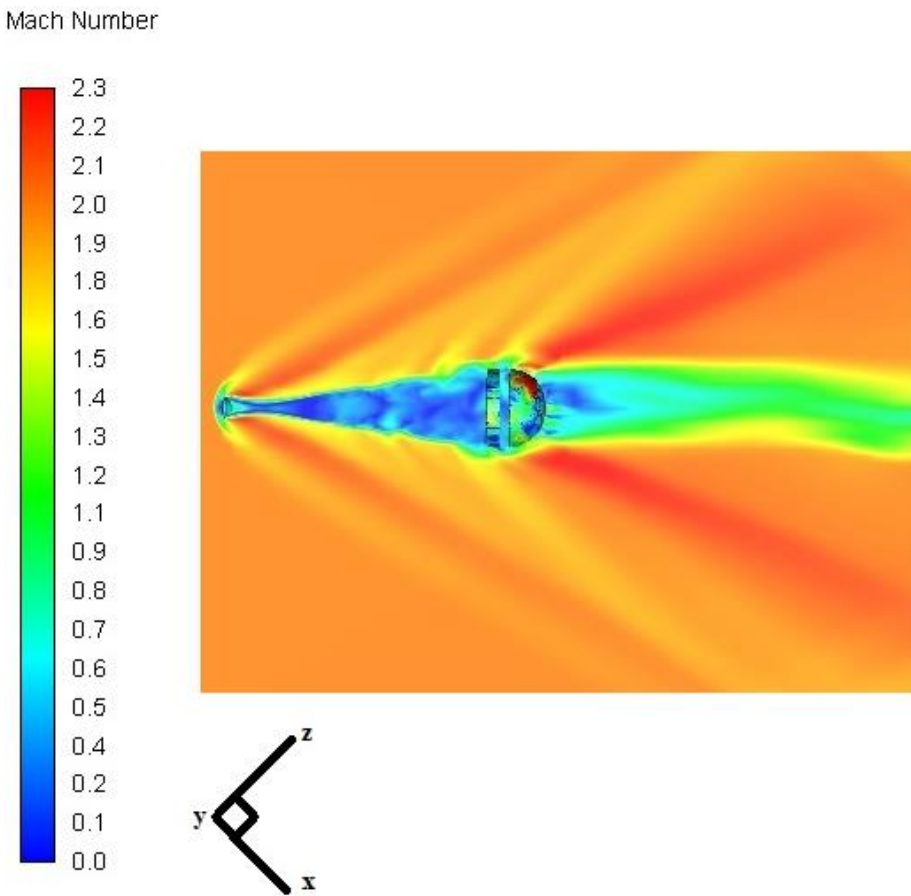


Fig 156. Velocity-Mach number contours for Re-entry parachute at $\alpha = 0^\circ$, $H=10\text{km}$ and $M=2.04814$

Fig 156 shows the interaction between the region of the shock wave downstream of the capsule and the parachute. The turbulent wave (TW_2) interaction has formed at backside of the canopy.

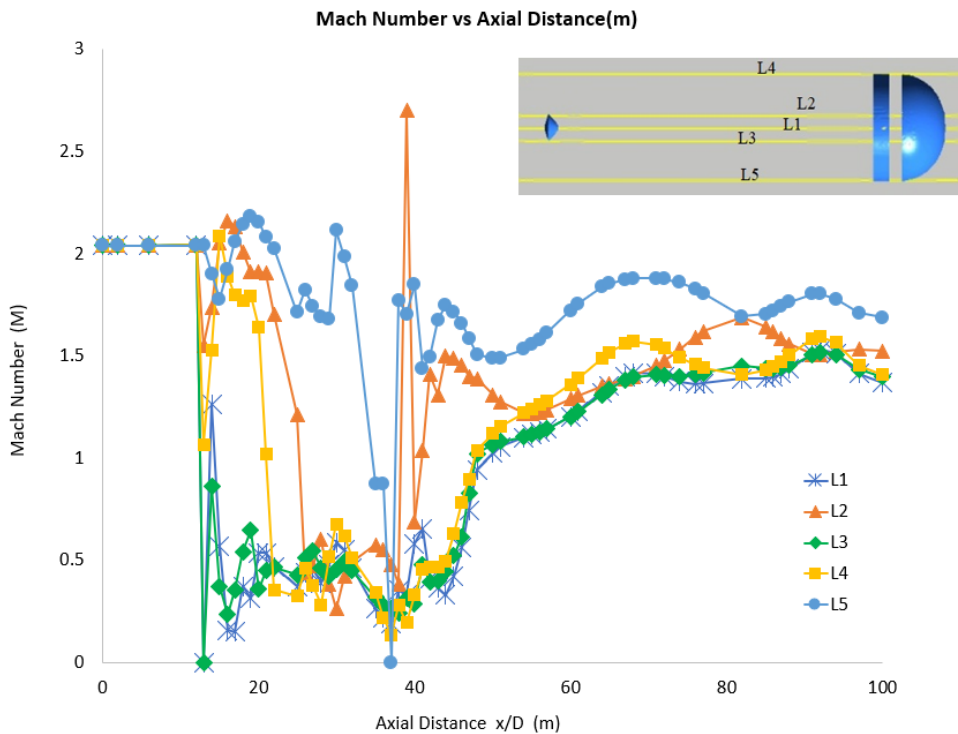


Fig 157. Velocity-Mach number along the domain axial distance at $\alpha = 0^\circ$, $H=10\text{km}$, $M=2.04814$ and domain length = 120m

Fig 157 shows that the Mach number is constant from 0m to 12m and varies from 12m till 100m position due to pulsation of parachute at straight path as shown in Fig 156. The peak Mach number is observed as $M=2.701$ in the direction of Line L2 which is maximum among of all lines L1, L3, L4 and L5 (see Fig 157).

Static Temperature

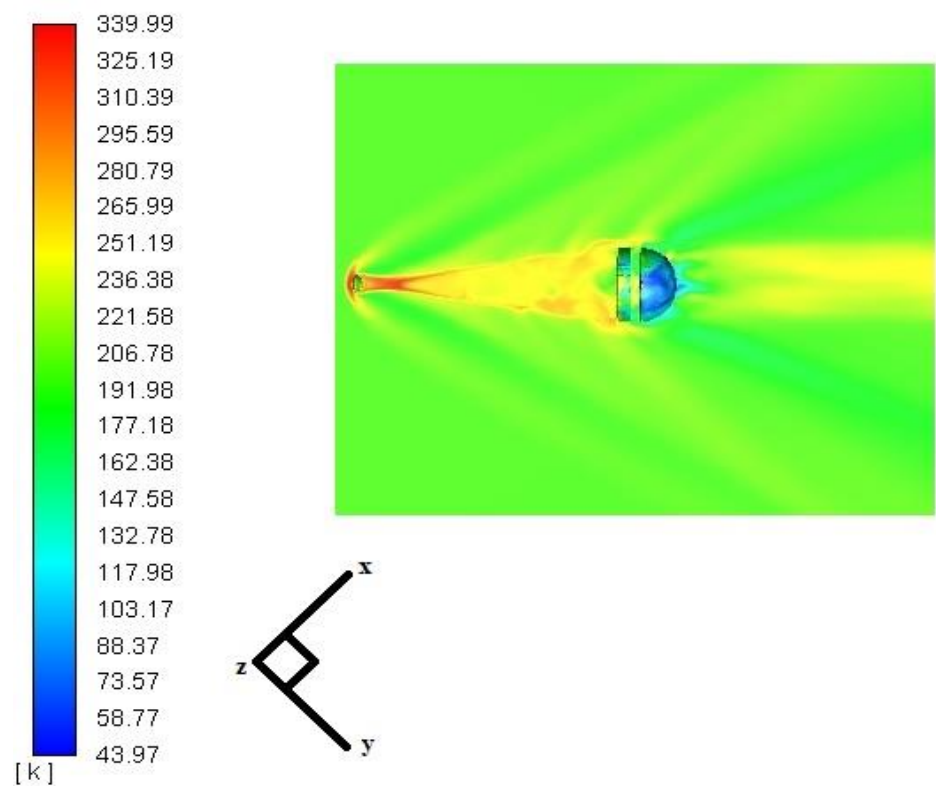


Fig 158. Static temperature contours for Re-entry parachute at $\alpha = 0^\circ$, $H=10\text{km}$ and $M=2.04814$

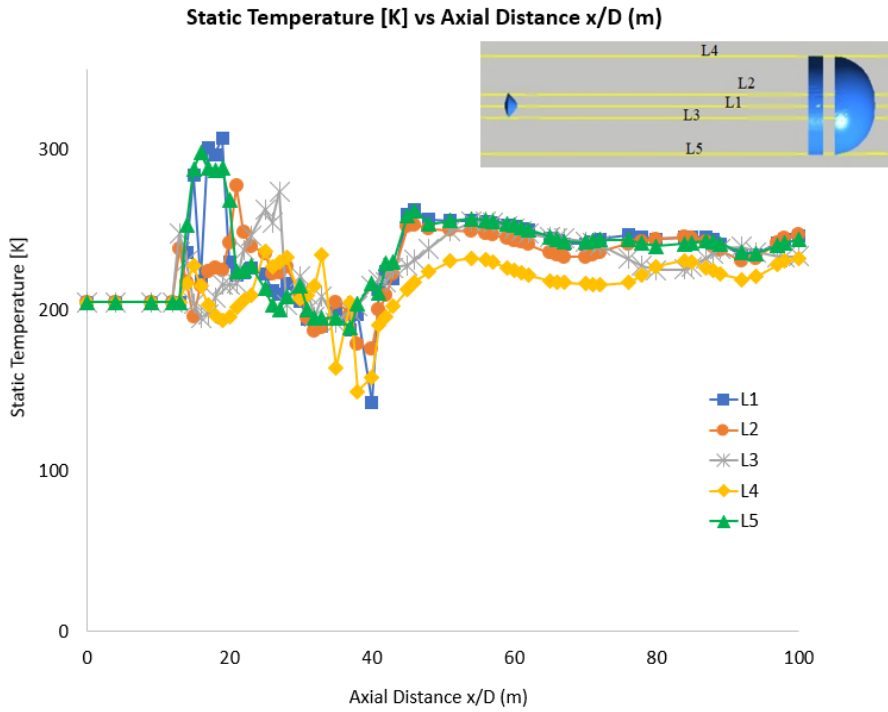


Fig 159. Static temperature(K) along the domain axial distance at $\alpha = 0^\circ$, $H=10km$, $M=2.04814$ and domain length = 120m

Fig 158 shows the temperature field. Fig 159 shows that the peak temperature is observed in the Line L1: it is 307.02 K which is maximum among all the lines L2, L3, L4 and L5 (see Fig 158). The peak value of temperature observed in the line L2 is observed as 277.111 K. The peak value of temperature is observed in the line L3 is 273.744 K. The peak value of temperature is observed in the line L4 is 236.67 K. The peak value of temperature is observed in the line L5 is 297.86 K (see Fig 159).

Mass fraction of co2

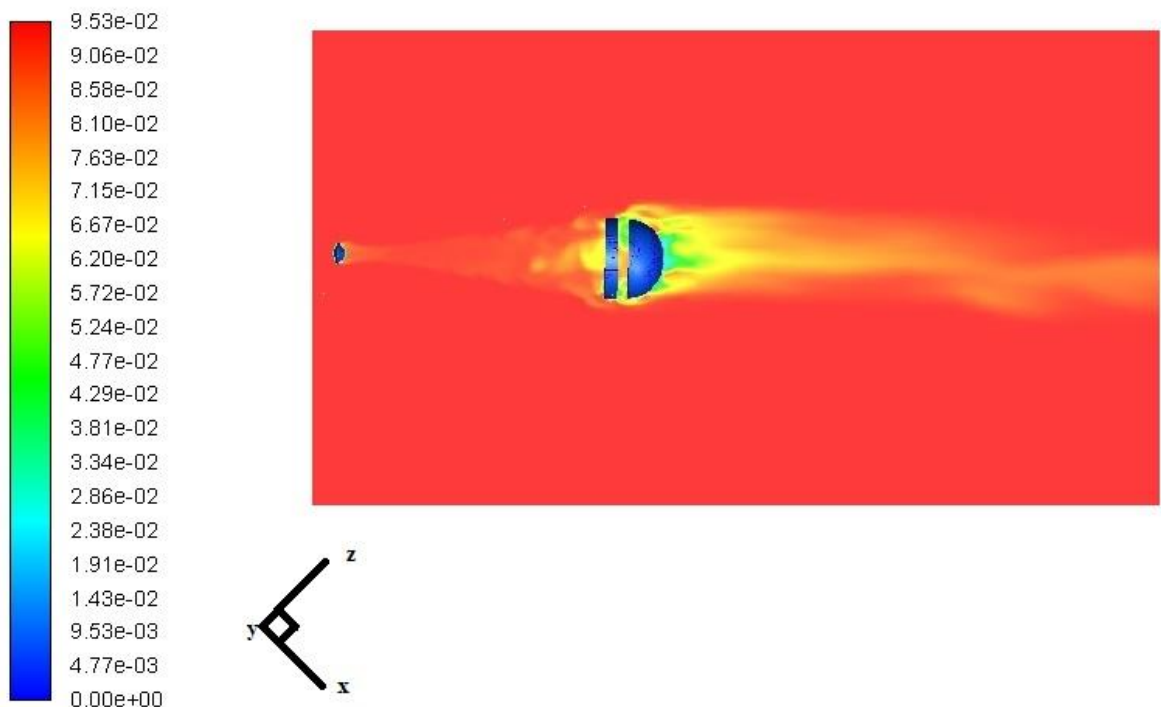


Fig 160. CO₂ Mass fraction contours for Re-entry parachute at $\alpha = 0^\circ$, H=10km and $M=2.04814$

When the shockwaves are detached at band gap of the parachute and formation of turbulent wake (TW₂) at backside of parachute, the CO₂ mass fraction observed is 0.9532 is shown in Fig 160.

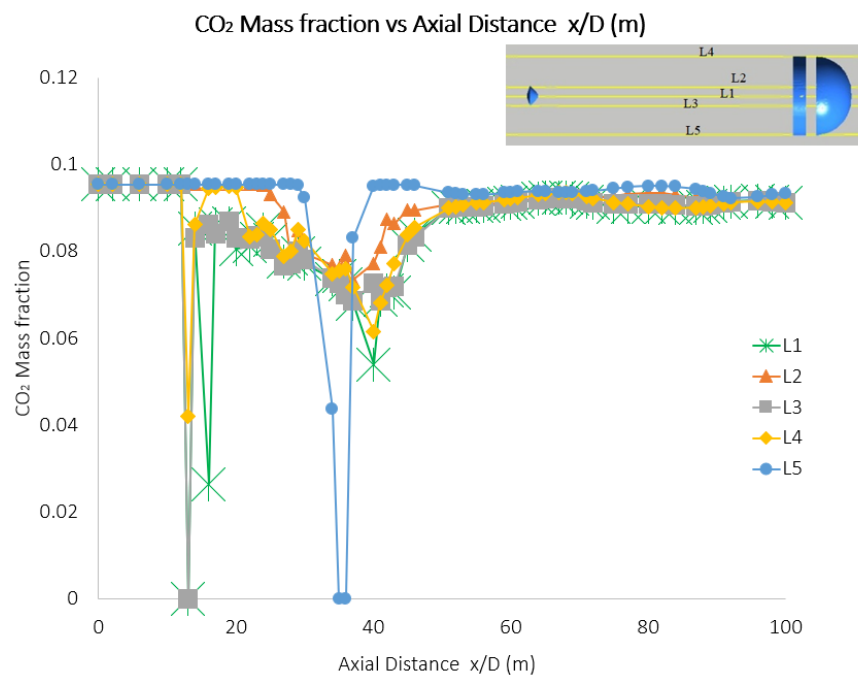


Fig 161. CO₂ Mass Fraction along the domain axial distance at $\alpha = 0^\circ$, H=10km, M=2.04814 and domain length = 120m

Fig 161 shows the Mass fraction of CO₂ is constant from 0m to 30 m at L9 till 12m in L6 and decreases till 38m distance and increases again from 39m to 52 m (L9 and L6).

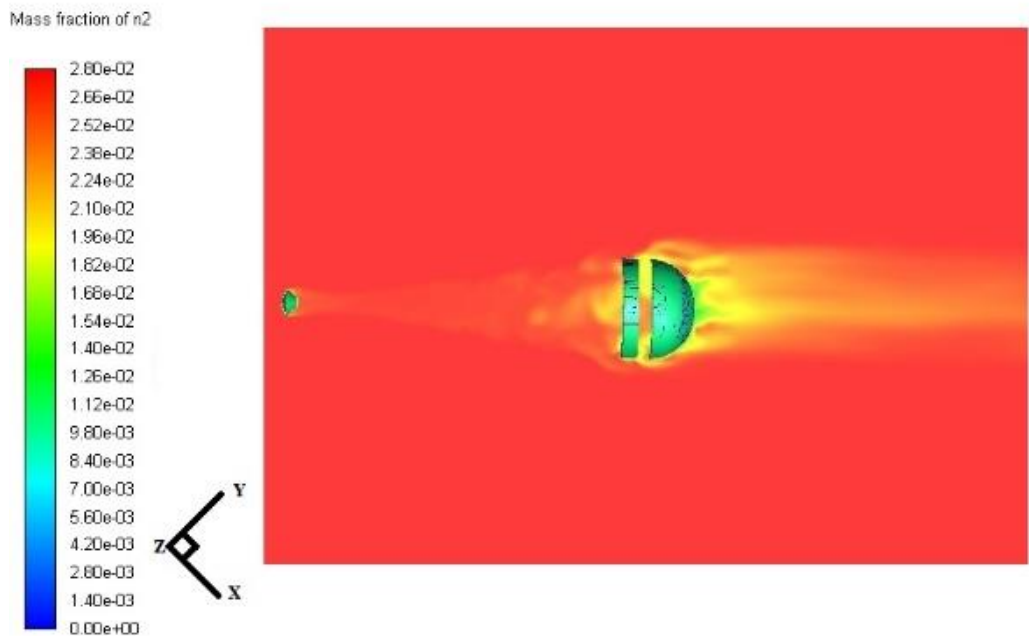


Fig 162. N_2 Mass Fraction Contours for Re-entry parachute for $H=10\text{km}$ above mars at $\alpha = 0^\circ$ and $M=2.04814$

When the shockwaves are arised at band gap of the parachute and backside of parachute, the N_2 Mass fraction observed is 0.028 (see Fig 162).

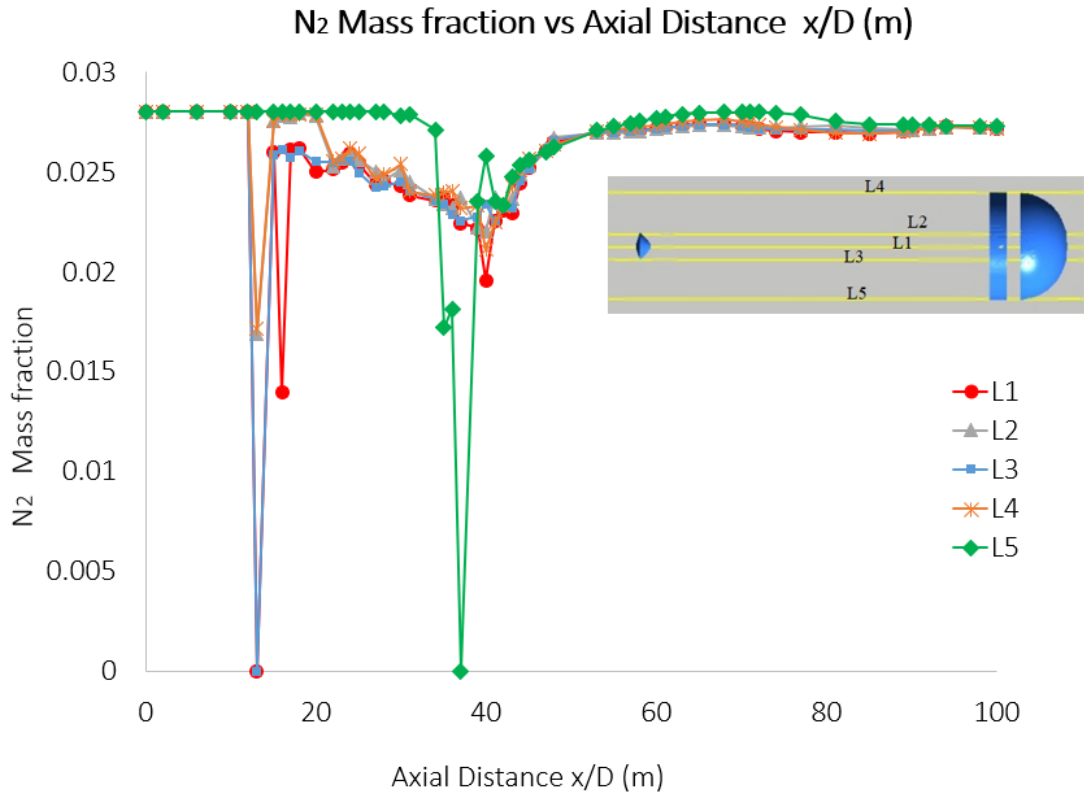


Fig 163. N_2 Mass fraction Mass Fraction along the domain axial distance $\alpha = 0^\circ$, $H=10\text{km}$, $M=2.04814$ and domain length = 120m

Fig 163 shows the Mass fraction of N_2 is constant from 0m to 18 m at L3 and L5 and till 3m in L2 and L4, L1(constant till 12) and decreases till 38m distance and increases again from 39m to100 m (in all lines) due to turbulent wake (TW_1) formation between capsule and canopy is shown in Fig 162.

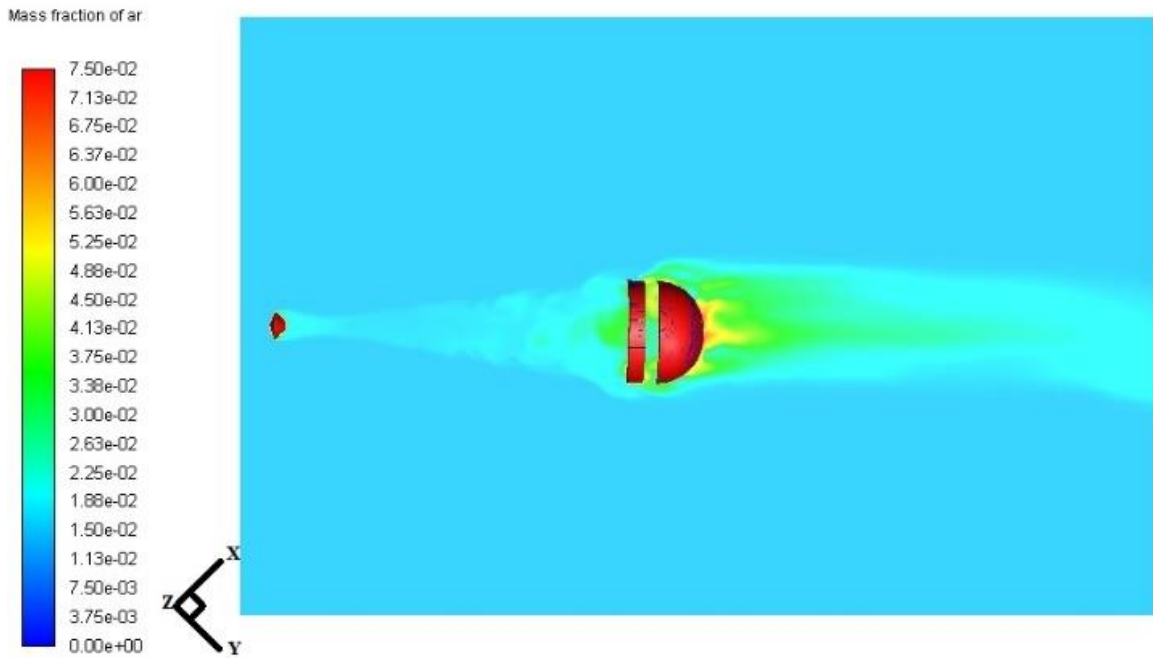


Fig 164. Ar Mass fraction contours for Re-entry parachute at $\alpha = 0^\circ$, $H=10\text{km}$ and $M=2.04814$

When the shockwaves are arised at band gap of the parachute and turbulent wake (TW_2) is formed at its backside, the Ar Mass fraction observed is 0.0525 (see Fig 164). The Maximum Mass fraction of Ar is 0.075 which is observed at the region of jet at aft body of the canopy.

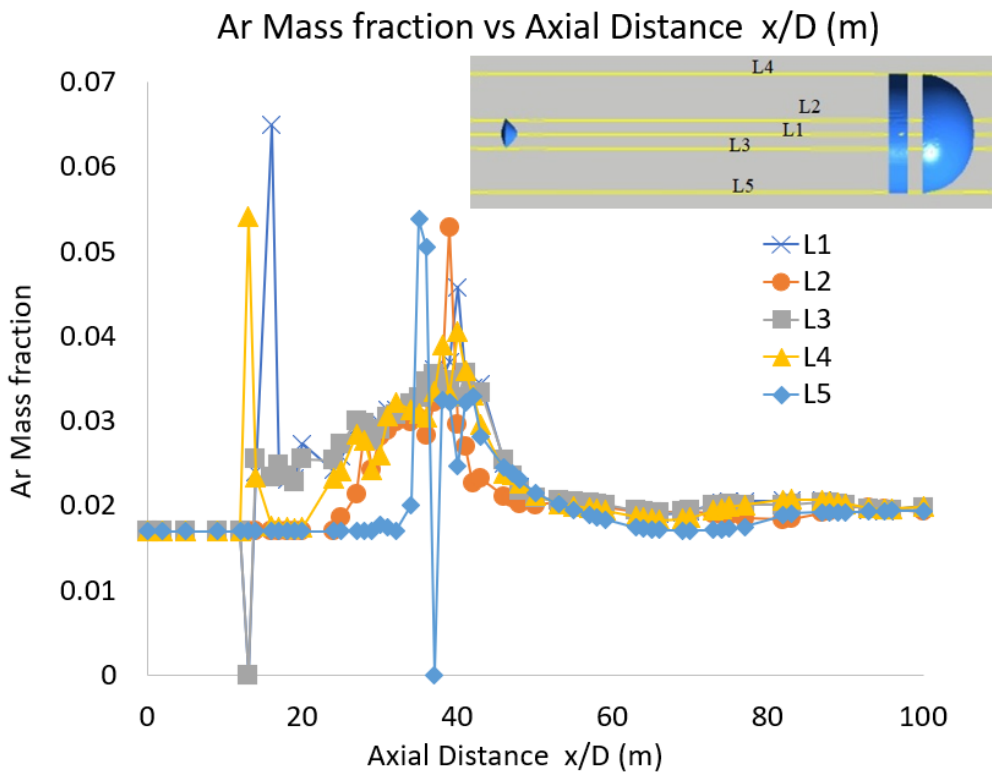


Fig 165. Ar Mass fraction along the domain axial distance $\alpha = 0^\circ$, $H=10\text{km}$, $M=2.04814$ and domain length = 120m

Fig 165 shows the Mass fraction of Ar is constant from 0m to 30 m at L5. It increases and decreases till 39m distance and increases again from 39m to 52 m (L1-L5) due to strong bow shockwaves (BS_1 and BS_2) arises from 1m distance at the front end of capsule and 5m distance at front end of parachute in the region of wake shock interaction due to pulsation as shown in Fig 164. It again increases and decreases slightly from 52m to 100 (L1-L5) m (see Fig 165) due to Turbulent Wake (TW_1) arises as at backside of canopy shown in Fig 164.

When compared the real gas model to the perfect gas model, in real gas model the bow shock is not located at front end of the capsule and canopy. there is a wake shock interaction arises at distance of 24000m between capsule and canopy (shown in Fig 160-Fig 165) and maximum pressure is observed as 751.10 Pa as shown in Fig 152 at $H= 10\text{km}$.

7.1.4.2 Simulation of Parachute using LES at M= 1.75 and Pressure= 538Pa

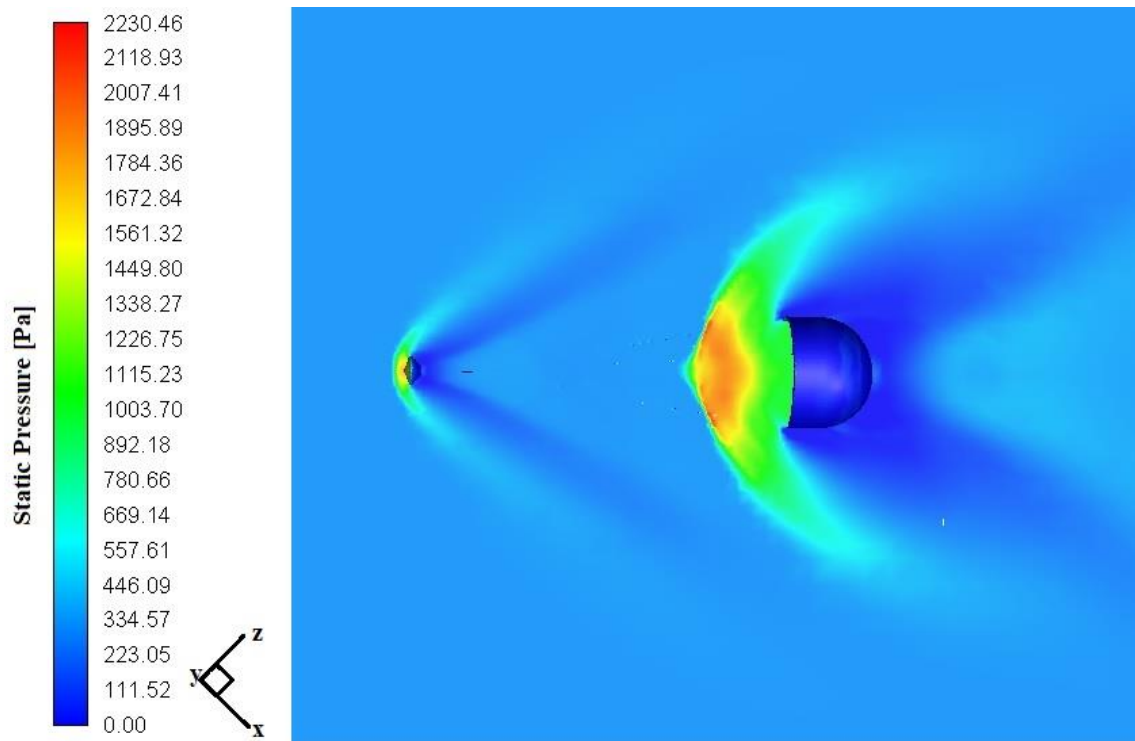


Fig 166. Static pressure contour for Re-entry parachute at $\alpha = 0^\circ$, $H=10\text{km}$ and $M=1.75$

When Schiaparelli parachute with Capsule at $H=10\text{km}$ and $M=1.75$, $P=538\text{Pa}$ [34] with same angle of attack, the strong bow shock (BS_1 and BS_2) detaches at 1.5 m from the front end of both Re-entry capsule with and 3.5 m from the front end of the parachute with high pressure and dominates flow body forefield due to pulsation. At $M=1.75$, the shock layer is wider at Angle of attack (α) = 0° . So, there is rise in pressure due to the strong shockwave arises as shown in Fig 166. The Turbulent wake region (TW_1 and TW_2) is formed at low pressure at backside of Canopy. The maximum static pressure observed is 2230.46Pa.

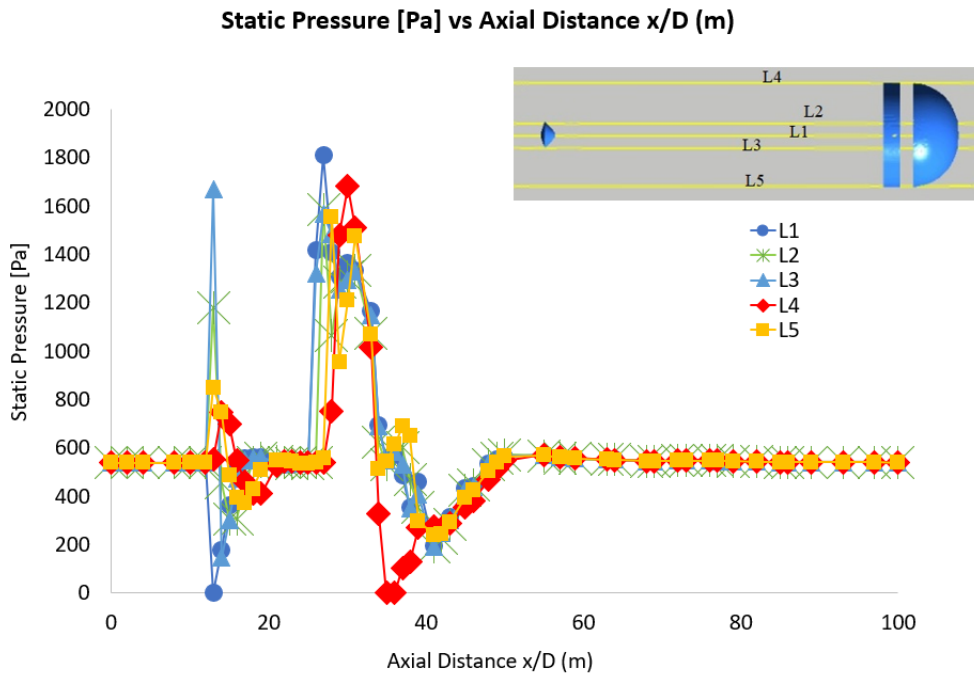


Fig 167. Static pressure along the domain axial distance at $H=10\text{km}$, $M=1.75$, $\alpha=0^\circ$ and domain length = 120m

Fig 167 shows, the pressure is constant from 0m to 12m (L1-L5) and 21m to 26m. There is increase and decrease in pressure from 13 m to 21m and from 26m to 50 m position. It becomes constant from 50m to 100m due to shockwave arises as shown in Fig 165. The pressure rises at peak level of 1809.19 Pa in the line L1 which is maximum among the remaining line of directions L2, L3, L4 and L5 (see Fig 167). The peak value of pressure observed in the line L2 is observed as 1584.82 Pa. The peak value of pressure is observed in the line L3 is 1668.037 Pa. The peak value of pressure is observed in the line L4 is 1681.171 Pa. The peak value of pressure is observed in the line L5 is 1555.59 Pa which is least among all the lines (see Fig 167).

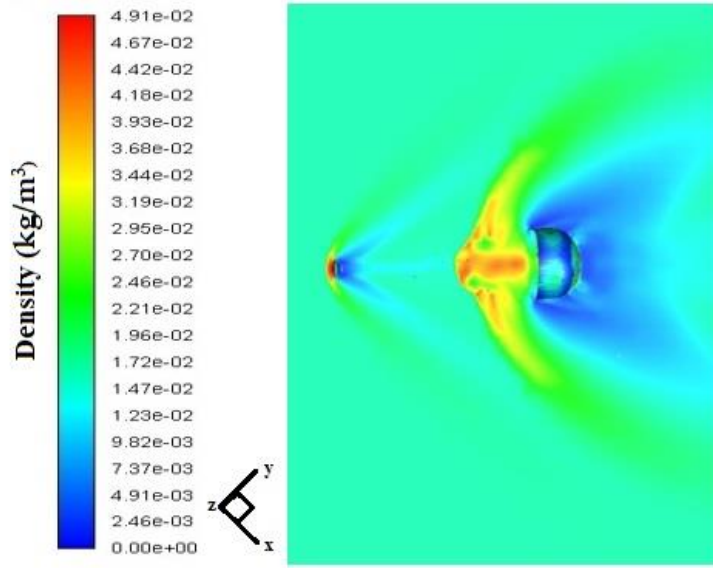


Fig 168. Density contour for Re-entry parachute at $\alpha = 0^\circ$ and $M=1.75$

At $H=10\text{km}$, the Bow Shock (BS_2) layer is wider at fore body of the parachute. So, there is a rise in density due to strong shockwave arises as shown in Fig 168. The recompression shock arised between capsule and canopy in the range of 0.0123 kg/m^3 . The Recompression shock (RS_2) is arised at the back side of canopy at lower density.

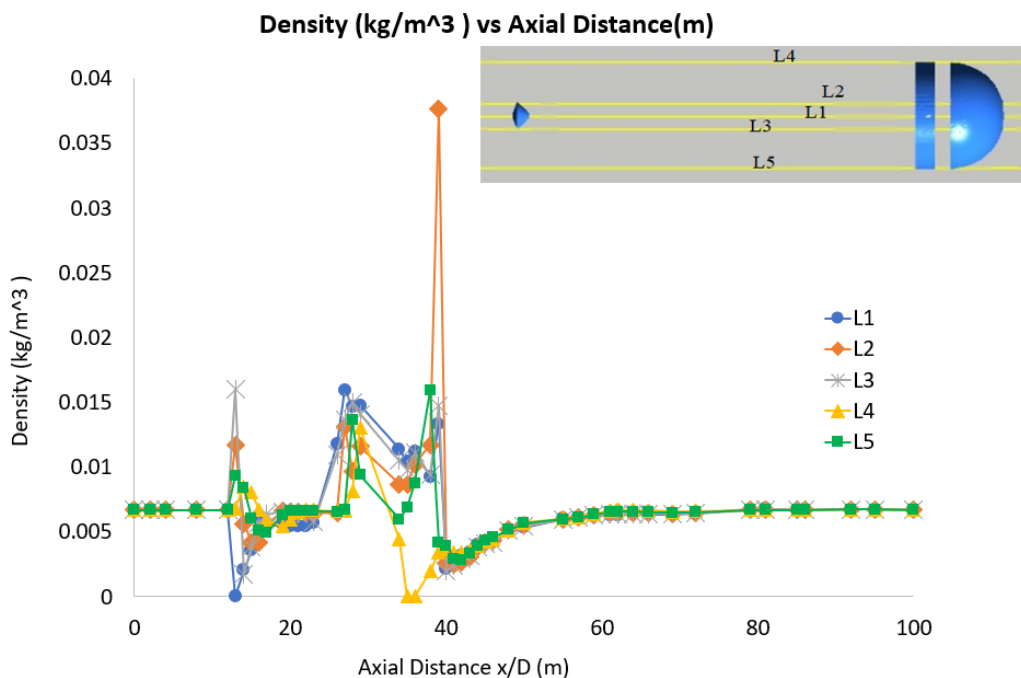


Fig 169.Density along the domain axial distance at $M=1.75$, $\alpha = 0^\circ$ and domain length = 120m

Fig 169 shows the density is constant from 0m to 10m (L1-L5). It decreases and increases till 15m distance and increases again from 18m to 60m due to strong Bow shocks (BS₁ and BS₂) arises from 1m distance at the front end of capsule and 5m distance at front end of parachute in the region of wake shock interaction due to pulsation as shown in Fig 168. It becomes constant from 60 m to 100m (see Fig 169) due to recompression shock (RS₂) arises at backside of canopy shown in Fig 168.

At M=1.75, the peak density is observed in the Line L2 is 0.037561908 kg/m³ which is maximum among all the lines. L1, L3, L4 and L5. The peak value of density observed in the line L1 is observed as 0.015962116 kg/m³. The peak value of density is observed in the line L3 is 0.015971074 kg/m³. The peak value of density is observed in the line L4 is 0.015903551 kg/m³. The peak value of density is observed in the line L5 is 0.013040675 kg/m³ (See Fig 169).

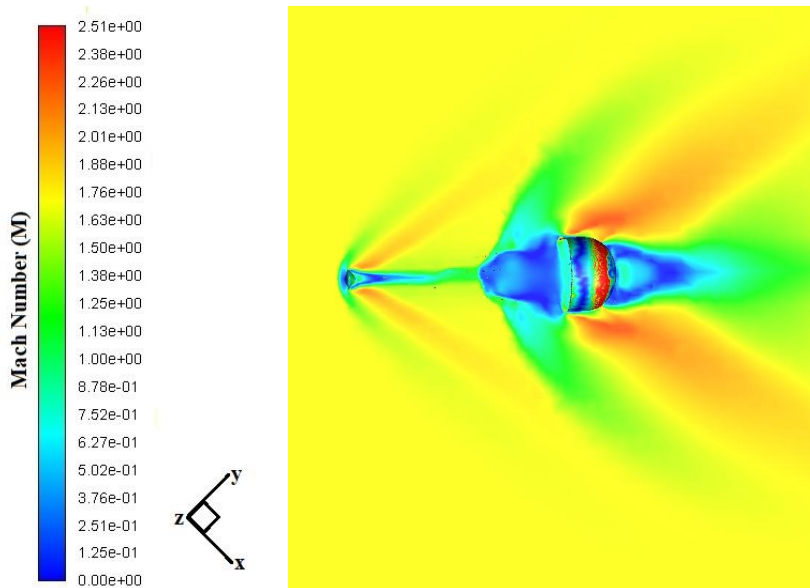


Fig 170. Velocity-Mach number Contour for Re-entry parachute at $\alpha = 0^\circ$, $M = 1.75$

Fig 170 shows that the strong bow shock (BS₁ and BS₂) detaches in front end of the Re-entry Capsule at the distance of 1m and 4m form front of the parachute and dominates the flow body forefield at M=1.745. The recompression shock (RS₂) layer is narrower at backside of canopy at H= 10km at $\alpha= 0^\circ$. The wake shock region is formed between middle end of the capsule and front end of the parachute at the trailing distance of

27239 mm. The supersonic jet leaving the hole behind the canopy at the range of $M = 2.51$.

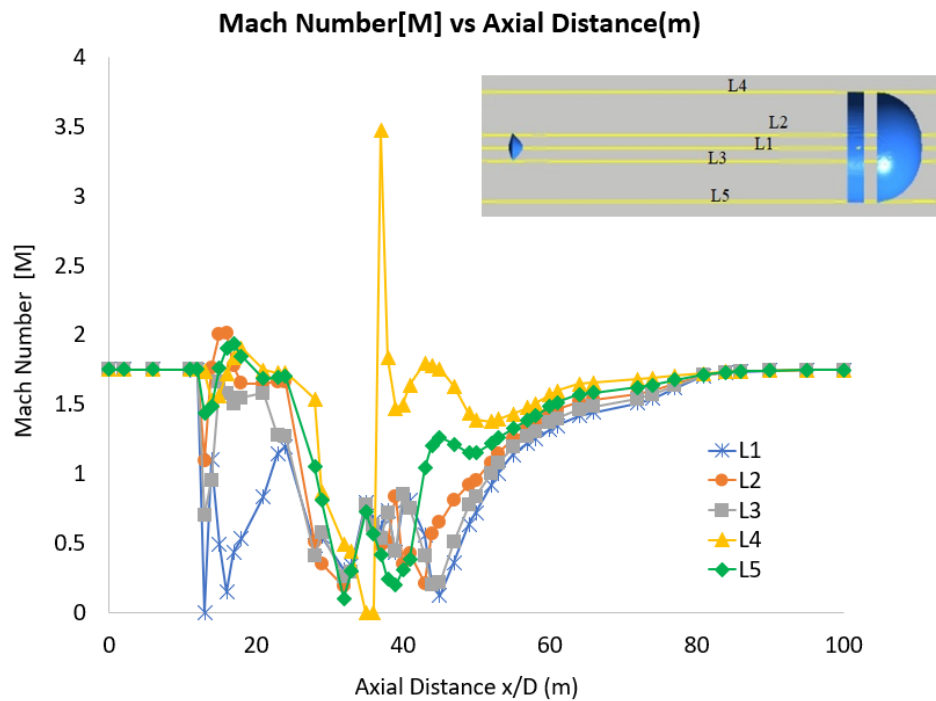


Fig 171. Velocity-Mach Number along the domain axial distance at $H=10\text{km}$, $M=1.75$, $\alpha=0^\circ$ and domain length = 120m

Fig 171 shows that the Mach number is constant from 0m to 10m in the direction of lines L1, L2, L3, L4 and L5. It varies from 11m to 100m (L1-L5) position due to pulsation of parachute at straight path as shown in Fig 170. There is a Peak level rise of Mach number at 30m position in L5 ($M=3.5$).

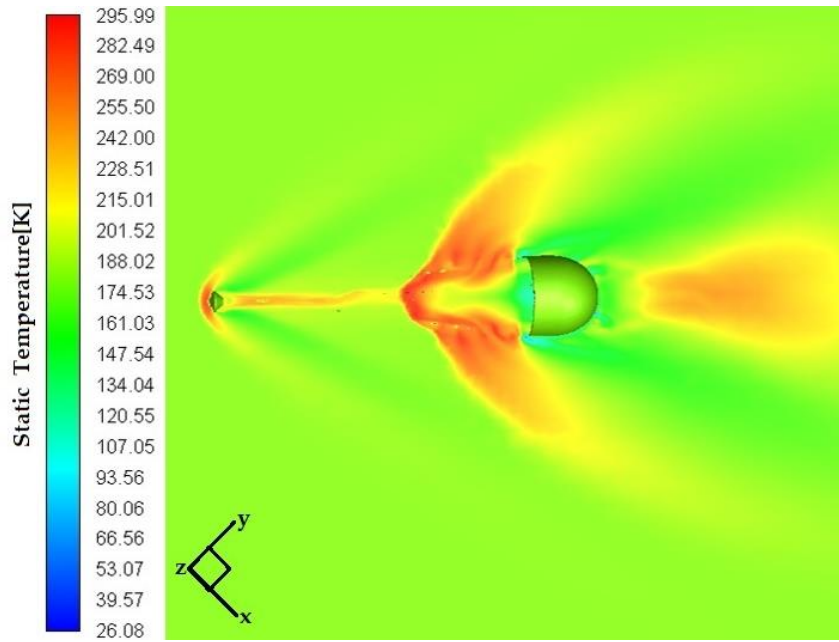


Fig 172. Static temperature contour for Re-entry parachute at $\alpha = 0^\circ$ and $M=1.75$

The wake shock interaction is formed between aft body of the and forebody of canopy as showed in Fig 172. The temperature is observed as 228.51 K in wake-shock interaction between Capsule and Canopy and at the region of Turbulent Wake (TW_2) which is formed at back side of canopy.

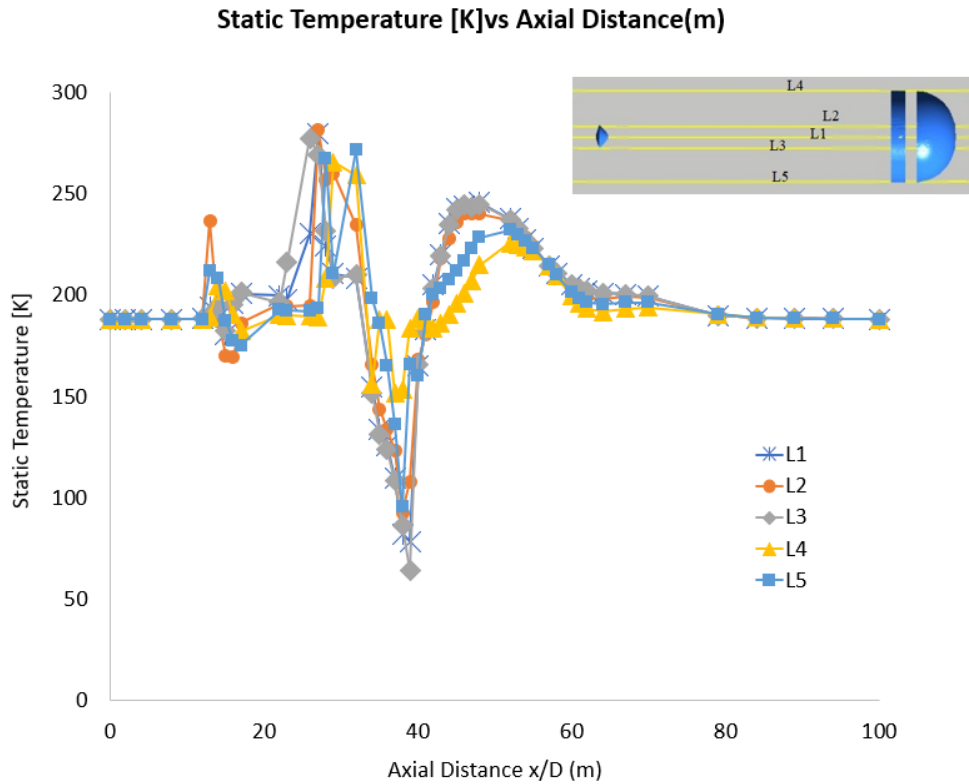


Fig 173. Static Temperature along the domain axial distance at $H=10\text{km}$, $M=1.75$, $\alpha=0^\circ$ and domain length = 120m

Fig 173 shows that the static temperature is constant from 0m to 10m, and it became increases and then decreases form 11m to 100m (See Fig 173) due to there is a detachment of shockwave at front end of capsule and slightly at front end of parachute at high temperature due to pulsation as shown in Fig 172. At 10km and $\alpha=0^\circ$, the peak static temperature is observed in the Line L2 is 282.091 K which is maximum among all the lines. L1, L3, L4 and L5 (see Fig 173). The peak value of temperature observed in the line L1 is observed as 279.863 K. The peak value of temperature is observed in the line L4 is 266.023 K. The peak value of static temperature is observed in the line L5 is 271.7263K which is least among all the remaining lines of direction (see Fig 173).

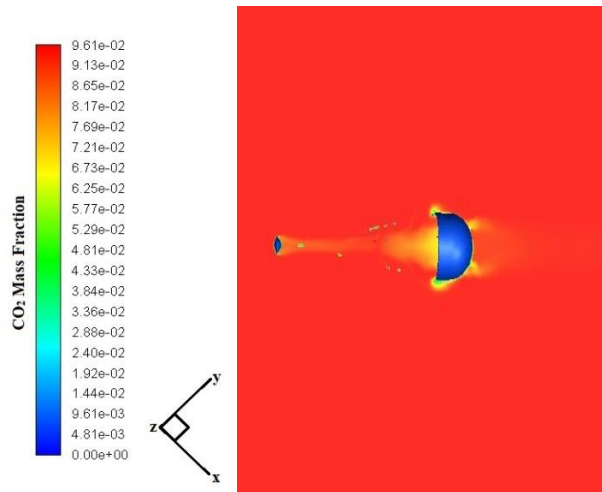


Fig 174. CO_2 Mass Fraction Contour for Re-entry parachute at $\alpha = 0^\circ$, $H=10km$ and $M=1.75$

At $M=1.75$ in same Altitude(H) and Angle of attack (α), the shockwave detached at the forebody of parachute with minimum range of $1*10^{-6}$ m distance at the front end of capsule and 3m distance at front end of parachute, maximum mass fraction is observed at 0.0961. The average wake shock interaction has been arised between the capsule and the canopy at range of mass fraction at 0.0721. When the shockwaves are arised at band gap of the parachute and backside of parachute due to pulsation, the CO_2 mass fraction observed is 0.0769 is shown in Fig 174. The recirculation zones are formed near the tips at the sides of the canopy.

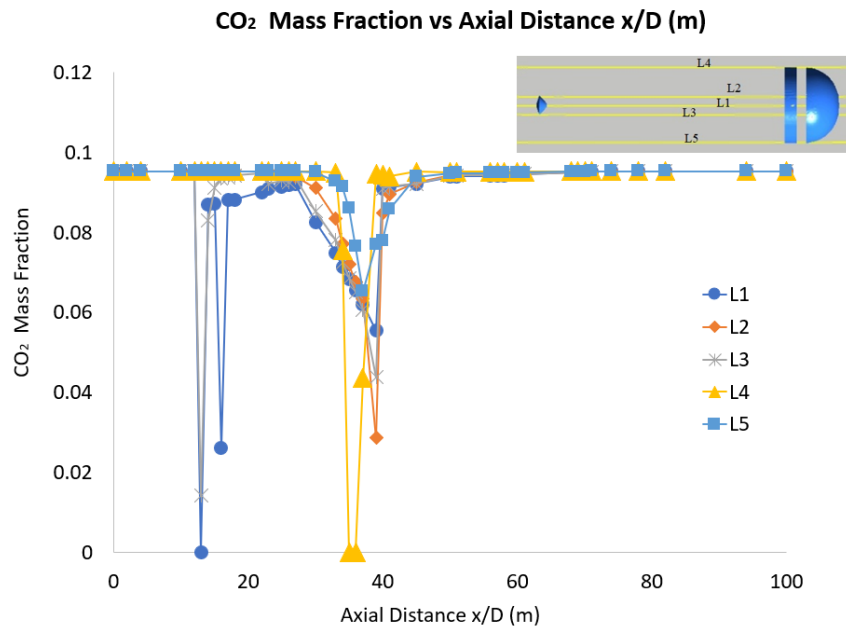


Fig 175. CO₂ Mass fraction along the domain axial distance at H=10km, M=1.75, $\alpha=0^\circ$ and domain length = 120m

Fig 175 shows the Mass fraction of CO₂ is constant from 0 m to 30 m (L2-L5) till 30 m and till 11m in L1. It decreases and increases again from till 50m in line 9 and till 51m in L1, L2, L3, L4 and L5 due to strong shockwaves arises from 0.1m distance at the front end of capsule and 0.5m distance at both sides of canopy in the region of wake shock interaction due to pulsation as shown in Fig 174. Mass fraction of CO₂ becomes zero at L5 from 35 m to 36 m distance (see Fig 175).

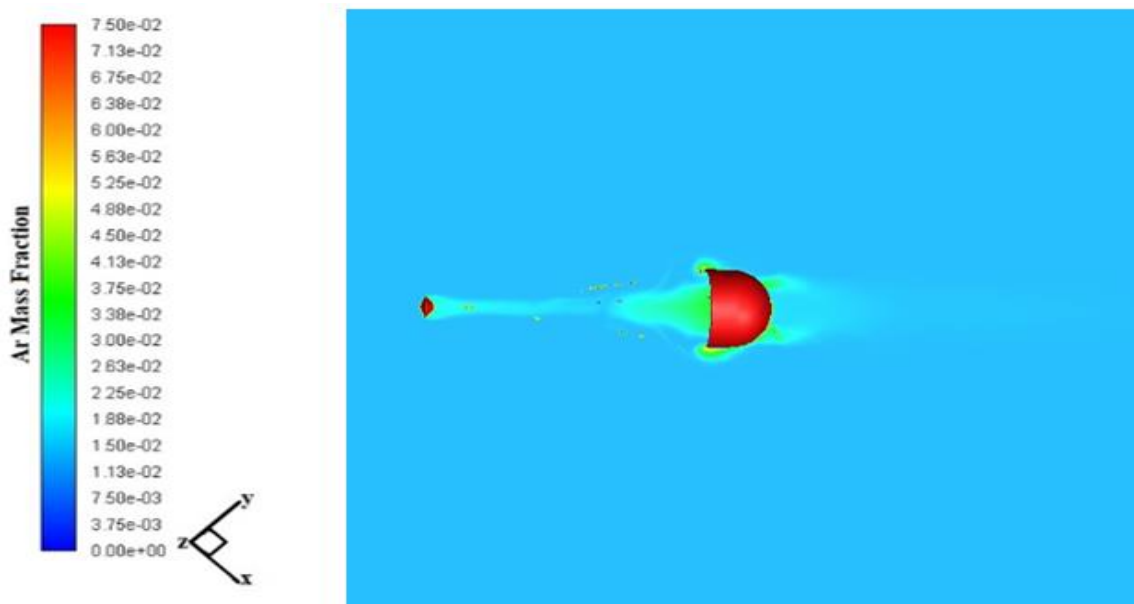


Fig 176. Ar Mass Fraction Contour for Re-entry parachute at $\alpha = 0^\circ$, $H=10\text{km}$ and $M=1.75$

At $M=1.75$ in same altitude(H) and Angle of attack (α), that the shockwaves arise from the front of the Capsule at 0.0001m and the wake is narrower at the aft body of the capsule is shown in Fig 176. There is a turbulent wake shock (TW_1) interaction occurs between the capsule and the parachute in the high mass fraction of Argon. There is a medium Ar mass fraction at 0.00413 due to the re-circulation zones are formed in the fore end and rear ends of the canopy (see Fig 176).

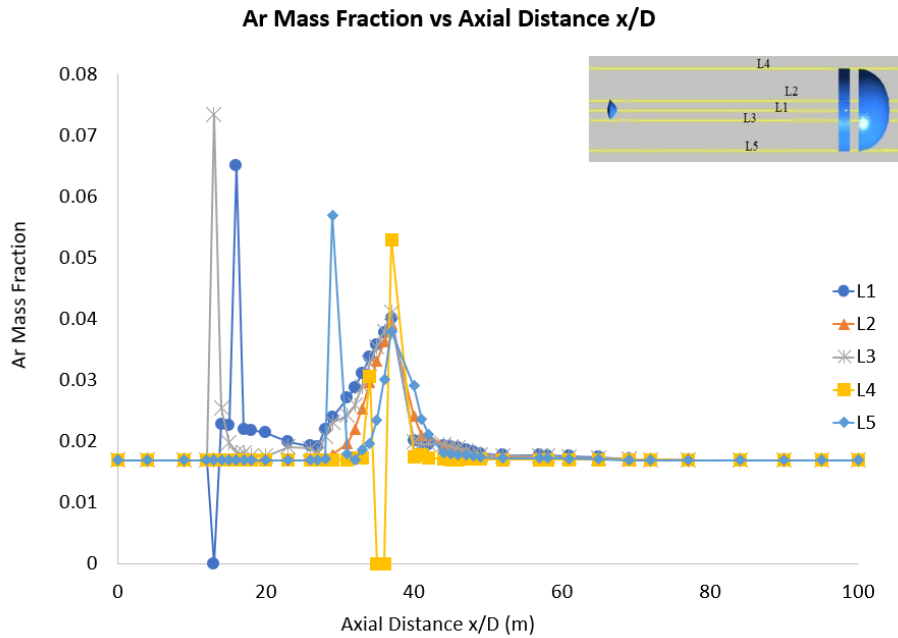


Fig 177. Ar mass fraction along the domain axial distance at $H=10\text{km}$, $M=1.75$, $\alpha=0^\circ$ and domain length = 120m

Fig 177 shows the Mass fraction of Argon is constant from 0m to 29m at L5. It increases and decreases till 45m distance (L1-L5) and till 50m (L3) due to strong shockwaves arises from 0.0051m distance at the front end of capsule and 0.001m distance at sides in the region of wake shock interaction due to pulsation as shown in Fig 176. It again increases and decreases slightly from 52m to 100m in all lines (See Fig 177) due to narrow shockwave arises as at backside of canopy shown in Fig 176.

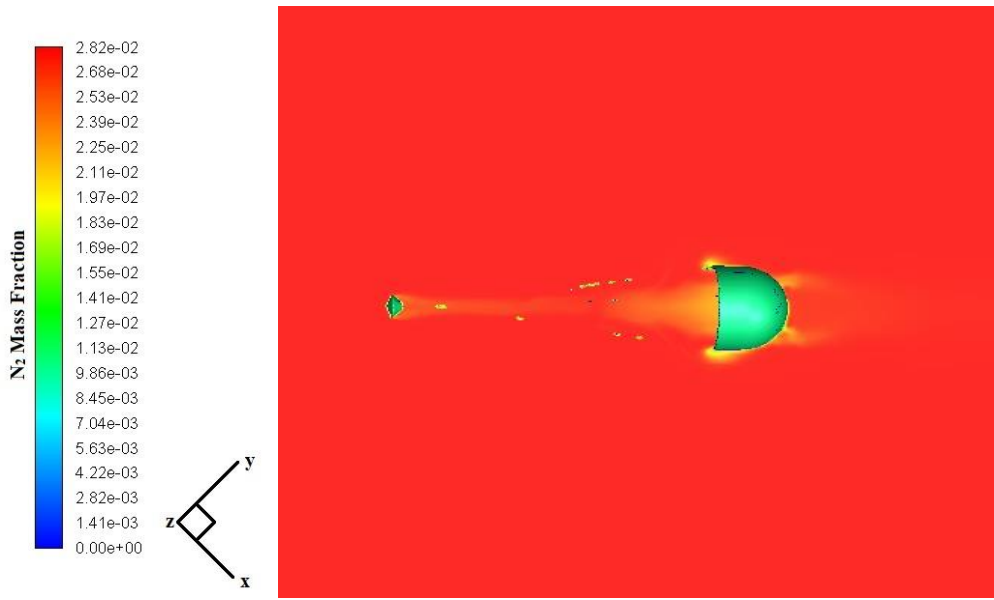


Fig 178. N_2 Mass Fraction Contour for Re-entry parachute at $\alpha = 0^\circ$, $H=10\text{km}$ and $M=1.75$

At $M=1.75$ in same Altitude (H) and Angle of attack(α), the shockwave detached at the forebody of parachute with minimum range of $1*10^{-8}\text{ m}$ distance at the front end of capsule and 3m distance at front end of parachute, maximum N_2 mass fraction is observed at 0.0282 . The average wake shock interaction has been arised between the capsule and the canopy at range of mass fraction at 0.02115 . When the shockwaves are arised at band gap of the parachute and backside of parachute due to pulsation, the N_2 mass fraction observed is 0.0211 due to formation of recirculation zones near the tips at the sides of the canopy is shown in Fig 178. The turbulent wake and bow shock interactions are formed between capsule and canopy with addition of gases in Martian atmosphere (see Fig 174, Fig 176, Fig 178).

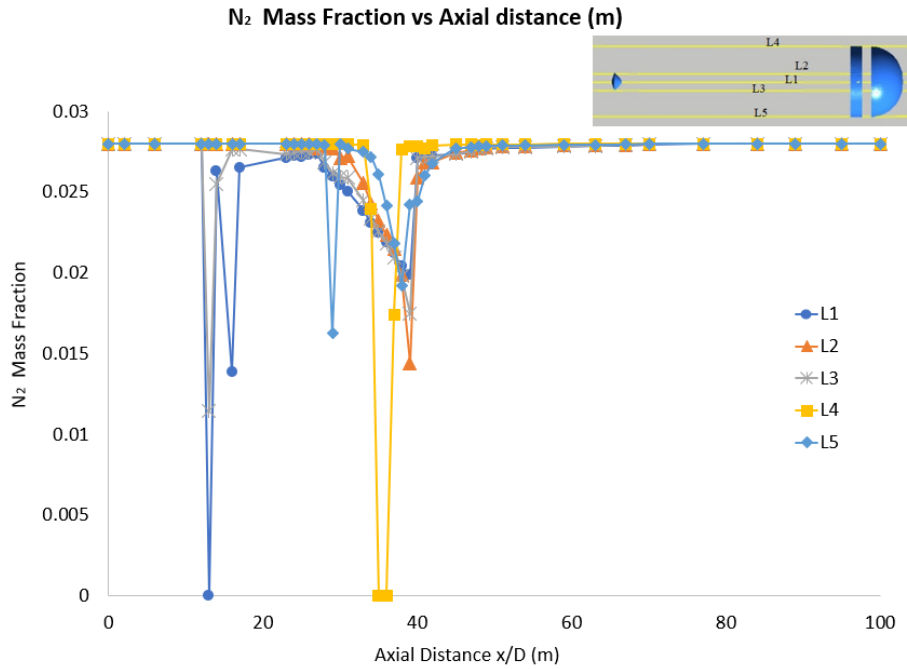


Fig 179. N_2 mass fraction along the domain axial distance at $H=10\text{km}$, $M=1.75$, $\alpha =0^\circ$ and domain length = 120m

Fig 179 shows the Mass fraction of N_2 is constant from 0m to 11 m(L1, L2) and till 26m (L3, L4) and till 32m in L5 .It decreases and increases from 13m to 50 m (L1, L2) and from 27m to 50m in remaining distance of lines (see Fig 179) due to strong shockwaves arises from 0.011m distance at the front end of capsule and 0.01m distance sides of parachute in the region of wake shock interaction due to pulsation (see Fig 178).

When compared the real gas model to the perfect gas model, in real gas model the bow shock is not located at front end of the capsule and canopy. there is a wake shock interaction arises at distance of 24000m between Capsule and Canopy (see Fig 174 – Fig 179) and Maximum Pressure is observed as 2230.46 Pa as shown in Fig 166 at $H = 10\text{km}$.

7.1.4.3 Simulation of Parachute at using SST k- ω $\alpha = 20^\circ$ and $M = 2.04814$

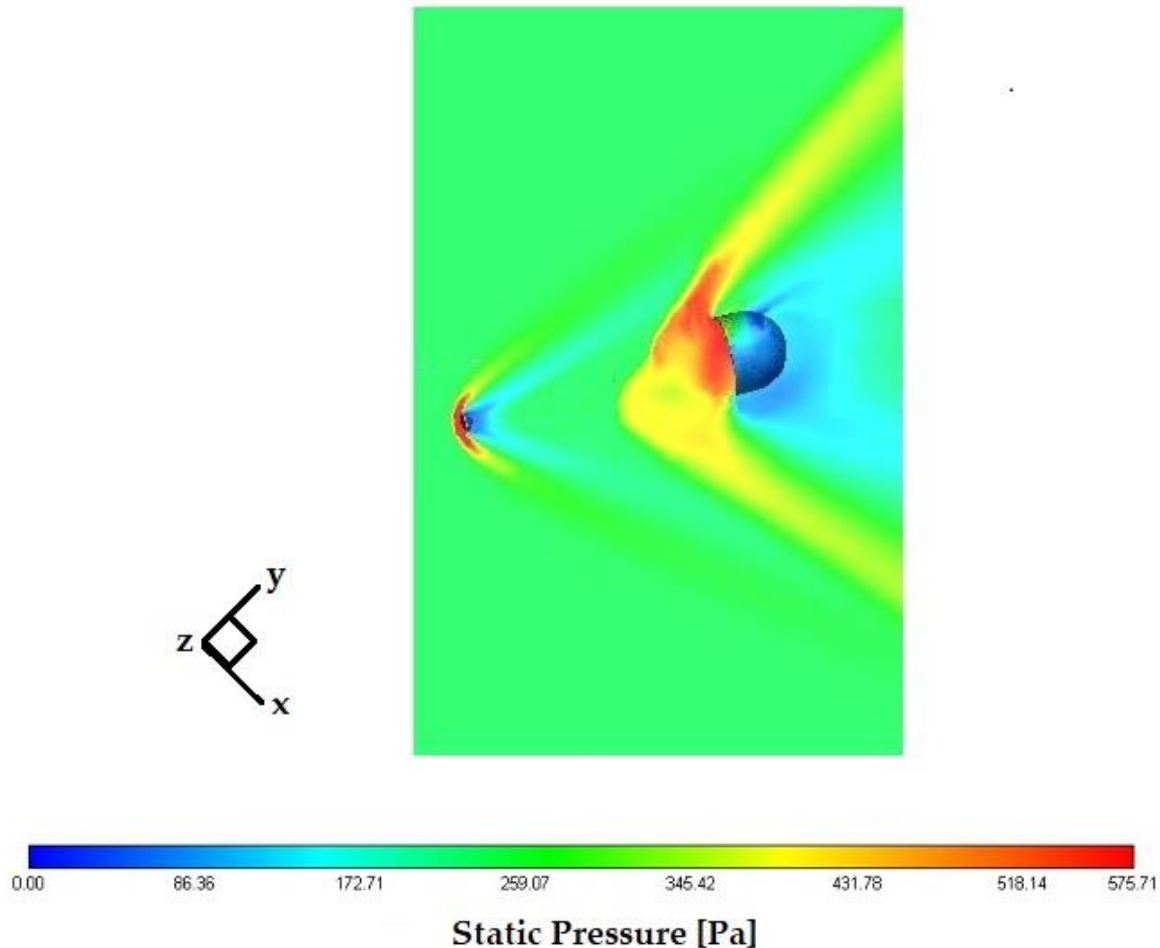


Fig 180. Static pressure contour for Re-entry parachute at $\alpha = 20^\circ$, H=10km and M=2.04814

When Schiaparelli parachute with Capsule at $H = 20\text{km}$ and $\alpha = 20^\circ$ with high Mach number at supersonic speed, the strong bow shock detaches at 0.8m form front end of Re-entry Capsule (BS₁) with high pressure and at 0.4m form front end of the parachute (BS₂) with medium pressure and dominates flow body forefield. At $M=2$, the shock layer is wider at back side of canopy due to its oscillation at Angle of attack (α)= 20° . So, there is increase in pressure at 575.71 Pa due to the strong shockwave arises as shown in Fig 180. The wake shock interaction between capsule and canopy has minimum pressure of 86.36 Pa.

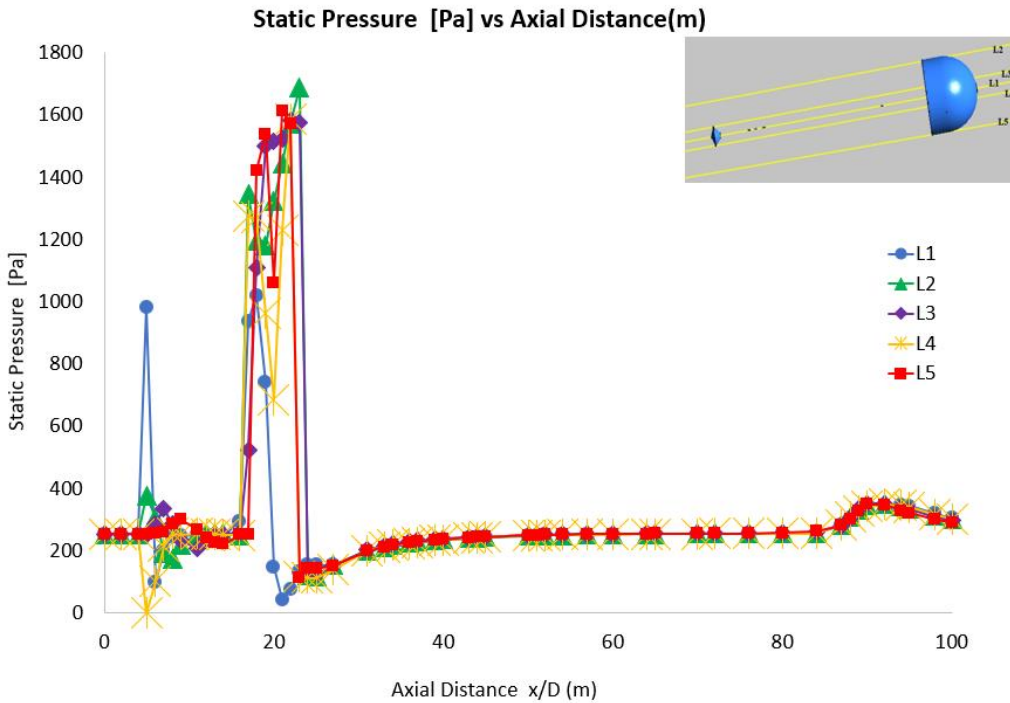


Fig 181. Static pressure along the domain axial distance at $H=10\text{km}$, $M=2.04814$, $\alpha = 20^\circ$ and domain length = 120m

Fig 181 shows, the pressure is constant from 0m to 4m (L1, L2, L3) and 0 to 6m in lines L4 and L5. It becomes constant from 11m to 14m. There is increase and decrease in Pressure till 25m position due to the interaction of turbulent shock wave (TW_1) and bow shock (BS_2) is shown in Fig 180. The pressure rises at peak level in Line L3, L4, L5. At 10km and $\alpha = 20^\circ$, the peak pressure is observed in the Line L2 is 1688.61 Pa which is maximum among all the lines. L1, L3, L4 and L5. The peak value of pressure observed in the line L1 is observed as 982.15 Pa. The peak value of pressure is observed in the line L3 is 1588.84 Pa. The peak value of pressure is observed in the line L4 is 1582.59 Pa. The peak value of pressure is observed in the line L5 is 1612.77 Pa (see Fig 181).

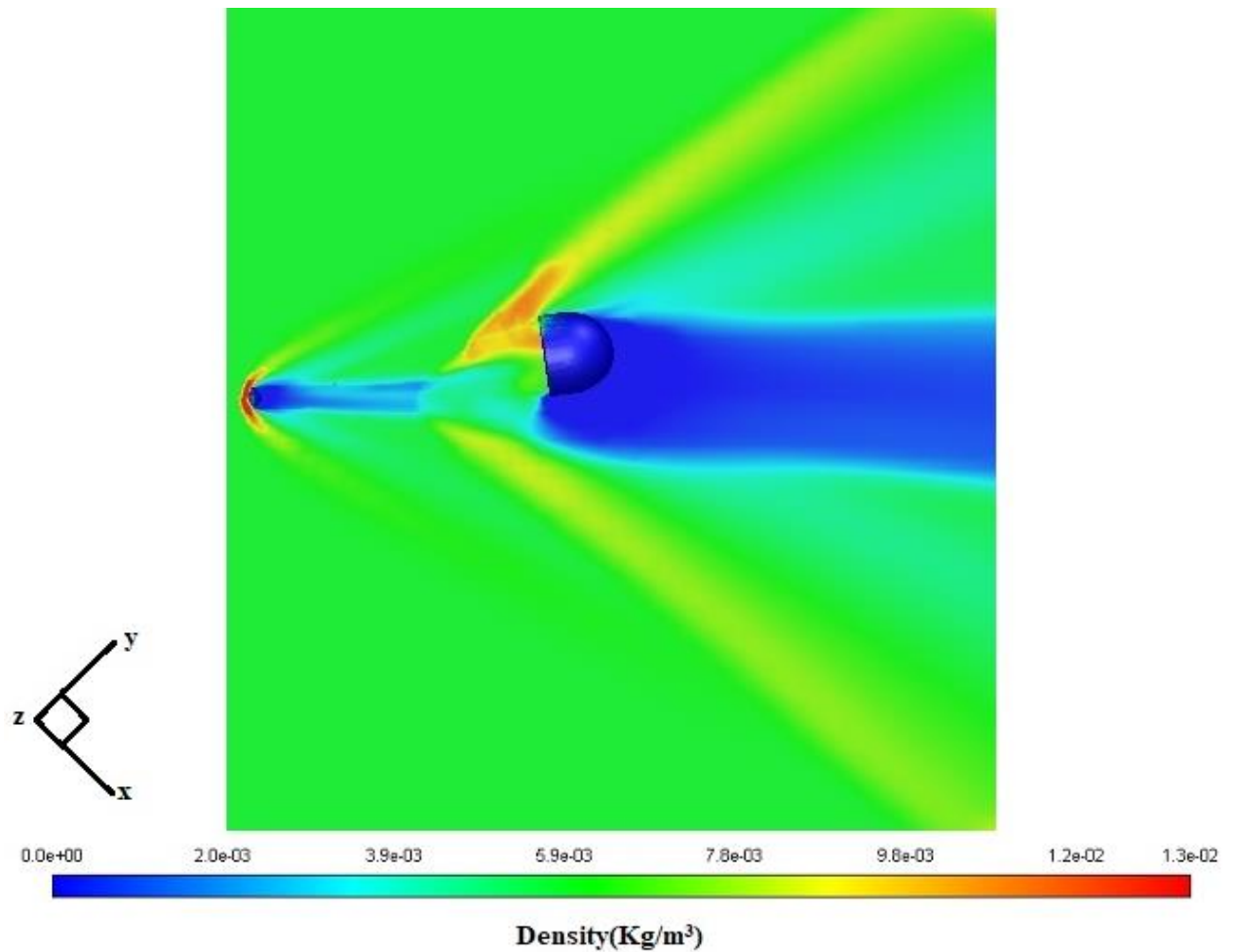


Fig 182. Density Contour for Re-entry parachute at $\alpha = 20^\circ$, $H=10\text{km}$ and $M=2.04814$

When Schiaparelli parachute with capsule results at $H = 10\text{km}$ and $\alpha = 20^\circ$ with high Mach number of supersonic speeds, the strong bow shock detached at 0.3m from the front end of both Re-entry capsule with high density and slightly at front end of the parachute with medium density and dominates flow body forefield. As the turbulent wake layer is narrow due to oscillation at $\alpha = 20^\circ$, there is low in density as shown in Fig 182. The wake shock interaction arises from aft body of capsule till the front end of parachute from minimum to maximum density (see Fig 182).

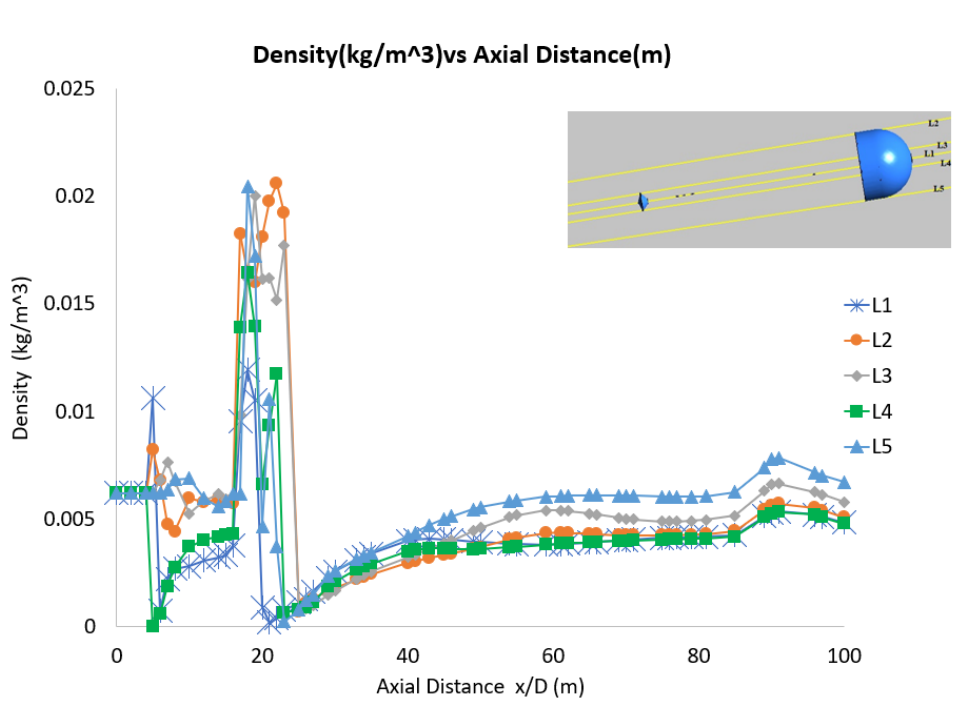


Fig 183. Density along the domain axial distance at $\alpha = 20^\circ$, $H=10\text{km}$, $M=2.04814$ and domain length = 120m

Fig 183 shows the density is constant from 0m to 4m (L1, L2, L3) and 0 to 5m in L4 and 0 to 6m in L5. It rises and falls till 25m distance and increases gradually again from 31m to 90m due to strong shockwaves arises from 1m distance at the front end of capsule and 3m distance at front end of parachute in the region of wake shock interaction due to pulsation as shown in Fig 182. It falls again from 91m to 100m due to wake region arises at backside of capsule at lower density in less pulsation. At 10km and $\alpha=0^\circ$, the peak density is observed in the line L2 is 0.020576 kg/m^3 which is maximum among all the lines L1, L3, L4 and L5 (see Fig 183). The peak value of density observed in the line L1 is observed as 0.01192 kg/m^3 . The peak value of density is observed in the line L3 is 0.0200074 kg/m^3 . The peak value of density is observed in the line L4 is 0.016450 kg/m^3 . The peak value of density is observed in the line L5 is 0.020450 kg/m^3 (see Fig 183).

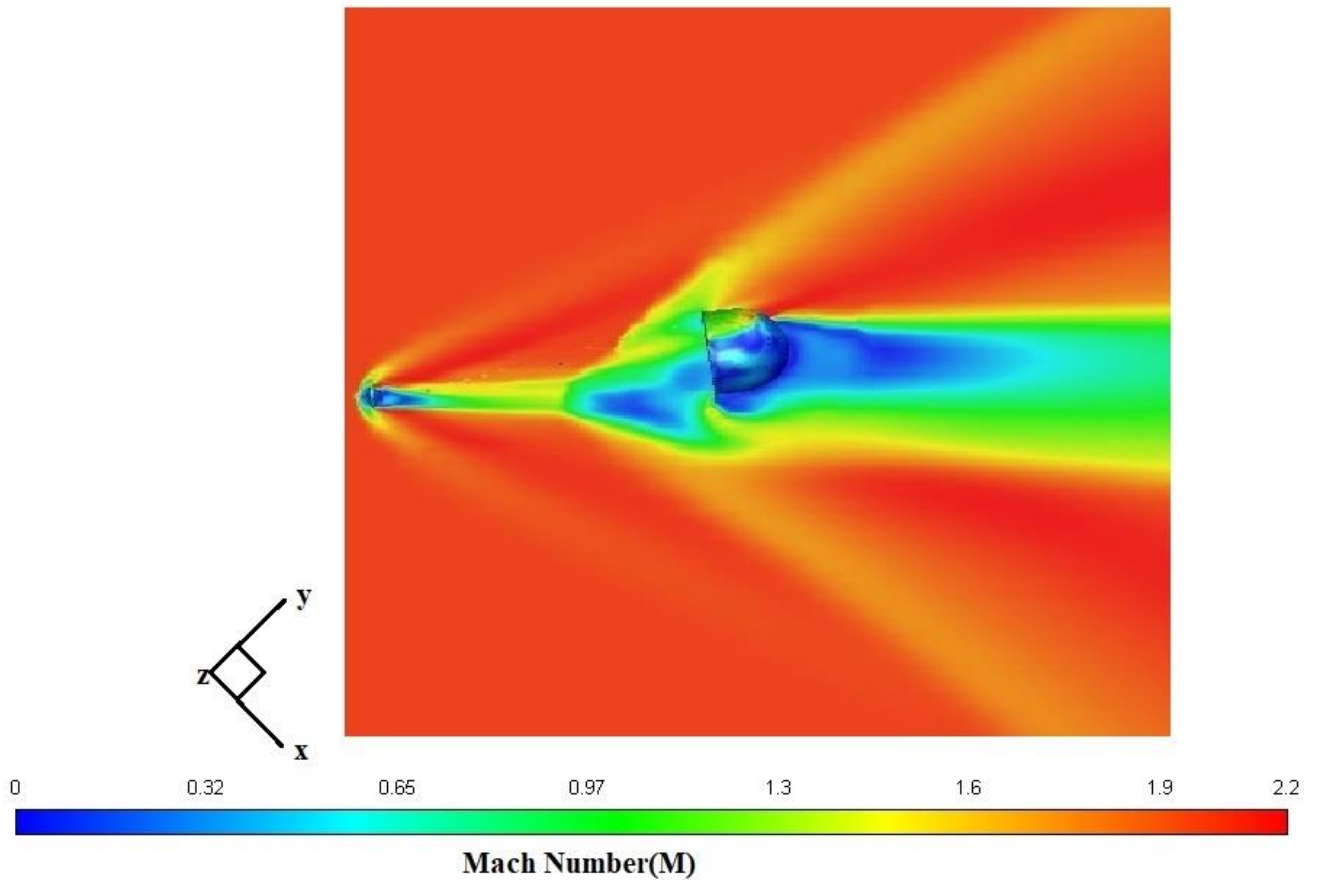


Fig 184. Velocity-Mach number contour for Re-entry parachute at $\alpha = 20^\circ$, $H=10\text{km}$ and $M=2.04814$

Fig 184 shows that the strong bow shock detaches in front end of the Re-entry capsule and slightly in front of the parachute and dominates the flow body forefield at low Mach number range. The Mach number is low at turbulent wake between capsule and Canopy (TW_1). The turbulent wake (TW_2) is narrower at backside of canopy at $H=10\text{km}$ due to its oscillation at $\alpha = 20^\circ$ with supersonic speed. The higher Mach number is observed in the Martian atmosphere at $M= 2.2$ (Velocity (c) = 1031.8m/s).

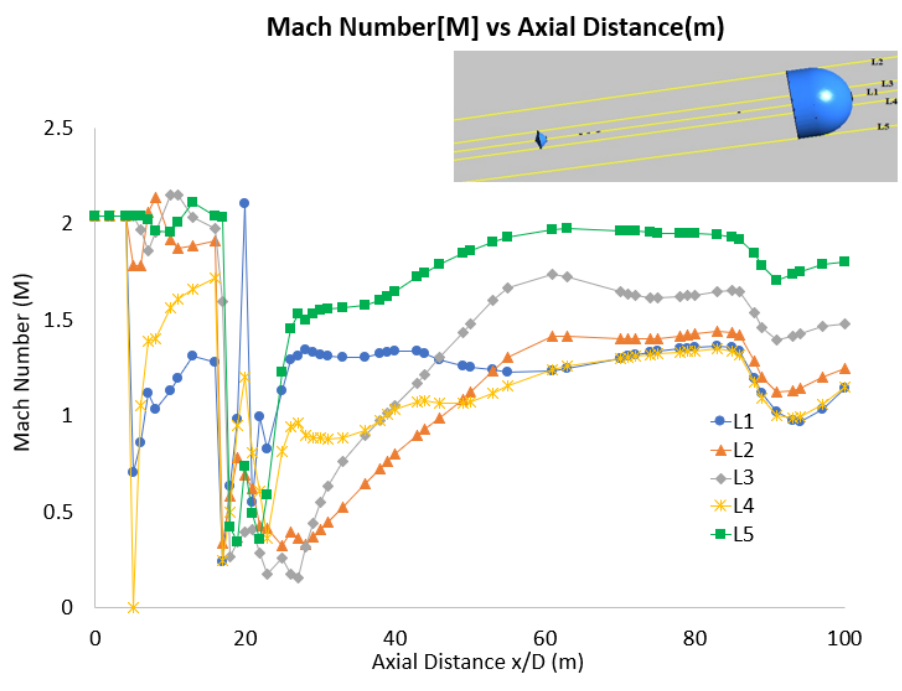


Fig 185. Velocity-Mach Number along the domain axial distance at $\alpha = 20^\circ$, $H=10\text{km}$, $M=2.04814$ and domain length = 120m

Fig 185 shows that the Mach number is constant from 0m to 4m in the lines L1, L2, L3 and from 0 to 5m in the line L4 and became constant till 6m in the line L5. It rises and falls till 100m in the lines of directions L1 to L5 due to pulsation of parachute at straight path as shown in Fig 184.

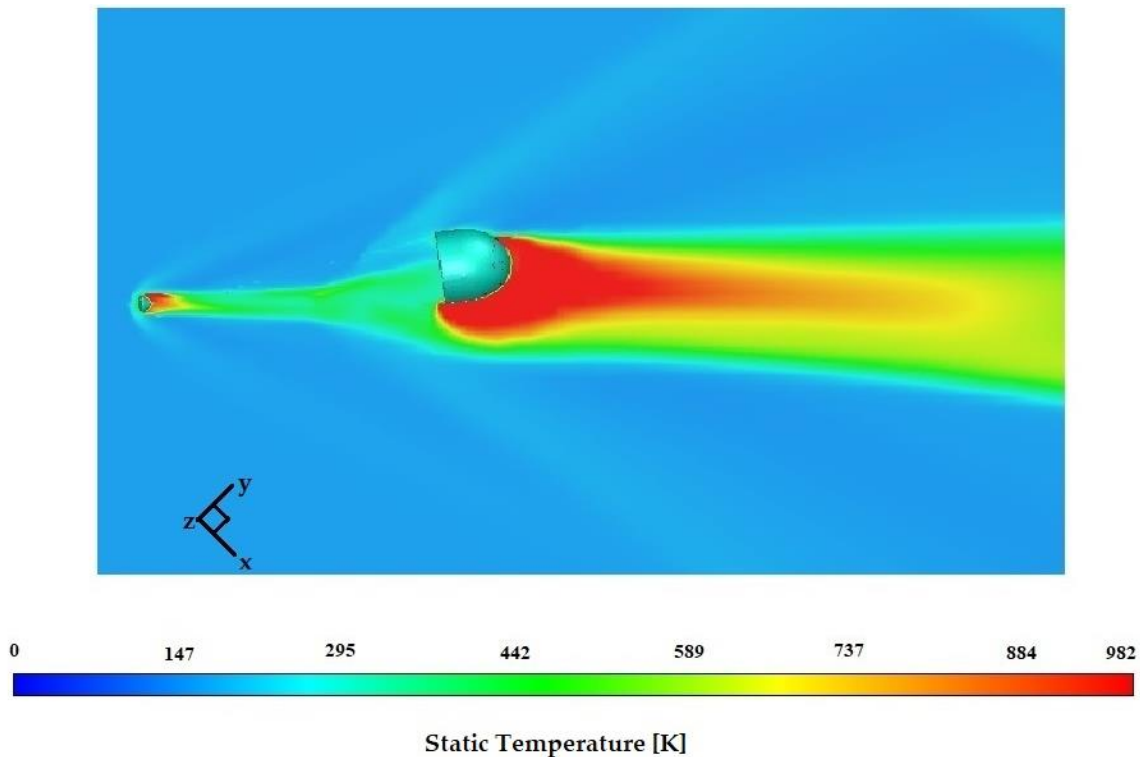


Fig 186. Static Temperature Contour for Re-entry parachute at $\alpha = 20^\circ$, H=10km and M=2.04814

Fig 186 shows that the maximum temperature is observed on the re-compression shock (RS₁ and RS₂) layers which are formed at rear end of capsule and canopy is 982K.

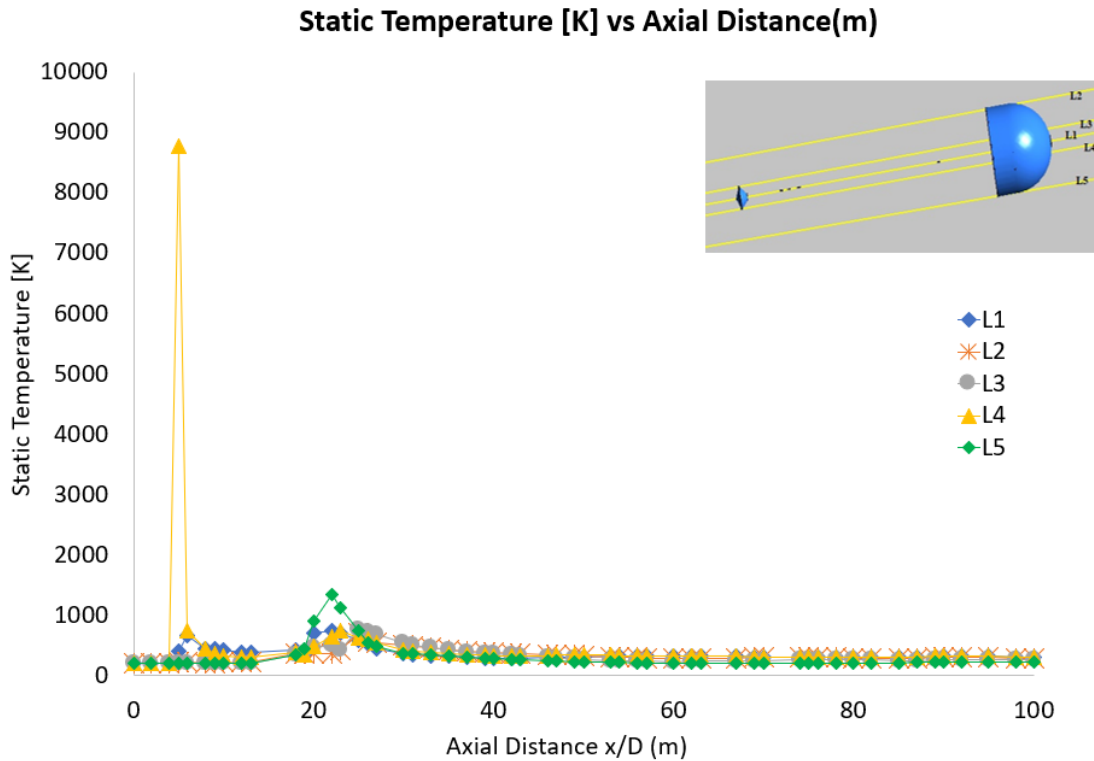


Fig 187. Static temperature along the domain axial distance at $\alpha = 20^\circ$, $H=10\text{km}$, $M=2.04814$ and domain length = 120m

Fig 187 shows the Static temperature increases in line of direction L5 (1.5m) is maximum as of the shockwave near to the left side border of the canopy (see Fig 186).

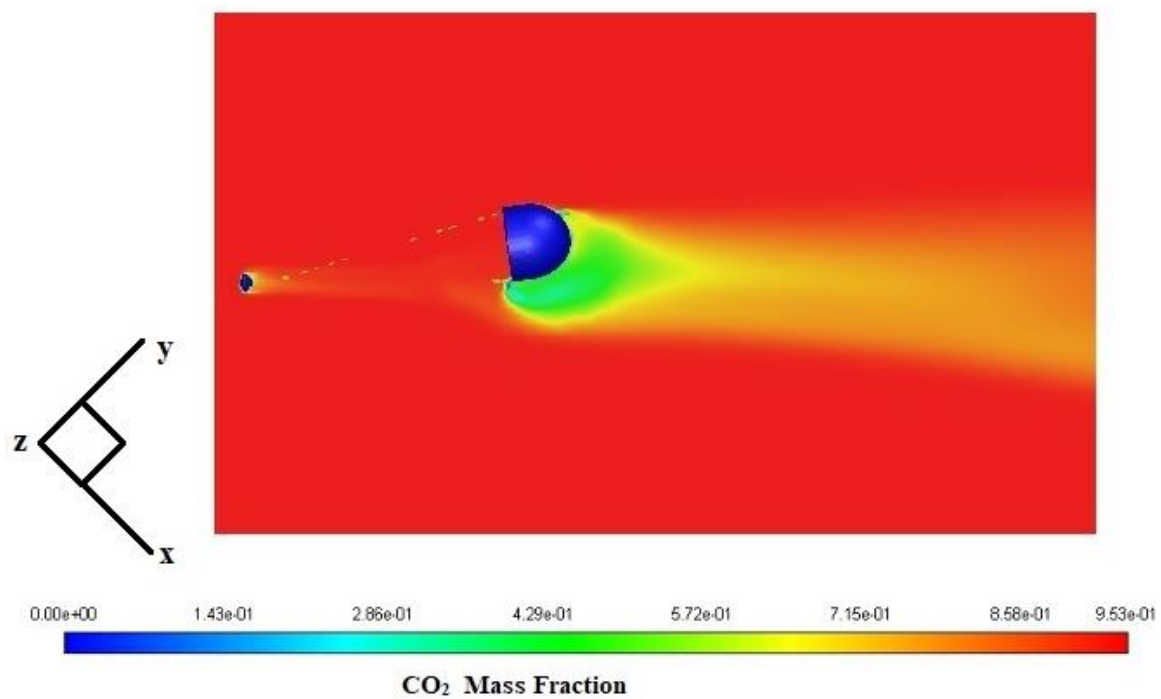


Fig 188. CO₂ Mass fraction contour for Re-entry parachute at $\alpha = 20^\circ$, $H=10\text{km}$ and $M=2.04814$

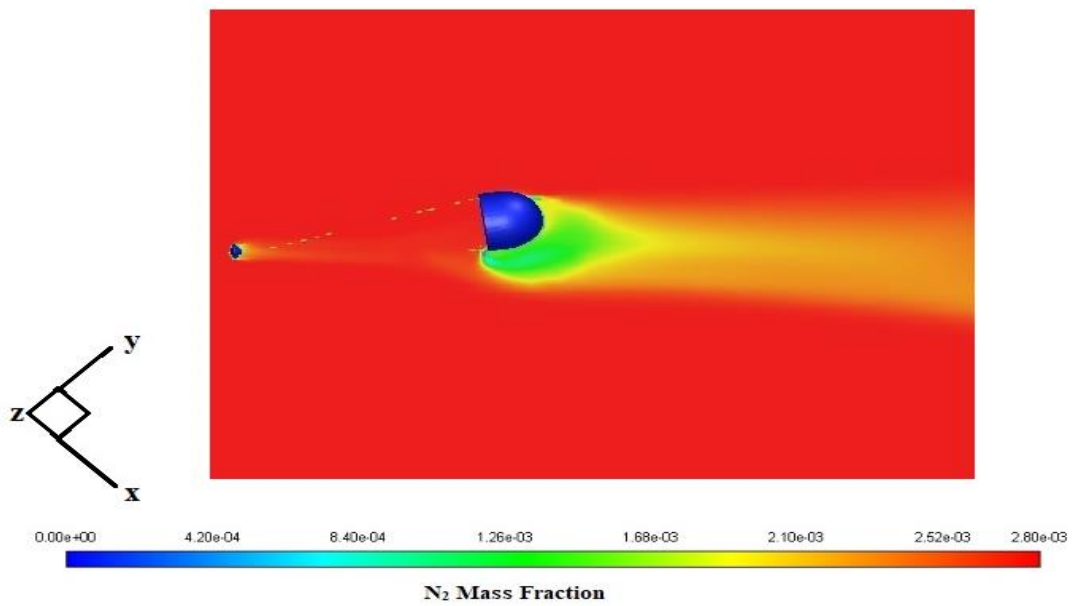


Fig 189. N₂ Mass fraction contour for Re-entry parachute at $\alpha = 20^\circ$, $H=10\text{km}$ and $M=2.04814$

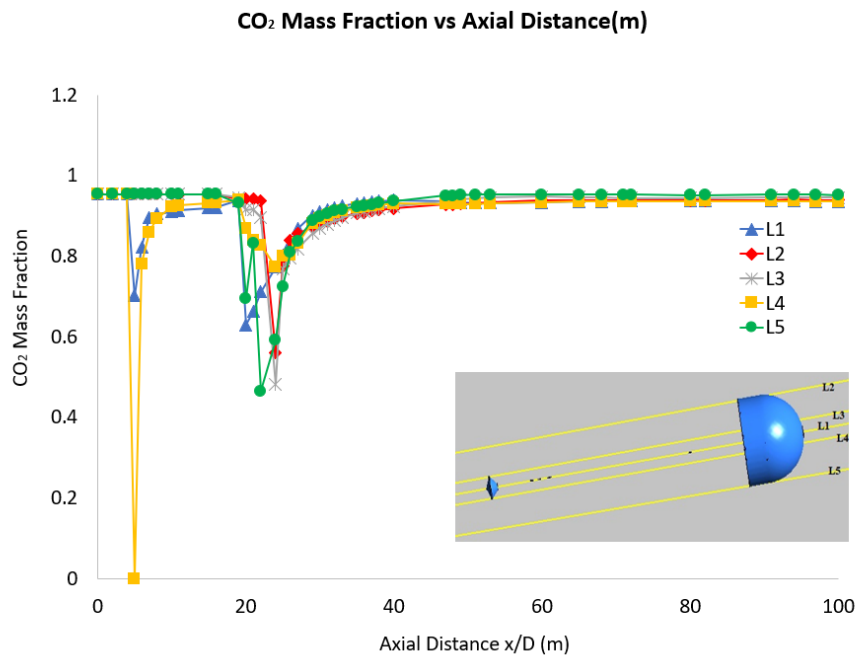


Fig 190. CO₂ Mass fraction along the domain axial distance at $\alpha = 20^\circ$, H=10km, M=2.04814 and domain length = 120m

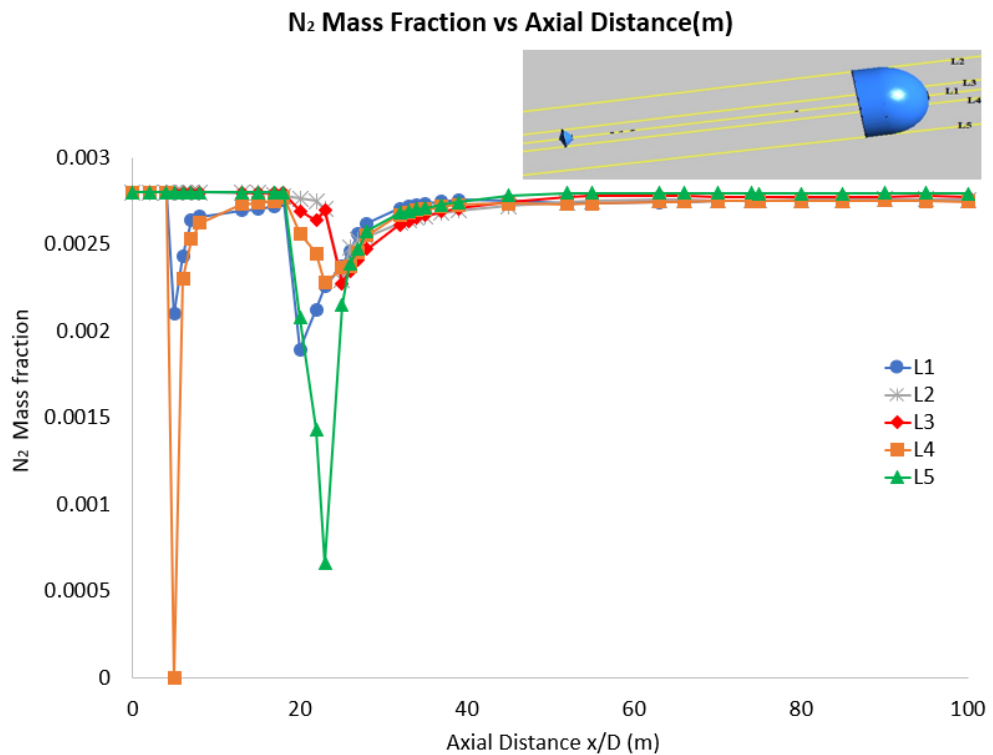


Fig 191. N₂ Mass fraction along the domain axial distance at $\alpha = 20^\circ$, H=10km, M=2.04814 and domain length = 120m

Fig 190 and Fig 191 shows the Mass fraction of CO₂ and N₂ is constant from 0m to 16 m (L2, L3 and L5) whereas Mass fraction of CO₂ is constant till 4m in L1 and L4. This happens due to the shockwave detached at lower mass fraction from front end of capsule at same 0.0001m(see Fig 188 – Fig 189). The mass fraction becomes zero at 5m in the direction of L4. It decreases and increases again from till 55m (see Fig 190 - Fig 191) in all the direction of lines as recompression shocks arises at aft body of canopy due to oscillation of Schiaparelli parachute in Martian atmosphere at $\alpha=20^\circ$ (see Fig 188 -Fig 189). The CO₂, N₂ Mass fraction become constant till from 55m to 100m (see Fig 190 and Fig 191) due to turbulent wake (TW₂) region travels at cross path at aftbody of canopy (see Fig 188, Fig 189 and Fig 192).

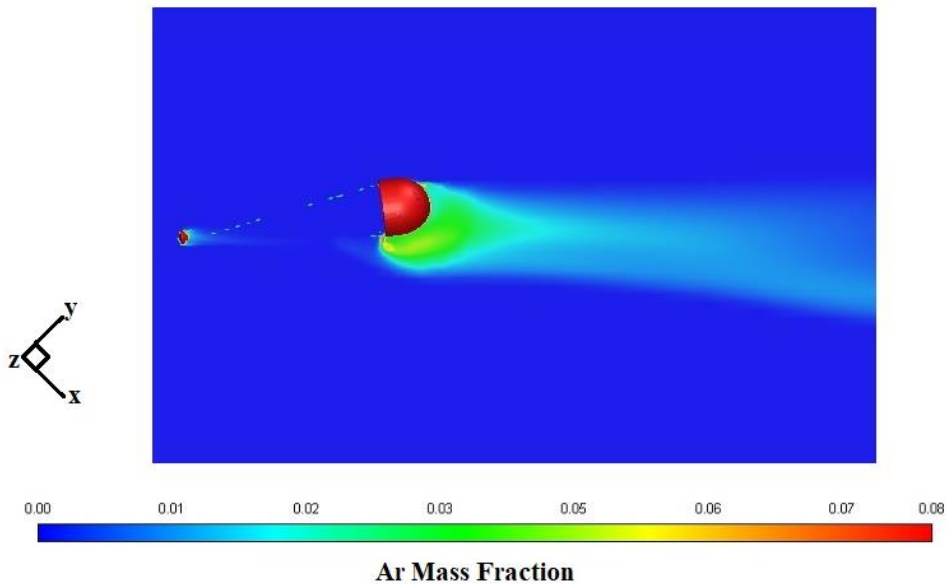


Fig 192. Ar Mass fraction contour for Re-entry parachute at $\alpha = 20^\circ$, H=10km and M=2.04814

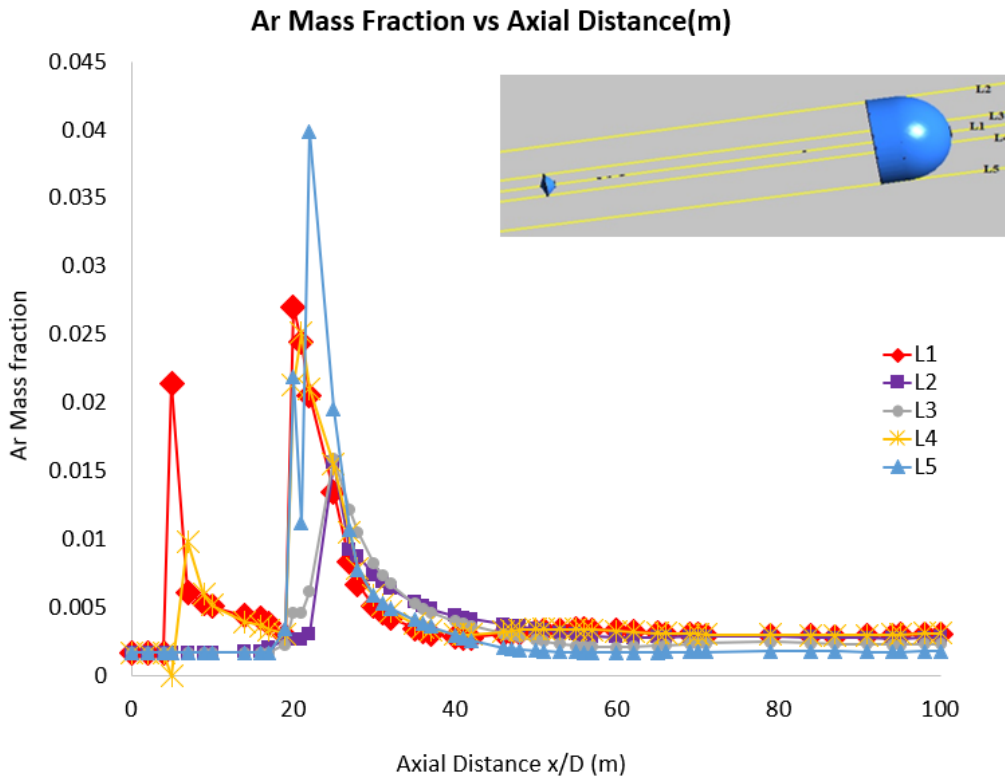


Fig 193. Ar Mass fraction along the domain axial distance at $\alpha = 20^\circ$, $H=10\text{km}$, $M=2.04814$ and domain length = 120m

Fig 192 Shows the Mass fraction of Argon at $\alpha = 20^\circ$. Fig 193 shows the mass fraction of Ar has a peak of 0.0398979 in the direction of line L5.

Among all these in final trajectory of the Schiaparelli re-entry parachute the flow of wake shock interaction ($\text{RS}_1\text{-TW}_1\text{-BS}_1$) between the Capsule and Canopy became stable at $\alpha=0^\circ$ whereas the wake shock interaction is crossed at $\alpha = 20^\circ$. The shockwaves are detached in front of capsule and Parachute at high pressure, density, Temperature, Mach number and also maximum mass fraction of perfect gases like CO_2 , N_2 and Ar. So, the trajectory of Schiaparelli re-entry parachute travels in right direction at $\alpha = 0^\circ$ at $M = 1.75$ to 2.

CHAPTER 8

FINAL REMARKS

The present work made deals with an analysis of Schiaparelli Re-Entry anomaly on Mars. The pre-flight aerodynamic results generated by the TAS-I, the company in charge of the mission, were used together with a three-dimensional Navier-Stokes and Euler computational fluid dynamics simulations performed here. In particular, the supersonic flow field past the Schiaparelli capsule seems to be relevant to generate a potential asymmetry of the wake arriving to the parachute.

In the present analysis, only continuum regime (supersonic speed ranges) of the flow was modelled, both as ideal gas and reacting gas mixture. A comparison of results with various research articles has been done based on hypersonic panel methods with the help of RANS and Chemical Transport which have been relevant to develop a preliminary capsule and canopy database at Mach number range between $M=1.94$ and $M= 20$. Engineering based analysis based on supersonic and transonic panel methods has been extensively used to rapidly develop a very preliminary capsule and canopy aerodynamic database.

The numerical computation has been done at various altitudes i.e., the ideal gas (at $H=10\text{km}$ above mars) and reacting gas (at $H = 20\text{km}$ and $H = 50\text{km}$ above Mars) method of simulation is performed for Capsule and only the ideal gas (at $H = 10\text{km}$ from mars) method is performed for Canopy at $M=2.04814$ which follows supersonic regime.

The numerical investigation about final trajectory of Schiaparelli Capsule with Canopy in Aereal oscillations and Parachute deployment has undergone at $H = 10\text{km}$ above Mars with $\alpha = 0^\circ$ and 20° . This research follows the possible oscillating regime

of supersonic between $M=1.75$ and $M=2.04814$ with the help of RANS and Large Eddy Simulations (LES) by using chemical transport.

Finally, numerical results show that ideal and real gas effects increase in the aerodynamic drag and Lift whereas the ballistic is only slightly influenced. Pressure flow field is not axisymmetric due to formation of wake at downstream of the capsule and shockwaves at upstream of parachute which creates turbulence flow at the time of final trajectory. So, It is critical to find the interaction between wake of the capsule and canopy.

Moreover, several results comparisons highlight that experimental and CFD aerodynamic findings available for the Schiaparelli in Martian's atmosphere adequately represent the static coefficients of the other space anomalies in the Mars atmosphere.

Concerning the Schiaparelli anomaly, the results presented here suggests that the lateral aerodynamic coefficients of the parachute can be bigger than the maximal values expected not including the instability effects on the parachute due to the wake asymmetry (only for experimental). These larger values are compatible with the fast oscillations that saturated the gyro of the inertial unit system and produced a useless and fatal chain of commands to recover the wrong attitude measured by the on-board computer by the too long duration of the saturation persistence.

REFERENCES

1. Toni Tolker-Nielsen, "EXOMARS 2016 - Schiaparelli Anomaly Inquiry", DG-I/2017/546/TTN, Issue 1, May 2017 p33-p128, European Space Agency (ESA).
2. ESA notes about Schiaparelli Capsule Design by Prof. Paolo Teofilatto.
3. ESA notes about Schiaparelli Mission and Parachute by Prof. Paolo Teofilatto.
4. ESA notes on Schipparelli <http://www.esa.gov.it>.
5. Davide Bonetti, Gabriele De Zaiacomo, Gonzalo Blanco Arnao, Irene Pontijas Fuentes, "Exo-Mars Mission Analysis Phase-E, ExoMars 2016 Phase E4, EDL Post Flight Analyses", EXM16E-DMS-TEC-TNO10-E-R, Issue 1, February 2017, pp1-pp135.
6. F. Cianfrocca, S. Potrigliotti, EXOMARS EDM- Consolidated Report on E2E Analyses, EXM-DM-VRP-AI-0015, Issue 12,April 2016,Thales Alenia Space Agency.
7. P. Smith, Bryan C. Yount, Ethiraj Venkatapathy, Eric C. Stern, Dinesh K. Prabhu, Daniel K. Litton, "Progress in Payload Separation Risk Mitigation for a Deployable Venus Heat Shield" AIAA 2013-1371, Mar 2013, <https://doi.org/10.2514/6.2013-1371>.
8. Paolo Teofilatto, "Schiaparelli anomaly by aerodynamic torque", Note for Schiaparelli Inquiry Bord, March 13, 2017.
9. Calculations of zonal harmonic representation of planetary gravity - Simulink - MathWorks Italia Mars Fact Sheet (nasa.gov),MATLAB 2021a.
10. Antonio Genova, PGDA - Mars Gravity Field: GMM-3 (nasa.gov).
11. Mars' atmosphere: Facts about composition and climate (space.com).

12. Francois Forget, Franck Montmessin, Jean-Loup Bertaux, Francisco Gonza'lez-Galindo, Sebastien Lebonnois, Eric Quemerais, Aurelie Reberac, Emmanuel Dimarellis, Miguel A, "Density and temperatures of the upper Martian atmosphere measured by stellar occultations with Mars Express SPICAM", JOURNAL OF GEOPHYSICAL RESEARCH, VOL. 114, E01004, 28 January 2009, doi:10.1029/2008JE003086.
13. <https://www.grc.nasa.gov/WWW/K-12/airplane/atmosmrm.html>-Mars Atmospheric Models-Metric units.
14. Laxmi Narayana Phaneendra Peri, "Numerical Investigation of the Aerothermodynamics of a Hypersonic Re-entry Capsule", Master Thesis Report, Università La Sapienza Di Roma, 2021.
15. Fletcher C.A.J.: 1988, "Computational Techniques for Fluid Dynamics (Vol I)", Springer Verlag, Berlin
16. Amsden A.A., O'Rourke P.J., Butler T.D.: 1989, "KIVA-II: A Computer Program for Chemically Reactive Flows with Sprays", Los Alamos National Laboratory Report LA-11560-MS, Los Alamos, NM.
17. Versteeg H.K., Malalasekera W.: 1995, "An Introduction to Computational Fluid Dynamics", Pearson Education Limited, Harlow.
18. ANSYS Inc.:2009-02-09, "ANSYS fluent 12.0 Solver Theory Guide", ANSYS Europe Ltd.
19. O.R. Kummitha, Numerical analysis of hydrogen fuel scramjet combustor with turbulence development inserts and with different turbulence models, Int. J. Hydrogen Energy 42 (9) (2017) 6360– 6368. <https://doi.org/10.1016/j.ijhydene.2016.10.137>.
20. O.R. Kummitha, L. Suneetha, K. Pandey, Numerical analysis of scramjet combustor with innovative strut and fuel injection techniques, Int. J. Hydrogen Energy 42 (15) (2017) 10524–10535. <https://doi.org/10.1016/j.ijhydene.2017.01.213>.

21. C. Park, J. T. Howe, R. L. Jaffe, and G. V. Candler, "Review of chemical-kinetic problems of future NASA missions—II: Mars entries," *Journal of Thermophysics and Heat Transfer*, vol. 8, no. 1, pp. 9–22, 1994.
22. V. Hannemann and A. Mack, "Chemical non equilibrium model of the Martian atmosphere," in *Proceedings of the 6th European Symposium on Aerothermodynamics for Space Vehicles*, ESA, Versailles, France, 2008, ESA SP-659.
23. E. V. Kustova, E. A. Nagnibeda, Y. D. Shevelev, and N. G. Syzranova, "Comparison of non-equilibrium supersonic CO₂ flows with real gas effects near a blunt body," in *Proceedings of the 6th European Symposium on Aerothermodynamics for Space Vehicles*, ESA, Versailles, France, 3–6 November 2008 (ESA SP-659, January 2009).
24. Pezzella G, Viviani A., "Aerodynamic Analysis of a Manned Space Vehicle for Missions to Mars. *Journal of Thermodynamics*" 2011; 2011:1–13. <https://doi.org/10.1155/2011/857061>.
25. D. K. Prabhu, "System design constraints-trajectory aerothermal environments," in *Critical Technologies for Hypersonic Vehicle Development*, RTO AVT/VKI Lecture Series, Von Karman Institute for Fluid Dynamics, Rhode Saint Genese, Belgium, 2004.
26. J. D. Anderson, *Hypersonic and High Temperature Gas Dynamics*, McGraw-Hill, New York, NY, USA, 1989.
27. P. Gnoffo, R. Braun, K. Weilmuenster, R. Mitcheltree, W. Engelung, and R. Powell, "Prediction and validation of Mars pathfinder hypersonic aerodynamic data base," in *Proceedings of the 7th AIAA/ASME Joint Thermophysics and Heat Transfer Conference*, Albuquerque, NM, USA, 1998.
28. P. A. Gnoffo, K. J. Weilmuenster, R. D. Braun, and C. I. Cruz, "Influence of sonic-line location on Mars Pathfinder Probe aerothermodynamics," *Journal of Spacecraft and Rockets*, vol. 33, no. 2, pp. 169–177, 1996.

29. R. N. Gupta, K. P. Lee, and C. D. Scott, "Aero thermal study of Mars Pathfinder aeroshell," *Journal of Spacecraft and Rockets*, vol. 33, no. 1, pp. 61–69, 1996.
30. C. Park, J. T. Howe, R. L. Jaffe, and G. V. Candler, "Review of chemical-kinetic problems of future NASA missions—II: Mars entries," *Journal of Thermophysics and Heat Transfer*, vol. 8, no. 1, pp. 9–22, 1994.
31. J. J. Bertin, *Hypersonic Aero thermodynamics*, AIAA Education Series, AIAA, Washington, DC, USA, 1994.
32. C. Anbu Serene Raj, M. Narasimha Vardhan, N. Vaishnavi, S. Aravindan, A. Al-Arjani, S. Nadarajapillai "Aerodynamics of ducted re-entry vehicles" Volume 33, Issue 7, July 2020, Pages 1837-1849 <https://doi.org/10.1016/j.cja.2020.02.019>.
33. A. Aboudan, G. Colombatti , C. Bettanini , F. Ferri , S. Lewis , B. Van Hove, O. Karatekin, S. Debei "ExoMars 2016 Schiaparelli Module Trajectory and Atmospheric Profiles Reconstruction- Analysis of the On-board Inertial and Radar Measurements" *Space Sci Rev* (2018) 214:97 ,<https://doi.org/10.1007/s11214-018-0532-3>.
34. Xiaopeng Xue , Chih-Yung Wen, "Review of unsteady aerodynamics of supersonic parachutes", *Progress in Aerospace Sciences*,Volume 125, 1 August 2021, 100728, <https://doi.org/10.1016/j.paerosci.2021.100728>.
35. Raudhah Saim, Sofian Mohd, Syariful Syafiq Shamsudin, Mohd Fadhli Zulkafli, Siti Nur Mariani Mohd Yunos, Muhammad Riza Abd Rahman "Computational Fluid Dynamic (CFD) Analysis of Parachute Canopies Design for Aludra SR-10 UAV as a Parachute Recovery Systems (PRS)" ISSN: 2180-1363, *CFD Letters* 12, Issue 2 (2020) 46-57.
36. Gao Xinglong, Zhang Qingbin, Tang Qiangang , "Parachute dynamics and perturbation analysis of precision airdrop system", *Chinese Journal of Aeronautics* ,Volume 29, Issue 3, June 2016, Pages 596-607, <https://doi.org/10.1016/j.cja.2016.04.003>.
37. K. Karagiozis, R. Kamakoti, F. Craik, C. Pantano, "A computational study of supersonic disk-gap-band parachutes using Large-Eddy Simulation coupled to a

- structural membrane”, Journal of Fluids and Structures, Volume 27, Issue 2, February 2011, Pages 175-192.
38. Johari, H., Levshin, A., “Interaction of a line vortex with a round parachute canopy”, Journal of Fluids and Structures 25 (8), 1258–1271, 2009.
39. Johnson, C., “Investigation of the characteristics of 6-foot drogue-stabilization ribbon parachutes at high altitudes and low supersonic speeds”, Technical Report X-448, NASA, Washington, D.C., USA, 1960.
40. Barnhardt, M., Drayna, T., Nompelis, I., Candler, G., Garrard, W., “Detached eddy simulations of the MSL parachute at supersonic conditions”, In: 19th AIAA Aerodynamic Decelerator Technology Conference and Seminar, Williamsburg, VA, USA, 2007.
41. Ross, R., Nebiker, F., “Survey of aerodynamic deceleration systems”, In: Third AIAA Annual Meeting, No. 66–988, Boston, MA, USA, 1966.
42. Xue YANG , Li YU , Min LIU , Haofei PANG , “Fluid structure interaction simulation of supersonic parachute inflation by an interface tracking method”, Chinese Journal of Aeronautics, Volume 33, Issue 6, June 2020, Pages 1692-1702, <https://doi.org/10.1016/j.cja.2020.03.005>.
43. Clara O'Farrel, Suman Muppudi, Joseph Brock, John W. Van Norman, Ian G. Clark “Development of Models for Disk-Gap-Band Parachutes Deployed Supersonically in the Wake of a Slender Body” 978-1-5090-1613-6/17/\$31.00, 2017 IEEE.
44. H. Akash, S. Aravind Raj, D. Sathish, A. Anish Kumar, H. Balaji, “Design and Computational Analysis of Da Vinci Parachute: Design in Steady and Unsteady Flow with Varying Vent Hole Ratio”, International Journal of Research in Engineering, Science and Management Volume 4, Issue 4, April 2021 [https://www.ijresm.com | ISSN \(Online\): 2581-5792](https://www.ijresm.com | ISSN (Online): 2581-5792).
45. M. Dawoodian, A. Dadvand, and Amir Hassan Zadeh, “A Numerical and Experimental Study of the Aerodynamics and Stability of a Horizontal Parachute,

Hindawi Publishing Corporation", ISRN Aerospace Engineering ,Volume 2013, Article ID 320563, 8 pages <http://dx.doi.org/10.1155/2013/320563>.

46. Yu Li, Cheng Han, Zhan Yanan, Li Shaoteng "Study of parachute inflation process using fluid–structure interaction method", Chinese Journal of Aeronautics, 27(2), April 2014, Pages 272-279, <https://doi.org/10.1016/j.cja.2014.02.021>.
47. Daniel Z. Huang, Philip Avery, Charbel Farhat "Modelling simulation and validation of supersonic parachute inflation dynamics during Mars landing" AIAA SciTech Science Forum January 2020, <https://doi.org/10.2514/6.2020-0313>.
48. Giorgio Guglieri, "Parachute-Payload System Flight Dynamics and Trajectory Simulation", International Journal of Aerospace Engineering Volume 2012, Article ID 182907, 17 pages <https://doi:10.1155/2012/182907>.
49. Xiaopeng XUE, Hiroto KOYAMA and Yoshiaki NAKAMURA, "Numerical Simulation of Supersonic Aerodynamic Interaction of a Parachute System" Trans. JSASS Aerospace Tech. Japan Vol. 11, pp. 33-42, 2013.
50. Xiaopeng Xue, Yoshiaki Nakamura, Koichi Mori, Chih-Yung Wen, He Jia "Numerical investigation of effects of angle-of-attack on a parachute-like two-body system", Aerospace Science and Technology, Volume 69, October 2017, Pages 370-386. <https://doi.org/10.1016/j.ast.2017.06.038>.
51. Hang Yu, Carlos Pantano, Fehmi Cirak, "Large-Eddy Simulation of Flow Over Deformable Parachutes using Immersed Boundary and Adaptive Mesh", AIAA SciTech Science Forum, January 2019, DOI: 10.2514/6.2019-0635.
52. Xiaoping XUE , He JIA, Wei RONG , Qi WANG , Chih-yung Wen, "Effect of Martian atmosphere on aerodynamic performance of supersonic parachute two-body systems", Chinese Journal of Aeronautics, Volume 35, Issue 4, April 2022, Pages 45-54, <https://doi.org/10.1016/j.cja.2021.05.006>.
53. Xiaopeng XUE and Yoshiaki NAKAMURA, "Numerical Simulation of a Three-Dimensional Flexible Parachute System under Supersonic Conditions" Trans.

JSASS Aerospace Tech. Japan Vol. 11, pp. 99-108,
2013,<https://doi.org/10.2322/tastj.11.99>.

54. Lingard, J., Darley, M. and Underwood, J.C.: "Simulation of Mars Supersonic Parachute Performance and Dynamics", AIAA Paper 2007-2507, 2007,<https://doi.org/10.2514/6.2007-2507>.
55. Xue XP, Nishiyama Y, Nakamura Y, Chin Yung wen, "Parametric study on aerodynamic interaction of supersonic parachute system" AIAA Journals 2015;53(9):2796–801. <https://doi.org/10.2514/1.J053824>
56. Xue XP, Koyama H, Nakamura Y, et al. "Effects of suspension line on flow field around a supersonic parachute" Aerospace Science and Technology 2015; 43:63–70. <https://doi.org/10.1016/j.ast.2015.02.014>.